An Innovative Dual Concentrically-Braced Moment-Resisting Steel Frame for Increased Seismic Resilience

Marco Baiguera

Submitted for the degree of Doctor of Philosophy

Heriot-Watt University

School of Energy, Geoscience, Infrastructure & Society

November 2017

Abstract

Improving seismic resilience of buildings is one of the current challenges in structural engineering. In the context of steel structures, design of conventional systems in accordance to current codes aims at preventing collapse and ensuring life safety under the design earthquake. However, in major seismic events, these systems have experienced extensive damage in the main structural members and large residual drifts, causing downtime and significant socio-economic losses.

This thesis presents the development and validation of an innovative dual steel frame that reduces structural damage and residual drifts for enhanced seismic performance. The proposed system consists of a moment-resisting frame with concentric braces equipped with seismic dampers. These are stainless steel pins with high post-yield stiffness, placed in series with the bracing members. Replaceable elements are inserted in the beams to absorb plastic deformations that would concentrate in the beam-column connections.

The seismic performance of the proposed dual frame is evaluated using experimentally-validated finite element models of a prototype steel building. The numerical results show that, under the design and maximum earthquakes, residual storey drifts are minimised due to the high post-yield stiffness of the seismic dampers and the elastic deformation capacity of the moment frame. Structural damage is concentrated in the replaceable seismic devices, indicating the potential for a quick recovery after a strong earthquake.

The collapse potential of the proposed frame is also investigated. The fracture capacity of the seismic dampers is experimentally evaluated using two full-scale geometries in a configuration reproducing the damper-brace connection. Criteria for predicting ductile fracture under ultra-low cycle fatigue are calibrated using coupon specimens and complementary finite element analyses, and validated performing explicit simulations of the full-scale tests. The collapse of the dual frame is studied by means of incremental dynamic analyses explicitly simulating the ductile fracture of the seismic dampers. The results show that the dual frame has a superior seismic resistance against collapse as a result of the large energy dissipation and fracture capacities of the seismic dampers.

Acknowledgments

I would like to express my sincere gratitude to my supervisor, Dr. George Vasdravellis, for his guidance, dedication and support throughout my research. I would also like to thank Prof Theodore L. Karavasilis for his invaluable advice and the fruitful discussions.

I wish to acknowledge the financial support of EPSRC and James Watt Scholarship for my studies at Heriot-Watt University.

I gratefully acknowledge the valuable assistance of the technical staff of the Heavy Structures Lab at Heriot-Watt University, Mr. Tom Ferguson, Mr. Tom Stenhouse, Mr. David Murray and Mr. Alastair MacFarlane. I would like to truly thank David Reichardt for his enthusiastic help during the lab experiments, without whom I would not have been able to run the tests so easily.

A great thanks to all the fellow PhDs from the office (now portakabin!), who have shared these years with me. A special mention to Sash, Zanyar, DJ and Dr. Ji for the breaks together and the nice gatherings. Thanks to Liam and Federica for being such generous hosts and also good friends.

To Francesca, words can not express how much I owe you for your tireless support and constant encouragement.

Thanks to my family, for their endless support and optimism.

ACADEMIC REGISTRY
Research Thesis Submission

Name*:*	Marco Baiguera		
School:	School of Energy, Geoscience, Infrastructure and Society		
Version: *(i.e. First, Resubmission, Final)*	Final	Degree Sought:	PhD

Declaration

In accordance with the appropriate regulations I hereby submit my thesis and I declare that:

1) the thesis embodies the results of my own work and has been composed by myself
2) where appropriate, I have made acknowledgement of the work of others and have made reference to work carried out in collaboration with other persons
3) the thesis is the correct version of the thesis for submission and is the same version as any electronic versions submitted*.
4) my thesis for the award referred to, deposited in the Heriot-Watt University Library, should be made available for loan or photocopying and be available via the Institutional Repository, subject to such conditions as the Librarian may require
5) I understand that as a student of the University I am required to abide by the Regulations of the University and to conform to its discipline.
6) I confirm that the thesis has been verified against plagiarism via an approved plagiarism detection application e.g. Turnitin.

* *Please note that it is the responsibility of the candidate to ensure that the correct version of the thesis is submitted.*

Signature of Candidate*:*		Date:	

Submission

Submitted By *(name in capitals):*	
Signature of Individual Submitting:	
Date Submitted:	

For Completion in the Student Service Centre (SSC)

Received in the SSC by *(name in capitals):*			
Method of Submission *(Handed in to SSC; posted through internal/external mail):*			
E-thesis Submitted ***(mandatory for final theses)***			
Signature:		Date:	

Please note this form should be bound into the submitted thesis.
Academic Registry/Version (1) August 2016

Contents

List of Figures

List of Tables

List of Publications by the Candidate

Referred Journals

Baiguera M., Vasdravellis G. & Karavasilis T.L. (2016), 'Dual seismic-resistant steel frame with high post-yield stiffness braces for residual drift reduction: numerical evaluation', *Journal of Constructional Steel Research*, **122**, 198−212.

Baiguera M., Vasdravellis G. & Karavasilis T.L. (under review), 'Ultra-low cycle fatigue tests and fracture prediction models for duplex stainless steel devices of high-performance braced frames', *Journal of Structural Engineering*.

Vasdravellis G., Baiguera M. & Al-Samaraie D. (2018), 'Progressive collapse simulation of a steel self-centering moment resisting frame', *Journal of Constructional Steel Research*.

Refereed Journals (in preparation)

Baiguera M., Vasdravellis G. & Karavasilis T.L., 'Earthquake-induced collapse performance of a dual seismic-resistant frame with high post-yield stiffness dampers', *Earthquake Engineering & Structural Dynamics*.

Refereed Conference Proceedings

Baiguera M., Vasdravellis G. & Karavasilis T.L. (2017), Seismic collapse assessment of an innovative dual steel frame with high post-yield stiffness energy dissipation devices, *in* 'International Workshop on Performance-Based Seismic Design of Structures (PESDES 2017)', Beskos D., Zhou Y., Qian J., Lu X. eds., 13-15 October, Tongji University, Shanghai, China.

Baiguera M., Vasdravellis G. & Karavasilis T.L. (2017), Experimental evaluation and explicit fracture simulations of stainless steel seismic dampers, *in* '8th European Conference on Steel and Composite Structures (Eurosteel 2017)', 13-15 September, Copenhagen, Denmark.

Baiguera M., Vasdravellis G. & Karavasilis T.L. (2016), Experimental validation of high post-yield stiffness dampers for residual drift reduction, *in* '8th International Conference on Steel and Aluminium Structures (ICSAS 2016)', 7-9 December, Hong Kong, China.

Baiguera M. & Vasdravellis G. (2015), Dual seismic-resistant steel frame with high post-yield stiffness braces for residual drift reduction: numerical evaluation, *in* '3rd Infrastructure and Environment Scotland Postgraduate Conference (IES 2015)', 9 December, Heriot-Watt University, Edinburgh.

Baiguera M., Vasdravellis G. & Karavasilis T.L. (2015), Seismic resistant steel frame with replaceable fuses and dissipative braces: numerical analysis and design, *in* '8th International Conference on Advances in Steel Structures (ICASS 2015)', 21-24 July, Lisbon, Portugal.

List of Abbreviations

BRB Buckling-Restrained Brace

BRBF Buckling-Restrained Braced Frame

BRBF-MRF Dual Moment-Resisting Buckling-Restrained Braced Frame

CA Constant Amplitude

CBF Concentrically Braced Frame

CBF-MRF Dual Moment-Resisting Concentrically-Braced Frame

CNS Circumferentially-Notched Specimen

CVGM Cyclic Void Growth Model

DBE Design-Basis Earthquake (475-year return period, 10% probability of exceedance in 50 years)

EBF Eccentrically Braced Frame

ED Energy Dissipation Capacity

EDP Engineering Demand Parameter

FEM Finite Element Model

FOE Frequently-Occurred Earthquake (95-year return period, 50% probability of exceedance in 50 years)

FP Friction pads

IDA Incremental Dynamic Analysis

IM Intensity Measure

LCF Low Cycle Fatigue

MCE Maximum Considered Earthquake (2475-year return period, 2% probability of exceedance in 50 years)

MRF Moment-Resisting Frame

PT Post-Tensioned

SC Self-Centering

SMCS Stress Modified Critical Strain

SSD Duplex Stainless Steel

SSP Stainless Steel Pins

ULCF Ultra-Low Cycle Fatigue

VGM Void Growth Model

Chapter 1

Introduction

1.1 Research background

Current seismic design provisions focus on preventing building collapse under the design earthquake. This is achieved by introducing energy-dissipation mechanisms that ensure a ductile response of the structure. In conventional steel structures, such as moment-resisting frames (MRFs) and braced frames, specific structural elements are designed to dissipate the hysteretic energy while undergoing large inelastic deformations. This ductile behaviour ensures the paramount objective of life safety, but results in structural damage and permanent deformations that can translate into high repair costs and disruption to building use. For instance, MRFs have a highly ductile behaviour, but the formation of plastic hinges in the beams can cause extensive damage and residual drifts. Braced frames are generally employed to reduce storey drifts due to their high initial stiffness. However, conventional concentrically-braced frames (CBFs) have a degrading hysteretic behaviour that may result in damage concentration in certain stories, fracture and increased collapse potential. Buckling-restrained braced frames (BRBFs) and eccentrically-braced frames (EBFs) represent an improved class of braced frames that provide a highly ductile response, nonetheless they are prone to large residual drifts and structural damage when subjected to the design-basis earthquake.

Recent earthquakes have shown that economic losses due to extensive damage and residual storey drifts can be substantial, leading to costly repairs, downtime or even the building demolition. While a trade-off between the need for repairs and the rarity of a major earthquake is accepted in current seismic

design provisions, modern society demands for seismic resilient buildings that minimise the socio-economic losses due to structural damage and large residual drifts, and ensure a swift recovery after a major earthquake.

1.2 Research aim and objectives

This thesis aims to develop and validate a novel steel frame for improved seismic resilience. The proposed system is a moment-resisting frame equipped with concentric braces, denoted as dual CBF-MRF. Energy-dissipating stainless steel pins (SSPs) with high post-yield stiffness are placed in series with the concentric braces, and structural fuses are located in the beams where plastic hinges are expected to develop. The dual CBF-MRF is designed for: (a) residual drift reduction, by combining the elastic stiffness of the MRF with the high post-yield stiffness of the SSPs; and (b) damage mitigation in main structural members, by using replaceable energy-dissipating devices, i.e., the SSPs and beam fuses.

The objectives of this thesis are:

- To design a prototype building using the dual CBF-MRF as seismic-resistant system, following a performance-based design procedure and according to Eurocodes 3 and 8 (EC3 2003, EC8 2004).
- To numerically evaluate the seismic performance of the dual CBF-MRF, and to provide a comparison with a similar dual frame equipped with buckling restrained braces (BRBs).
- To experimentally evaluate the hysteretic response and fracture capacity of the SSPs used in the CBF-MRF.
- To numerically predict and simulate the fracture capacity of SSPs under cyclic loading using different fracture models.
- To assess the seismic collapse performance of the dual CBF-MRF in accordance with U.S. Federal Emergency Management Agency P695 guidelines (FEMA P695 2008).

1.3 Thesis outline

This thesis is divided into eight chapters, including this introduction, and four appendices.

Chapter 2 reviews the current seismic design strategies for steel buildings. First, conventional seismic-resistant steel frames are reviewed by examining their performance in terms of seismic resilience. Then, the latest design approaches for improving seismic resilience of steel structures are discussed.

Chapter 3 describes the design of the dual CBF-MRF proposed in this work. This frame is designed to have stiffness and strength comparable to a similar dual frame using an MRF coupled with BRBs, denoted as BRBF-MRF. A 6-storey prototype building is designed as either the dual CBF-MRF or the BRBF-MRF, following the provisions of EC3 (2003) and EC8 (2004) and appropriate capacity design rules.

Chapter 4 provides a comparison between the seismic performance of the proposed CBF-MRF and the conventional BRBF-MRF, by means of experimentally-validated finite element models (FEM). The hysteretic behaviour of the energy-dissipating devices of the CBF-MRF, i.e. the SSPs and the beam fuses, is calibrated against previous experimental data. Monotonic and cyclic nonlinear static analyses, as well as nonlinear dynamic analyses, are carried out to investigate the global and local behaviour of both systems. The dynamic time-history analyses are performed using a set of 22 earthquake records scaled to three different seismic hazard levels: the frequently-occurring earthquake (FOE, 95-year return period), the design-basis earthquake (DBE, 475-year return period), and the maximum-considered earthquake (MCE, 2475-year return period).

Chapter 5 presents the experimental full-scale tests on the SSPs, carried out in the Heavy Structures Lab at Heriot-Watt University. Two geometries of SSPs are tested in a configuration reproducing the SSP-brace connection. A total of sixteen tests are conducted under various loading protocols, including ultra low-cycle fatigue (ULCF) and monotonic loading. The results for the two SSP geometries are presented in terms of hysteretic behaviour, energy-dissipation, and ductile fracture capacity.

Chapter 6 is dedicated to the study of the fracture capacity of the SSPs. First, a review of the approaches for predicting ductile fracture in steel structures under cyclic loading is presented. Two types of fracture models are considered: a low-cycle fatigue (LCF) model and mechanics-based fracture criteria. The LCF parameters are calibrated against the experimental results on the SSPs. Two mechanics-based fracture criteria, i.e., the Cyclic Void Growth Model (CVGM) and the Abaqus fracture model, are also calibrated using experimental results from coupon notched specimens, and complementary FEM simulations. These two fracture models are validated through explicit numerical simulations of the ULCF experimental tests of SSPs, and their ability to predict the SSP fracture capacity is discussed.

Chapter 7 presents the assessment of the collapse potential of the dual CBF-MRF. Incremental dynamic analyses (IDA) are conducted on a simplified FEM model of the dual CBF-MRF that explicitly simulates the ductile fracture of the SSPs. A set of 24 ground motions are scaled to increasing intensities up to collapse according to FEMA P695 (2008). The IDA results are used to construct a fragility curve for the probabilistic evaluation of the collapse capacity of the proposed CBF-MRF.

Chapter 8 provides a detailed summary of the results obtained in this work, the main conclusions and recommendations for future research.

Chapter 2

Literature Review

This chapter presents a review of the seismic design approaches currently employed for steel structures, and discusses the need for improving their seismic resilience. First, conventional steel systems are described by identifying advantages and limitations of their seismic behaviour. Then, performance targets and the latest design strategies for seismic resilience are presented.

2.1 Conventional seismic-resistant steel structures

In this section, a review of the most commonly-used seismic-resistant steel frames is presented. Four framing systems are discussed: (1) moment-resisting frames (MRFs); (2) concentrically-braced frames (CBFs); (3) eccentrically-braced frames (EBFs); and (4) buckling-restrained braced frames (BRBFs). Their typical configuration is shown in Figure 2.1.

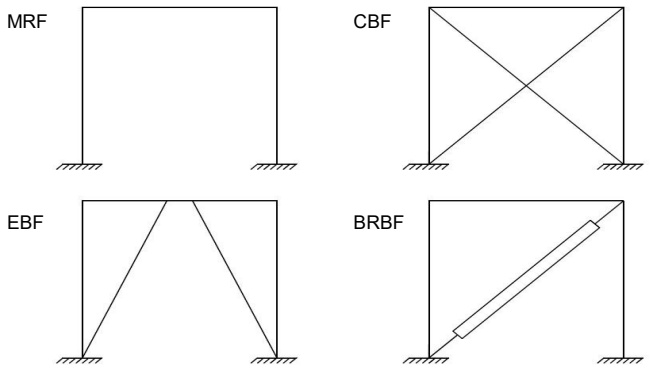

Figure 2.1. Conventional seismic-resistant steel frames

MRFs are highly ductile systems with appreciable lateral flexibility. In MRFs, lateral forces are resisted by bending, where energy is dissipated by the formation of plastic hinges. As soft storey mechanisms induced by plastic hinge formation in the columns are undesirable (Figure 2.2a), MRFs are designed according to the weak beam/strong column design approach, which promotes the formation of plastic hinges in the beams and at the base of the columns (Figure 2.2b). Since this global sway plastic mechanism ensures a large energy dissipation, current seismic codes assign to MRF the largest force reduction factors [American National Standards Institute/American Institute of Steel Construction 341/10 (ANSI/AISC 341/10 2010), Eurocode 8 (EC8 2004)]. However, due to their inherent low lateral stiffness, MRFs may be subjected to large drifts that can cause excessive non-structural damage and stability issues (Bruneau et al. 2011).

(a) (b)

Figure 2.2. Plastic hinging in MRFs: (a) strong beam/weak column; and (b) weak beam/strong column

The ductile behaviour of MRFs primarily relies on the performance of the beam-column connections, which are usually designed to be fully rigid. Prior to the 1994 Northridge earthquake, these connections typically consisted in welded beam flanges and a shear tab, as illustrated in Figure 2.3a (Chen et al. 1996). However, following the unexpected extent of weld failures observed in the aftermath of that earthquake, new moment connection configurations were introduced in seismic codes to ensure high plastic rotations without excessive strength degradation. The common strategy consisted in designing new details to ensure that plastic hinging would develop in the beam, away from the column face. Among the various connections proposed, the reduced beam

section (RBS) or 'dog-bone' connection is one of the most widely used. As shown in Figure 2.3b, a typical RBS is obtained by tapering the beam flanges according to a circular profile. However, as a result of their improved design, this new generation of connections experience extensive permanent deformations and local buckling under the design earthquake, resulting in large residual drifts (Ricles et al. 2001).

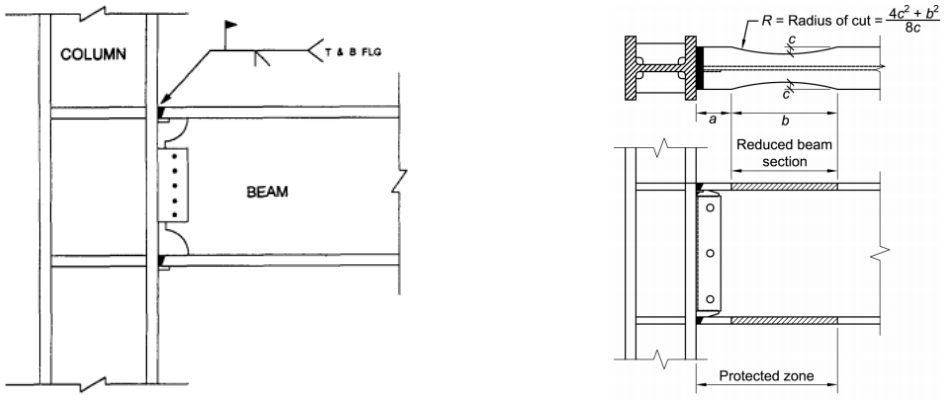

Figure 2.3. Moment-resisting beam-column connections: (a) Pre-Northridge (Ricles et al. 2001); and (b) RBS (ANSI/AISC 358/10 2010)

Due to the poor response of MRFs in the 1994 Northridge and 1995 Kobe earthquakes, CBFs gained more popularity, despite their comparatively limited architectural versatility (Bruneau et al. 2011). A CBF is a truss system that resists the seismic forces through the axial response of the braces, beams and columns. This system represents an effective and economical alternative to MRFs for controlling storey drifts due to their high lateral stiffness. Under severe earthquakes, the braces dissipate the hysteretic energy through tensile yielding, while, in compression, they experience elastic buckling and undergo large lateral deflections. Due to the strength degradation of the brace in compression, the typical post-buckling hysteretic behaviour of a CBF, illustrated in Figure 2.4, is asymmetric, resulting in a reduced energy dissipation capacity of the system. For this reason, current seismic provisions recommend for CBFs a lower behaviour factor than MRFs. According to capacity design principles, columns, beams and connections should be designed to be elastic (EC8 2004). However, in the case of out-of-plane buckling of the brace, the gusset connection should be carefully designed to accommodate large inelastic deformations (ANSI/AISC 341/10 2010). The reduced energy dissipation capacity is therefore associated

with significant damage in the bracing members and connections (Elghazouli 2009). This response can also limit the re-distribution of forces over the height of the building, resulting in a concentration of structural damage to few storeys and thus in an increase in the collapse potential of the structure (Sabelli et al. 2013). In addition, excessive deformation of the bracing members may produce significant damage on non-structural elements.

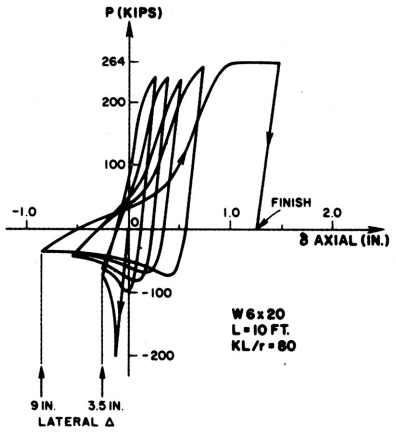

Figure 2.4. Hysteresis of a concentric brace under cyclic and axial loading (ANSI/AISC 341/10)

In the last decades, new framing systems have been developed to address the limitations concerning the MRFs and CBFs. EBFs and BRBFs represent an improved class of braced frames that provide both large energy dissipation capacity and high lateral stiffness, combining the advantages of MRFs and CBFs.

In EBFs, the brace axial forces are transferred either to a column or to another brace using a carefully-designed beam segment, typically referred as link (Popov & Engelhardt 1988). Figure 2.5 shows some representative configurations of EBFs, in which the hysteretic energy is dissipated by the link through yielding in shear or flexure. According to current seismic standards (EC8 2004, ANSI/AISC 341/10 2010), links are designed to act as the weakest elements, while the main structural members are designed to be elastic. This design strategy prevents the braces from buckling. The global behaviour of the system is governed by the link length (e), where the stiffness and strength of the frame typically increases for shorter links. In terms of yielding mechanism, long links yield in flexure, where short links dissipate energy through shear. Experimental studies have shown that the energy dissipation capacity of short links is greater than the one provided by flexural

plastic hinges (Okazaki et al. 2005). However, being the energy-dissipating link a segment of the beam, EBFs are prone to structural damage due to extensive inelastic deformations and localised buckling experienced by the link (Mansour et al. 2011). This can lead to disruptive and high cost repairs. In addition, large link rotations may cause non-structural damage to the concrete floor deck (Popov & Engelhardt 1988).

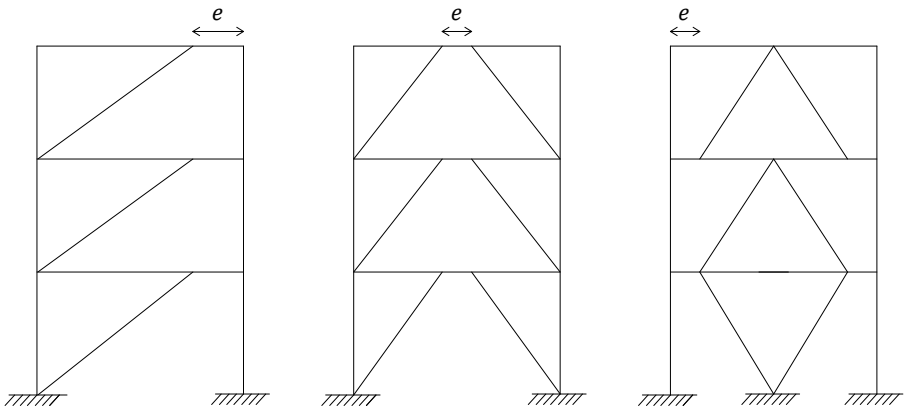

Figure 2.5. Typical configurations of eccentrically-braced frames

BRBFs are a relatively recent system, first proposed in Japan in the 1970s and extensively studied in North America after the 1994 Northridge earthquake (Fahnestock et al. 2007b). This system has been developed to overcome the disadvantages of CBFs in terms of hysteretic capacity and stiffness degradation due to brace buckling. A buckling-restrained brace consists of a steel core plate, which is restrained by a steel casing that allows the brace to yield in tension and compression (ANSI/AISC 341/10 2010). Strength is provided mainly by the energy-dissipating steel core, while the external casing is designed to provide sufficient flexural stiffness for preventing global buckling of the bracing member (Watanabe et al. 1988). As illustrated in Figure 2.6a, the steel casing is typically filled with mortar or concrete, while an unbonding material is inserted between the core and the mortar to allow the lateral expansion of the steel core under compression. Different configurations have been developed in the last two decades, as shown in Figure 2.6b. More recently, all-steel BRBs that do not use mortar or concrete have been proposed as an economical and demountable configuration. Instead of the traditional layer of unbonding material, a relatively small gap is left between the core and the casing (D'Aniello et al. 2008, Chou & Chen 2010).

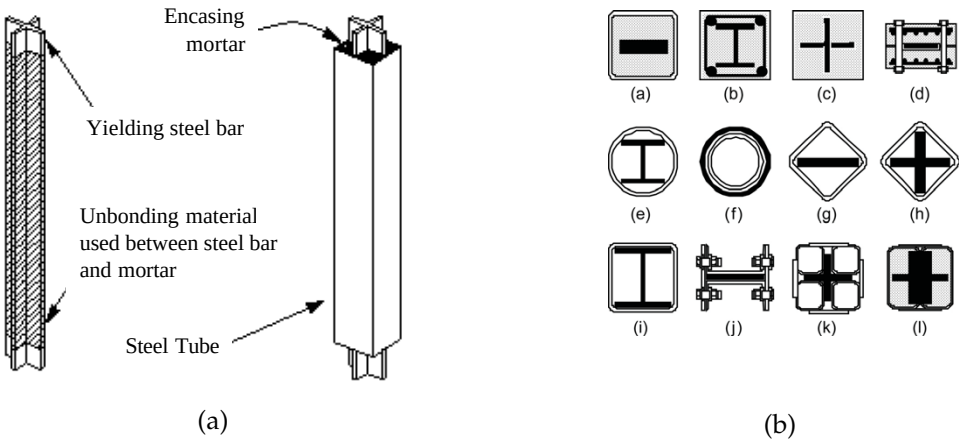

Figure 2.6. Buckling-restrained braces: (a) typical geometry (Sabelli et al. 2003); and (b) representative BRB cross-section configurations (Xie 2005)

BRBs typically ensure a full and symmetric hysteretic response with relatively low post-yield stiffness, providing large energy dissipation capacity to the frame. Experimental and numerical studies have shown that BRBs have the ability of withstanding significant ductility demands (Black et al. 2004, Fahnestock et al. 2007a). However, due to their low post-yield stiffness, damage may be concentrated at certain stories (Sabelli et al. 2003), causing significant residual drifts of the frame. In all-steel BRBs, excessive lateral thrusts exerted by the core against the casing may lead to the failure of bolted connections of the brace (Genna & Gelfi 2012). Also, detection and removal of the damaged BRB may result in a complex and rather disruptive task (Bruneau et al. 2011).

System	Advantages	Limitations
MRF	Excellent hysteresis	- Low lateral stiffness - Damage in beams (residual drifts)
CBF	High lateral stiffness	- Reduced energy dissipation - Damage in braces and connections
EBF	- High lateral stiffness - Excellent hysteresis	Damage in beams and floor deck
BRBF	- High lateral stiffness - Excellent hysteresis	Low post-yield stiffness (residual drifts)

Table 2.1. Review of conventional seismic-resistant steel framing systems

In conclusion, a summary of the advantages and limitations of the four conventional steel frames is provided in Table 2.1. Overall, these systems perform well under the design earthquake, but their main drawback is that they experience extensive structural damage and significant residual drifts.

2.2 Socio-economic impact of damage and residual drifts

The review presented in the previous section highlights how structural damage and residual drifts are the main issues affecting the seismic performance of conventional lateral load-resisting systems.

When a building experiences significant inelastic deformations, direct economic losses associated with repair, combined with the indirect economic losses due to downtime, can be substantial (Arup 2013). This was confirmed by recent seismic events, such as the 2010-2011 Christchurch earthquake series. After the most intense earthquake (6.3 magnitude) occurred on 22 February 2011, which caused widespread damage and the death of 185 people, field investigations recognised that the scale of devastation was mostly attributed to the collapse of unreinforced masonry buildings and few reinforced concrete buildings, while steel buildings performed fairly well (Clifton et al. 2011). The fact that most of the steel structures were recent, and therefore built according to the latest seismic provisions, greatly contributed to their satisfactory response. However, structural reports of steel buildings equipped with EBFs documented residual deformations at certain stories and, in few cases, unexpected fractures of the energy-dissipating links (Clifton et al. 2012, Kanvinde et al. 2015). Two examples of fractures of EBF links were reported in the Pacific Residential Tower, a 22-storey steel building, and in the parking garage of the Christchurch Hospital. These fractures did not lead to the collapse of the structures because of the redundancy provided by the EBF systems (Clifton et al. 2011). The Pacific Tower sustained a relatively low level of damage given the severity of the earthquake, but, despite that, it was reopened only two years later, following repair works that involved the replacement of several beam sections with the EBF links and the repair of cracked concrete slabs (Clifton et al. 2012). This example highlights the impact that repairing damage of structural elements can have on the ability of conventional steel systems to quickly return to service

after a strong earthquake.

Analytical and experimental studies have demonstrated that buildings that sustain large inelastic deformations are likely to experience residual drifts (MacRae & Kawashima 1997, Ruiz-Garcia & Miranda 2006*b*). Residual drifts may pose further complications for the resilience of steel frames. Iwata et al. (2006) studied the economic impact of residual drifts for a 12-storey steel building damaged during the 1995 Kobe earthquake. It was found that direct and indirect repair costs were not financially viable because residual drifts were greater than 0.5%. The same residual drift limit is also identified by McCormick et al. (2008), who established permissible residual deformation levels accounting not just for the economic losses, but also for the physiological and psychological effects on the building occupants. It was demonstrated that residual drifts greater than 0.5% are perceived by building occupants, causing dizziness and nausea. In addition, it was confirmed that such drifts would result in repairs that are more expensive than the demolition of the building.

Based on this evidence, Erochko et al. (2011) conducted a numerical study aimed to compare the residual drift response of a large number of MRFs and BRBFs designed in accordance with American Society of Civil Engineers/Structural Engineering Institute 7-16 (ASCE/SEI 7-16 2016). The residual drift value of 0.5% was assumed as the limit beyond which the building is no longer usable. It was found that the average MRF or BRBF has the potential of experiencing significant residual drifts under the design basis earthquake (DBE, 10% probability of exceedance in 50 years), with values in the range 0.8-1.8% for BRBFs and 0.5-1.2% for MRFs. These results indicate that, for a design-level seismic hazard, conventional steel frames are likely to be unusable due to large residual drifts, leading to costly repairs or possibly demolition.

2.3 Performance targets for seismic resilience

According to current seismic design provisions (ASCE/SEI 7-16 2016, EC8 2004), the performance objective for ordinary buildings under the DBE is ensuring life safety. For this performance level, structural and nonstructural damage is expected. As discussed in the previous sections, structural damage may translate into significant residual drifts that lead to economic losses and

downtime. To achieve seismic resilience, buildings should be designed to return to service within a short time after the DBE. Where current seismic codes do not provide an explicit performance index for residual drifts, the 0.5% residual drift limit previously discussed can be used as performance target.

Moreover, a resilient structure should provide a superior collapse margin than conventional seismic-resistant systems. In current regulations, collapse prevention under the Maximum Considered Earthquake (MCE, 2% probability of exceedance in 50 years) is implicitly guaranteed once the structure is designed to ensure life safety under the DBE. FEMA P695 (2008) has recently set a permissible probability of collapse for a seismic-resistant system equal to 10% under the MCE. Therefore, a resilient steel frame should offer far lower probabilities of collapse for this seismic hazard level (Tzimas et al. 2015).

In summary, seismic resilience can be achieved when the following performance targets are met:

1. under the DBE, residual drifts should not be greater than 0.5% to allow for a quick recovery after the seismic event.
2. under the MCE, the probability of collapse should be well below 10%.

2.4 Design strategies for increased seismic resilience

Innovative resilient-based design approaches have recently been proposed to mitigate the limitations of conventional steel systems and thus to enable a swift recovery in the aftermath of a strong earthquake (Arup 2013). This section presents an overview of some recently-proposed design approaches to mitigate the impact of structural damage and residual drifts.

2.4.1 Structural fuses

To reduce the impact of repair works, an effective strategy is to concentrate damage in replaceable devices, typically named in the literature as structural fuses. They represent an improved class of energy-dissipating devices that are designed to be easily inspected, repaired and replaced in the aftermath of an earthquake. As the main structural members are designed to be elastic, the

removal and replacement of structural fuses may facilitate the recentering of the structure (Bruneau et al. 2011).

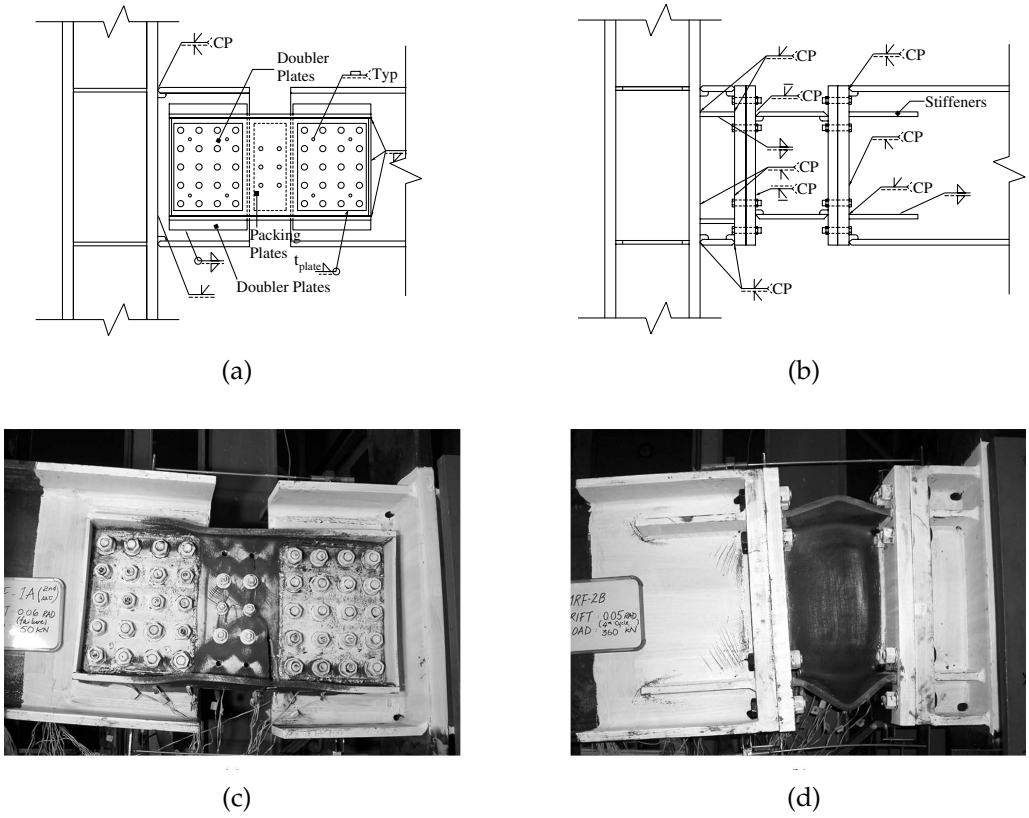

Figure 2.7. Geometry and experimental deformed shape of nonlinear replaceable links for MRFs: (a and c) bolted web link; and (b and d) end-plate link (Shen et al. 2011)

This section presents typical examples of structural fuses that have been developed to increase the repairability of MRFs and braced frames. The design of structural fuses for MRFs was first presented by Balut & Gioncu (2003). Disposable dog-bone connections were proposed as an alternative to conventional RBS connections. Instead of trimming the beam flanges, a reduced flexural capacity in the beam is achieved using either a bolted web connection or an I-section with bolted end-plates. The seismic performance of these structural fuses was experimentally investigated by Shen et al. (2011). Figures 2.7a and b illustrate the geometry of the replaceable elements, respectively a bolted web link and an end-plate link. The design rules for their implementation in a conventional MRF were discussed. It was demonstrated that, unlike the RBS, the design of the replaceable link has the advantage of being uncoupled from that of the beam, leading to a more efficient design of the moment-resisting

connections. The results of the experimental tests showed that connections equipped with replaceable links can achieve a comparable performance to RBS connections (Shen et al. 2011). The end-plate link was found to provide an enhanced and stable hysteretic dissipation. Strength degradation occurred only at high storey drifts (around 4%), due to local buckling in the beam flanges, as shown in Figure 2.7d. The bolted web links (Figure 2.7c) sustained higher plastic rotations without strength degradation, but exhibited a reduced energy dissipation capacity due to the slipping of the bolts. Castiglioni et al. (2012) conducted full-scale tests on a composite MRF with similar replaceable bolted connections. The results demonstrated the ability of the fuse elements to reduce damage in the main structural members.

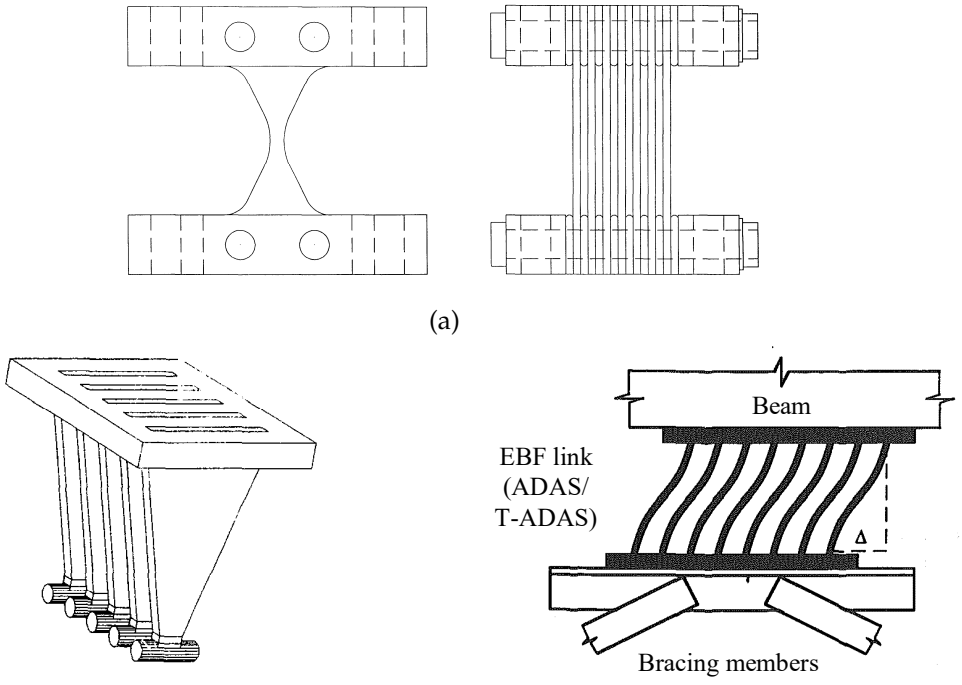

Figure 2.8. Steel yielding devices: (a) ADAS damper (Whittaker et al. 1991); (b) T-ADAS damper (Tsai & Li 1994); and (c) EBF link with ADAS/T-ADAS dampers (Xia & Hanson 1992)

In braced frames, yielding metallic devices have been typically used to increase the energy dissipation capacity and thus to reduce damage in the main structural members. However, these devices are not always designed to be replaceable. Based on the first concepts developed in New Zealand in the 1970s (Skinner et al. 1975, Kelly et al. 1972), a wide range of steel yielding devices were

proposed. Among these, plates and bars with a variable cross-section that follows the bending moment diagram are used to provide a uniform yielding and therefore avoid localised deformations. Whittaker et al. (1991) developed a hysteretic device, referred as added damping and stiffness (ADAS) flexural-beam damper, which consists of a series of hourglass-shaped flat steel plates, as illustrated in Figure 2.8a. A triangular-plate version of the ADAS damper, known as T-ADAS (Figure 2.8b), was developed by Tsai & Li (1994). Similarly, hourglass or single-tapered bars were used in proprietary energy-dissipating systems (Kajima 1991, Bruneau et al. 2011). As a result of their optimised shape, these devices offer enhanced energy dissipation and long-cycle fatigue life under flexure.

The ADAS and T-ADAS dampers were implemented in either EBFs or chevron CBFs (Figure 2.8c). In such configurations, these devices are designed to resist shear forces and the plates are subjected to flexure. However, the ADAS and T-ADAS were not specifically detailed as replaceable elements. More recently, Mansour et al. (2011) developed and validated two replaceable EBF links, following a design concept similar to the one described for the replaceable links in MRFs. The experimental tests showed that, on top of their satisfactory seismic performance, the links can be replaced even if the residual drifts are greater than 0.5%.

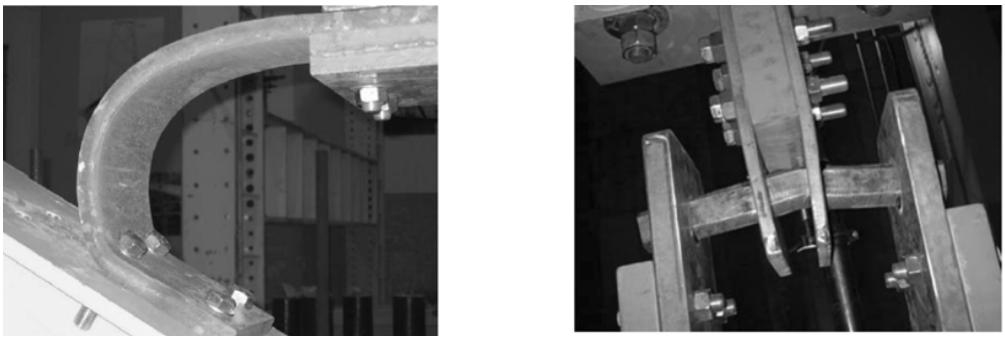

(a) (b)

Figure 2.9. INERD connections (Vayas & Thanopoulos 2005): (a) U-shaped connections; and (b) pin connection

Vayas & Thanopoulos (2005) developed two types of replaceable energy-dissipating devices for CBFs, known as INERD connections: a U-connection and a pin connection (Figure 2.9). The U-connection consist of a

pair of U-shaped steel plates that are tied to the brace and other structural members. Energy dissipation is provided by flexural yielding due to the axial force of the brace. Similarly, pin connections consist of a pin running through external eye-bars tied to the column and internal eye-bars tied to the brace. Experimental tests showed that these devices improve the energy dissipation capacity of bracing systems, and inelastic deformations are concentrated in the dissipative elements.

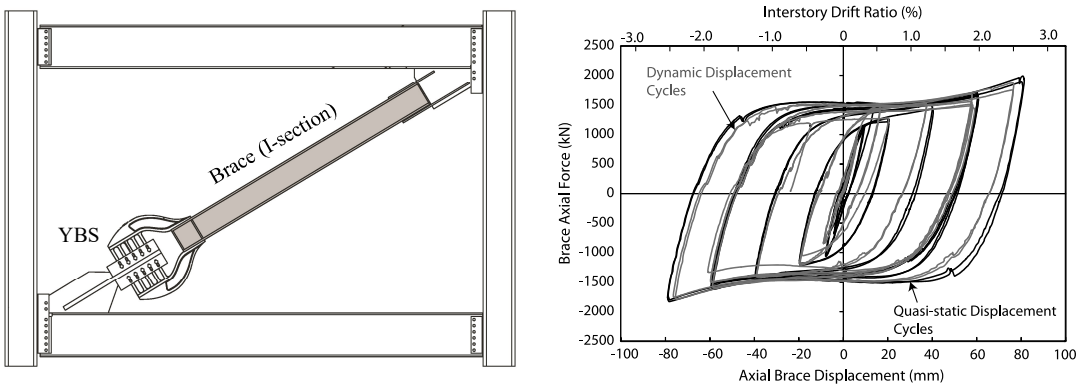

(a) (b)

Figure 2.10. YBS connector (Gray et al. 2017): (a) geometry of full-scale test; and force-displacement response

Inspired by the T-ADAS damper, Gray et al. (2014) developed a novel cast steel yielding connector, denoted as YBS, which can be used as structural fuse in a conventional CBF. The YBS connector (Figure 2.10a) is placed at one end of the bracing member, and it consists of two steel castings with yielding fingers and a splice plate assembly. Energy dissipation is provided by flexural yielding of the fingers designed with an optimised shape that matches the bending moment diagram. The main structural members, including the brace, are designed to be elastic. Experimental tests on a full-scale frame with the proposed cast steel system (Figure 2.10b) showed that, like the BRBs, braces with the YBS connector provide a full symmetric hysteresis. At large displacement cycles, due to the influence of second-order effects, the response of the YBS exhibited a significant increase in post-yield stiffness, which may reduce peak and residual drifts and prevent the development of soft-storey mechanisms.

2.4.2 Self-centering post-tensioned systems

The use of post-tensioning technology in steel frames has been proved an effective strategy to reduce residual drifts, as it allows for the self-centering (SC) of the structure after an earthquake. Researchers have often designed SC systems in combination with innovative structural fuses to ease the repair process. This section presents some recently developed SC steel systems: SC-MRFs with post-tensioned (PT) connections; SC-CBFs with vertical PT bars; and SC energy-dissipating braces.

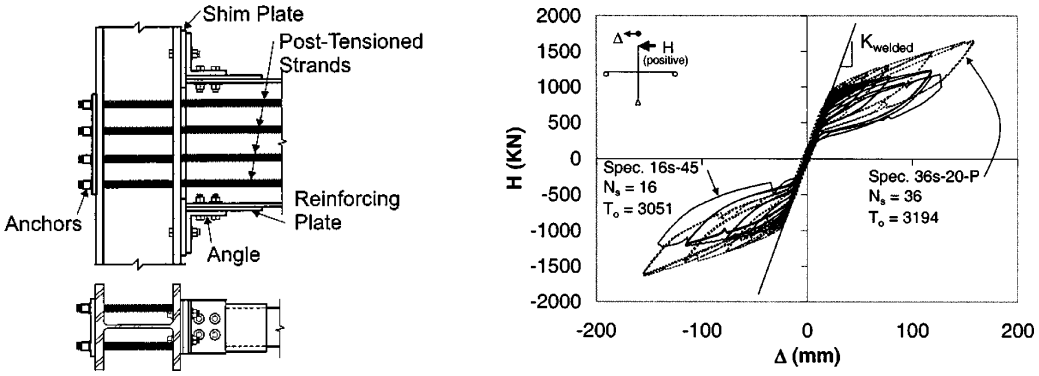

(a) (b)

Figure 2.11. Post-tensioned connection in a self-centering MRF: (a) geometry (Ricles et al. 2001); and (b) experimental force-displacement behaviour (Garlock et al. 2005)

Ricles et al. (2001) first developed a SC-MRF with PT connections that reduces structural damage in the beams, resulting in little residual deformations. Unlike the typical moment-resisting connections, the proposed PT connection, shown in Figure 2.11a, uses high-strength steel strands to clamp the beams on columns. Under cyclic loading, the connection behaviour is characterised by a gap opening and closing mechanism at the beam-column interface, where contact stresses develop and provide flexural resistance. Energy is dissipated by top and seat angles that yield when the gap opens. This system typically exhibits a flag-shaped hysteretic behaviour (Figure 2.11b), demonstrating the ability of the SC-MRF to recenter upon unloading due to the restoring forces of the PT strands. Experimental tests showed that significant damage concentrates only in the structural fuses, i.e. bolted top and seat angles, minimising the residual deformations in the connection (Ricles et al. 2002, Garlock et al. 2005).

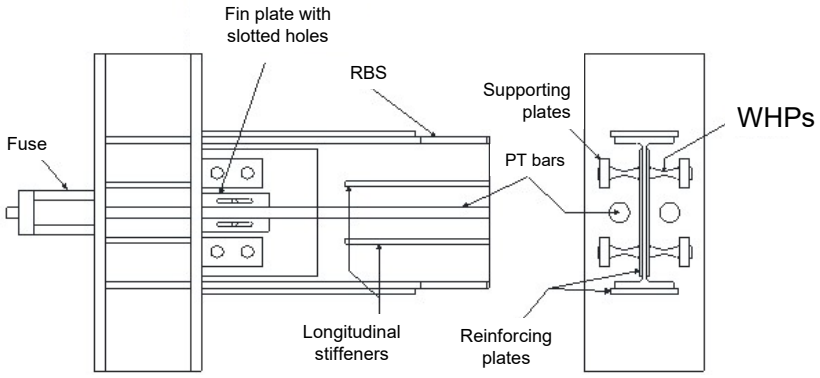

(a)

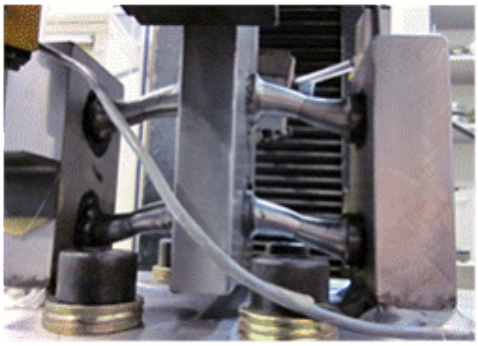

(b)

(c)

Figure 2.12. Post-tensioned connection with WHPs (Vasdravellis et al. 2013): (a) geometry details; (b) component test on WHPs; and (c) large-scale test

Several configurations of SC-MRFs have been developed, with the main difference being the type of energy dissipating device used, i.e. steel yielding based or friction based. In the first category, buckling-restrained steel bars that dissipate energy through axial yielding were proposed by Christopoulos et al. (2002), while Chou. et al. (2006) developed a device consisting of reduced flange plates welded to the column and bolted to the beam flange. Recently, Vasdravellis et al. (2013) have proposed a novel PT connection using as structural fuses steel cylindrical hourglass-shaped pins (named WHPs), placed between the flanges of the beam, as illustrated in Figure 2.12a. Similarly to the ADAS damper, the WHPs subjected to bending provide ehnanced large energy dissipation and fracture capacity. This excellent behaviour was confirmed by component tests on WHPs (Figure 2.12b) made of high-strength or stainless steel (Vasdravellis et al. 2013, 2014). Large-scale experimental tests on the proposed post-tensioned connection (Figure 2.12c) demonstrated that the connection

ensures a self-centering behaviour, with the advantage of damage concentrating in the WHPs. This indicated the potential for an easy repair process in the aftermath of a major earthquake.

A friction-based alternative to the steel yielding angles proposed in Ricles et al. (2001) was developed by Rojas et al. (2005) and Kim & Christopoulos (2008), where SC-MRFs were equipped with friction devices placed at the top and bottom of the beam. Other solutions consisted in using friction-based devices placed in the web of the beam (Tsai et al. 2008) or on the bottom flange of the beam (Wolski et al. 2009).

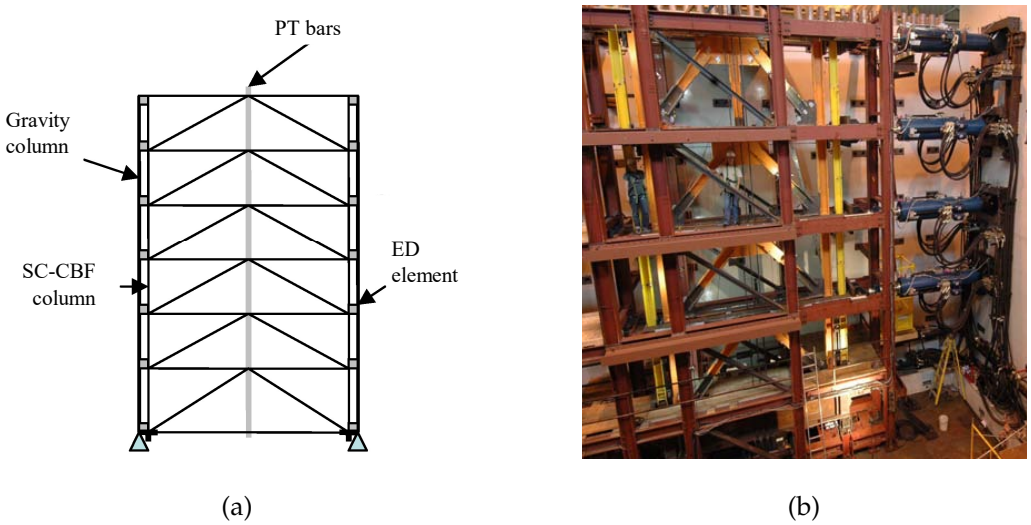

Figure 2.13. Self-centering CBF (Sause et al. 2010): (a) configuration with additional gravity columns; and (b) large-scale experimental tests

The excellent performance of SC-MRFs in reducing residual drifts indicated the potential of applying the post-tensioning technology to braced frames. An innovative SC-CBF has been recently developed by Roke et al. (2009). This system is a conventional CBF with the column bases detailed to permit the column uplifting from the foundation, initiating a rigid rocking mechanism. PT strands anchored at the top of the columns and at the foundations provide a restoring force, along with the gravity loads. The resulting self-centering mechanism is similar to that provided by rocking structures (Bruneau et al. 2011). Due to the post-tensioning forces, the design of the SC-CBF requires strong columns. Alternatively, two additional gravity columns can be added to the frame, and PT bars can be placed at mid-bay to limit their elongation demand, as illustrated in Figure 2.13a. Sause et al. (2010) tested this

configuration in a large-scale 4-storey frame, shown in Figure 2.13b. The results of hybrid simulation tests showed that the SC-CBF experiences far less residual drifts than a conventional CBF. In addition, structural damage was negligible under the DBE and was minimal under the MCE.

A self-centering energy dissipative steel brace, named as SCED, has been recently developed as an alternative to conventional BRBs (Christopoulos et al. 2008, Tremblay et al. 2008). The SCED system consists of a bracing member with pre-tensioned tendons and friction-based energy-dissipating devices (Figure 2.14). The bracing members are steel rectangular hollow sections, arranged in a concentric configuration. Guiding elements are used to constrain the relative motion of the inner and outer tubes, being these only welded to end plates. Inside the inner tube, there is a system of post-tensioned members that are anchored to the outer surface of the end plates. The overall strength of SCED is provided by the post-tensioned elements and the friction devices. Shake table tests conducted on a reduced-scale three-story CBF equipped with SCED braces showed that this system ensures a full self-centering response under the DBE and a drastic reduction in residual drifts under the MCE (Erochko et al. 2013).

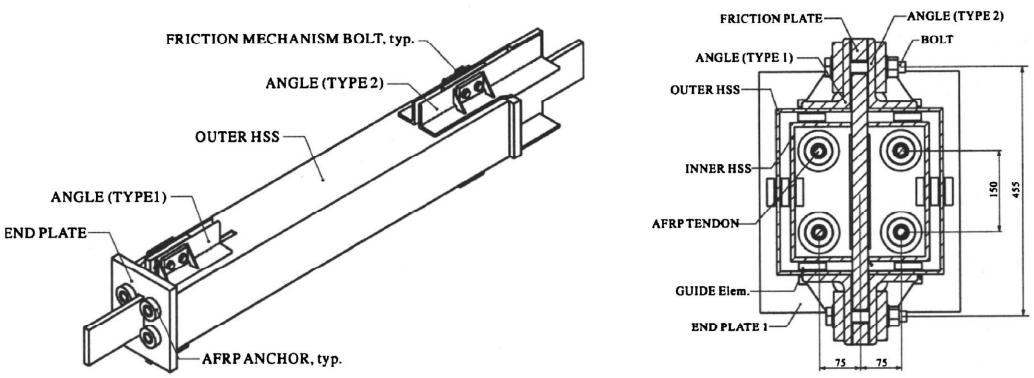

Figure 2.14. SCED bracing system geometry (Christopoulos et al. 2008)

Overall, post-tensioned steel systems are effective in minimising residual drifts of steel frames. However, implementing such systems in current practice can be challenging, since they involve additional complexity in design, fabrication and erection (Chancellor et al. 2014). Moreover, post-tensioned tendons require to be regularly maintained, resulting in frequent disruptions and high costs.

2.4.3 High post-yield stiffness systems

Recent studies on the impact of residual deformations have highlighted how providing high post-yield stiffness to the structure can effectively limit residual drifts (MacRae & Kawashima 1997, Pampanin et al. 2003, Ruiz-Garcia & Miranda 2006*a*). Design measures to increase the post-yield stiffness of conventional reinforced-concrete and steel frames systems, without the use of post-tensioning systems, were discussed in Pettinga et al. (2008). Residual drifts can be reduced either by increasing the post-yield stiffness of the material used for specific structural elements (e.g., reinforcement steel in concrete frames), or by introducing a secondary elastic frame in parallel with the primary frame. This second strategy is supported by the results of a study presented by Kiggins & Uang (2006), where an internal gravity frame was designed as secondary MRF to reduce the residual drift of a perimeter BRBF. This type of systems are commonly named as dual frames. Kiggins & Uang (2006) conducted a numerical evaluation on 3- and 6-storey prototype buildings designed as either BRBFs or dual BRBF-MRFs. Figure 2.15 illustrates the comparison between the peak and residual story drift performances of the dual BRBF-MRF and the conventional BRBF for a 6-storey building. Their study showed that the dual BRBF-MRF was able to provide a significant decrease in residual drifts, while limiting the peak storey drifts.

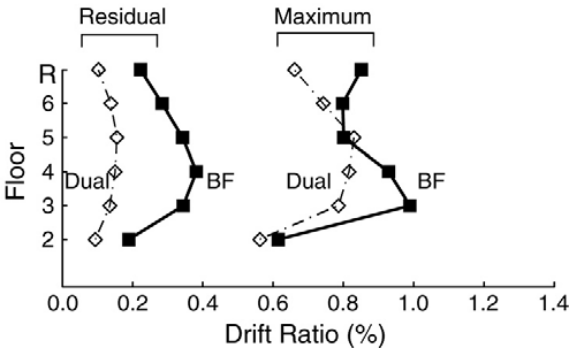

Figure 2.15. Comparison between peak and residual storey drifts of a dual BRBF-MRF and a conventional BRBF (Kiggins & Uang 2006)

2.4.4 Summary

This section presented three different design approaches to mitigate the impact of structural damage and to reduce residual drifts after a major earthquake. The main advantages and drawbacks of these solutions are outlined in Table 2.2. Structural fuses have been proved effective in reducing damage in main structural members. In addition, they are designed to be easily replaced if damaged, allowing for the structure to re-center, and, thus, mitigating residual drifts. On the other hand, post-tensioning technology or increasing high post-yield stiffness can achieve a further reduction of residual drifts. Post-tensioned systems ensure the full self-centering of the structure and also reduce damage in main structural members, due to the gap opening mechanism. However, such systems involve additional complexity in design and construction, along with expensive maintenance. A valid alternative to post-tensioning is increasing the high post-yield stiffness of the structure, but this strategy alone can not prevent damage in main structural members.

To achieve increased seismic resilience, these strategies can be combined together. For instance, post-tensioned systems are often equipped with structural fuses to prevent damage in main structural members, while ensuring the self-centering of the frame. However, no work has been done so far on studying the potential of high post-yield stiffness frames with structural fuses.

Strategy	Advantages	Limitations
Structural fuses	- Damage reduction in main structural members - Improved energy dissipation	No residual drift minimisation
Post-tensioned	- Residual drift minimisation - Damage reduction in main structural members	- Complex design, manufacture, and erection - Expensive maintenance
High post-yield stiffness	- Residual drift minimisation - Simple structural details	No damage reduction in main structural members

Table 2.2. Review of design strategies for increased seismic resilience

2.5 Conclusions

This chapter provided a review of the conventional approaches used for the design of steel structures and presented the latest strategies developed to improve their seismic resilience. The following conclusions are drawn:

- Conventional seismic-resistant steel frames designed according to current seismic provisions prevent collapse, and ensure life safety under the design earthquake. However, two major drawbacks are the significant permanent deformations in main structural members and the large residual storey drifts experienced after a strong seismic event.
- Socio-economic losses due to damage in structural members include high repair costs and excessive disruption to building occupation. Residual storey drifts may pose further complications. Recent studies on the economic impact of residual drifts showed that direct and indirect repair costs are not financially viable when residual drifts are greater than a repairability limit of 0.5%.
- Resilient-based design strategies aim at ensuring residual drifts below the repairability limit of 0.5% under the DBE, and a probability of collapse well below 10% under the MCE.
- Steel framing systems with structural fuses, i.e., energy-dissipating devices designed to be easily replaceable after a major earthquake, experience minimal plastic deformations in the main structural members under the DBE, since damage is concentrated in the fuses.
- Self-centering frames with post-tensioning technology are efficient in minimising residual drifts, but they introduce complexity in design, manufacture, and erection, and require high maintenance costs.
- Another approach for reducing residual drifts is increasing the post-yield stiffness of the structure. This can be achieved by increasing the post-yield stiffness of individual elements, or by introducing a secondary MRF in parallel with the primary seismic-resistant system.

- Design strategies combining high post-yield stiffness with the use of structural fuses can potentially minimise both the impact of structural damage and residual drifts after a major earthquake.

Chapter 3

Dual CBF-MRF System Concept and Prototype Building Design

3.1 Introduction

This chapter introduces the concept and design of a novel steel frame for enhanced seismic resilience. The proposed system is an MRF equipped with concentric braces, denoted as dual CBF-MRF. To reduce residual drifts and minimise damage in the main structural members, the system uses simple structural details: (a) braces equipped with high post-yield stiffness energy-dissipating devices; and (b) structural fuses in the beams. A 6-storey prototype building is designed using as seismic resistant system the proposed CBF-MRF. The frame is designed to have similar strength and stiffness of a conventional MRF coupled with BRBs (BRBF-MRF), following a perfomance-based seismic design procedure and capacity design rules.

This chapter has been published in Baiguera et al. (2016).

3.2 Steel dual CBF-MRF

Figure 3.1a shows the configuration of the proposed dual CBF-MRF. Energy-dissipating stainless steel pins, named as SSPs, are placed in series with the concentric braces, and structural fuses are installed in the beams.

The SSPs are installed at one end of the braces and pass through aligned holes between the gusset plate, welded to the beam and column, and a strong U-shaped plate, connected by either welding or bolting to the brace member

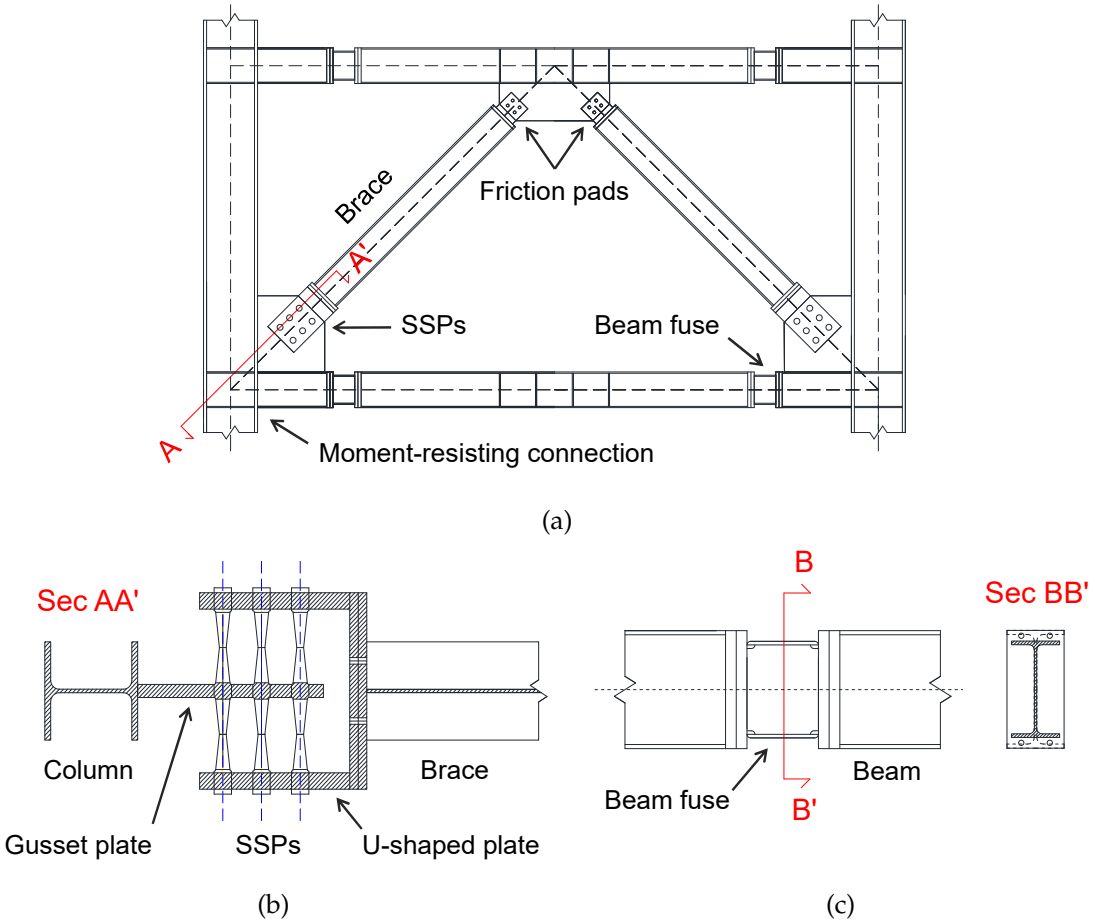

Figure 3.1. Geometry of the proposed dual CBF-MRF: (a) frame overview; (b) detail of brace-column connection with SSPs; and (c) beam fuse detail

(Figure 3.1b). SSPs are hourglass-shaped pins made of duplex stainless steel, which dissipate energy due to bending inelastic deformations. The hourglass shape promotes a constant curvature profile and a uniform distribution of plastic deformations to delay fracture and increase energy dissipation. Similar hourglass-shaped pins made of high strength steel (WHPs) have been previously used by Vasdravellis et al. (2013) in the post-tensioned connection described in Section 2.4.2, where they provided stable hysteresis and high fracture capacity. A further experimental investigation by Vasdravellis et al. (2014) compared the cyclic behaviour of WHPs made of high-strength steel and two grades of stainless steel, i.e. austenitic grade 304 and duplex stainless steel (SSD). The results showed that the WHPs made of SSD have excellent energy dissipation capacity and high post-yield stiffness, indicating the potential benefits of using SSPs made of SSD for the proposed CBF-MRF.

Replaceable fuses are placed in the main beams immediately after the gusset plates, where plastic hinges are expected to develop, as shown in Figure 3.1a. They are designed following the same concept of the replaceable link proposed by Shen et al. (2011), as presented in Section 2.4.1. The fuses are I-sections smaller than the main beam, and are welded on strong end-plates bolted to the main beam (Figure 3.1c).

The dual CBF-MRF frame aims: a) to provide high initial stiffness, which controls storey drifts and, thus, damage in drift-sensitive non-structural elements; b) to eliminate damage in main structural members, by concentrating plastic deformations in the SSPs and the beam fuses; and c) to minimise residual drifts, due to the high post-yield stiffness of the SSPs combined with the elastic deformation capacity of the MRF.

The proposed system is designed to have stiffness and strength similar to a conventional dual system with BRBs. This design choice is based on the assumption that bracing members with SSPs have a comparable seismic response to the BRBs, in terms of initial stiffness, yield strength, and hysteresis. Therefore, a prototype building is first designed using as seismic resistant system the conventional BRBF-MRF, and then the proposed CBF-MRF.

3.3 Prototype building

The prototype building is a 6-storey office building. Figure 3.2a shows the plan view having three 6-m bays in each direction. The inter-storey height is 3 m. Seismic resistance is provided by the perimeter frames, whereas the interior frames support gravity loads only. Figure 3.2b shows the elevation of the perimeter frame selected for the design of the dual systems.

The gravity loads for the prototype building, listed in Table 3.1, are based on the characteristic values specified in EC1 (2004) and Accelor Mittal (2008).The total dead load is equal to 4.9 kN/m^2, while the imposed load is equal to 3.5 kN/m^2 for a typical floor and 1.5 kN/m^2 for the roof. The design basis earthquake (DBE) has a return period of 475 years, and it is expressed by the elastic response spectrum of EC8 (2004) with a PGA equal to 0.36 g and soil type B. The total seismic mass is 4695 kN.

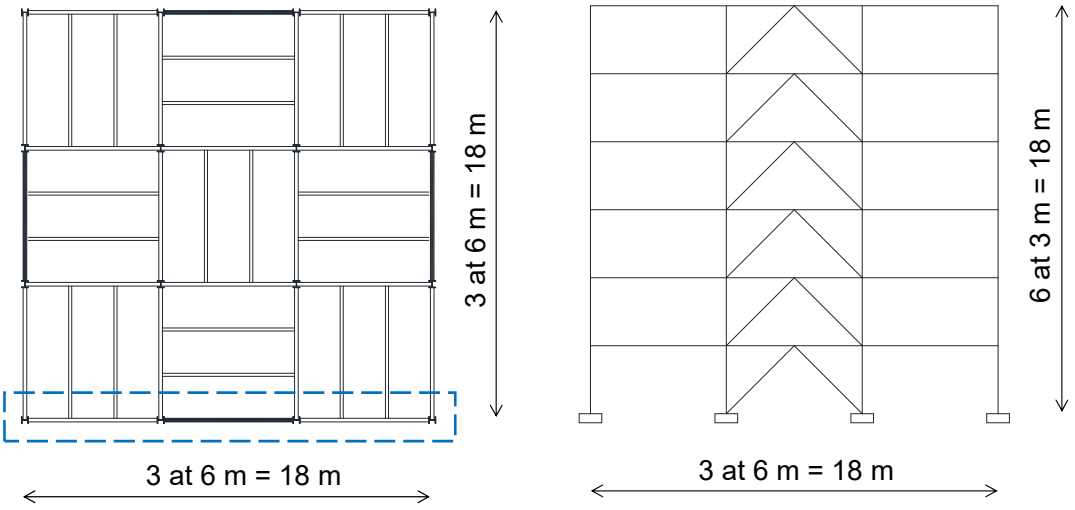

(a) (b)

Figure 3.2. Prototype building: (a) plan view; and (b) elevation of a perimeter frame

Type of load	Description	Value
Dead load	Concrete slab	2.6 kN/m^2
	Steelwork	0.5 kN/m^2
	Facade	8 kN/m
Imposed load	Office	2.5 kN/m^2
	Partitions	1.0 kN/m^2
	Roof	1.5 kN/m^2

Table 3.1. Summary of gravity loads for the prototype building

3.4 Design of the dual BRBF-MRF

The conventional dual BRBF-MRF consists of a moment-resisting frame with BRBs acting as the primary seismic-resistant system. All-steel BRBs are used; the inner steel core plate, restrained by a steel casing, yields in tension and compression. The inner BRB geometry (Figure 3.3) consists of a energy-dissipating core (length L_0 and area A_0), a connection area (L_1, A_1), a stiffened section (L_2, A_2), and a tapered section (L_3, A_3).

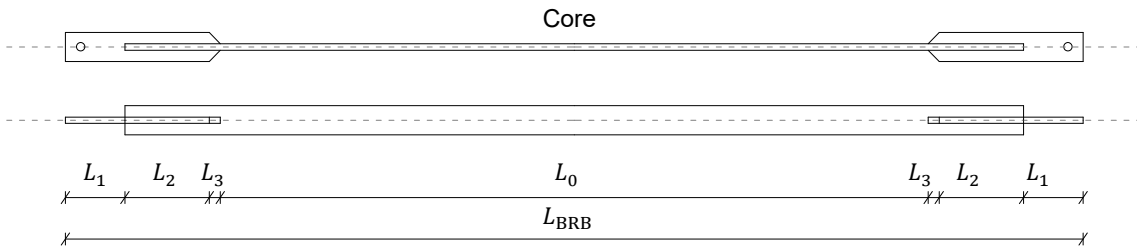

Figure 3.3. BRB core geometry

Currently, EC8 (2004) does not include BRBFs among the main seismic-resistant steel frames. Nevertheless, the BRBFs can be designed to EC8 (2004) following the provisions for CBFs, since the seismic forces are mainly resisted by axially loaded members in both systems. However, adjustments factors should be introduced in the capacity design requirements of the main structural members to account for the different response of BRBs.

The dual BRBF-MRF is expected to provide a highly ductile response and, therefore, a behaviour factor q = 7 is assumed. EC8 (2004) specifies $q = 5\alpha_u/\alpha_1$ for comparable highly ductile systems (e.g., MRFs and EBFs), where α_u/α_1 is a factor accounting for the dissipation capacity and ductility of a system, and should not exceed 1.6 (Elghazouli 2009). For the design of the dual BRBF-MRF, α_u/α_1 = 1.4 is used. Using the approach proposed in EC8 (2004) (Cl. 4.3.2.2) and a fundamental period of vibration of the structure of 0.77 sec, the total base shear is 400 kN.

A linear elastic analysis using the estimated seismic loads is carried out using the SAP software (Computers and Structures Inc. 2005). The global stiffness of the BRB (K_{BRB}) is given by the axial stiffnesses of the various sections (K_i) working in series, as expressed in Eq. (3.1):

$$K_{BRB} = \frac{1}{\sum \frac{1}{K_i}} \tag{3.1}$$

The yield force of the BRB $F_{y,BRB}$ is calculated as:

$$F_{y,BRB} = f_y \cdot A_0 \tag{3.2}$$

where f_y is the yield strength of the core (300 MPa).

Beams and columns are designed using capacity design requirements specifically adjusted to account for the typical hysteresis of BRBs. Under cyclic

loading, BRBs typically exhibit high strain-hardening and larger compressive forces than in tension. The adjustment factors proposed by ANSI/AISC 341/10 (2010) are used in this study: these are the strain hardening factor ω and the compression strength factor β. For capacity design, the total overstrength Ω_{tot} is therefore calculated as:

$$\Omega_{tot} = 1.1\gamma_{ov}\omega\beta\Omega \tag{3.3}$$

where γ_{ov} is the material overstrength factor (γ_{ov} = 1.25), and Ω is the lowest $F_{y,BRB}/N_{Ed}$ value, N_{Ed} being the axial seismic demand in the BRB. The adjustment factors ω and β are typically obtained from testing or provided by the manufacturer; this study adopts the following values from literature: ω = 1.25 and β = 1.2 (Romero et al. 2007, Bruneau et al. 2011). The steel yield stress for columns and beams is assumed equal to 275 MPa.

EC8 (2004) imposes a serviceability limit on peak storey drifts, $\theta_{s,max}$, under the frequently-occurred earthquake (FOE). In this study, the limit on $\theta_{s,max}$ is 0.5%, which corresponds to the lower bound set for non-ductile structural elements.

Storey	Column	Beam	BRB core cross-section area (mm^2)	$F_{y,BRB}$ (kN)	K_{BRB} (N/mm)
6	HEB400	IPE330	500	150	30,000
5	HEB400	IPE330	1,100	330	59,000
4	HEB400	IPE330	1,530	460	80,000
3	HEB400	IPE330	1,900	570	100,000
2	HEB500	IPE330	1,950	585	108,000
1	HEB500	IPE330	1,950	585	108,000

Table 3.2. Design details of the conventional BRBF-MRF

Table 3.2 lists the final sections obtained for the BRBF-MRF following an iterative design procedure to satisfy the storey drift limits and capacity design requirements. The amplified overstrength factors led to large column sections. The MRF carries about 25% of the total base shear of the frame. This proportion, determined by performing pushover analysis using either the dual BRBF-MRF and the MRF only, is in accordance with the 25% rule identified in previous studies on the design of dual BRBF-MRFs (Kiggins & Uang 2006, Sahoo & Chao 2015). The estimated maximum peak storey drift $\theta_{s,max}$ is 0.48% under the FOE,

0.96% under the DBE, and 1.44 % under the MCE.

3.5 Design of the dual CBF-MRF

The proposed CBF-MRF has the same beam and column cross-sections as the BRBF-MRF, and the BRBs are replaced by HEA300 sections connected in series to the SSPs.

3.5.1 Design of bracing members with SSPs

Bracing members with SSPs are designed to provide initial elastic stiffness and yield force comparable to the BRBs of the BRBF-MRF. An iterative design procedure based on analytical and numerical predictions is used.

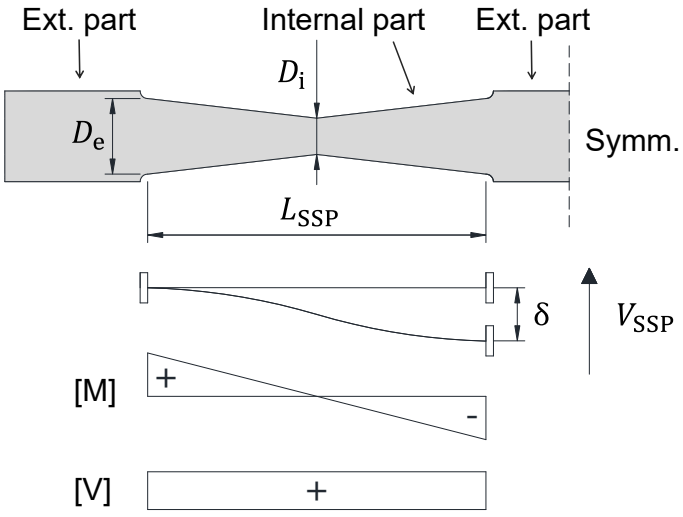

Figure 3.4. Stainless steel pin (SSP): geometry, deflection, elastic bending moment and shear diagram

SSPs are made of two hourglass-shaped bending parts. The geometric properties of the bending part are shown in Figure 3.4. The internal bending parts have length L_{SSP}, maximum diameter D_e, and minimum diameter D_i at mid-length.

Preliminarily, the design of the SSPs is carried out using the analytical equations proposed in Vasdravellis et al. (2013) for WHPs. The assumed static system for the bending part assumes fixed boundary conditions at the sections

of diameter D_{e}. The yield force of half of a SSP, V_{SSP}, is controlled either by the plastic moment of resistance, M_{pl}, or the plastic shear resistance, V_{pl} (EC3 2003):

$$M_{\mathrm{pl}} = \left(\frac{D_{\mathrm{e}}^3}{6}\right) f_{\mathrm{y,SSP}} \tag{3.4}$$

$$V_{\mathrm{pl}} = 0.9\,\frac{\pi D_{\mathrm{i}}^2}{4}\,f_{\mathrm{y,SSP}}/\sqrt{3} \tag{3.5}$$

where $f_{\mathrm{y,SSP}}$ is the yield strength of the SSP material. To avoid that the M_{pl} is reached at the ends before the V_{pl} is reached at the mid-length, the following condition must be satisfied:

$$V_{\mathrm{SSP}} = \frac{2M_{\mathrm{pl}}}{L_{\mathrm{SSP}}} < V_{\mathrm{pl}} \tag{3.6}$$

The yield force of a SSP, $F_{\mathrm{y,SSP}}$, is then calculated as:

$$F_{\mathrm{y,SSP}} = 2V_{\mathrm{SSP}} \tag{3.7}$$

The elastic stiffness K_{fe} of a SSP is given by:

$$K_{\mathrm{fe}} = 2\beta\frac{9\pi D_{\mathrm{e}}^3 D_{\mathrm{i}} EG}{(40ED_{\mathrm{e}}^2 L_{\mathrm{SSP}} + 48GL_{\mathrm{SSP}}^3)} \tag{3.8}$$

where E is the modulus of elasticity and G is the shear modulus of the SSP material. β is a parameter that accounts for the additional flexibility due to local yielding in the supporting plates observed in the experimental validation (Vasdravellis et al. 2013) and is equal to 0.5. In the proposed system, a defined number of SSPs (n_{SSP}), working in parallel to each other, are placed in series with the brace, and, therefore, the yield force $F_{\mathrm{y,tot}}$ and the global stiffness K_{tot} of the energy-dissipating braces are calculated as follows:

$$F_{\mathrm{y,tot}} = n_{\mathrm{SSP}}\,F_{\mathrm{y,SSP}} \tag{3.9}$$

$$\frac{1}{K_{\mathrm{tot}}} = \frac{1}{K_{\mathrm{SSPs}}} + \frac{1}{K_{\mathrm{brace}}} = \frac{1}{n_{\mathrm{SSP}}\,K_{\mathrm{fe}}} + \frac{1}{\frac{EA_{\mathrm{brace}}}{L_{\mathrm{brace}}}} \tag{3.10}$$

where K_{SSPs} is the stiffness of all SSPs, and K_{brace} is the stiffness of the bracing member having length L_{brace} and cross-sectional area A_{brace}. Strong HEA 300 sections are used to ensure that the braces remain elastic. The yield strength of the SSD is equal to 540 MPa, based on the coupon test results from Vasdravellis et al. (2014). The yield force $F_{\text{y,tot}}$ and global stiffness K_{tot} are initially calculated using the above equations.

To verify the accuracy of the analytical predictions, three-dimensional FEM models of the SSPs are developed using experimentally-validated parameters for the SSD material, which are described in detail in Section 4.2.1. The comparison between the analytical and numerical strength and stiffness values is shown in Table 3.3. It can be observed that there is a good correlation between the analytical and numerical global stiffness of the bracing members, but a substantial overestimation in the corresponding analytical $F_{\text{y,tot}}$ values. This indicates that the plastic mechanism controlling the response of the SSPs is different from that of the WHPs. In fact, as shown by the FEM simulations and later confirmed by the experimental tests on full-scale SSPs, presented in Chapter 5, the formation of plastic hinges occurs in the middle of half bending part. A modification of the analytical model, taking into account the exact plastic mechanism of SSPs, will be discussed in Section 5.7.3. At this stage, the design of the CBF-MRF employs the numerical predictions for $F_{\text{y,tot}}$ and K_{tot} values.

	SSP Geometry				Analytical Eqs.		FEM		
Storey	n_{SSP}	D_{e} (mm)	D_{i} (mm)	L_{SSP} (mm)	$F_{\text{y,tot}}$ (kN)	K_{tot} (N/mm)	$F_{\text{y,tot}}$ (kN)	K_{tot} (N/mm)	u_{y} (mm)
6	4	36	18	210	320	39,500	240	42,000	5.4
5	4	42	24	230	464	60,900	350	59,000	5.6
4	4	50	24	230	780	94,150	540	80,000	6.3
3	4	50	24	225	800	99,200	580	80,000	6.5
2	6	46	22	215	972	118,400	650	108,000	5.5
1	6	46	22	215	972	118,400	650	108,000	5.5

Table 3.3. Design details of SSPs and comparison between analytical and numerical strength and stiffness of the CBF-MRF bracing members

In the design process, to maximise the fracture capacity of SSPs, their geometry is designed in such a way that they provide the stiffness and yield force required by the seismic design while they have yield displacement as large

as possible. As shown by the experimental tests by Vasdravellis et al. (2014), the SSPs under cyclic loading can achieve a ratio of fracture displacement to yield displacement of ten. Therefore, increasing the yield displacement allows the SSP to sustain larger imposed displacements. This can be easily achieved with different combinations of D_{e}, D_{i} and L_{SSP}. For the proposed frame, the yield displacement of each SSP geometry used on each floor is given in Table 3.3.

The SSPs are designed so that the CBF-MRF has a fundamental period of vibration comparable to that of the BRBF-MRF (i.e., 0.75 s to 0.77 s). As can be seen from Tables 3.2 and 3.3, the bracing members with SSPs have strength and stiffness similar to those provided by the BRBs.

The CBF-MRF is expected to exhibit high post-yield stiffness as a result of the SSD material behaviour. To meet capacity design requirements and avoid undesirable column failures due to high post-yield stiffness, friction pads are placed between the brace members and the beam gusset plate at the top of each floor, as indicated in Figure 3.1. The friction pad is activated, i.e. it yields, at a predefined storey drift level, and it has an elastic perfectly plastic force-displacement behaviour to ensure that the structure meets the capacity design requirements. The predefined storey drift level in the dual frame is 3%, as identified by the nonlinear pushover analysis conducted in Section 4.4, i.e., two times larger than the drift expected under the MCE.

3.5.2 Beam fuse design

The replaceable end-plate link concept of Shen et al. (2011), presented in Section 2.4.1, is considered for the design of the beam fuse. Plastic deformations are intended to concentrate in the beam fuse, thus protecting the beam and the beam-column connection from yielding. The geometric details of the beam fuse are shown in Figure 3.5, where the beam is weakened at a distance S from the column face.

The beam fuse is designed according to the procedure presented in Shen et al. (2011). The geometry of the beam fuse is defined by the length l_{fuse}, the distance from the gusset plate a, and the fuse depth d_{fuse}. The beam fuse size is subject to the limits expressed by:

$$0.5\, b_{\mathrm{beam}} \leq a \leq 0.75\, b_{\mathrm{beam}} \tag{3.11}$$

$$0.65\ d_{\text{fuse}} \leq l_{\text{fuse}} \leq 0.85\ d_{\text{fuse}} \tag{3.12}$$

where b_{beam} is the width of the main beam section.

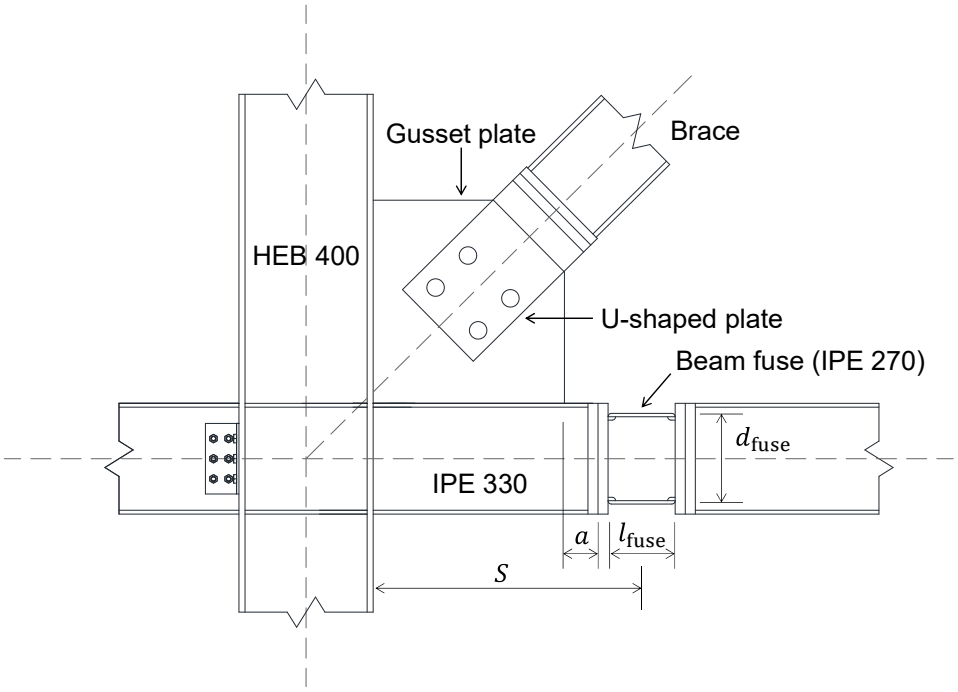

Figure 3.5. Beam-column connection with the beam fuse of the dual CBF-MRF

Limits on the plastic moment ratio for the beam fuse are defined on the basis of limits on the flange cut recommended for RBS connections in ANSI/AISC 358/10 (2010). The limits on the plastic moment ratio are:

$$0.6 \leq \frac{M_{\text{pl,fuse}}}{M_{\text{pl,beam}}} \leq 0.85 \tag{3.13}$$

where $M_{\text{pl,fuse}}$ and $M_{\text{pl,beam}}$ are the plastic moments of the beam fuse and the main beam, respectively.

The maximum moment at the face of the column, $M_{\text{max,col}}$, must satisfy the condition:

$$M_{\text{max,col}} = \frac{L}{L-S}\ M_{\text{pl,fuse}} \leq M_{\text{pl,beam}} \tag{3.14}$$

where L is half the beam length. The above design procedure results in IPE270 sections for the beam fuses on each floor of the prototype building. Table 3.4 gives the geometric details of the beam fuse.

	Section	b_{beam} (mm)	d_{fuse} (mm)	l_{fuse} (mm)	a (mm)	S (mm)	M_{pl} (mm)	$M_{\text{max,col}}$ (kNm)	$\frac{M_{\text{pl,fuse}}}{M_{\text{pl,beam}}}$ (kNm)
Fuse	IPE270	–	270	200	100	800	145	–	0.6
Beam	IPE330	160	–	42	–	–	241	198	–

Table 3.4. Design details of the beam fuse of the dual CBF-MRF

3.5.3 SSP-gusset plate connection design

The thickness of the lower gusset plates and the U-shaped plates (Figure 3.1b) is determined according to the design rules presented in Vasdravellis et al. (2014). In order to resist the bearing force $F_{\text{y,SSP}}$ from an SSP without yielding, the minimum required thickness of the gusset plates $t_{\text{gus,min}}$ and U-shaped plates $t_{\text{sp,min}}$ are given by:

$$t_{\text{gus,min}} = \frac{0.35\ F_{\text{y,SSP}} E}{f_{\text{y,gus}}^2\ k_{\text{d}}} \tag{3.15}$$

$$t_{\text{sp,min}} = \frac{3,546\ M_{\text{pl}}}{(38,809 F_{\text{y,SSP}}^2 + 40 M_{\text{pl}} k_{\text{d}} f_{\text{y,sp}})^{0.5} - 197 F_{\text{y,SSP}}} \tag{3.16}$$

where $f_{\text{y,gus}}$ and $f_{\text{y,sp}}$ are the yield strengths of the gusset plate and the U-shaped plate (275 MPa), respectively. k_{d} is a factor accounting for the clearance between the SSPs and the drilled holes in the U-shaped plates. In addition, the gusset and U-shaped plates are verified against buckling by using the strip column method proposed by Thornton (1984). The design results in gusset plates with thickness equal to 40 mm and U-shaped plates with thickness equal to 50 mm. The top gusset plates, i.e. those at the connection of the braces with the beam of the upper floor, are designed using the EC3 (2003) procedure, which results in 40 mm thick plates.

3.6 Concluding remarks

In this chapter, a dual steel system (CBF-MRF) consisting of a moment-resisting frame equipped with high post-yield stiffness braces and replaceable beam fuses was designed for improved seismic resilience. High post-yield stiffness is achieved by using duplex stainless steel pins, denoted as SSPs, placed in series

with the braces.

A 6-storey prototype building was designed using as seismic-resistant system either the proposed dual CBF-MRF or a conventional dual BRBF-MRF. The proposed frame was designed with similar strength and stiffness to the dual BRBF-MRF, following the seismic provisions of EC3 (2003) and EC8 (2004). Appropriate capacity design rules were adopted in the design of the dual frames. The seismic performance of the proposed and conventional dual systems is numerically evaluated in Chapter 4.

Chapter 4

Numerical Evaluation of the Dual CBF-MRF Seismic Performance

4.1 Introduction

This chapter presents the numerical evaluation of the seismic performance of the proposed dual CBF-MRF. For this purpose, nonlinear finite element (FEM) analyses are performed using the Abaqus software (Dassault Systèmes 2014). Two FEM models of the CBF-MRF are employed: a detailed three-dimensional model, based on the use of solid and shell elements, to study both the local and global behaviour of the system and to identify all possible failure modes through nonlinear monotonic and cyclic pushover analyses; and a simplified version of the detailed model, based on the use of beam elements, to evaluate the global seismic response of the structure through nonlinear static and dynamic analyses. The nonlinear dynamic analyses are performed using a set of 22 earthquake records scaled to three different seismic intensities. The hysteretic behaviour of the seismic devices, i.e., the SSPs and the beam fuses, is calibrated using available experimental data.

The results of the nonlinear static and dynamic analyses of the CBF-MRF are compared with those obtained for the conventional BRBF-MRF, for which a simplified FEM model is developed.

This chapter has been published in Baiguera et al. (2016).

4.2 Detailed solid-shell FEM model

Figure 4.1 shows the detailed FEM model of the dual CBF-MRF. The geometry of the central bay of the prototype building perimeter frame (see Figure 3.2) is reproduced in full detail. To reduce computational time, both solid and shell elements are adopted. Beams, columns and bracing members are modelled using shell elements with reduced integration, namely S4R in Abaqus. The SSPs, gusset plates, U-shaped plates and beam fuses are modelled using solid elements with reduced integration, namely C3D8R. Solid-shell coupling constraints are used to allow for the correct transition of stresses between shell and solid elements. The friction pads are not modelled since the detailed model is employed to study the frame response for roof drifts up to 3%, i.e., the drift level at which the friction pads yield.

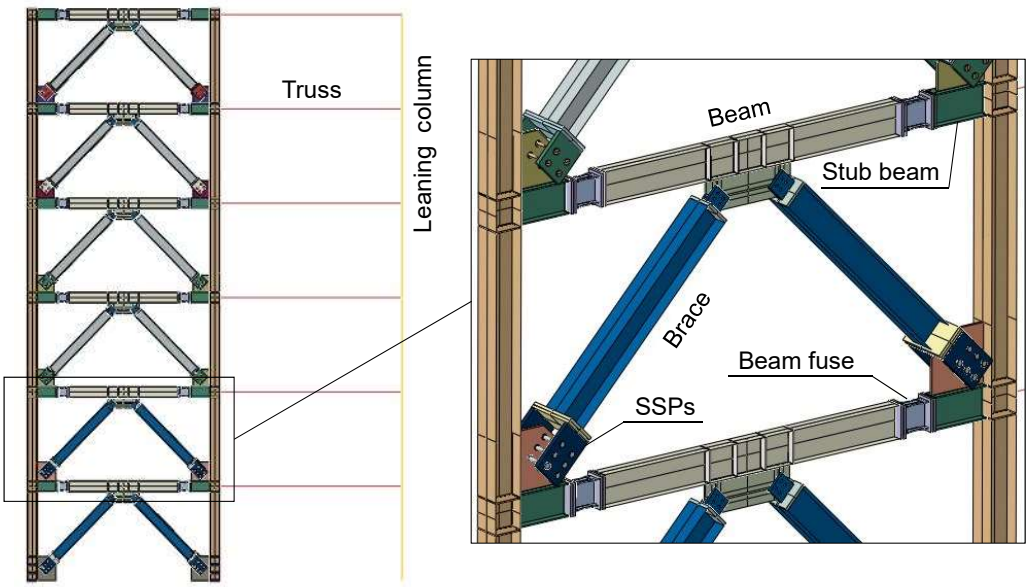

Figure 4.1. View of the detailed solid-shell FEM model of the CBF-MRF

To account for P-Δ effects from the gravity frame of the prototype building, a lean-on column is added and truss elements are used to link it to the frame. The moment of inertia and area of the lean-on column are the sum of the moments of inertia and areas of all gravity columns. Figure 4.2a shows the mesh discretisation used. The mesh density is refined in the regions of the frame where plastic deformations are expected to develop, i.e. the SSP-gusset plate connections and the beam fuses, based on sub-models of these regions, as described in the next sections.

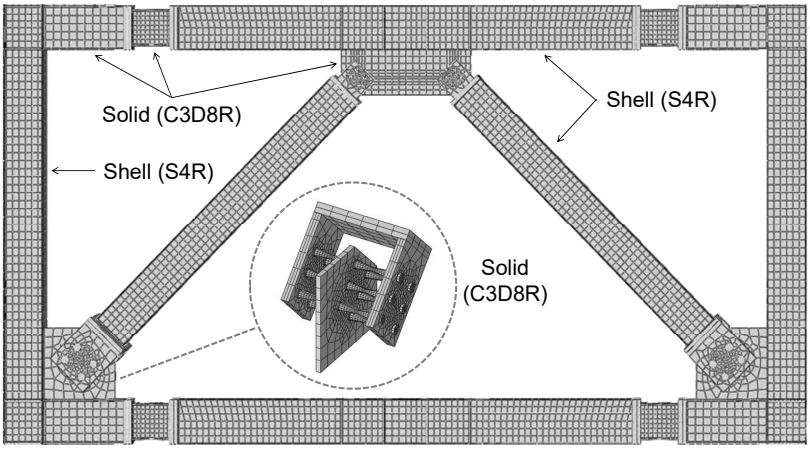

(a)

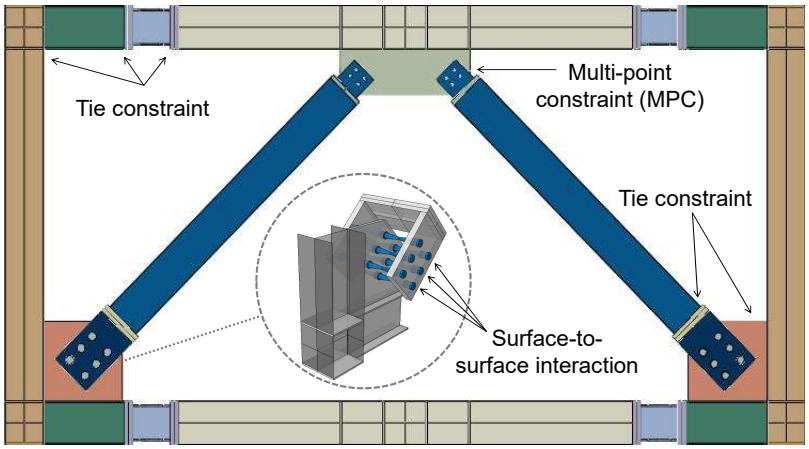

(b)

Figure 4.2. Detailed solid-shell FEM model of the dual CBF-MRF: (a) mesh discretisation; and (b) interaction and constraint definitions

Surface-based tie constraints, which impose equal displacements among the nodes of two surfaces, are defined between all welded regions, i.e., the beam-column connections, the end-plates welded to the beam fuses, the U-shaped plates welded to the bracing members, and the gusset plates welded to the beam and column flanges, as indicated in Figure 4.2b. Surface-to-surface contact interactions are defined between the external surfaces of the SSPs and the holes of the U-shaped plates and gusset plates. This requires the definition of a master and a slave contact surface. The choice of the master and slave surface is made considering the mesh discretisation, i.e., the surface with the coarser mesh was chosen as master surface because it results in a smoother solution (Dassault Systèmes 2014). A contact property with normal and tangential behaviour is defined, assigning a friction coefficient of 0.2. The diaphragm

action of the slab is simulated by a linear equation constraint, imposing equal horizontal displacements on the nodes of the top flanges of the beam.

The yield stress of the main structural members is 275 MPa and the yield stress of the SSD material of the SSPs is 540 MPa. An elastoplastic material with isotropic hardening behaviour is defined for the main structural members.

4.2.1 Calibration of cyclic hardening parameters for SSPs

The material properties of the SSPs are calibrated using the experimental results reported in Vasdravellis et al. (2014). In that study, several cyclic tests on pins made of high-strength or stainless steel (named as WHPs) were carried out using the testing apparatus shown in Chapter 2 (Figure 2.12b). Figure 4.3a shows the three-dimensional FEM model that was developed in Vasdravellis et al. (2014) to simulate the hysteretic response of the steel pins. That model is used to calibrate the material parameters of the SSD material. Only half of the WHP is modelled due to its symmetric geometry. Both the WHP and the supporting plates are discretised using C3D8R elements. In order to capture the pinching behaviour at zero force observed in the experimental curve (Figure 4.3b) due to the slip of SSPs within the surrounding holes, a small clearance of 0.1 mm is left between the cylindrical external surfaces and the holes of the U-shaped plates, where surface-to-surface contact interactions are defined. The cyclic loading protocol described in ANSI/AISC 341/10 (2010) is applied to reproduce the corresponding test in Vasdravellis et al. (2014). Displacement-controlled analysis is conducted under quasi-static loading conditions in the large displacement/strain nonlinear regime, along with automatic stabilisation in order to overcome numerical issues related to the contact interactions.

The hysteretic behaviour of SSPs is simulated by an elastoplastic material model with combined isotropic and kinematic hardening. The material model is defined by the yield surface $\varphi(\boldsymbol{\sigma})$ defined as (Dassault Systèmes 2014):

$$\varphi(\boldsymbol{\sigma}) = \sqrt{\frac{3}{2}(\boldsymbol{S}-\boldsymbol{\alpha})^t(\boldsymbol{S}-\boldsymbol{\alpha})} - \sigma^0 \tag{4.1}$$

where σ^0 is the yield stress, t is the transposition operation, $\boldsymbol{S}$ is the stress deviator, $\boldsymbol{\sigma}$ is the stress vector and $\boldsymbol{\alpha}$ is the backstress vector. The hardening

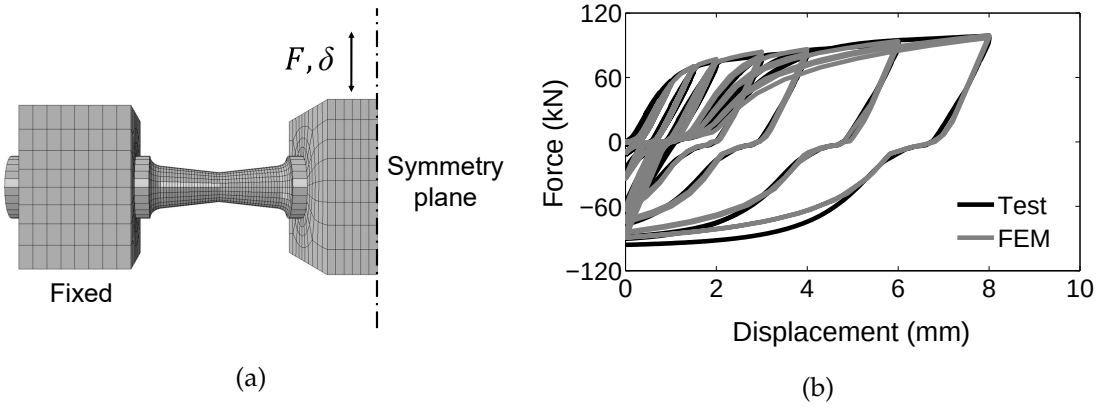

(a) (b)

Figure 4.3. Calibration of SSP hysteretic behaviour: (a) FEM model of half of a WHP from Vasdravellis et al. (2014); and (b) experimental and numerical hysteresis under the ANSI/AISC 341-10 loading protocol

laws for each backstress are defined as:

$$\boldsymbol{\alpha} = \sum_{k=1}^{B} \boldsymbol{\alpha}_{\mathrm{k}} \tag{4.2}$$

$$\dot{\boldsymbol{\alpha}}_{\mathrm{k}} = \frac{C_{\mathrm{k}}}{\sigma^0}(\boldsymbol{\sigma} - \boldsymbol{\alpha})\dot{\bar{\varepsilon}}^p - \gamma_{\mathrm{k}}\boldsymbol{\alpha}_{\mathrm{k}}\dot{\bar{\varepsilon}}^p \tag{4.3}$$

where a superimposed dot indicates an incremental quantity, B is the total number of the backstresses, C_{k} and γ_{k} are the constitutive material parameters to be calibrated against the experimental results, and $\dot{\bar{\varepsilon}}^p$ is the equivalent plastic strain rate. Figure 4.3b shows that a good agreement is found with the experimental cyclic force-displacement curve reported in Vasdravellis et al. (2013) using B = 1, σ^0 = 500 MPa, C_1 = 11,000 MPa, and γ_1 = 40. These values are iteratively determined by using a trial and error method.

4.2.2 Calibration of cyclic hardening parameters for the beam fuse

To ensure that the numerical model for the fuse is reliable and capable of capturing the deterioration of stiffness and strength due to buckling phenomena, the material parameters are calibrated against the experimental results of full-scale tests on a beam-column connection with a replaceable link reported by Shen et al. (2011). The tested specimen is reproduced in Abaqus using the same modelling features as for the whole frame model, i.e. shell (S4R) elements for the beam and column, and solid (C3D8R) elements for the fuse.

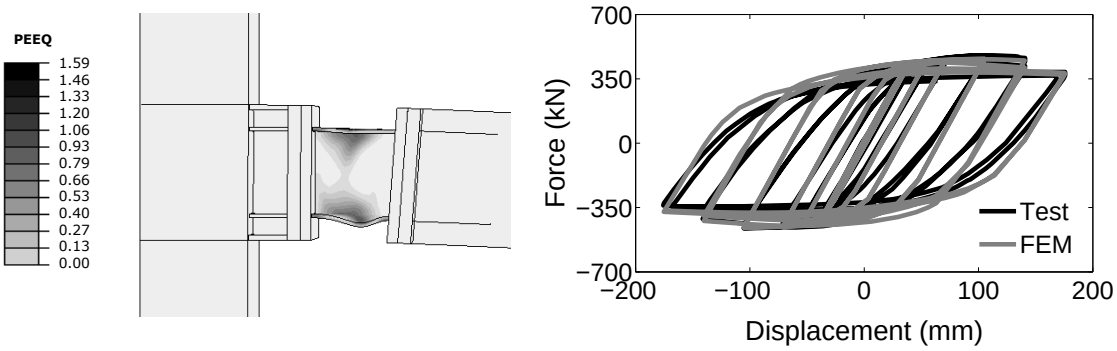

(a) (b)

Figure 4.4. Beam fuse calibration: (a) local flange and web buckling in the replaceable link (deformed shape and PEEQ distribution at 175 mm beam tip displacement); and (b) numerical results compared against the experimental behaviour of the replaceable link from Shen et al. (2011)

Similar to the calibration procedure presented in the previous section, the constitutive material parameters of the fuse are identified iteratively by conducting several simulations. Figure 4.4a shows that the FEM model is capable of capturing the buckling of the replaceable link, and Figure 4.4b shows that a good correlation between the experimental and the numerical results is achieved adopting the following values for the combined hardening parameters [see Eqs. (4.1-4.3)]: B = 1, σ^0 = 390 MPa, C_1 = 4,000 MPa, and γ_1 = 80.

4.3 Simplified beam-solid FEM model

The central bay of the prototype building perimeter frame is modelled using a simplified modelling approach and the response is compared against the pushover results of the detailed model. In the simplified version of the numerical model, beams and columns are modelled using two-node linear beam elements, namely B31 in Abaqus. A lean-on column is added to the frame to account for P-Δ effects from the gravity frame using the same modelling features described for the detailed model. Figure 4.5 shows the simplified model, with a detailed view of the second storey. Beam-column and brace-beam connections are modelled using appropriate multi-point constraints. The diaphragm action of the slab is simulated by a linear equation constraint, imposing equal horizontal displacements to the nodes of the beams.

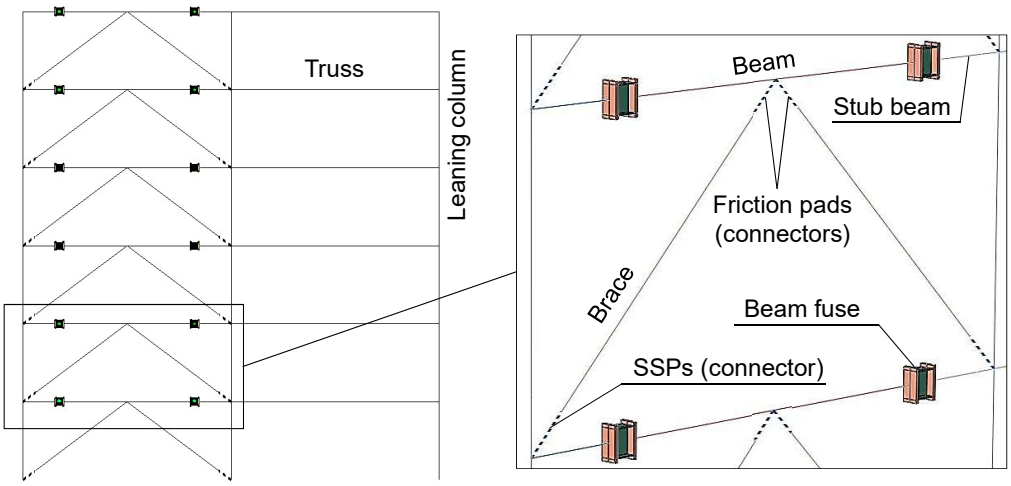

Figure 4.5. View of the simplified beam-solid FEM model of the dual CBF-MRF

To capture the local buckling and the strength and stiffness deterioration due to cycling inelastic loading, the fuses and the end plates bolted on the fuses are modelled using C3D8R solid elements. Appropriate multi-point constraints are defined between the beam elements and the fuse end plates to allow for the correct transition of stresses. To evaluate the accuracy of this more simplified model, a beam-column sub-model is constructed and calibrated against the results by Shen et al. (2011). Figure 4.6a shows the beam-solid sub-model and Figure 4.6b illustrates that it can still capture the experimental force-displacement hysteresis with acceptable accuracy by using the same material parameters adopted for the more detailed model of the beam fuse.

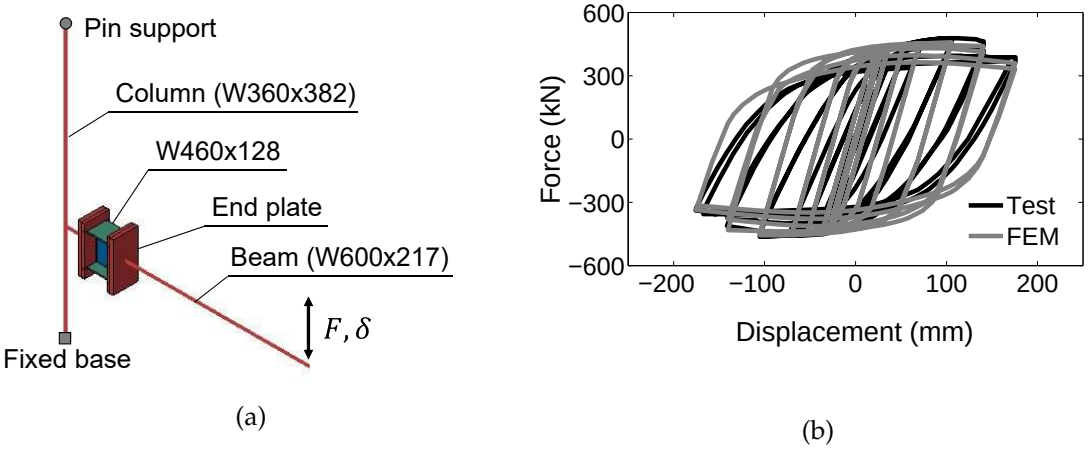

Figure 4.6. Beam-column connection with the beam fuse: (a) view of the beam-solid FEM sub-model; (b) comparison of numerical force-displacement response with the experimental results from Shen et al. (2011)

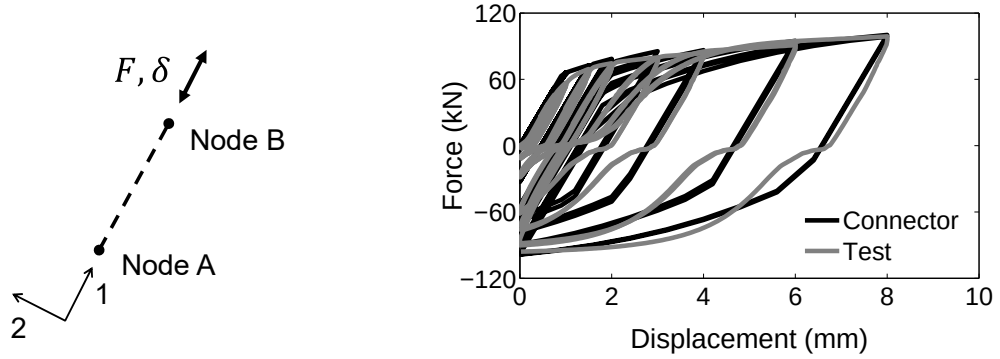

(a) (b)

Figure 4.7. Connector model of SSP: (a) definition; and (b) comparison of the connector response with the experimental WHP behaviour from Vasdravellis et al. (2013), under the ANSI/AISC 341-10 loading protocol

The SSPs and the friction pads are modelled using nonlinear connector elements. As shown in Figure 4.7a, connectors are spring-like elements with an elastoplastic force-displacement law. For the connectors modelling the friction pads, an elastic perfectly plastic force-displacement law is defined. The cyclic hardening parameters of the connectors modelling the WHPs are calibrated based on tests and additional FEM analyses, as follows. First, the experimental force-displacement response of an SSP, given in Vasdravellis et al. (2014), is used to define the response parameters of the connector element as 'half-cycle' data. This force-displacement law definition is convenient if the experimental data is available because it can capture the combined isotropic-kinematic hardening without the need for iterative simulations. Figure 4.7b shows the force-displacement comparison of a connector element with a tested WHP made of SSD from Vasdravellis et al. (2014) under the ANSI/AISC 341-10 loading protocol and indicates that connectors are effective in modelling the cyclic response of the steel pin. The pinching behaviour at zero force observed in the tests is not captured due to the more simplified uniaxial nature of the connector element behaviour.

Subsequently, for each SSP geometry used in each storey of the prototype frame, a detailed solid sub-model of the SSP-gusset plate connection is constructed using a refined mesh discretisation, as shown in Figure 4.8a. Each sub-model is subjected to the ANSI/AISC 341-10 cyclic loading protocol using the material hardening parameter calibration adopted in the detailed model. The resulting hysteretic response is extracted and used as input for a half-cycle

in the force-displacement law definition of the corresponding connectors. A typical comparison between the detailed sub-model and a connector element is shown in Figure 4.8b. Taking into account that three-dimensional effects (i.e., the pinching effect and plate deformability) cannot be captured by a connector element, the agreement is considered acceptable.

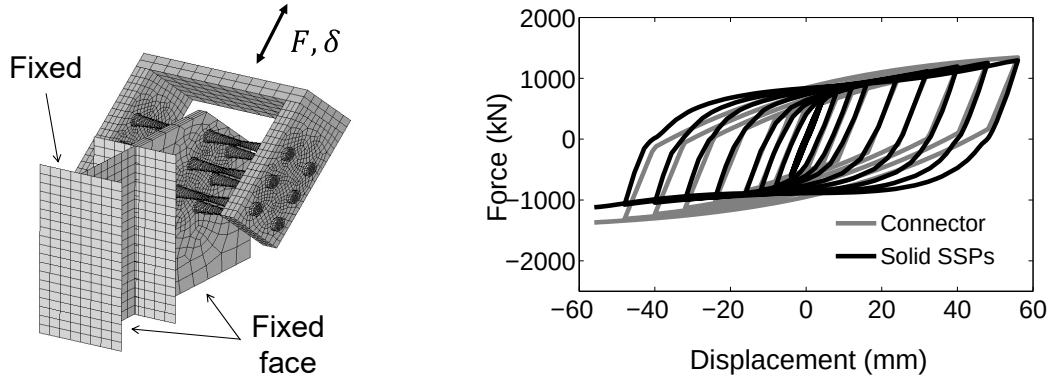

(a) (b)

Figure 4.8. SSP-gusset plate connection: (a) FEM solid sub-model; and (b) comparison between cyclic responses of the solid sub-model and the connector model

To compare the seismic performance of the proposed CBF-MRF with that of the BRBF-MRF, a simplified model of the dual BRBF-MRF is also constructed. The geometry is identical to the beam-solid model of the dual CBF-MRF, but the SSPs are removed and concentric BRBs are used to resist the lateral force. The BRBs are modelled as connector elements with elastoplastic behaviour, assuming a post-yield stiffness ratio of 0.01 based on component test results reported in Ariyaratana & Fahnestock (2011).

4.4 Nonlinear static analyses

This section presents the results of nonlinear static monotonic and cyclic analyses for the proposed CBF-MRF and the conventional BRBF-MRF. A comparison between the detailed and simplified models of the dual CBF-MRF is provided.

4.4.1 Nonlinear monotonic static analysis

Nonlinear monotonic static (pushover) analyses on the dual CBF-MRF are performed using both the detailed model and the simplified model. A triangular pattern of the lateral forces based on the height-wise mass distribution is used for the pushover analyses. A comparison of the base shear coefficient, i.e. V normalised by the seismic weight (W) of the building, versus roof drift, i.e. the roof horizontal displacement over the height of the building denoted as θ_r, responses of the two models is shown in Figure 4.9 and demonstrates a very good agreement between the two modelling techniques. The curve corresponding to the simplified model has a plateau at 3% roof drift, because of the activation of the friction pads, as intended. Figure 4.10 shows contour plots of the equivalent plastic strain on the deformed shapes of the SSP-gusset plate connection and the beam-column-fuse region at θ_r = 1.35% (i.e. the roof drift expected under the MCE) and θ_r = 3%. The results show that the beams, columns and braces are damage-free for roof drifts far beyond those expected under the MCE, whereas the SSPs and beam fuses are the only elements that experience plastic deformations.

A comparison between the dual CBF-MRF and the conventional BRBF-MRF is performed using the simplified models. The base shear coefficient versus the roof drift responses of the dual frames are compared in Figure 4.11. The target FOE, DBE and MCE roof drifts are indicated on the graphs, along with the sequence of the failure modes of the two frames. For the proposed dual CBF-MRF, the failure modes and corresponding roof drift levels are: SSP yielding at θ_r = 0.25%; beam fuse yielding at θ_r = 0.4%; and column base yielding immediately above the base gusset plates at θ_r = 0.65%. For the conventional BRBF-MRF, the failure modes and corresponding roof drift levels are: BRB yielding at θ_r= 0.3%; beam fuse yielding at θ_r = 0.45%; and column base yielding at θ_r = 0.64%. The two systems have comparable initial stiffness and similar base shear strength at first yield. The BRBF-MRF responds inelastically due to yielding of the BRBs, whereas the dual CBF-MRF yields due to yielding of SSPs and the beam fuses. However, the proposed dual CBF-MRF shows significantly higher post-yield stiffness. This is entirely attributed to the increased post-yield stiffness of the SSPs. As a result of the high post-yield stiffness, the dual CBF-MRF exhibits a considerably higher over-strength ratio (defined as the base shear at a given drift divided by the first

yield base shear) than the BRBF-MRF. The over-strength ratios at the DBE level are 1.24 and 1.75 for the BRBF-MRF and the dual CBF-MRF, respectively.

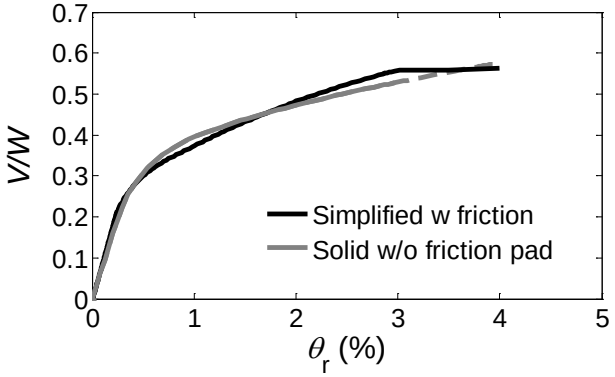

Figure 4.9. Comparison of base shear coefficient-roof drift behaviour between simplified and solid FEM models of the dual CBF-MRF from nonlinear monotonic static analysis

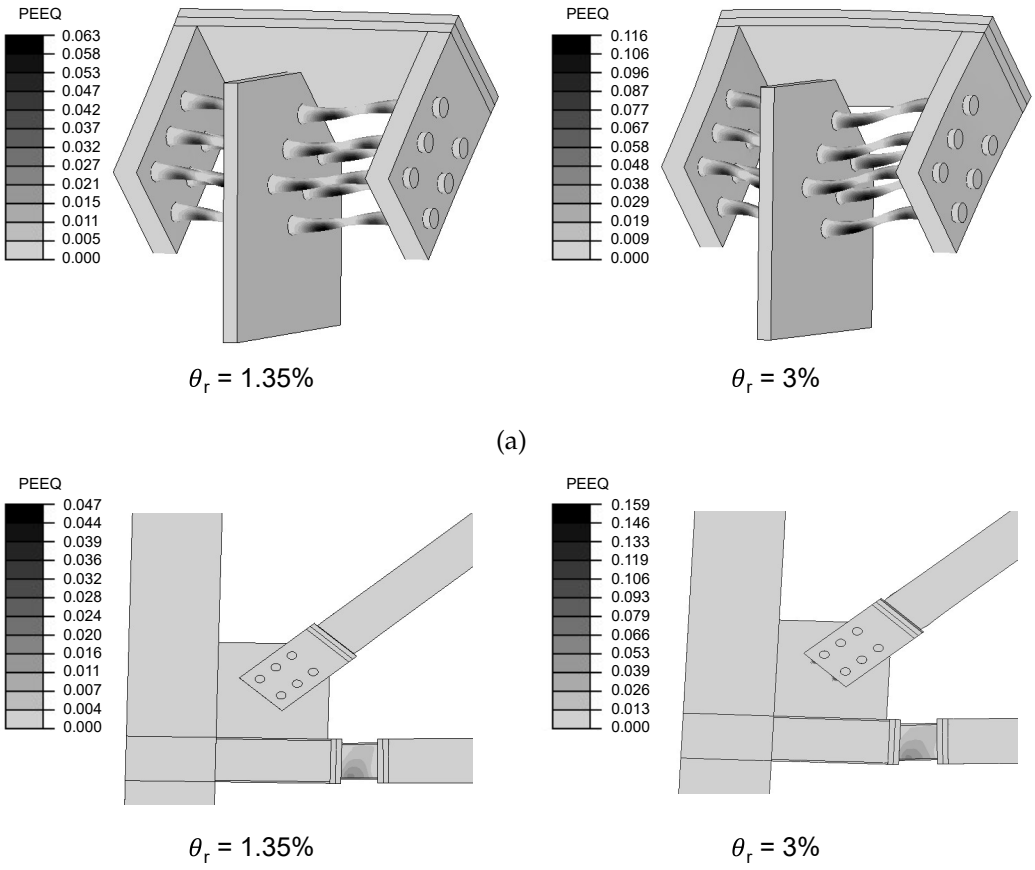

Figure 4.10. Equivalent plastic strain (PEEQ) distribution: (a) connection with SSPs; and (b) beam-column connection with the beam fuse

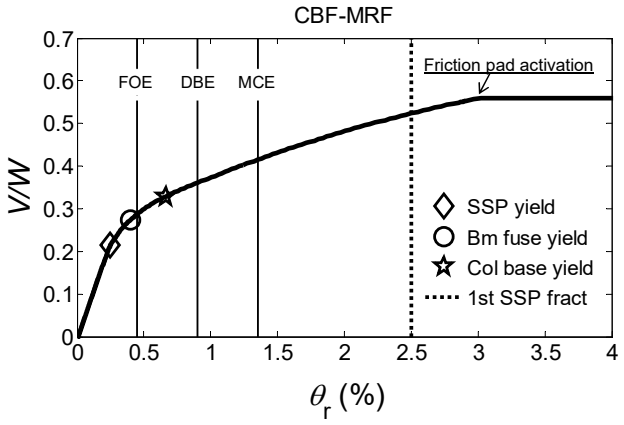

(a)

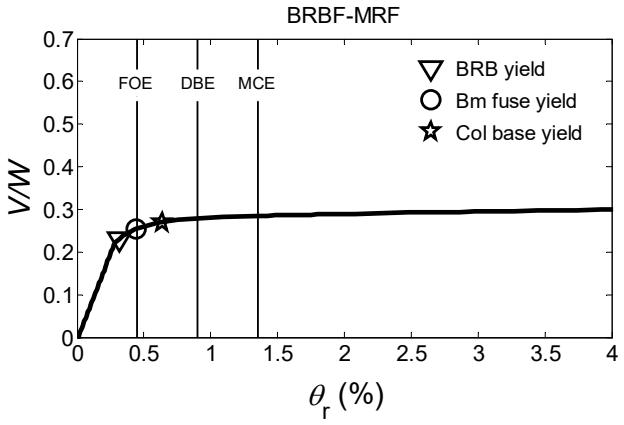

(b)

Figure 4.11. Base shear coefficient-roof drift response from nonlinear monotonic static analysis on the simplified models: (a) CBF-MRF; and (b) BRBF-MRF

The SSP fracture is not modelled explicitly, but it is crucial for the proposed frame, since it may result in a sudden drop of strength, accelerating the collapse of the frame. At this preliminary stage, a reasonable assumption on the likelihood of the SSP fracture is based on the experiments conducted by Vasdravellis et al. (2014), which showed that SSPs can achieve a ratio of fracture displacement to yield displacement, i.e. cyclic ductility, at least equal to ten under the standard seismic loading protocols recommended by ANSI/AISC 341/10 (2010) and FEMA 461 (2007). This observation was consistent for all the three steel grades and two different geometries of WHPs tested in that study, where two tests on WHPs made of SSD material achieved a cyclic ductility of ten and twelve. Under monotonic loading, they reached an ultimate displacement ratio even greater without fracture. From this, it is conservatively assumed that

SSPs fracture when they reach a displacement of ten times the yield displacement. This means that, for example, the SSPs installed on the fourth storey, having a yield displacement of 6.3 mm, will fracture at an imposed displacement of 63 mm. However, it should be noted that the assumed fracture capacity of the SSPs is based on limited experimental data, especially for the SSD material; for this reason, an experimental programme on full-scale SSPs and numerical investigation on their ductile fracture are carried out, as described later in Chapters 5 and 6.

The fracture of SSPs defines another limit state for the dual CBF-MRF, indicated in Figure 4.11 as "1st SSP fracture", i.e. denoting when the displacement demand exceeds ten times the yield displacement for the first time in the SSP. The monotonic pushover curve shows that the first SSP will fracture at θ_r = 2.5%.

4.4.2 Nonlinear cyclic static analysis

Nonlinear cyclic (push-pull) static analyses are performed on the detailed and simplified FEM models of the dual CBF-MRF. Displacement-controlled analyses are performed using a triangular force distribution. The frame is subjected to three cycles up to the FOE, DBE and MCE target drifts.

The $V/W - \theta_r$ responses obtained from the detailed and the simplified FEM models are shown in Figure 4.12a. A good agreement is observed between the responses of the two models, with a slightly lower base shear strength showed by the simplified model. Therefore, it can be concluded that the simplified FEM model can be reliably used for nonlinear dynamic analyses.

The cyclic response of the dual CBF-MRF is compared to the one of the conventional BRBF-MRF resulting from nonlinear cyclic (push-pull) static analyses. Figure 4.12b shows that both frames show large energy dissipation capacity. Similarly to the monotonic pushover analyses results, the cyclic inelastic behaviour of the two systems is noticeably different: the proposed frame possesses a significantly higher post-yield stiffness than the conventional frame as a result of the SSD material used for the SSPs.

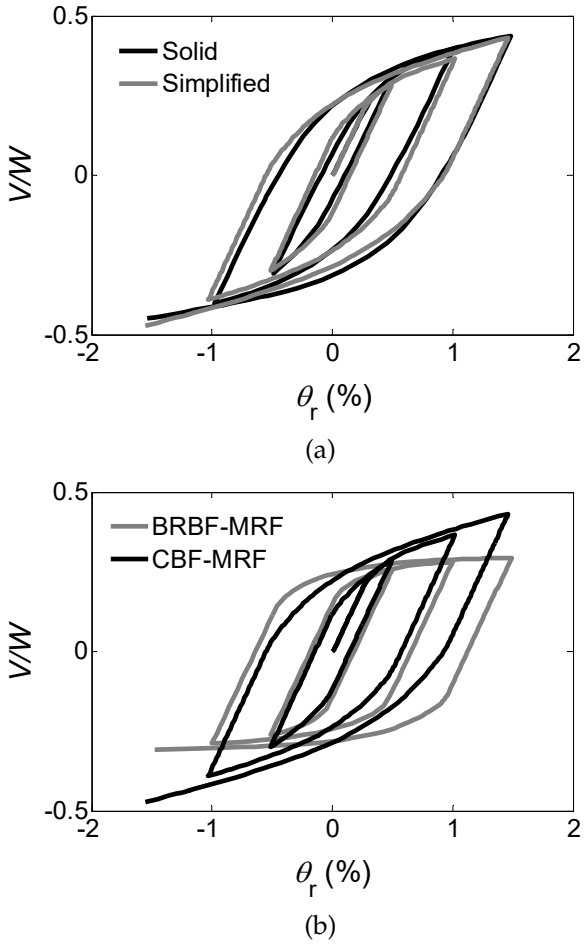

Figure 4.12. Cyclic push-pull response: (a) detailed and simplified FEM models of the dual CBF-MRF; and (b) CBF-MRF and conventional BRBF-MRF

4.5 Nonlinear dynamic analyses

Nonlinear dynamic analyses are conducted to evaluate the dynamic response of the dual CBF-MRF and the BRBF-MRF. Ground motions are selected from the FEMA P695 (2008) far-field ground motion database, which includes 22 record pairs, each with two horizontal components. To reduce the computational cost of the study, only the direction 1 component is used. The records are selected without consideration of spectral shape. It is noted that, while the 44 records are not supposed to present near-fault directivity effects, a recent study by Champion & Liel (2012) has shown that nine of them have pulses in the velocity history.

The 22 ground motion records (Table 4.1) are scaled to the FOE, DBE and

No.	Earthquake	Year	Recording Station	M	Scale factors		
					FOE	DBE	MCE
1	Northridge, USA	1994	Beverly Hills	6.7	0.36	0.72	1.08
2	Northridge, USA	1994	Canyon Country	6.7	0.52	1.05	1.58
3	Duzce, Turkey	1999	Bolu	7.1	0.35	0.71	1.06
4	Hector Mine, USA	1999	Hector	7.1	0.96	1.92	2.88
5	Imperial Valley, USA	1979	Delta	6.5	0.61	1.21	1.82
6	Imperial Valley, USA	1979	El Centro Array #11	6.5	0.86	1.72	2.57
7	Kobe, Japan	1995	Nishi-Akashi	6.9	0.45	0.91	1.36
8	Kobe, Japan	1995	Shin-Osaka	6.9	0.58	1.17	1.76
9	Kocaeli, Turkey	1999	Duzce	7.5	0.66	1.33	2.00
10	Kocaeli, Turkey	1999	Arcelik	7.5	1.96	3.89	5.83
11	Landers, USA	1992	Yermo Fire Station	7.3	0.69	1.38	2.07
12	Landers, USA	1992	Coolwater	7.3	0.91	1.81	2.72
13	Loma Prieta, USA	1989	Capitola	6.9	0.39	0.78	1.17
14	Loma Prieta, USA	1989	Gilroy Array #3	6.9	0.69	1.24	1.86
15	Manjil, Iran	1990	Abbar	7.4	0.48	0.97	1.46
16	Superstition Hills, USA	1987	El Centro Imp. Co.	6.5	0.5	1.02	1.53
17	Superstition Hills, USA	1987	Poe Road	6.5	0.85	1.69	2.54
18	Cape Mendocino, USA	1992	Rio Dell Overpass	7.0	0.54	1.08	1.63
19	Chi-Chi, Taiwan	1999	CHY101	7.6	0.50	1.00	1.50
20	Chi-Chi, Taiwan	1999	TCU045	7.6	0.66	1.33	1.99
21	San Fernando, USA	1971	LA - Hollywood Stor	6.6	1.61	3.23	4.85
22	Friuli, Italy	1976	Tolmezzo	6.5	0.82	1.65	2.47

Table 4.1. Ground motion records used for the dynamic analyses

MCE seismic hazard levels, according to the S_a-component scaling procedure. Spectra of the record set are scaled to match the spectral acceleration for the given hazard level at the fundamental period of the structure, which is computed using eigenvalue analysis. Given the similar fundamental periods of the dual frames, i.e., T = 0.75 s for CBF-MRF and 0.77 s for BRBF-MRF, the ground motions are scaled using T = 0.75 s.

4.5.1 Nonlinear dynamic analysis modelling

The time history analyses are performed using the simplified FEM models of the proposed dual CBF-MRF and the conventional BRBF-MRF. To take into account the seismic masses of the perimeter frame, the two external bays are also

included in the models along with the corresponding gravity loads. The mass is calculated on the basis of the dead plus one-third live load combination. Additional lumped masses are assigned to the beam elements to account for the total tributary mass to the perimeter frame. Beam elements with pinned beam-column connections are used to define the additional bays. The dynamic analyses are performed using the implicit dynamic algorithm of Abaqus (Dassault Systèmes 2014). The Hilber-Hughes-Taylor method is used by default to integrate the dynamic equations along with a Newton-like method to trace the nonlinear solution within a time step. The maximum time step is set ten times smaller than the input time step of the accelerogram to allow for an accurate estimation of the nonlinear response. Rayleigh damping equal to three percent of the critical damping is assigned to the first and second modes of the structures, following the approach recommended in Zareian & Medina (2010). A nonlinear load-controlled static analysis under gravity loads is first performed, and then the nonlinear dynamic time history analysis for each ground motion is executed. Each dynamic analysis is extended well beyond the actual earthquake time to allow for damped free vibration decay and accurate calculation of residual drifts.

4.5.2 Nonlinear dynamic analysis results

Figure 4.13 shows the obtained θ_r time histories of the dual CBF-MRF and BRB-MRF under the no. 16 record scaled to the DBE and MCE ground motions. Comparison of the response time histories reveals a significant difference in the residual drift values between the two systems. It is seen that, at the end of the ground motion, the BRBF-MRF oscillates and finds static equilibrium with appreciable residual drifts, whereas the dual CBF-MRF has a clear tendency to re-centre. While both systems experience a $\theta_{s,max}$ of approximately 1% under the DBE, the BRBF-MRF has a maximum residual drift $\theta_{s,res,max}$ of 0.4%, whereas the proposed CBF-MRF has a negligible $\theta_{s,res,max}$ of 0.09%. Under the MCE ground motion, the BRBF has $\theta_{s,max}$ = 1.88% and $\theta_{s,res,max}$ = 1.07%, while the corresponding values of the dual CBF-MRF are 1.56% and 0.38%. It is concluded that, under this particular accelerogram, even though the two systems experience similar peak storey drifts, the higher post-yield stiffness of the proposed frame results in a drastic reduction of residual drifts, avoiding repair

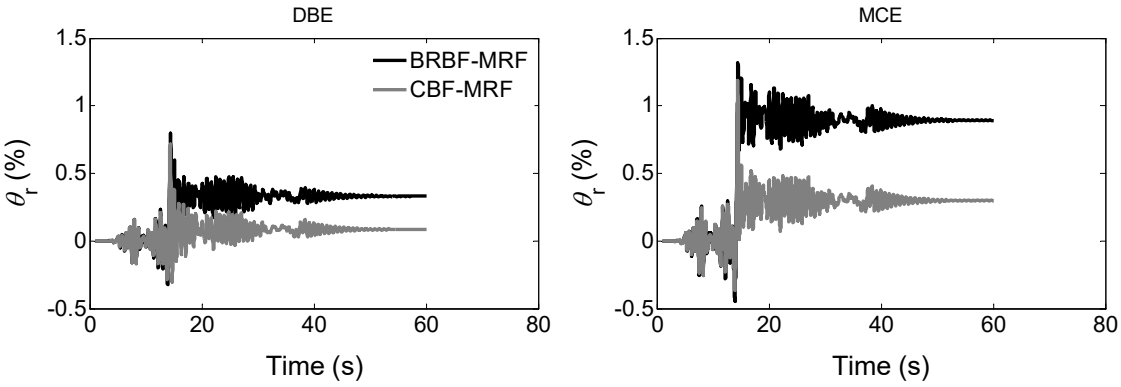

Figure 4.13. Roof drift time histories of the CBF-MRF and BRBF-MRF under no. 16 ground motion scaled to the DBE and MCE seismic hazard levels

and disruption even after the MCE record. In addition, the integrity of the main structural members is preserved as damage is concentrated in the SSPs and the beam fuses. Figure 4.14 shows the deformed shape of the connection with the beam fuse under no. 16 record scaled to MCE, where the equivalent plastic strain contours are shown for the peak imposed deformation. The results clearly indicate that plastic deformations (damage) are concentrated only in the replaceable beam fuse.

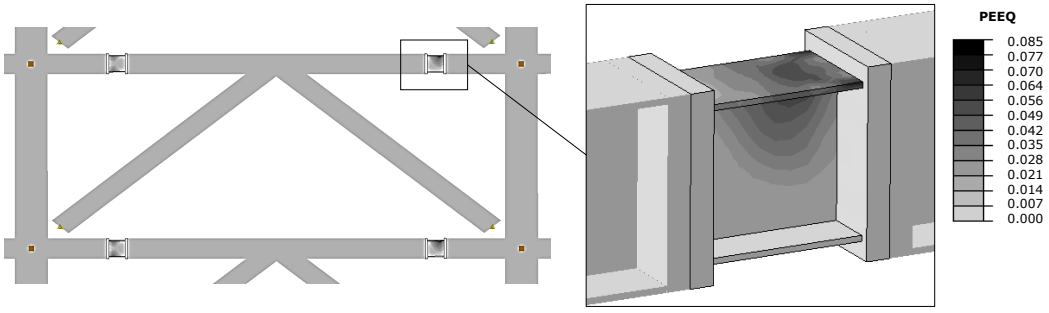

Figure 4.14. Equivalent plastic strain (PEEQ) distribution: beam-column connection with beam fuse under no. 16 record scaled to the MCE seismic hazard level (idealised beam element profiles are displayed)

Figure 4.15 shows the statistics of the storey drifts (θ_s) and residual drifts ($\theta_{s,res}$) throughout the height of the dual CBF-MRF under the FOE, DBE and MCE records, in terms of mean (m), median, and mean plus standard deviation ($m+\sigma$) values. Similar statistics are shown in Figure 4.16 for the BRBF-MRF under the DBE and MCE records. The $\theta_{s,max}$ and $\theta_{s,res,max}$ values typically occur in the third storey for the dual CBF-MRF and in the sixth storey for the BRBF-MRF.

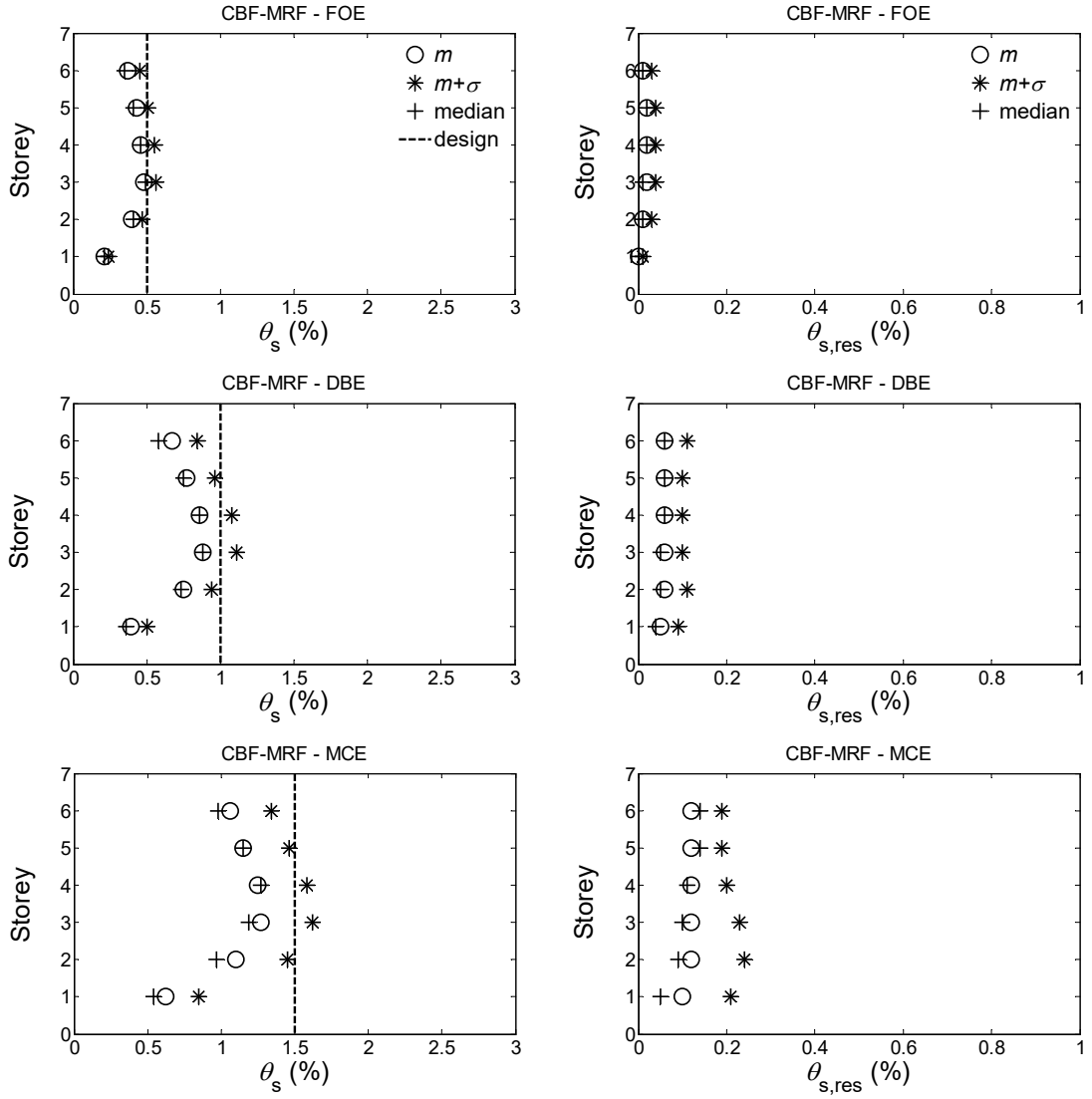

Figure 4.15. Statistics of response profiles of the CBF-MRF under 22 earthquake ground motions scaled to the FOE, DBE and MCE seismic hazard levels: (a) peak storey drifts; and (b) residual storey drifts

Comparison of the graphs in Figures 4.15 and 4.16 reveals that, while the storey drift profiles of the two frames are comparable and close to the target design values, the residual drifts of the proposed frame are significantly reduced. In particular, the residual drifts experienced by the dual CBF-MRF have values that are negligible under the FOE, very low under the DBE and well below the assumed reparability limit of 0.5% under the MCE records. In addition, even under the most severe MCE ground motions, the friction pads are

not activated, having no impact on the drift behaviour. The BRBF-MRF has significantly greater residual storey drifts than the dual CBF-MRF under the DBE and MCE earthquake records. It is observed that the standard deviation of the residual drifts is much smaller in the dual CBF-MRF system, with the $m+\sigma$ under the MCE being still well below 0.5%. The higher standard deviation of the residual drifts of the BRBF-MRF implies that the system can experience residual drifts greater than the 0.5% limit, as shown in Figure 4.16, with $m+\sigma$ reaching 0.80% under the MCE records. It is noted that the scaling procedure, which is based on the fundamental period of the CBF-MRF, may have contributed to the high standard deviation in the drift response of the BRBF-MRF.

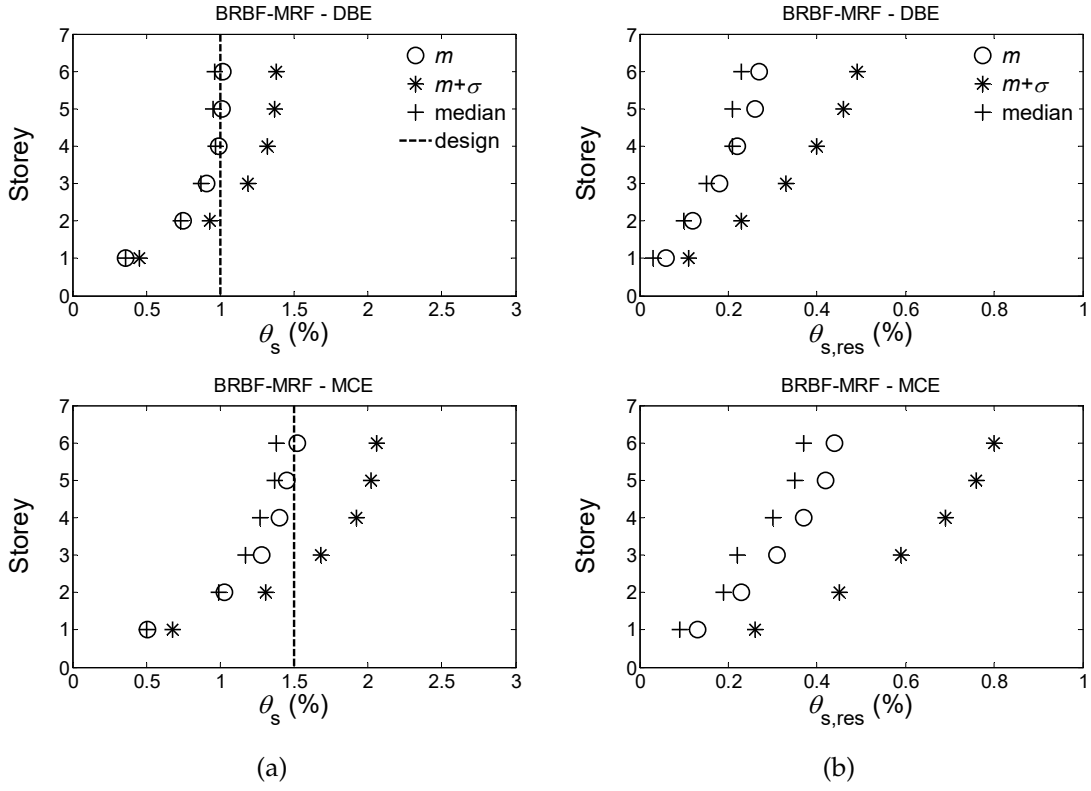

Figure 4.16. Statistics of response profiles of the BRBF-MRF under 22 earthquake ground motions scaled to the DBE and MCE seismic hazard levels: (a) peak storey drifts; and (b) residual storey drifts

Table 4.2 provides a summary of the statistics of $\theta_{s,max}$ and $\theta_{s,res,max}$ values for the two systems. The proposed dual frame has mean $\theta_{s,max}$ equal to 0.47% under the FOE, 0.88% under the DBE and 1.27% under the MCE. These values are slightly lower than the design target values (i.e. 0.48%, 0.96%, and 1.44%). The BRBF-MRF has slightly greater mean $\theta_{s,max}$ than the CBF-MRF, i.e. 1.02% and

1.52% under the DBE and MCE, respectively. The mean $\theta_{s,res,max}$ for the dual CBR-MRF is 0.02% under the FOE, 0.06% under the DBE and 0.12% under the MCE. The BRBF-MRF exhibited nearly five times larger mean $\theta_{s,res,max}$ under the DBE (0.27%) and almost four times larger mean $\theta_{s,res,max}$ under the MCE (0.44%). The m+σ of $\theta_{s,res,max}$ for the dual CBF-MRF are 0.10% and 0.23% under the DBE and MCE, respectively, i.e. still very low. The corresponding values for the BRBF-MRF are 0.49% and 0.80%, demonstrating a much higher scatter in the results. Therefore, the results of the dynamic analyses show that the proposed dual CBF-MRF is able to drastically reduce the residual drifts and, thus, enable a swift recovery even after a very rare MCE seismic event.

Dual frame type		$\theta_{s,max}$ (%)			$\theta_{s,max,res}$ (%)		
		m	$m+\sigma$	Median	m	$m+\sigma$	Median
CBF-MRF	FOE	0.47	0.56	0.49	0.02	0.04	0.01
	DBE	0.88	1.11	0.88	0.06	0.10	0.05
	MCE	1.27	1.62	1.19	0.12	0.23	0.10
BRBF-MRF	DBE	1.02	1.38	0.96	0.27	0.49	0.23
	MCE	1.52	2.06	1.38	0.44	0.80	0.37

Table 4.2. Storey drift statistics for the CBF-MRF and BRBF-MRF (see Appendix A for detailed results)

Reference	Frame type	Stories	T (s)	$\theta_{s,res,max}$ (%)		
				FOE	DBE	MCE
Sabelli et al. (2003)	BRBF	6	0.90	0.40	0.70	2.20
Kiggins and Uang (2006)	BRBF	6	0.77	-	0.29	-
	BRBF-MRF	6	0.77	-	0.13	-
Fahnestock et al. (2007)	BRBF	4	-	-	0.50	1.20
Fahnestock et al. (2007)	BRBF	4	0.71	0.20	1.30	2.70
Erochko et al. (2011)	BRBF	6	1.05	-	1.30	3.90
Sahoo and Chao (2014)	BRBF	6	0.97	-	0.41	-
This study	BRBF-MRF	6	0.77	-	0.27	0.44

Table 4.3. BRBF nonlinear dynamic analysis results from previous studies

To evaluate the fracture capacity of the SSPs employed in the dual CBF-MRF, the maximum displacement demands recorded in the connector elements are

compared with the assumed fracture limit of ten times the yield displacement. Figure 4.17 shows the statistics of the maximum displacement demands on the SSPs under the FOE, DBE, and MCE ground motion records in each storey, along with the yield displacement u_{y} and the assumed fracture limit $10u_{\mathrm{y}}$. The mean values of maximum displacement demand under the FOE and DBE are 8.4 mm and 17 mm, respectively. For the MCE hazard level, SSPs reach displacements with a mean value equal to 23 mm in the third storey. These results suggest that the displacement demands imposed on the SSPs are well below the assumed fracture value of ten times the yield displacement; therefore, there is a very small likelihood of fracture for seismic events up to MCE.

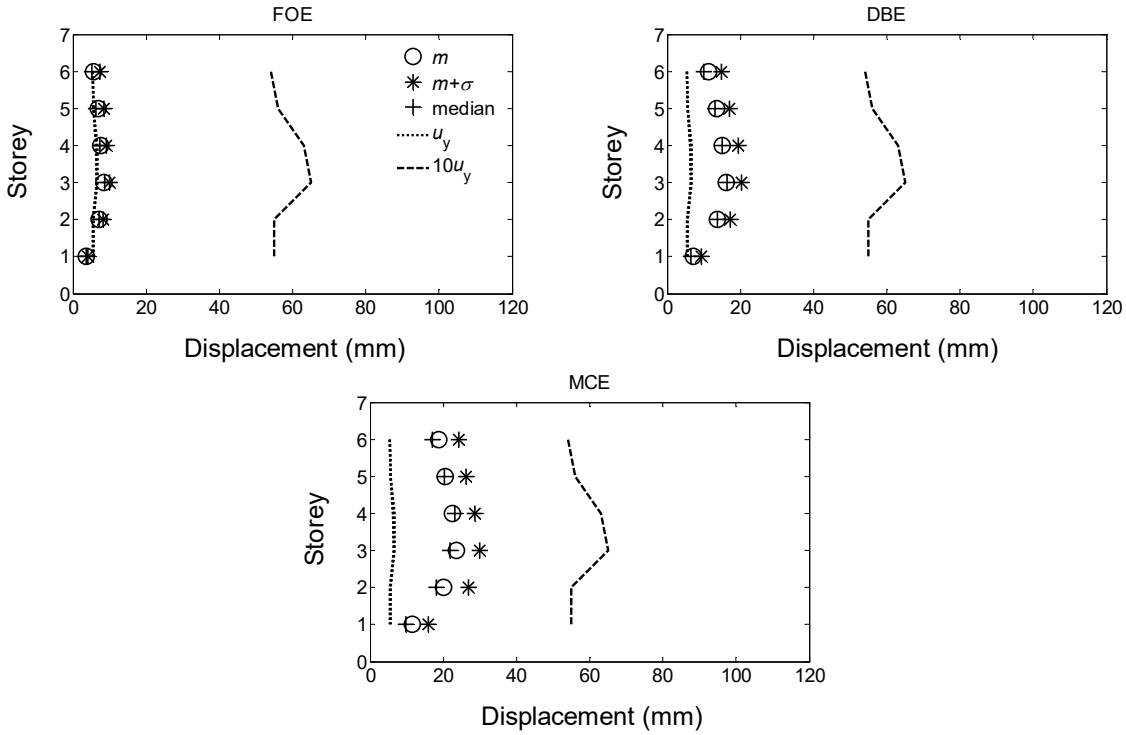

Figure 4.17. Maximum displacements in SSPs under 22 earthquake ground motions scaled to the FOE, DBE and MCE seismic hazard levels

4.6 Conclusions

In this chapter, the seismic performance of the dual CBF-MRF was evaluated by means of advanced numerical simulations using models of different complexity, i.e., a detailed and a simplified FEM model. Comparisons were drawn between the proposed CBF-MRF and the conventional BRBF-MRF. The results of the

numerical investigation led to the following conclusions:

- The simplified model of the CBF-MRF, using beam elements for the main structural members, nonlinear connector elements for the SSPs, and solid elements for the beam fuses, was found to provide a similar level of accuracy with the detailed FEM model using shell and solid elements.
- Nonlinear static monotonic and cyclic analyses performed on the detailed FEM model showed that the proposed design methodology guarantees that inelastic deformations are concentrated only in the SSPs and beam fuses, whereas the main structural components are essentially elastic even for drifts expected under the MCE.
- The proposed CBF-MRF exhibited a much higher post-yield stiffness than the BRBF-MRF having similar strength and stiffness, as a result of the properties of the duplex stainless steel material used for the SSPs.
- Nonlinear dynamic analyses on the simplified FEM model showed that the proposed CBF-MRF and the conventional BRBF-MRF experience comparable peak storey drifts. However, residual drifts of the CBF-MRF are drastically reduced as a result of the high post-yield stiffness of the frame. The maximum residual drift of the proposed CBF-MRF is negligible under the FOE, has a mean value of 0.06% under the DBE and a mean value of 0.12% under the very rare MCE. The maximum residual drift of the BRBF-MRF is five times larger under the DBE, and nearly four times larger under the MCE.
- The likelihood of fracture of the SSPs is low under the DBE and MCE, with displacement demands well below the assumed fracture limit of ten times the yield displacement. This fracture limit is based on relatively limited experimental data from Vasdravellis et al. (2014), indicating the need for further research on the fracture capacity of the SSPs. As such, an experimental programme is carried out to investigate the cyclic response of SSPs (Chapter 5), along with a numerical study on their ductile fracture (Chapter 6). The effect of the SSP fracture on the collapse capacity of the CBF-MRF is assessed in Chapter 7.

Chapter 5

Experimental Evaluation of Stainless Steel Pins (SSPs)

5.1 Introduction

The seismic evaluation of the dual CBF-MRF, presented in Chapter 4, was carried out using numerical FEM models calibrated against previous experimental data. Ductile fracture of stainless steel pins (SSPs) was not explicitly modelled, but a preliminary assessment of their fracture response was based on tests conducted on WHPs made of SSD (Vasdravellis et al. 2014). However, the available experimental data refers to a limited number of cyclic tests conducted under one-side loading protocols, as they were used to study the response of WHPs in a beam-column PT connection. Therefore, a further experimental investigation is conducted with the following aims:

- To test the SSPs in a configuration reproducing in full-scale the SSP-gusset plate connection of the dual CBF-MRF.
- To assess the seismic behaviour of the SSPs under full-cycle loading protocols.
- To reliably evaluate the fracture capacity of the SSPs.

This chapter describes the full-scale tests carried out in the Heavy Structures Laboratory at Heriot-Watt University (HWU). The results of sixteen tests on two different geometries of SSPs are presented. Tests were conducted under various loading protocols, representative of the seismic loading expected in the dual CBF-MRF. The material properties of SSD were evaluated using monotonic coupon tests on round bars.

Technical drawings of the full-scale SSP specimens, the test apparatus and the coupon specimens are attached in Appendix B.

5.2 Full-scale SSP specimens

In the dual CBF-MRF, each SSP-brace connection is made of four or more identical SSPs that work in parallel with each other (Figure 5.1). Since all SSPs undergo the same displacement when loaded, tests were conducted on a single SSP for each connection. Tests involved two different SSP geometries, representing the devices at the third and sixth storey of the prototype building, and denoted as SSP1 and SSP2, respectively. Figure 5.2 shows the geometries of the two specimens. SSP1 has D_e = 50 mm, D_i = 24 mm, and L_{SSP} = 225 mm (see Figure 3.4 for the geometry parameters). SSP2 has the same length of SSP1, but smaller external and internal diameters (D_e = 40 mm and D_i = 18 mm).

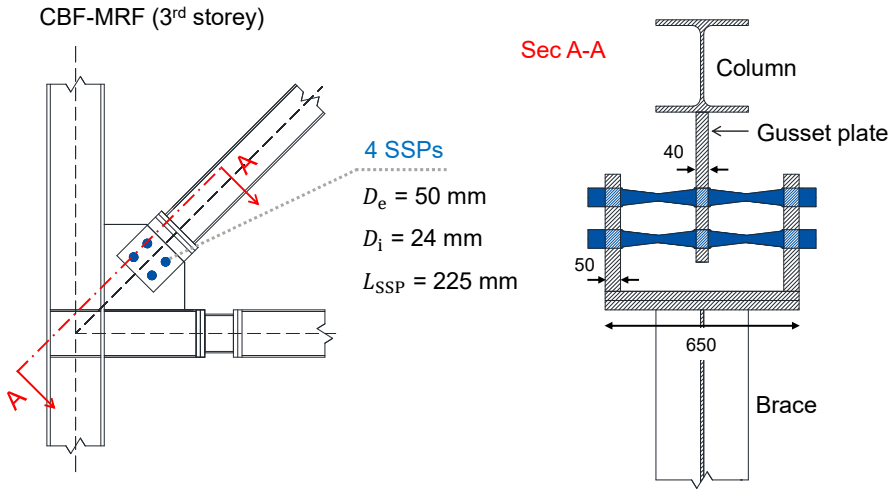

Figure 5.1. Brace-column connection with SSPs at the 3rd storey of the prototype 6-storey CBF-MRF (all the dimensions are in mm)

Eight specimens of each geometry were manufactured by machining 740-mm-long SSD round bars, having diameters equal to 65 mm and 51 mm, respectively. Figure 5.3a shows the cutting machine at the HWU Heavy Structures Lab used to lath the bars down to the required diameter. For an accurate and quick fabrication, a Computer Numerical Control (CNC) machine was used to grind the bars into the desired shape (Figure 5.3b). The specimens were fabricated with a slighly reduced maximum external diameter (nominal

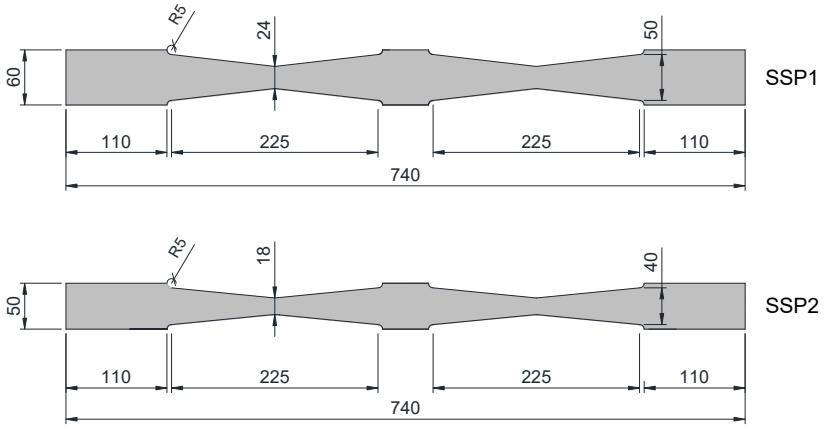

Figure 5.2. Geometry of the full-scale SSP specimens (all dimensions in mm)

value: D_e+10 mm) to allow for a small clearance of 0.2 mm in the holes of the supporting plates.

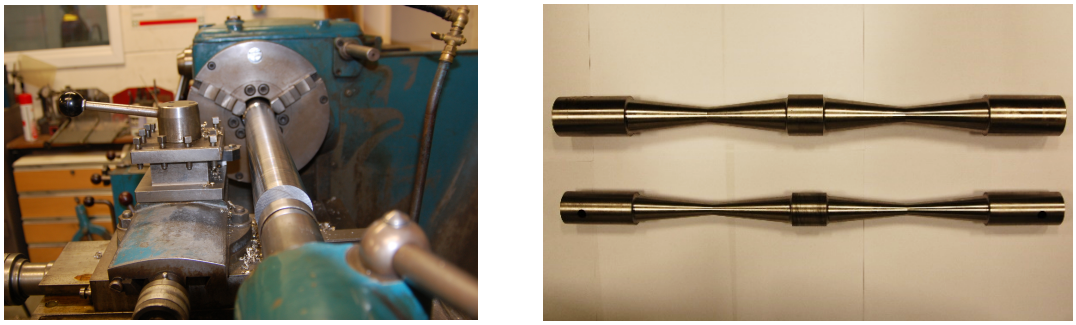

(a) (b)

Figure 5.3. SSP manufacturing: (a) Cutting machine at the HWU Structures Lab; and (b) SSP specimens

The material is duplex stainless steel (SSD), certified as UNS S31803 F51 by the manufacturer (UGITECH, France). The round bars were supplied in the solution annealed condition, because of the material yield strength in excess of 450 MPa. This type of stainless steel is much stronger (i.e., twice or more) than the common austenitic stainless steels.

5.3 Material coupon tests

Tensile coupon tests were carried out before testing the SSPs. Three uniaxial tests were conducted on uniform round bars, designed in accordance with EN 10002-1 (2001). The specimens were manufactured by machining 200-mm long round bars of 16-mm diameter, which were supplied along with the bars used for the

SSPs. As shown in Figure 5.4a, the coupon specimens have a nominal external diameter of 16 mm and are tapered to a reduced diameter of 12 mm for 80-mm length.

5.3.1 Testing machine and instrumentation

Three coupon specimens were tested using the Instron 8803 testing machine, shown in Figure 5.4b. The Instron machine has a maximum load capacity of 500 kN, with ±75 mm travel. Tests were run in displacement control at a rate of 1 mm/min until fracture. Vee-serrated jaw faces were fitted in the machine to grip the round specimens.

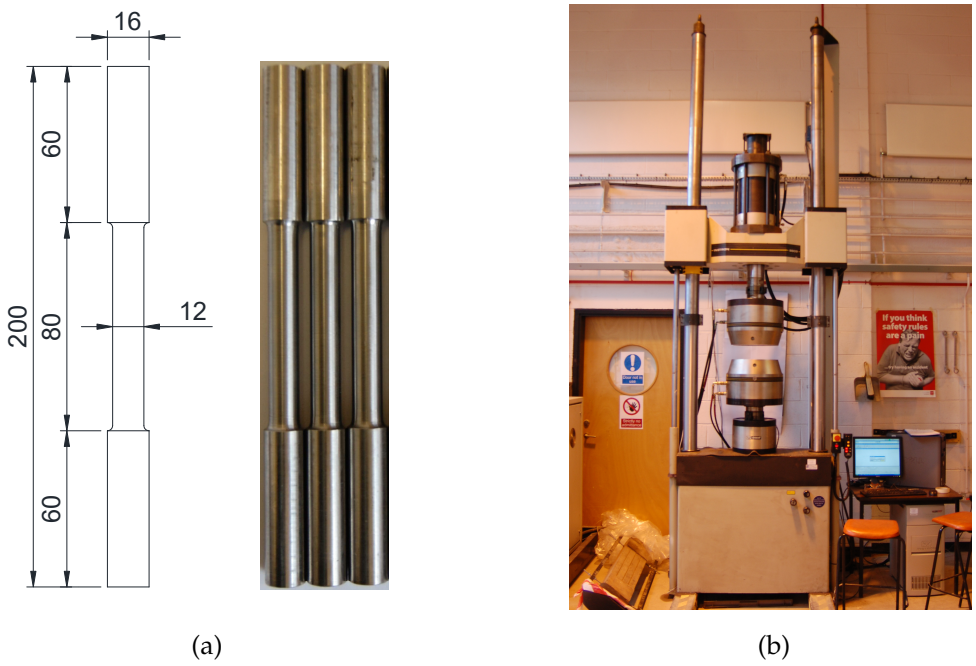

(a) (b)

Figure 5.4. Round coupon specimens: (a) geometry (all dimensions in mm); and (b) Instron 8803 testing machine

An axial clip-on extensometer of gauge length L_0 = 50 mm and +100%/-10% maximum strain was used to measure strain at the centre of the specimen, as shown in Figure 5.5a. To avoid damage of the extensometer, this was removed after the onset of necking (Figure 5.5b). The imposed displacement, the force F, and the extensometer elongation L were logged with a frequency of 10 Hz. The initial cross-sectional area A_0 and the reduced final area A_f were measured for each test.

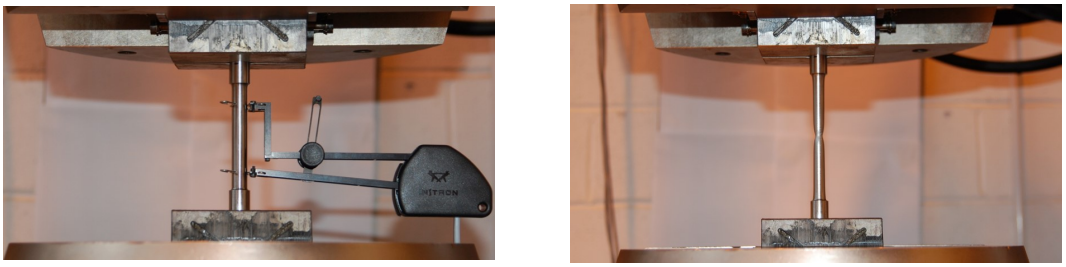

(a) (b)

Figure 5.5. Round bar test: (a) extensometer with 50 mm gauge length; and (b) necking in the centre of the specimen

5.3.2 Coupon test results

The force-displacement curves and the corresponding engineering stress-strain curves of the monotonic tests are shown in Figure 5.6a and 5.6b, respectively. The engineering stress S and strain e are defined in Eqs. (5.1) and (5.2):

$$S = \frac{F}{A_0} \tag{5.1}$$

$$e = \frac{L - L_0}{L_0} \tag{5.2}$$

Table 5.1 lists the mechanical properties of SSD. The Young's modulus E is the slope of the linear portion of the stress-strain curve. The yield stress f_y is calculated using the definition of the 0.2% strain offset. The ultimate stress f_u is the maximum load P_{max} divided by the original cross-sectional area of the specimen A_0, as expressed in Eq. (5.3):

$$f_u = \frac{P_{max}}{A_0} \tag{5.3}$$

Specimen	f_y (MPa)	f_u (MPa)	ε_f	E (MPa)
Round bar 1	530	752	45.7	189,655
Round bar 2	513	751	47.5	181,250
Round bar 3	518	746	47.9	187,500
Mean	520	750	47.0	186,135

Table 5.1. Summary of mechanical properties of SSD from coupon tests

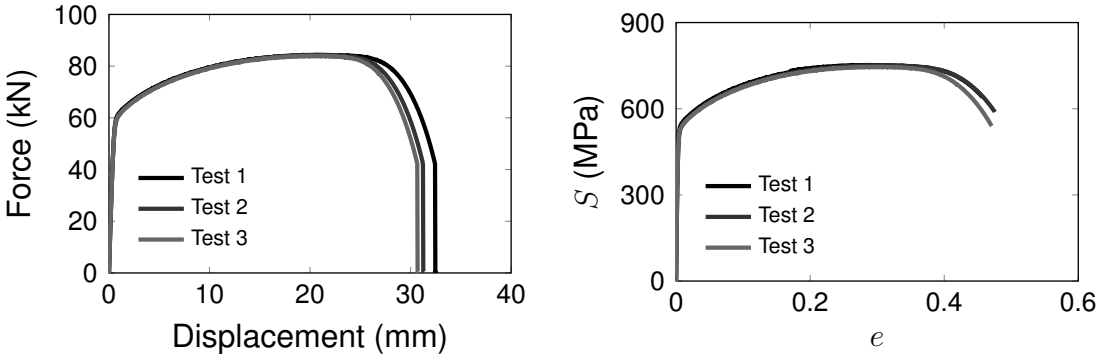

(a) (b)

Figure 5.6. Round bar monotonic tests: (a) force-displacement curves; and (b) engineering stress-strain curves

The SSD has average f_{y} and f_{u} equal to 520 MPa and 750 MPa, respectively, in agreement with the material certificates. The yield stress is also consistent with the one adopted in the design of the SSPs (see Section 3.5.1). Figure 5.6a shows that SSD is characterised by large ductility and high post-yield stiffness. The ratio of the post-yield stiffness to the elastic stiffness is 1/125.

After the onset of necking, the cross-sectional area of the specimen rapidly decreases, leading to a drop in the load-carrying capacity and, thus, in the engineering stress, calculated using the initial area of the specimen (see Eq. 5.1). In fact, the hardening of the material continues up to fracture with strain increases that are produced by a rise in stress (ASM 2002). A true description of the material behaviour is obtained with the true-stress/true-strain curve (also known as flow curve), where the true stress is computed using the actual cross-sectional area of the specimen and the true strain is based on instantaneous measurement. The true stress σ is dependent on S and e, as expressed in Eq. (5.4):

$$\sigma = S(e+1) \tag{5.4}$$

The true strain ε is calculated using e, as expressed in Eq. (5.5):

$$\varepsilon = \ln(e+1) \tag{5.5}$$

Therefore, the true plastic strain can be calculated as:

$$\varepsilon^{pl} = \ln(e+1) - \frac{S}{E} \tag{5.6}$$

Eqs. (5.4) and (5.6) are valid up to the onset of necking, when localised strains develop in the necked region. After this stage, the behaviour of the material is defined by a linear relationship up to the fracture point, where the true stress σ_{f} and true strain ε_{f} are computed as expressed in Eqs. (5.7) and (5.8), respectively:

$$\sigma_{\mathrm{f}} = \frac{P_{\mathrm{f}}}{A_{\mathrm{f}}} \tag{5.7}$$

$$\varepsilon_{\mathrm{f}} = \ln \frac{A_0}{A_{\mathrm{f}}} \tag{5.8}$$

Figure 5.7 illustrates the true-stress/true-plastic-strain curve for SSD, obtained from test 3. This curve is used to define the material properties in FEM simulations.

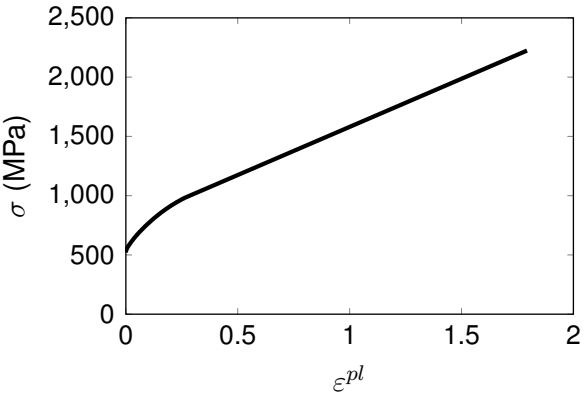

Figure 5.7. SSD true stress-true plastic strain curve

5.4 Testing apparatus

The full-scale component tests on SSPs were conducted using the Losenhausen UPS2000 testing machine, shown in Figure 5.8a. The self-reacting testing machine (LOS machine) has 2000 kN force capacity in tension and compression, and ±120 mm displacement capacity. Displacements are imposed by the top grip, where the bottom grip is fixed to the strong floor.

A configuration reproducing the SSP-gusset plate connection of the CBF-MRF was used. Figure 5.8b shows the test setup designed to accommodate the two different SSP geometries. It consists of two assemblies of steel plates, indicated as upper and lower supporting plates, which represent the gusset plate tied to the

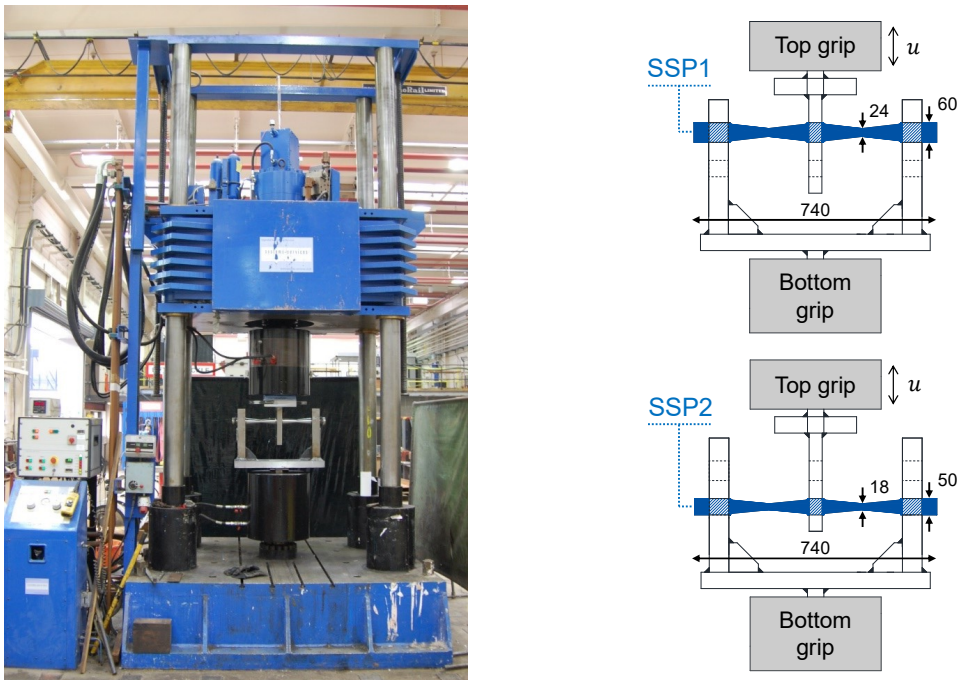

(a) (b)

Figure 5.8. SSP testing apparatus: (a) Losenhausen UPS2000 testing machine; and (b) testing configuration for SSP1 and SSP2 (all the dimensions are in mm)

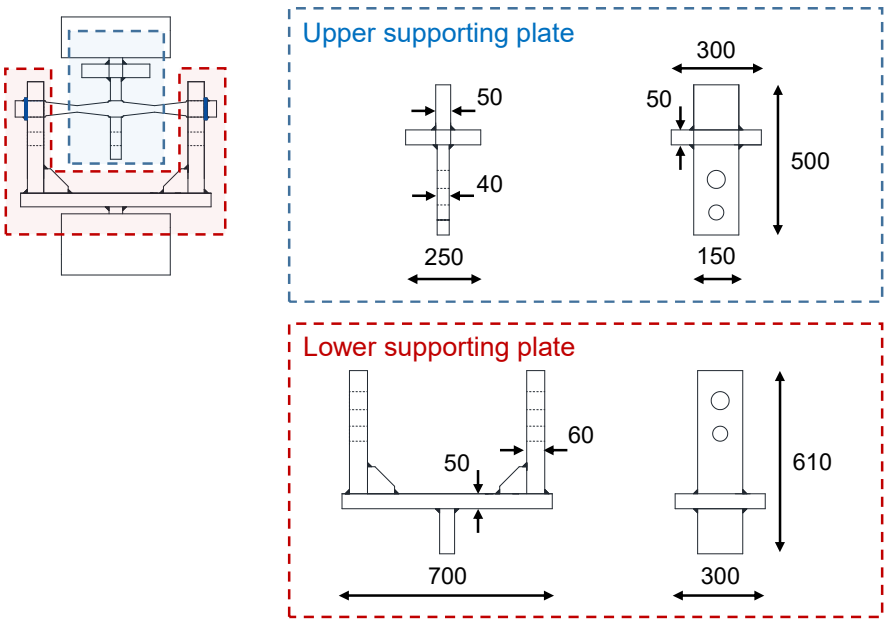

Figure 5.9. Geometry of the supporting plates of the testing apparatus (all the dimensions are in mm)

beam-column connection, and the U-shaped plate tied to the bracing member, respectively (see Figure 5.1). The SSPs were inserted into aligned holes drilled in the vertical plates. The top row of holes was used for the SSP1, whereas the bottom row was used for the SSP2.

The geometry of the two assembly plates is shown in Figure 5.9. The top assembly is made of a 40-mm thick vertical plate welded normally onto a 50-mm thick 300x200 mm horizontal plate. The bottom assembly is made of two vertical 60-mm thick plates welded normally onto a 700x150x50 mm horizontal plate. Two 150x300x50 mm plates welded onto the top and bottom horizontal plates are gripped by the testing machine. The supporting plates are designed following the rules for the design of the U-shaped and gusset plates, described in Section 3.5.3.

To prevent excessive bending of the vertical plates of the bottom assembly as the SSP deforms, 30 mm-thick triangular stiffeners were welded at the base of the plates, as shown in Figure 5.9. This reinforcement was added after the first two tests, in which excessive bending of the plates was observed for large imposed displacement.

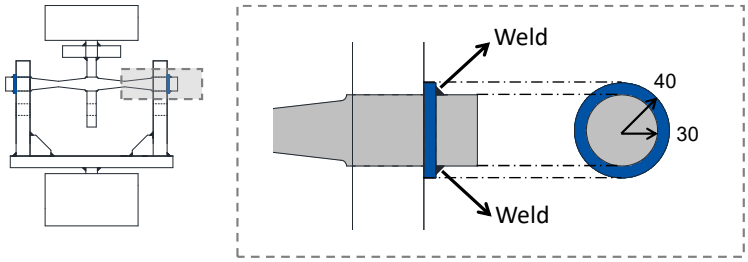

(a)

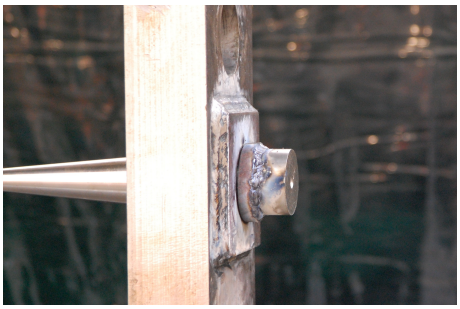

(b)

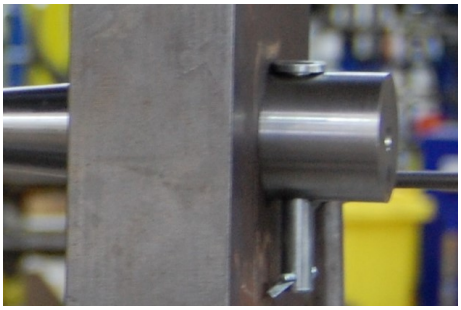

(c)

Figure 5.10. SSP axial constraint: (a) steel collar geometry for SSP1 (all dimensions in mm); (b) collar welded onto SSP2 with additional steel plate; and (c) 12-mm diameter clevis pin used in first test on SSP2

The SSPs were axially constrained using a 10-mm thick steel collar welded onto their ends (Figure 5.10a). At the start of each test, the collar was just in contact with the vertical plates, as illustrated in Figure 5.10b. The need for such constraint was highlighted by the experimental work of Vasdravellis et al. (2014), in which non-axially-constrained SSPs had experienced some slip. Figure 5.10c shows the constraint initially adopted in this experimental work to axially restrain the specimens: it consisted of a 12-mm diameter clevis pin passing through a 13-mm hole drilled at the ends of the specimen. However, the clevis pin failed during the first AISC test on SSP2, causing the specimen to slip and deform the holes of the lower vertical supporting plates. To restore the correct clearance between the specimen and the drilled holes, a 100x100x10 mm steel plate with a 50-mm drilled hole was welded to the vertical plates in the remaining SSP2 tests, as shown in Figure 5.10b.

5.5 Testing instrumentation

Two linear variable differential transformers (LVDTs) were used to measure the relative displacement between the top and bottom plate assemblies. The LVDTs, indicated as LVDT-1 and LVDT-2, had ±150 mm travel length and were fixed to the bottom horizontal plate by magnetic bases, with their tip attached to the top horizontal plate, as shown in Figure 5.11.

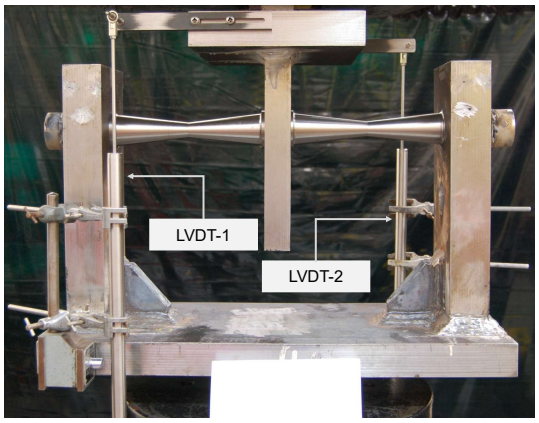

Figure 5.11. SSP testing instrumentation: LVDTs

The actuator of the LOS machine was controlled by a MOOG FCS controller. All the tests were performed in position control. The position and force feedback signals were logged by the controller with a frequency of 2 Hz. Since the

controller accommodates only two input signals, an independent data acquisition board and host computer were used to log the output from the LVDTs, along with the load and displacement feedback signals. The signal from transducers was recorded with the same frequency of 2 Hz.

5.6 Loading protocols

The SSPs were subjected to a range of different loading protocols, as listed in Table 5.2. The loading protocols were applied under displacement control at a rate ranging from 5 to 40 mm/min at ambient temperature.

Specimen	Test no.	Protocol
SSP1	1	AISC
	2	CA = $7u_y$
	3	CA = $6u_y$
	4	CA = $5u_y$
	5	CA = $4u_y$
	6	Random-1
	7	Random-2
	8	Monotonic

(a)

Specimen	Test no.	Protocol
SSP2	9	AISC
	10	CA = $8u_y$
	11	CA = $7u_y$
	12	CA = $6u_y$
	13	CA = $5u_y$
	14	CA = $4u_y$
	15	Random
	16	Monotonic

(b)

Table 5.2. Loading protocols of the full-scale tests: (a) SSP1; and (b) SSP2

Phase	No. of cycles	Amplitude
1	2	u_y
2	2	$0.5u_{DBE}$
3	2	u_{DBE}
4	2	$1.5u_{DBE}$
5	2	$2u_{DBE}$

Table 5.3. The AISC loading protocol

The first loading protocol, denoted as AISC, is the one recommended in Annex K in ANSI/AISC 341/10 (2010) for the seismic evaluation of buckling restrained braces (BRBs). Since the behaviour of a brace with SSPs is similar to a BRB, it is reasonable to evaluate the SSPs with the qualification protocol of BRBs. The AISC loading history is presented in Table 5.3, where u_y is the yield

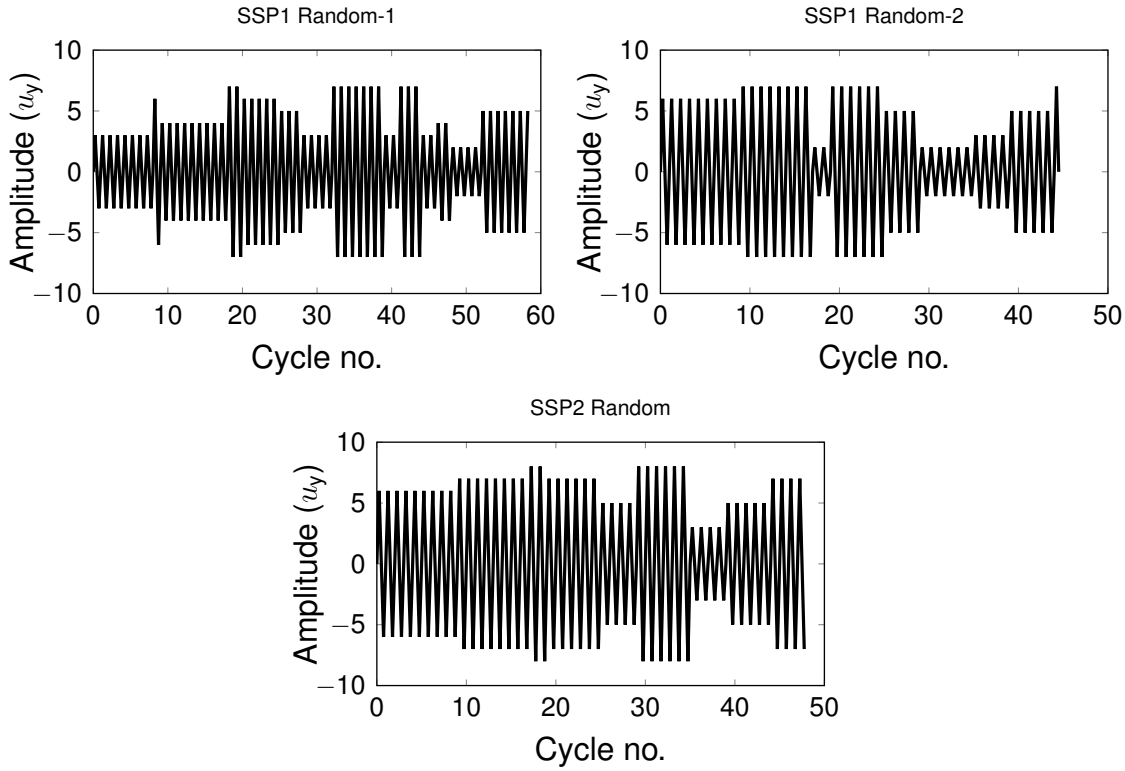

Figure 5.12. Random protocols for SSP1 and SSP2

displacement of the SSP and u_{DBE} is the displacement demand expected under the DBE. The values of u_{y} and u_{DBE} were preliminary calculated based on the numerical analyses presented in Chapter 4 as: u_{y} = 6.5 mm and u_{DBE} = 17 mm for SSP1; and u_{y} = 6 mm and u_{DBE} = 14 mm for SSP2. The AISC protocol prescribes cycles of increasing imposed displacements with amplitudes u_{y}, $0.5u_{\mathrm{DBE}}$, u_{DBE}, $1.5u_{\mathrm{DBE}}$, and $2u_{\mathrm{DBE}}$, each one applied for two cycles. To fully characterise the hysteretic response of each SSP up to fracture, the protocol was extended to include four additional cycles at $1.5u_{\mathrm{DBE}}$, followed by two cycles at $2.5u_{\mathrm{DBE}}$, and then a series of cycles with an amplitude increased by $0.5u_{\mathrm{DBE}}$ every two cycles.

Steel structures subjected to earthquake-induced loading typically undergo large cyclic inelastic deformations. Unlike low-cycle fatigue, highly inelastic cycles can induce ductile fracture after a relatively small number of cycles, generally less than 100 (Pereira et al. 2014) or even 20 (Kanvinde 2017). This type of loading is termed ultra-low cycle fatigue (ULCF). To investigate the ductile fracture response of the SSPs under ULCF, constant amplitude (CA) and random protocols are used. The imposed CA are defined as multiple of the SSP yield displacement u_{y}, where SSP1 was tested under CA = $4u_{\mathrm{y}}$, $5u_{\mathrm{y}}$, $6u_{\mathrm{y}}$, and $7u_{\mathrm{y}}$, and

SSP2 was tested under CA = $4u_y$, $5u_y$, $6u_y$, $7u_y$, and $8u_y$. A u_y value of 7 mm was obtained from the results of the AISC tests on the two SSPs. The random protocols consist of randomly-generated number of cycles and imposed displacements. These protocols, shown in Figure 5.12, were defined assuming displacement values in the range of 2 to 8 times u_y and cycles between 1 and 9.

In addition, to assess the response of SSPs under monotonic loading, a monotonic test was performed for each SSP geometry.

5.7 Results of full-scale SSP tests

Sixteen full-scale component tests were carried out to evaluate the hysteretic response, ULCF life, and energy dissipation of SSPs. For each SSP geometry, the AISC tests were performed first, followed by ULCF tests, i.e., CA and random protocols, and a monotonic test.

5.7.1 Cyclic hysteresis

Figure 5.14 shows the force-displacement hysteresis of the two specimens under the AISC protocol. The SSPs successfully passed the imposed protocol showing stable hysteresis and appreciable ductility. Figure 5.13 illustrates the deformed shapes of the SSPs under the AISC test.

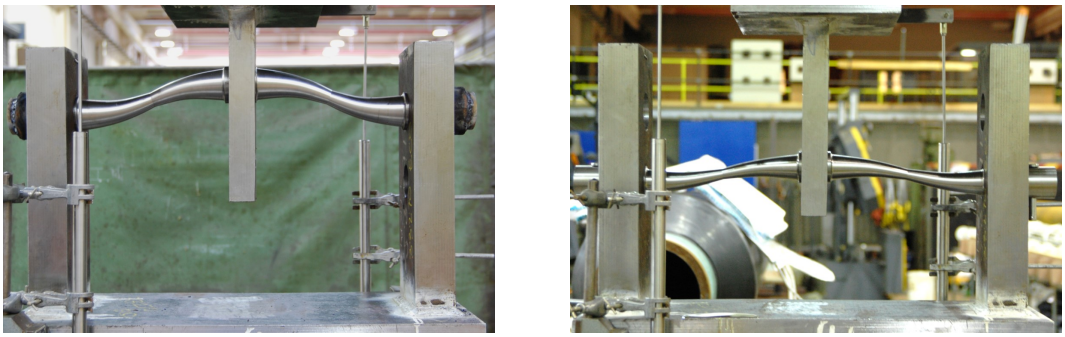

(a) (b)

Figure 5.13. Deformed SSP shape under the AISC protocol: (a) SSP1; and (b) SSP2

Both specimens were then subjected to an additional sequence of larger inelastic cycles, as discussed in the previous section. Figure 5.15 shows the response of SSPs under the extended AISC protocol. The test on SSP2 was first performed and was stopped after two cycles at $4.5u_{DBE}$ due to the failure of one

clevis pin used as axial constraint (see Figure 5.10c). No fracture initiation was observed in the specimen. A similar response was exhibited by the SSP1, which was axially constrained using the steel collar shown in Figure 5.10b. The test was terminated after the completion of two full cycles at $4.5u_{\mathrm{DBE}}$ as no signs of deterioration were observed. Under the extended AISC tests, the SSPs achieved a large cyclic ductility without reaching fracture. The ratio of maximum displacement to yield displacement is equal to eleven for SSP1 and nine for SSP2. This confirms the preliminary assumption on their fracture capacity adopted in the numerical evaluation of the dual CBF-MRF (see Section 4.4.1), where a cyclic ductility of ten was assumed.

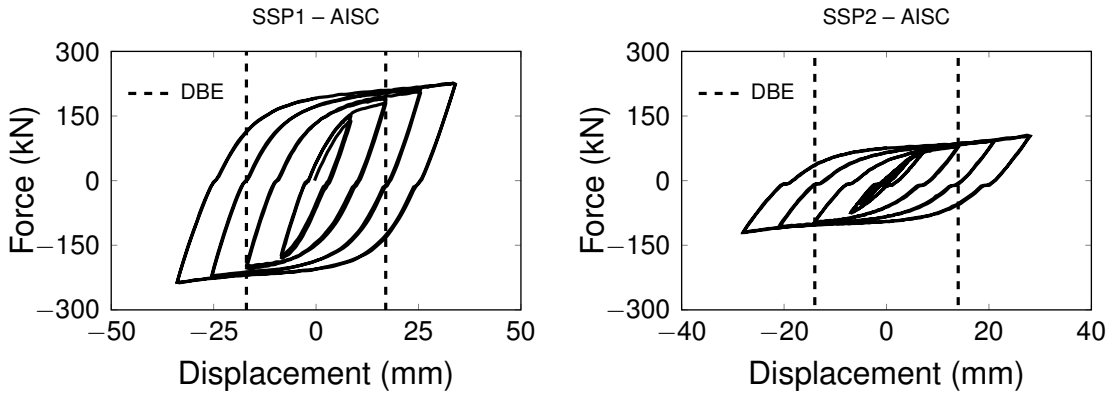

Figure 5.14. Hystereses of SSPs under the AISC protocol

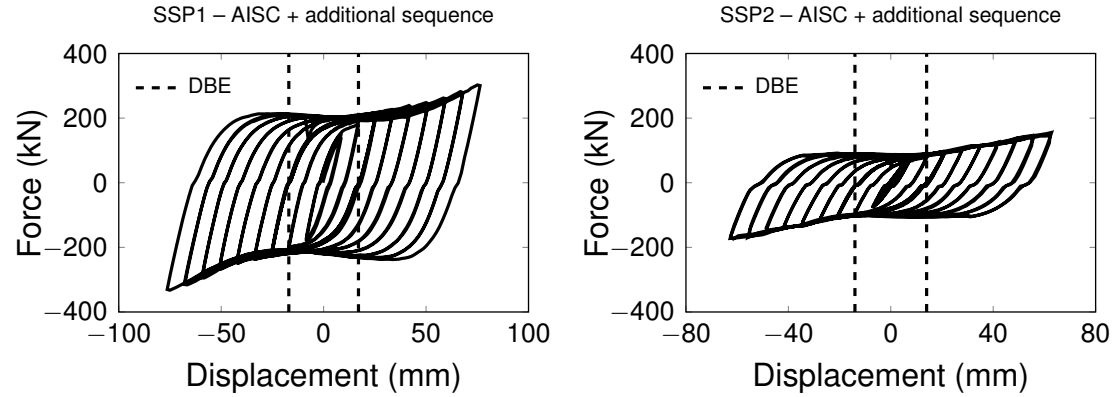

Figure 5.15. Hystereses of SSPs under the extended AISC protocol up to $4.5u_{\mathrm{DBE}}$

Figures 5.16 and 5.17 show the hysteresis of SSP1 and SSP2 under the ULCF loading protocols. Ductile fracture occurred in all tests. The SSPs sustained many inelastic cycles before fracture, showing a stable hysteretic behaviour and large energy dissipation capacity. The force-displacement curves are

characterised by a slight pinching at zero force, due to the small clearance in the holes of the supporting plates. This was also observed in Vasdravellis et al. (2014), where a small clearance allowed for the slip of the specimens. There is a noticeable hardening behaviour at large displacements, i.e. CA $> 5u_{\mathrm{y}}$. This can be attributed to the combination of two factors: a) the inherent high post-yield stiffness of the SSD material; and b) the elastic bending of the supporting plates at large displacements, which causes the response to 'harden' in each successive cycle of large imposed displacement. It can be observed that the hysteresis of

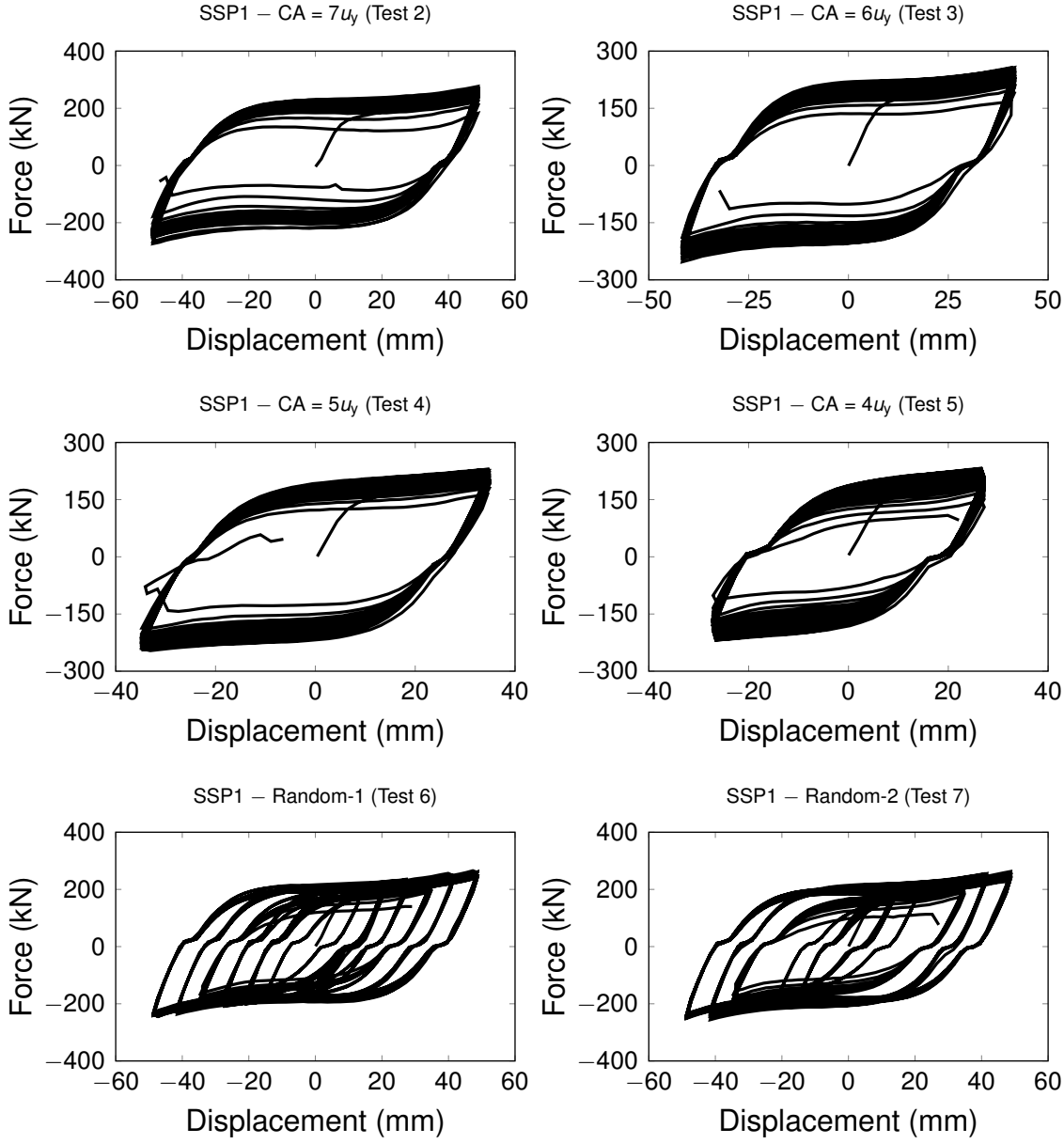

Figure 5.16. Hystereses of SSP1: constant amplitude (CA) and random tests

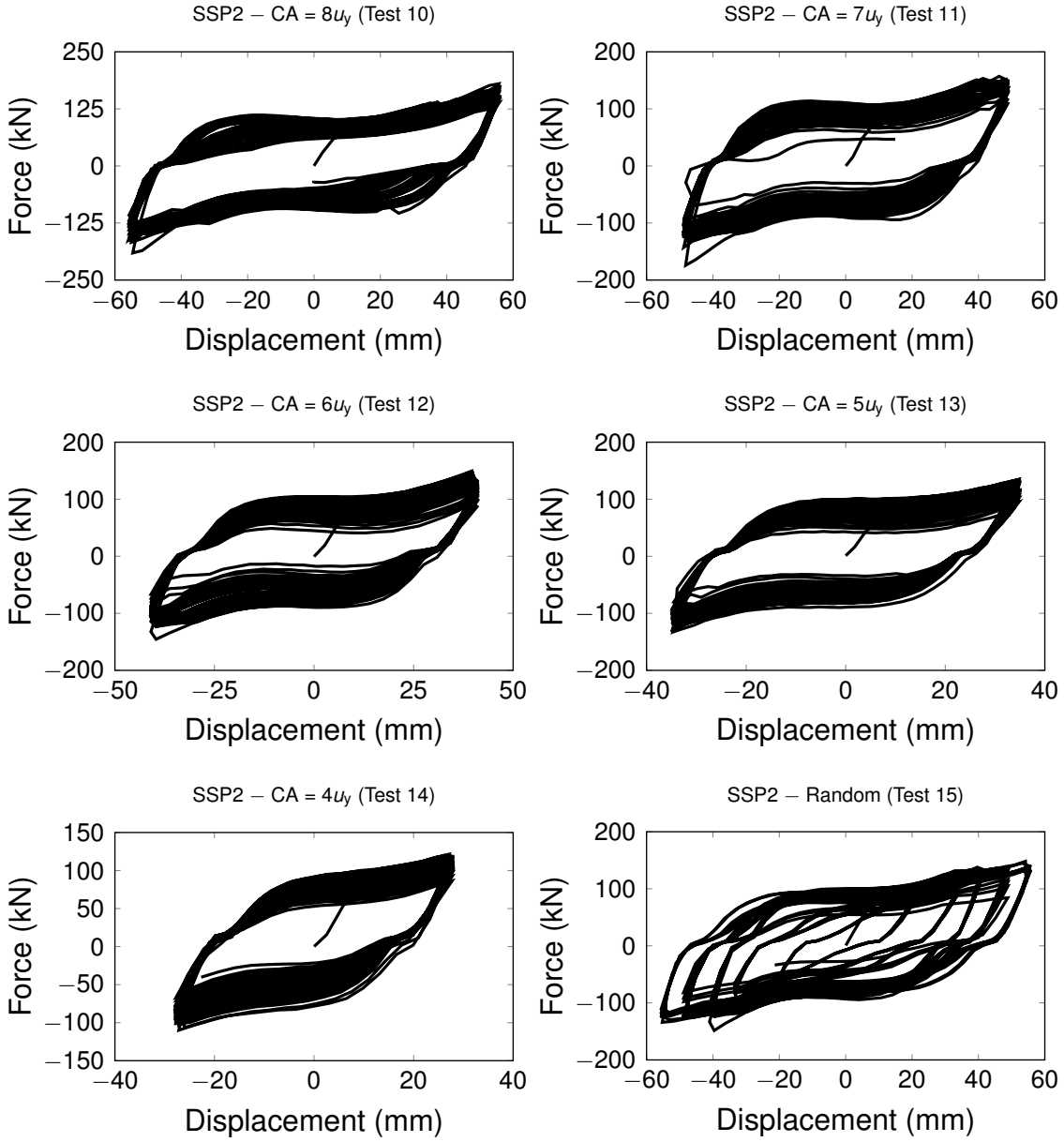

Figure 5.17. Hystereses of SSP2: constant amplitude (CA) and random tests

SSP2 in tests no. 10 to 12 is characterised by a reduced hardening, especially in compression. This was mainly due to the severe deterioration of the holes of the supporting plates. While the correct clearance was restored following the AISC test, some degree of damage in the holes might have affected the grip between the holes and the specimen.

The optimised shape of the SSPs resulted in large plastic deformations throughout the whole length of the bending parts. This caused a large axial elongation of the SSPs that increased with the cycles. Figure 5.18 shows the

(a) (b)

Figure 5.18. Axial elongation: (a) SSP1; and (b) SSP2

appreciable axial elongation of SSP2 after 30 cycles under CA = $7u_y$. The maximum elongation was in the range of 15-20 mm for SSP1 and 30-40 mm for SSP2. This indicates that plastic deformations in SSP2 were spread over a larger area than in SSP1.

5.7.2 Ductile fracture due to ULCF

Ductile fracture consistently initiated on the surface of the SSP at the middle sections of the bending parts, i.e., halfway between D_e and D_i, as illustrated in Figure 5.19. These fracture locations are denoted as section 1 and 2, where section 1 is the one closest to the lower supporting plate. The number of cycles to fracture initiation and full-section failure were recorded for each ULCF test, as reported in Table 5.4.

(a) (b)

Figure 5.19. Fracture locations: (a) SSP1; and (b) SSP2

Once fracture initiation occurred in sections 1 and 2, several micro-cracks gradually propagated to full-section fracture after several cycles. Figure 5.20a shows the evolution of ductile fracture in SSP1 tested under CA = $6u_y$. Small

Specimen	Test no.	Protocol	Failure mode	No. of cycles	
				Full fracture	Fracture initiation
SSP1	1	AISC	No fracture	–	–
	2	CA = $7u_y$	Ductile fracture	28	21
	3	CA = $6u_y$	Ductile fracture	35	25
	4	CA = $5u_y$	Ductile fracture	44	31
	5	CA = $4u_y$	Ductile fracture	78	43
	6	Random-1	Ductile fracture	59	35
	7	Random-2	Ductile fracture	45	25
	8	Monotonic	No fracture	–	–
SSP2	9	AISC	No fracture	–	–
	10	CA = $8u_y$	Ductile fracture	33	30
	11	CA = $7u_y$	Ductile fracture	43	36
	12	CA = $6u_y$	Ductile fracture	59	41
	13	CA = $5u_y$	Ductile fracture	76	45
	14	CA = $4u_y$	Ductile fracture	89	54
	15	Random	Ductile fracture	48	40
	16	Monotonic	No fracture	–	–

Table 5.4. Test matrix of the full-scale tests on SSPs

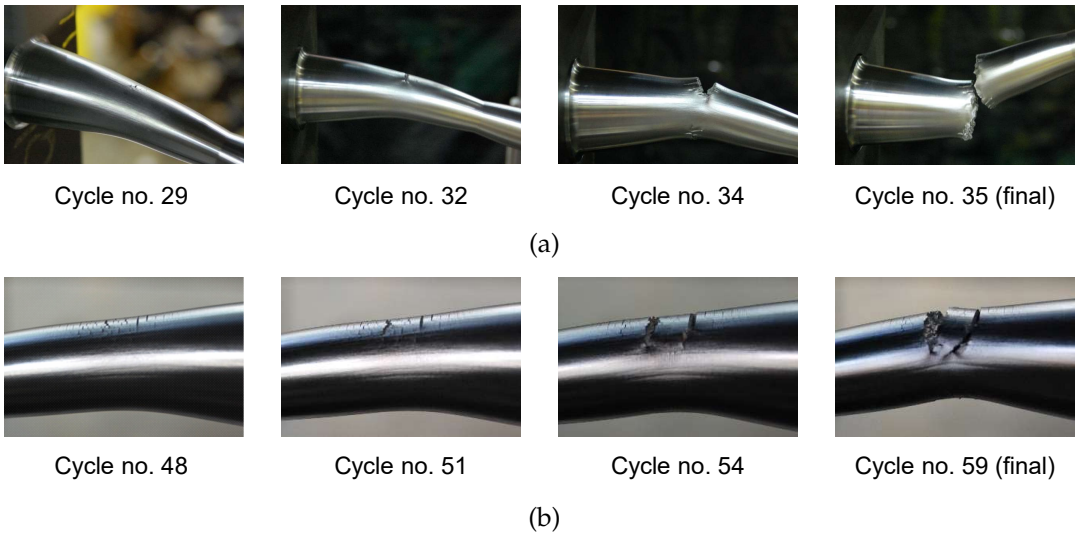

Figure 5.20. Ductile fracture under CA = $6u_y$: (a) SSP1; and (b) SSP2

cracks were first observed after 25 cycles, followed by the growth of larger crack during the 29th cycle, which propagated in the successive six cycles up to the full-section fracture of the specimen. The fracture mechanism observed in SSP2 under the same loading protocol is illustrated in Figure 5.20b: widespread cracks initiated at the free surface and gradually grew to form two large cracks

that led to the complete failure of the specimen.

The force histories of the same tests, plotted in Figure 5.22, show that, once fracture initiated, the load-carrying capacity of the SSPs remained stable for many cycles, and dropped just few cycles before failure. Figure 5.21 illustrates two examples of the typical full-section fracture observed in the tests.

(a) (b)

Figure 5.21. Final cycle with fracture: (a) SSP1 (test 6); and (b) SSP2 (test 13)

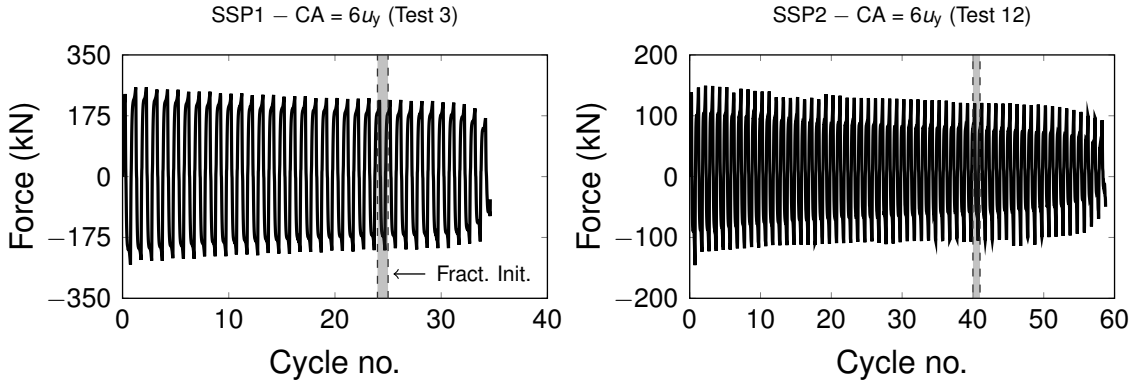

Figure 5.22. Force histories of SSPs under CA = $6u_y$

5.7.3 Prediction of SSP strength

The SSP fracture mechanism illustrated in Figure 5.19 indicates that plastic hinges form in the middle of half bending part. As preliminarily discussed in Section 3.5.1, the SSP plastic mechanism is different from the one assumed in the analytical model proposed by Vasdravellis et al. (2013). In fact, the latter was developed based on tests on stocky WHPs, where the maximum plastic moment was at the D_e sections. Based on the new experimental evidence, this analytical model is modified assuming that the maximum plastic moment is halfway

between D_e and D_i, as follows:

$$M_{pl} = \left(\frac{D_{PH}^3}{6}\right) f_{y,SSP} \tag{5.9}$$

where $D_{PH} = (D_e + D_i)/2$. The yield force is then calculated as:

$$F_{y,SSP} = \frac{4M_{pl}}{L_{PH}} = \frac{2D_{PH}^3}{3L_{PH}} f_{y,SSP} \tag{5.10}$$

where $L_{PH} = L_{SSP}/2$. Using Eq. (5.10), $F_{y,SSP1}$ = 156 kN and $F_{y,SSP2}$ = 75 kN. The analytical values for the yield strength are in excellent agreement with the experimental ones, i.e., 150 kN and 75 kN, respectively. Therefore, the modified analytical model can be used to predict the strength of the SSPs.

5.7.4 Energy dissipation capacity

The energy dissipation (ED) capacity of a SSP is evaluated by computing the amount of energy dissipated in each cycle, denoted as W. This is the area enclosed in the hysteresis of a single cycle. For a consistent comparison between the two SSPs, W is normalised by the product of u_y and the corresponding F_y.

Figure 5.23 compares the ED curves of the two SSP geometries under different cyclic protocols. While the ED capacity of SSP1 and SSP2 is similar during the first cycles, SSP2 experienced a more visible ED deterioration than SSP1. However, SSP2 was able to sustain a larger number of cycles than SSP1.

Figure 5.24 compares the ED capacity of the single SSPs under the CA loading protocols. It can be seen how the ED curves decrease proportionally to the imposed amplitude. A comparison of the energy dissipated by the SSPs between the CA and random tests is shown in Figure 5.25. It can be observed that the ED capacity under the random tests is similar to the corresponding CA tests over the first thirty cycles, while it decreases in the final phase due to the severity of the random loading protocol.

5.7.5 Monotonic tests

One monotonic test was carried out for each SSP geometry. Figure 5.26a shows the monotonic response of SSP1, where the test was terminated at a maximum displacement of 110 mm. The specimen exhibited a high post-yield stiffness

equal to 1/10 of the elastic stiffness. No signs of ductile fracture were observed at the maximum imposed displacement, indicating that ductile fracture is unlikely to occur even under extreme displacements of sixteen times the yield displacement. This largely exceeds the assumed limit of ten times the yield displacement adopted in Section 4.4.1. However, in the SSP1 test, the lower steel plate assembly experienced large bending, as shown in Figure 5.26b. The excessive deformation of the plates is related to the boundary conditions of the

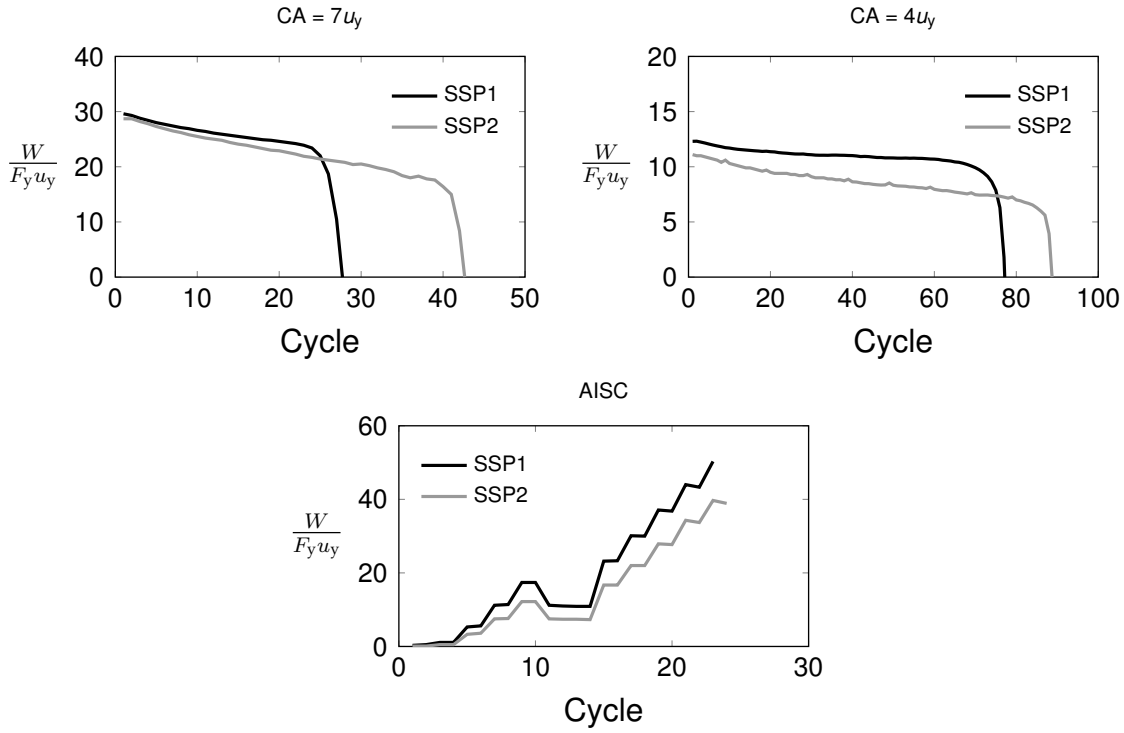

Figure 5.23. Comparison of energy dissipation (ED) between SSP1 and SSP2 under CA and AISC protocols

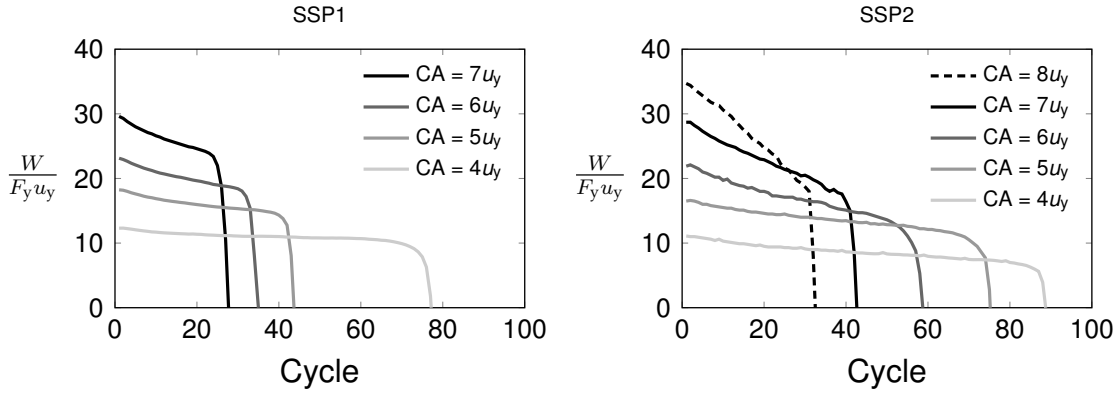

Figure 5.24. ED for individual SSPs under CA protocols

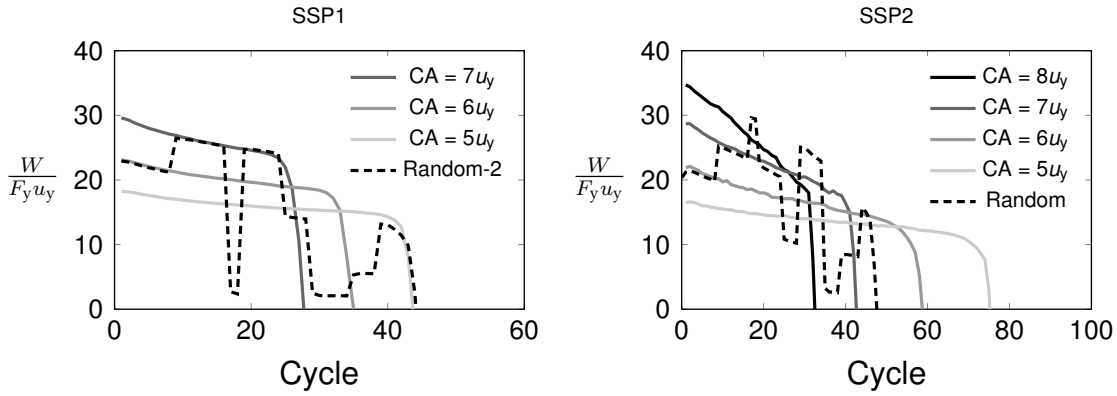

Figure 5.25. Comparison of ED between CA and random tests for individual SSPs

test apparatus, which could not be fully constrained to the ground. This could not exactly reproduce the constraint exerted in the CBF-MRF from the brace section, connected to the lower U-shaped plate. A reduced deformability of the lower supporting plate would provide a more accurate estimation of the fracture capacity of the SSPs under monotonic loading.

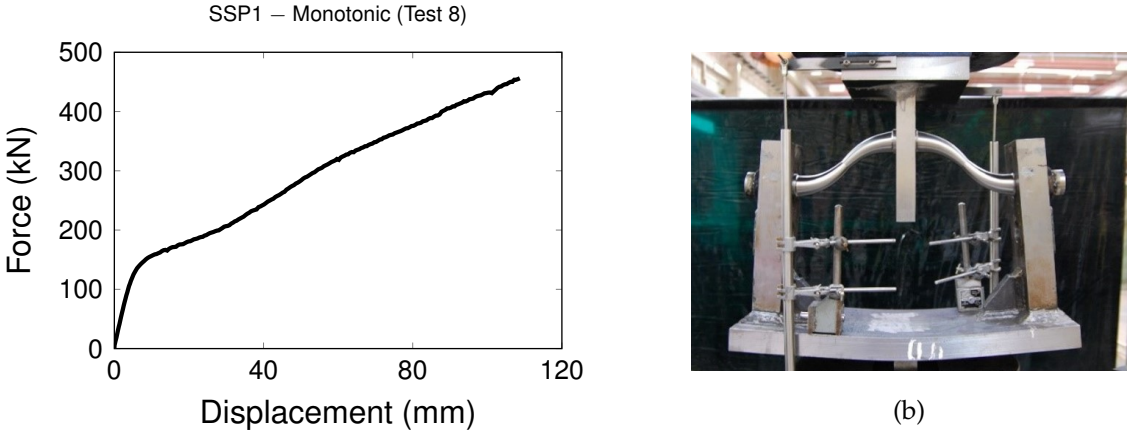

(a)

(b)

Figure 5.26. SSP1 monotonic test: (a) force-displacement curve; and (b) deformed shape at 110 mm imposed displacement

Figure 5.27a illustrates the force-displacement curve of the monotonic test on SSP2, which had to be prematurely terminated at 55 mm due to a sudden breakdown of the LOS machine. At the maximum displacement, the SSP did not show any sign of fracture. The specimen exhibited a post-yield modulus equal to 1/5 of the elastic modulus.

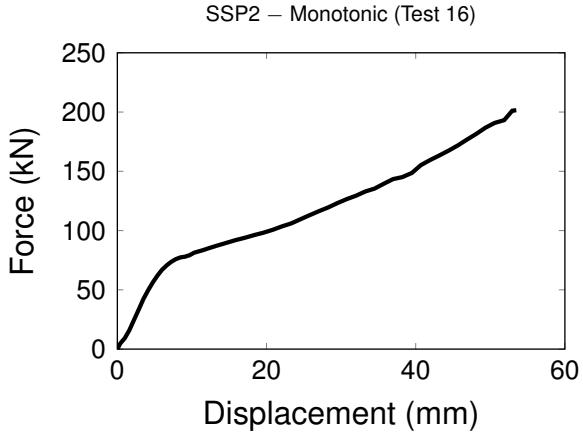

(a)

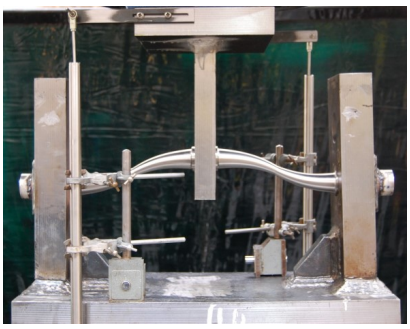

(b)

Figure 5.27. SSP2 monotonic test: (a) force-displacement curve; and (b) deformed shape at 55 mm imposed displacement

5.7.6 Imposed versus relative displacement

The test apparatus was instrumented with LVDTs to measure the relative displacement between the two supporting plates (see Section 5.5). The imposed displacements recorded by the LOS machine are verified against the displacements logged by the LVDTs for all tests.

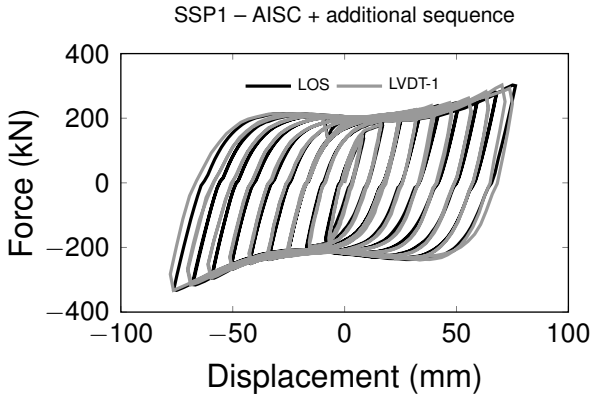

Figure 5.28. Comparison of force-displacement curves from LOS machine and LVDT-1

Figure 5.28 plots the comparison of the force-displacement curves under the extended AISC test on SSP1 between the LVDT-1 displacements and the imposed LOS displacements, respectively. The comparison shows an excellent agreement, apart from a small scatter in the large displacement range ($u > \pm 60$ mm), which is due to the bending of the lower horizontal plate. It can be

concluded that the displacements recorded by the LOS machine were not affected by elastic deformations of the testing apparatus.

5.8 Conclusions

This chapter presented the experimental programme carried out to assess the seismic response and the fracture behaviour of the stainless steel pins (SSPs). Two full-scale SSP geometries were tested in a configuration reproducing the SSP-gusset plate connection of the proposed dual CBF-MRF. The geometry of the specimens was representative of the SSPs employed in the design for the prototype building presented in Chapter 3. To characterise the duplex stainless steel (SSD) material used for the SSPs, monotonic tests on coupon specimens were carried out. The seismic performance of the SSPs was evaluated under a range of different loading protocols, including: the AISC protocol for buckling-restrained braces; ULCF protocols, i.e., constant amplitude (CA) and randomly-generated protocols; and a monotonic loading protocol. Based on the experimental results presented herein, the following conclusions are outlined:

- The SSPs met the requirements of the AISC protocol, showing a stable and full hysteresis. Under the extended AISC protocol, the SSPs sustained cycles of large amplitude up to four and half times the demand expected under the DBE. This validates the assumption on the SSP cyclic ductility adopted in the numerical evaluation of the dual CBF-MRF in Chapter 4.
- The SSPs provided large energy dissipation and fracture capacities under the CA and random loading protocols. Under ULCF, ductile fracture consistently initiated at sections halfway between the maximum and minimum diameters of the bending parts, demonstrating the advantages of the SSP optimised shape. Based on this evidence, a modified analytical equation is derived to predict the yield strength of SSPs.
- The SSPs exhibited high post-yield stiffness as a result of the SSD material properties, combined with the hardening effect due to the elastic bending of the supporting plates at large displacements.

- Comparison between the two SSP geometries showed that they had similar energy dissipation capacities, and SSP2 was able to sustain a larger number of cycles than SSP1. This improved fracture capacity of SSP2 is to be attributed to its optimised shape that promotes a more uniform distribution of plastic deformation, resulting in more widespread cracks along the length of the specimen.
- Under monotonic loading, SSP1 endured a displacement demand greater than sixteen times the yield displacement, indicating a very large fracture capacity. This may have been slightly overestimated due to the deformability of the test apparatus.

Chapter 6

Prediction and Numerical Simulation of Ductile Fracture in SSPs

6.1 Introduction

Ductile fracture of SSPs resulting from ultra-low cycle fatigue (ULCF) represents a critical failure mode in the global response of the CBF-MRF, as it may lead to a sudden drop in strength and a subsequent collapse of the structure. The aim of this chapter is to identify material parameters for the prediction and numerical simulation of ductile fracture in the SSPs under ULCF, based on the tests conducted in Chapter 5.

Following a review of the existing models for predicting fracture in metals under ULCF, three different approaches are considered in this study: a low-cycle fatigue (LCF) model that combines the Coffin-Manson relationship and the Palmgren-Miner rule; and two mechanics-based fracture models, i.e., the Cyclic Void Growth Model (Kanvinde & Deierlein 2007) and the fracture initiation criterion available in Abaqus. These two mechanics-based models are calibrated against ULCF tests on notched specimens, and their ability of predicting fracture initiation is validated against the ULCF tests of SSPs.

Furthermore, as the experimental tests showed that the SSPs are able to sustain additional cycles after fracture initiation before reaching full fracture, the fracture simulation of the SSPs requires to define an evolution criterion to trace the degradation of the material. In this work, the explicit simulation of the SSP fracture is performed using the Abaqus initiation and evolution criteria calibrated against coupon tests.

6.2 Review of models for predicting ductile fracture in metals

This section aims to identify suitable models for predicting and simulating ductile fracture of the SSPs under ULCF. A review of the available approaches for predicting fracture in metals is presented for different loading conditions, including monotonic loading, LCF and ULCF. While these loading conditions differ from each other, there are similarities in the fracture micromechanisms of metals under monotonic loading and ULCF, and similarly between LCF and ULCF, as discussed below.

6.2.1 Ductile fracture under monotonic loading

In structural steels, the initiation of ductile fracture is a complex multistep mechanism, where microvoids nucleate, grow in volume with plastic strain, and eventually coalesce to initiate a ductile crack (Anderson 2005). Since large-scale plasticity invalidates the assumptions of traditional fracture mechanics models, ductile fracture has been studied using the so-called local criteria that are based on stress and strain states (Myers et al. 2010). Local models for ductile fracture are generally classified in two different categories: mechanics-based criteria, which evaluate damage through a history variable computed using the evolution of stress and strain fields; and state-based criteria, which predict fracture when the strain exceeds a critical value (Kanvinde 2017).

The void growth method (VGM) and the stress modified critical strain (SMCS) are the most widely referenced criteria in the mechanics-based and state-based categories, respectively. The VGM and SMCS are based on the findings of McClintock (1968) and Rice & Tracey (1969). In two separate studies, it was found that the growth of microvoids is proportional to the equivalent plastic strain $\bar{\varepsilon}^{pl}$ and strongly influenced by the stress triaxiality T with an exponential dependency, as expressed in Eq. (6.1):

$$\mathrm{d}R/R = C\ \exp(1.5T)\ \mathrm{d}\bar{\varepsilon}^{pl} \tag{6.1}$$

where R is the average void radius, $\mathrm{d}R/R$ expresses the void growth, C is a constant, and T is defined as the ratio of the mean stress σ_{m} (i.e., hydrostatic pressure) to the Von Mises stress σ_{e} (i.e., equivalent stress).

The VGM has been extensively used to predict ductile fracture under monotonic loading (Panontin & Sheppard 1995, Kanvinde & Deierlein 2006). The aforementioned criterion derives from the integration of Eq. (6.1):

$$\ln \frac{R}{R_0} = C \int_0^{\bar{\varepsilon}^{pl}} \exp(1.5T)\, \mathrm{d}\bar{\varepsilon}^{pl} \tag{6.2}$$

where R_0 is the initial void size. According to the VGM, fracture initiates when the void reaches the critical value R_{D}, as expressed in Eq. (6.3):

$$C \int_0^{\bar{\varepsilon}^{pl}} \exp(1.5T)\, \mathrm{d}\bar{\varepsilon}^{pl} \geq \ln \frac{R_{\mathrm{D}}}{R_0} \tag{6.3}$$

The condition in Eq. (6.3) is simplified introducing the void growth index VGI, and its critical value $\mathrm{VGI}_{\mathrm{D}}^{\mathrm{mono}}$:

$$\mathrm{VGI} = \int_0^{\bar{\varepsilon}^{pl}} \exp(1.5T)\, \mathrm{d}\bar{\varepsilon}^{pl} \geq \frac{\ln \frac{R_{\mathrm{D}}}{R_0}}{C} = \mathrm{VGI}_{\mathrm{D}}^{\mathrm{mono}} \tag{6.4}$$

The SMCS model, first proposed by Mackenzie et al. (1977), assumes that triaxiality in Eq. (6.2) is constant over the loading history. Based on such assumption, fracture initiates when the equivalent plastic strain reaches the critical value $\bar{\varepsilon}_{\mathrm{D}}^{pl}$ at the onset of fracture, as expressed in Eq. (6.5):

$$\bar{\varepsilon}_{\mathrm{D}}^{pl} = \alpha_{\mathrm{mono}} \exp(-1.5T) \tag{6.5}$$

where α_{mono} is the toughness index. Johnson & Cook (1985) proposed a general form of the SMCS, which has been adopted by Abaqus (Dassault Systèmes 2014) and is expressed in Eq. (6.6):

$$\bar{\varepsilon}_{\mathrm{D}}^{pl} = [d_1 + d_2 \exp(-d_3 T)] \cdot (1 + d_4 \ln \dot{\varepsilon}^*) \cdot (1 + d_5 T^*) \tag{6.6}$$

where d_1, d_2, d_3, d_4, and d_5 are fracture constants, $\dot{\varepsilon}^*$ is the dimensionless strain rate, and T^* is the nondimensional temperature. Under quasi-static loading conditions and with no temperature dependance (i.e., $\dot{\varepsilon}^*$ = 1 and $T^* = 0$), the Johnson-Cook criterion reduces to the SMCS, with 1.5 being replaced by d_3.

The Abaqus software offers a general criterion for predicting fracture initiation that is given by:

$$\omega_{\mathrm{D}} = \int \frac{\mathrm{d}\overline{\varepsilon}^{pl}}{\overline{\varepsilon}^{pl}_{\mathrm{D}}(T)} \tag{6.7}$$

where ω_{D} is the fracture initiation index that increases monotonically with plastic deformations, and $\overline{\varepsilon}^{pl}_{\mathrm{D}}(T)$ is the equivalent plastic strain at fracture initiation, which depends on the instantaneous T value (Dassault Systèmes 2014). When ω_{D} = 1, fracture initiation is assumed to occur. In addition, Abaqus offers a capability for modelling progressive damage and failure of metals. This requires the specification of a fracture evolution response in combination with the initiation criterion (Eq. 6.7). Jia & Kuwamura (2014) simulated ductile fracture of structural steels under monotonic tension using the Abaqus fracture initiation criterion defining the $\overline{\varepsilon}^{pl}_{\mathrm{D}}(T)$ function as the SMCS criterion.

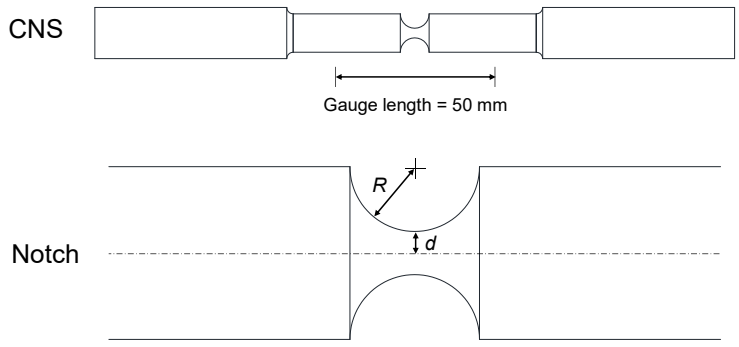

Figure 6.1. Typical geometry of a notched specimen (CNS)

Local fracture models are calibrated performing tensile tests on circumferentially-notched specimens (CNSs), shown in Figure 6.1. The material constants of the VGM and SMCS criterion (i.e., $\mathrm{VGI}^{\mathrm{mono}}_{\mathrm{D}}$ and α_{mono}) are calibrated using different notch geometries that vary the severity of stress triaxiality. Mackenzie et al. (1977) found that the maximum triaxiality is at the centre of the CNS and depends on the size of the notch, as expressed in Eq. (6.8):

$$T_{\mathrm{max}} = \frac{1}{3} + \ln\left(\frac{d}{2R} + 1\right) \tag{6.8}$$

where R is the radius of the notch and d is the radius of the minimum cross-section. Complementary finite element simulations provide the stress and strain in the notched minimum cross-section. Where the VGM evaluates fracture through numerical integration of Eqs. (6.4) and (6.7), respectively, the estimation

of the α_{mono} value in Eq. (6.5) is only based on the instantaneous $\bar{\varepsilon}_{\text{D}}^{pl}$ and T values at fracture initiation.

The VGM and SMCS models were originally developed to predict fracture under tensile axisymmetric and high triaxiality stress states. As discussed in the next section, researchers have proposed extensions of these models to different conditions, including ULCF and low triaxiality (Smith et al. 2017).

6.2.2 Ductile fracture under LCF and ULCF

ULCF is an intermediate loading condition between monotonic loading and LCF, as illustrated in Figure 6.2. Fracture under ULCF involves a relatively small number of cycles accompanied by large-scale plasticity, while LCF hundreds of cycles and limited plasticity. Several studies have demonstrated that the fracture mechanism for ULCF is similar to monotonic ductile fracture, since it involves cyclic growth and collapse of voids (Myers et al. 2010, Kanvinde 2017). However, mechanisms of LCF (such as slip and decohesion) may influence the ULCF response of metals, especially when the material is subjected to a large number of relatively small-amplitude cycles (Pereira et al. 2014, Kanvinde & Deierlein 2007). For this reason, established LCF models may still be able to characterise the ULCF response of structural steels.

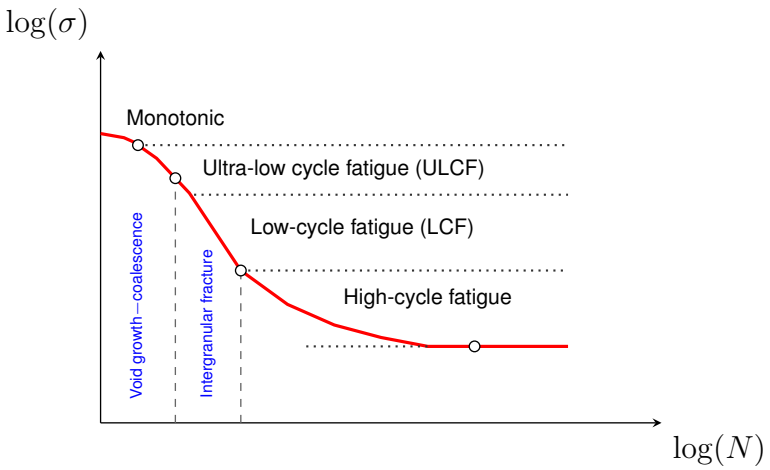

Figure 6.2. Fracture mechanism depending on number of cycles N (adapted from Bleck et al. 2009)

LCF resistance represents the ability of metals to sustain a finite number of cycles of variable inelastic strain amplitude (Bruneau et al. 2011). To quantify the

LCF life of a material, Coffin and Manson (Coffin 1954, Manson 1953) proposed a relationship that correlates the number of constant amplitude cycles to failure, $2N$, to the plastic strain amplitude, $\Delta\varepsilon_{\mathrm{p}}/2$, as expressed in Eq. (6.9):

$$\frac{\Delta\varepsilon_{\mathrm{p}}}{2} = \varepsilon'_{\mathrm{f}}(2N_{\mathrm{f}})^{c} \tag{6.9}$$

where $\varepsilon'_{\mathrm{f}}$ is the fatigue ductility coefficient and c is the fatigue ductility exponent.

To predict the LCF life of metals under protocols of variable amplitude, rainflow algorithms are used to convert the loading history in a sequence of regular cycles, and linear damage accumulation rules are applied (Bruneau et al. 2011). A widely-accepted damage accumulation model is the Palmgren-Miner rule (Miner 1945):

$$D_{\mathrm{f}} = \sum_{i=1}^{j} \frac{n_{\mathrm{i}}}{N_{\mathrm{f,i}}} \tag{6.10}$$

where n_{i} is the number of cycles applied at a given amplitude, $N_{\mathrm{f,i}}$ is the number of cycles to fracture at a given amplitude, and D_{f} is the damage index, which is equal to 1 when the specimen reaches failure .

Local approaches have been recently developed to simulate ductile fracture due to ULCF. In terms of micromechanism, as voids alternatively grow and shrink, T is positive in tension and negative in compression. Kanvinde & Deierlein (2007) proposed an extension of the VGM to ULCF, named Cyclic Void Growth Model (CVGM). The extended model takes into account reverse cycling and thus the sign of T, as shown in Eq. (6.11):

$$\mathrm{VGI}^{\mathrm{cyclic}} = \left(\int_{T\geq 0} \exp(1.5|T|)\, \mathrm{d}\overline{\varepsilon}^{pl} - \int_{T<0} \exp(1.5|T|)\, \mathrm{d}\overline{\varepsilon}^{pl} \right) \geq 0 \tag{6.11}$$

The cyclic void growth index $\mathrm{VGI}_{\mathrm{cyclic}}$ is assumed to be equal to zero if the expression in Eq. (6.11) is negative. Based on experimental and numerical data, Kanvinde & Deierlein (2007) observed that $\overline{\varepsilon}^{pl}$ is a strong indicator of cyclic degradation. Based on this assumption, the damage variable for cyclic loading, denoted as $\mathrm{VGI}_{\mathrm{D}}^{\mathrm{cyclic}}$, is estimated applying to $\mathrm{VGI}_{\mathrm{D}}^{\mathrm{mono}}$ the exponential decay function expressed in Eq. (6.12):

$$\mathrm{VGI}_{\mathrm{D}}^{\mathrm{cyclic}} = \mathrm{VGI}_{\mathrm{D}}^{\mathrm{mono}} \exp(-\lambda\, \bar{\varepsilon}_{\mathrm{start}}^{pl}) \tag{6.12}$$

where $\bar{\varepsilon}_{\mathrm{start}}^{pl}$ is the equivalent plastic strain at the start of each tensile excursion and λ is the rate of cyclic deterioration, which is in the range $0-1$ for structural steels. A small λ value reflects a slow cyclic deterioration process. The calibration of the CVGM parameters, i.e., $\mathrm{VGI}_{\mathrm{D}}^{\mathrm{mono}}$ and λ, requires tensile and cyclic tests on CNSs with different notch geometries. Kanvinde & Deierlein (2007) used two types of ULCF loading: constant amplitude tests; and tests with several cycles followed by a pull to fracture.

Jia & Kuwamura (2015) have recently simulated ductile fracture of specimens subjected to cyclic loading using the Abaqus software. To define an $\bar{\varepsilon}_{\mathrm{D}}^{pl}(T)$ function appropriate for cyclic loading, Jia & Kuwamura (2015) modified the SMCS model introducing a cut-off at $T = -1/3$. This assumption is based on the experimental evidence that ductile fracture is practically inhibited in compression (Bridgman 1964, Bao & Wierzbicki 2004). Below $T = -1/3$, ductile fracture is assumed to initiate for a infinite value of $\bar{\varepsilon}_{\mathrm{D}}^{pl}$ and thus no damage is accumulated, as expressed in Eqs. (6.13) and (6.14):

$$\bar{\varepsilon}_{\mathrm{D}}^{pl}(T) = \begin{cases} \alpha_{\mathrm{cyclic}} \exp(-1.5T) & \text{if } T \geq -1/3 \\ \infty & \text{if } T < -1/3 \end{cases} \tag{6.13}$$

i.e.,

$$\omega_{\mathrm{D}} = \begin{cases} \int \frac{\mathrm{d}\bar{\varepsilon}^{pl}}{\bar{\varepsilon}_{\mathrm{D}}^{pl}(T)} & \text{if } T \geq -1/3 \\ 0 & \text{if } T < -1/3 \end{cases} \tag{6.14}$$

Jia & Kuwamura (2015) validated this fracture criterion against the response of specimens monotonically pulled to fracture, after being subjected to few small inelastic cycles (fewer than five). For this purpose, the α_{cyclic} parameter was calibrated using monotonic tests on round specimens. However, its application to ULCF would require the calibration of α_{cyclic} based on cyclic coupon tests, similarly to the CVGM. In the latter, prediction of cyclic degradation is based on the cumulative plastic strain ($\bar{\varepsilon}^{pl}$) and is weighted by a triaxiality function (Pereira et al. 2014). It can be seen that the Abaqus fracture initiation index in Eq. (6.14) has a strong dependency on $\bar{\varepsilon}^{pl}$ as well, while triaxiality sign is accounted for in the modified SMCS. Unlike the CVGM, which can also be used for

monotonic fracture, the scope of the Abaqus criterion with α_{cyclic} is limited to ULCF conditions.

Furthermore, recent studies have found that, under low and moderate triaxiality conditions (i.e., $T < 1$), ductile fracture is strongly influenced by the deviatoric state parameter ξ, which is related to the Lode angle Θ, as expressed in Eq. (6.15):

$$\xi = \cos 3\Theta = \left(\frac{J_3}{\sigma_{\text{e}}}\right)^3 \tag{6.15}$$

where J_3 is the third invariant of deviatoric stress (Wierzbicki et al. 2005). The parameter ξ varies from -1, in case of axisymmetric compression, to 1, in case of axisymmetric tension, with $\xi = 0$ being the intermediate case in plain strain condition. Smith et al. (2014) recently proposed the stress-weighted damage model (SWDM), which is an enhanced version of the CVGM accounting for the effect of the deviatoric stress state. Bao & Wierzbicki (2004) presented a state-based criterion, expressed in Eq. (6.16), that includes the parameter ξ:

$$\overline{\varepsilon}_{\text{D}}^{pl} = C_1 \exp(-C_2\, T) - [(C_1 \exp(C_2\, T) - C_3 \exp(-C_4\, T)) \cdot (1 - \xi^{(1/n)})] \tag{6.16}$$

where C_1, C_2, C_3, C_4, and n are material parameters. Eq. (6.16) reduces to a general form of the SMCS model when the stress state is axisymmetric, i.e., $\xi = 1$. As described in detail in Wierzbicki et al. (2005), Smith et al. (2014), and Kanvinde (2017), the calibration of the SDWM and the model proposed by Bao & Wierzbicki (2004) requires a combination of coupon tests that aim to cover the entire range of stress states: tensile tests on CNSs ($\xi = 1$ and high or moderate triaxiality), grooved plate tests ($\xi = 0$ and high triaxiality), rectangular notched tests ($0 < \xi < 1$ and high triaxiality), inclined notched butterfly tests ($0 < \xi < 1$ and low triaxiality) or standard round tension coupon tests in a high-pressure chamber ($\xi = 1$ and low triaxiality).

As discussed in Section 6.9, complementary FEM simulations of the SSP tests showed that the fracture locations are characterised by axisymmetric stress state (i.e., $\xi = \pm 1$) and a maximum triaxiality in the range 0.4-0.5, which are typical values at the free surface (Myers et al. 2010). This indicates that the impact of the deviatoric state parameter ξ is minimal for the prediction of fracture in the SSPs.

6.2.3 Summary of models for predicting fracture under ULCF

This section examined different approaches for predicting fracture initiation in metals under different loading conditions, i.e., monotonic loading, LCF, and ULCF. The following models were identified for the prediction of ductile fracture under ULCF:

- **Coffin-Manson relationship and Palmgren-Miner rule**: these are established models for LCF that may also be employed to predict the ULCF life of metals. The Coffin-Manson equation is calibrated using various CA tests.
- **CVGM**: this extension of the established VGM to ULCF is capable of predicting monotonic and ULCF ductile fracture. The calibration of the CVGM involves monotonic and ULCF tests on notched specimens, and complementary FEM simulations.
- **Abaqus fracture initiation criterion**: this fracture model available in Abaqus has been applied in combination with a modified SMCS model (Eqs. 6.13 and 6.14) by Jia & Kuwamura (2015).

These models are employed in this work to predict ductile fracture of the SSPs. While the CVGM can only be used for prediction of fracture initiation, the Abaqus fracture initiation model can be combined with an evolution criterion to simulate the progressive damage and failure of SSPs.

6.3 Prediction of SSP failure using LCF model

As discussed in the previous section, LCF life of metals is typically characterised by calibrating a Coffin-Manson relationship (Eq. 6.9). To characterise the LCF life of SSPs, a Coffin-Manson-like relationship that correlates the imposed displacement amplitude Δ_f to the number of cycles applied to fracture N_f is used:

$$\Delta_\mathrm{f} = \Delta_0 \cdot (N_\mathrm{f})^m \tag{6.17}$$

where m and Δ_0 are parameters to be calibrated using experimental CA tests.

The m and Δ_0 values are obtained by fitting Eq. 6.17 to the Δ_f-N_f experimental data plotted in Figure 6.3. The resulting m value is -0.6, where the estimated Δ_0 values are 350 mm and 455 mm for SSP1 and SSP2, respectively.

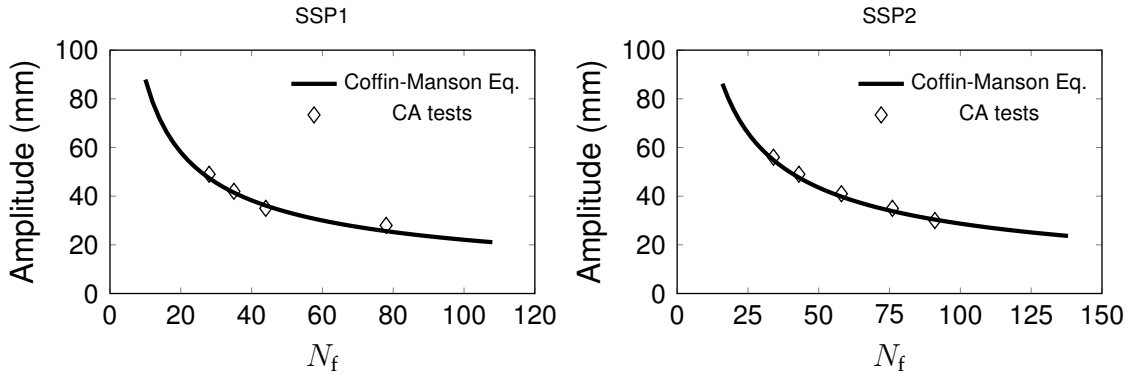

Figure 6.3. Coffin-Manson-like relationship for SSP1 and SSP2

The Palmgren-Miner rule (Eq. 6.10) is applied to the three random tests to verify the ability of the LCF model to predict fracture of the SSPs. Tables 6.1a-c lists the evolution of the failure index D_f over the phases of each random tests, where fracture is predicted when D_f = 1. The results indicate a good correlation with the experimental results: SSP1 reached full fracture at the end of phases 14 and 9 of Random-1 and Random-2 tests, for which the Miner-Palmgren rule estimates a value of D_f equal to 1.14 and 1.08, respectively; SSP2 fractured at the end of phase 9 of the random history, for which the damage accumulation rule estimates a D_f value of 0.99. Overall, the ULCF life of SSPs under random loading protocols can be predicted by the Miner-Palmgren rule.

The Coffin-Manson parameters can be used to simulate the effect of ULCF in phenomenological models of the SSPs that support collapse analyses. For instance, the fatigue material model available in the OpenSees software (Mazzoni et al. 2006) is based on the Miner-Palmgren rule, in combination with the Coffin-Manson relationship. As presented in Section 7.4.5, the OpenSees fatigue material is applied to predict the ductile fracture of SSPs.

Phase	Δ_f	n	N_f	D_f
1	$3u_y$	8	109	0.07
2	$6u_y$	1	35	0.10
3	$4u_y$	9	78	0.22
4	$7u_y$	2	28	0.29
5	$6u_y$	5	35	0.43
6	$5u_y$	3	44	0.50
7	$3u_y$	4	109	0.54
8	$7u_y$	7	28	0.79
9	$3u_y$	2	109	0.81
10	$7u_y$	3	28	0.91
11	$3u_y$	2	109	0.93
12	$4u_y$	2	78	0.96
13	$2u_y$	4	214	0.98
14	$5u_y$	7*	44	1.14

* = Experimental fracture

(a)

Phase	Δ_f	n	N_f	D_f
1	$6u_y$	9	35	0.26
2	$7u_y$	8	28	0.54
3	$2u_y$	2	214	0.55
4	$7u_y$	6	28	0.77
5	$5u_y$	4	44	0.86
6	$2u_y$	6	214	0.89
7	$3u_y$	4	109	0.92
8	$5u_y$	5	44	1.04
9	$7u_y$	1*	28	1.08

* = Experimental fracture

(b)

Phase	Δ_f	n	N_f	D_f
1	$6u_y$	9	59	0.15
2	$7u_y$	8	43	0.34
3	$8u_y$	2	33	0.40
4	$7u_y$	6	43	0.54
5	$5u_y$	4	76	0.59
6	$8u_y$	6	33	0.77
7	$3u_y$	4	168	0.80
8	$5u_y$	5	76	0.86
9	$7u_y$	5*	43	0.99

* = Experimental fracture

(c)

Table 6.1. Miner-Palmgren linear damage accumulation rule: (a) SSP1 Random-1; (b) SSP1 Random-2; and (c) SSP2 Random

6.4 Calibration of mechanics-based fracture initiation models

The calibration of the two mechanics-based fracture models, i.e., the CVGM and the Abaqus fracture initiation criterion, involves monotonic and cyclic tests on CNSs and complementary FEM analyses. The following steps are adopted for the calibration of both models:

(a) Monotonic and ULCF tests are conducted on CNSs.

(b) Complementary FEM analyses of the CNS tests are performed in Abaqus Explicit using a constitutive material model that does not simulate fracture.

(c) Equivalent plastic strain $\overline{\varepsilon}^{pl}$ and triaxiality T histories are extracted from the FEM models at the location where fracture initiates.

(d) $\overline{\varepsilon}^{pl}$ and T evolutions are used to integrate the equations of the CVGM and Abaqus fracture criterion, described in Section 6.2.2. The fracture parameters, i.e., $\text{VGI}_{\text{D}}^{\text{mono}}$ and λ for CVGM, and α_{cyclic} for the Abaqus fracture criterion, are identified.

6.4.1 Circumferentially-notched specimen (CNS) tests

CNSs are used for the investigation of ductile fracture initiation under stress states with high and moderate triaxiality ($T > 1/3$). The severity of triaxiality at the centre of the notched cross-section depends on the notch radius R (see Eq. 6.8). In this study, monotonic and cyclic tests were carried out on eighteen CNSs with three different radii, i.e., R = 2, 3, and 4.5 mm. The same geometries were also used in Vasdravellis et al. (2014) for the calibration of the SMCS and VGM for SSPs made of different steel grades. The notched specimens, shown in Figure 6.4, are denoted as CNS-2, CNS-3, and CNS-4.5, and were produced from 16-mm diameter round bars made of SSD. As summarised in Table 6.2, CNS-2 is characterised by high triaxiality ($T > 1$) at the centre of the notch, where CNS-3 and CNS-4.5 have moderate triaxiality ($1/3 < T < 1$).

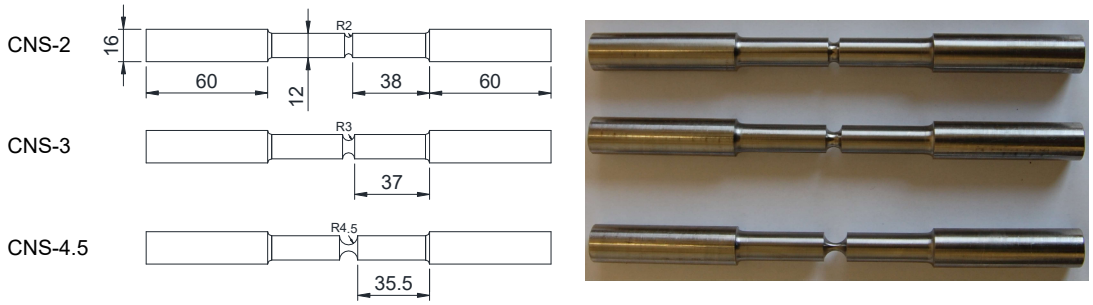

Figure 6.4. Geometry of the tested circumferentially-notched specimens (CNSs)

Specimen	R (mm)	d (mm)	T	u_y (mm)
CNS-2	2	4	1.02	0.14
CNS-3	3	3	0.74	0.094
CNS-4.5	4.5	1.5	0.48	0.063

Table 6.2. CNSs: notch geometry, triaxiality, and yield displacement

A total of six tests, three monotonic and three cyclic, were conducted for each CNS up to fracture. Two types of ULCF protocols were defined: (a) constant amplitude (CA), with cycles between 0 and a positive displacement multiple of the yield displacement u_y; and (b) increasing amplitude, i.e., the specimen is subjected to a series of CA cycles with an amplitude increased by $2u_y$ every four cycles. Table 6.3 provides a summary of the loading protocols used in this study. The specimens were instrumented with a 50-mm gauge length extensometer, as shown in Figure 6.5. The tests were performed in displacement control, applying a loading rate of 1 mm/min. The imposed displacement was measured by the extensometer.

The force-displacement curves of the monotonic tests are illustrated in Figure 6.5. The u_y values of each CNS are reported in Table 6.2. Figures 6.6-6.8 illustrate the force-displacement curves for all the cyclic tests. The results show that CNSs made of SSD have a stable hysteretic response under all the protocols.

Specimen	Test	ULCF loading protocol	N_0
CNS-2	1	(4)x[0;4u_y]+(4)x[0;6u_y]+(2)x[0;8u_y]+p.t.f.	p.t.f.
	2	(22)x[0;5u_y]	16
	3	(24)x[0;6u_y]	18
CNS-3	4	(4)x[0;4u_y]+(4)x[0;6u_y]+(4)x[0;8u_y]+(4)x[0;10u_y]+(1)x[0;12u_y]	16
	5	(21)x[0;8u_y]	16
	6	(39)x[0;5u_y]	32
CNS-4.5	7	(40)x[0;5u_y]+p.t.f.	p.t.f
	8	(4)x[0;4u_y]+(4)x[0;6u_y]+(4)x[0;8u_y]+(4)x[0;10u_y]+(2)x[0;12u_y]	18
	9	(19)x[0;8u_y]	18

Note: the number in parentheses indicates the number of cycles, followed by the prescribed amplitude in square brackets, i.e., (24)x[0;6u_y] refers to a specimen subjected to 24 cycles between 0 and 6 times u_y. p.t.f. = pull to fracture.

Table 6.3. Cyclic loading protocols of CNS tests

A final pull to fracture was applied in two cyclic tests (i.e., 1 and 7). When subjected to the increasing amplitude sequence (test 1), CNS-2 exhibited premature buckling at an imposed displacement of $10u_{\mathrm{y}}$, and therefore the specimen was pulled to fracture. The force-displacement curve in Figure 6.6 does not show the final pull, because the extensometer was removed. The remaining cyclic tests of CNS-2 were conducted applying displacements $< 10u_{\mathrm{y}}$ to avoid buckling. Figure 6.8 shows the force-displacement curve of CNS-4.5 under CA = $5u_{\mathrm{y}}$ (test 7). After 40 cycles, the specimen was pulled to fracture, as no signs of failure were observed. Cyclic histories consisting of several large inelastic cycles followed by a pull to fracture are still representative of ULCF (Kanvinde & Deierlein 2007).

Ductile failure of the specimen occurred in all the tests. It was empirically observed that fracture gradually propagated to free surface of the notch with increasing cycles, indicating that fracture initiation occurred earlier than the full-section failure of the CNS. Based on the experimental observations, the cycle at which fracture initiates in the CNSs, indicated as N_0, is identified with a 10% drop in the experimental force-displacement response. The experimental N_0 cycles are reported in Table 6.3.

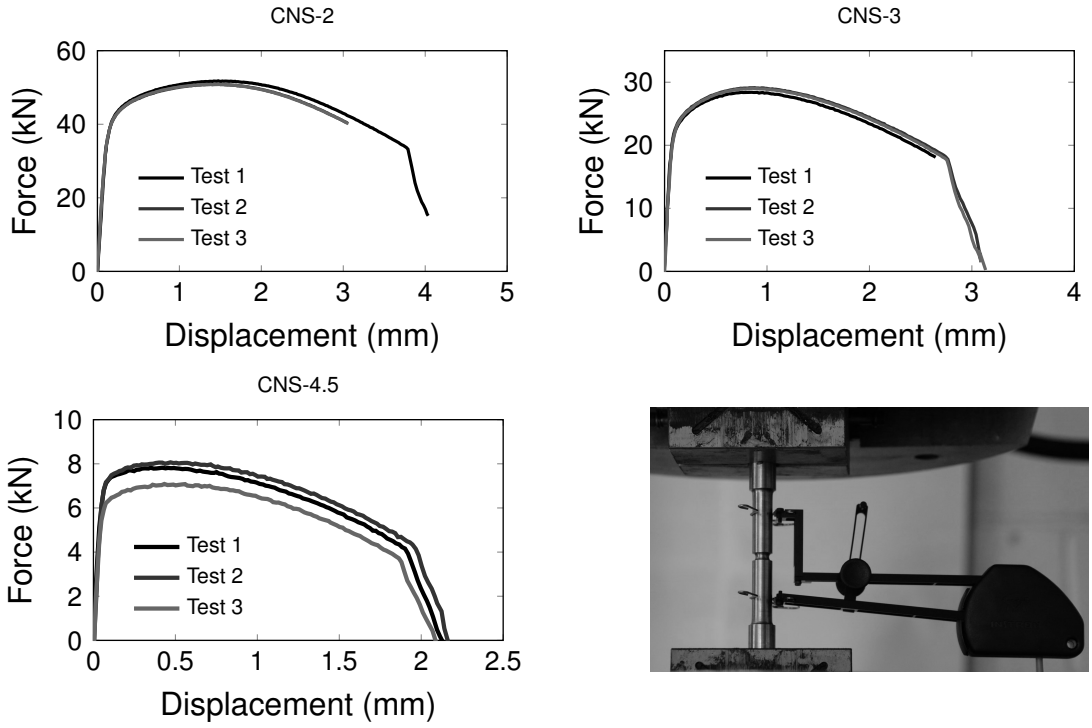

Figure 6.5. Monotonic tests on CNSs: force-displacement curves and test set-up

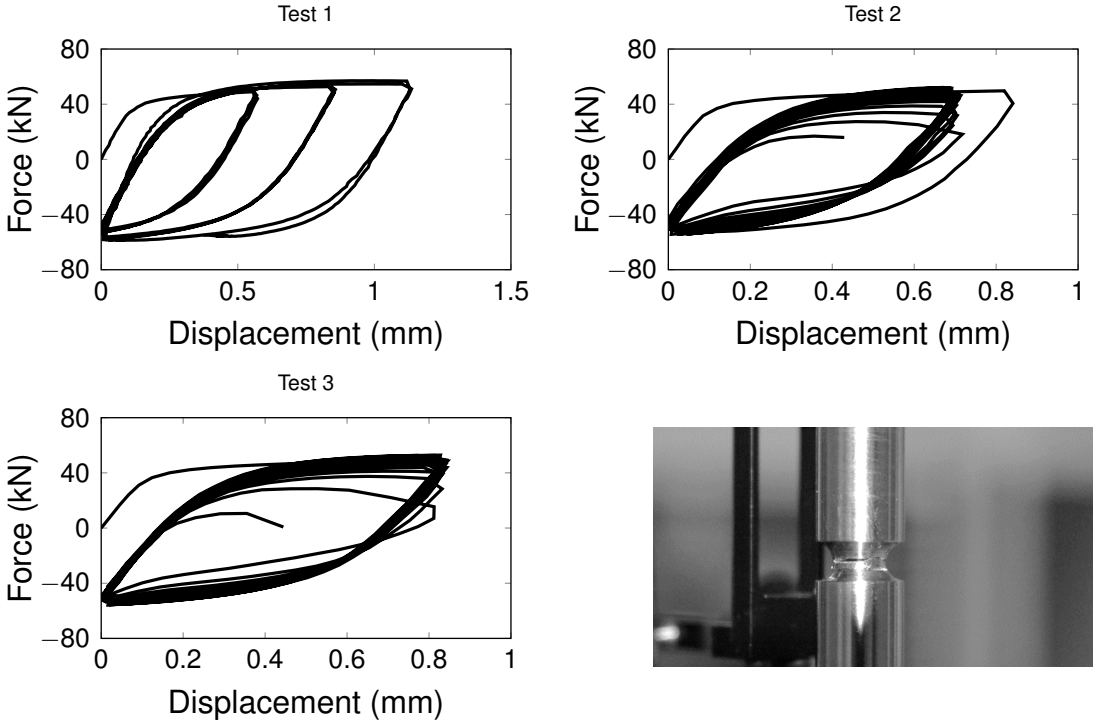

Figure 6.6. Cyclic tests on CNS-2: force-displacement curves and typical ductile fracture (from test 3)

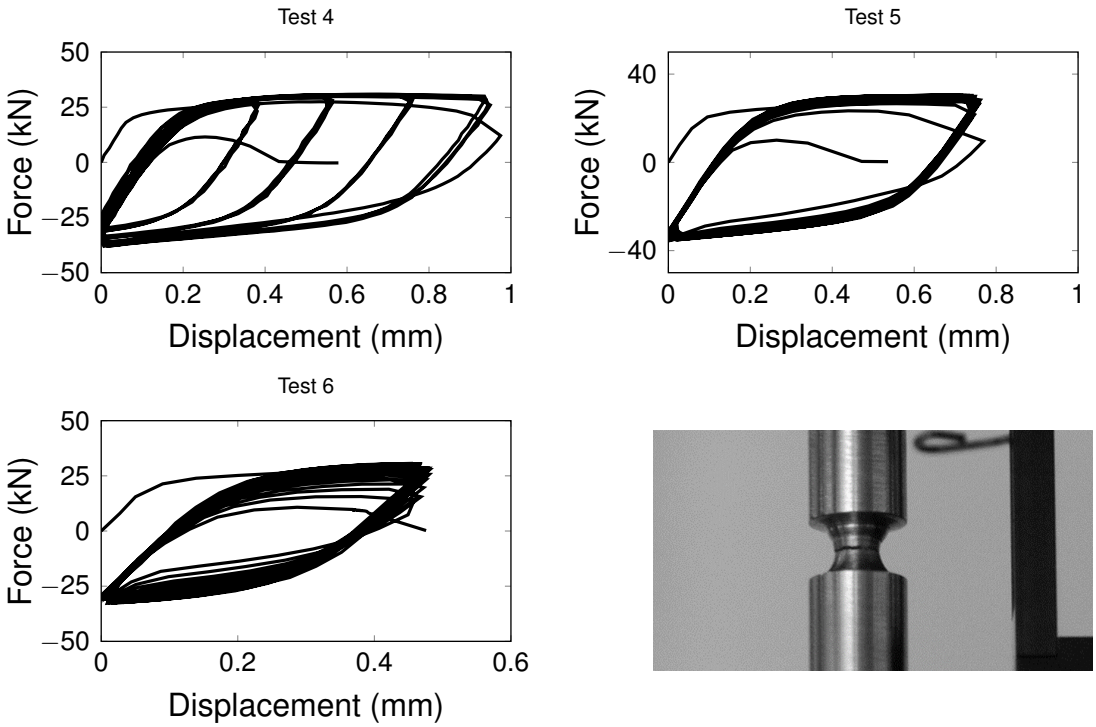

Figure 6.7. Cyclic tests on CNS-3: force-displacement curves and typical ductile fracture (from test 5)

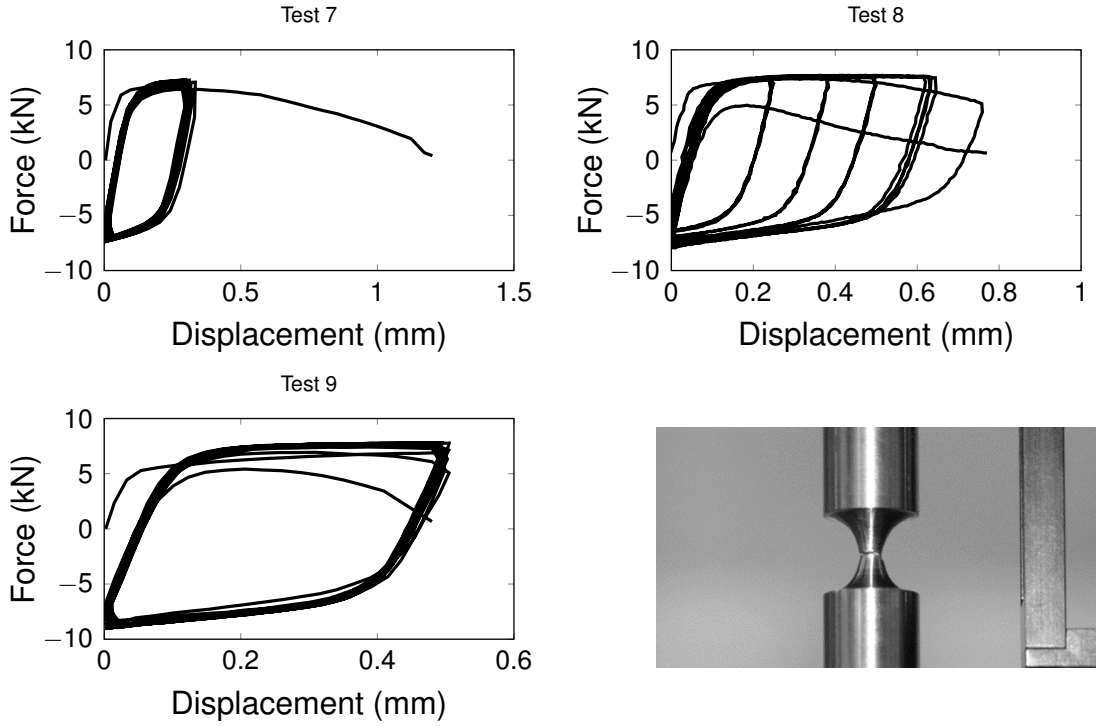

Figure 6.8. Cyclic tests on CNS-4.5: force-displacement curves; and typical ductile fracture (from test 9)

6.4.2 Complementary FEM simulations of CNS tests

Nonlinear three-dimensional FEM models of the CNSs are created in Abaqus. Figure 6.9 shows the geometry of the FEM model of CNS-2. Only the gauge length is modelled and it is discretised using C3D8R elements with reduced integration. The mesh is refined in the notch with an average element size of 0.45 mm along the notch, which was found accurate for capturing the material behaviour. The experimental displacement history measured by the extensometer is applied.

The FEM analyses are performed using an explicit direct integration procedure. While this is generally used for dynamic analysis, it can also be used for the simulation of highly discontinuous quasi-static problems that involve contact, damage and failure. In fact, simulating ductile fracture would be problematic using an implicit analyser (i.e., in Abaqus Standard), as severe convergence problems may occur (Dassault Systèmes 2014). To reduce the computational cost of the quasi-static explicit simulations, the numerical loading rate is set to be smaller that the experimental one, while the density of the material is decreased by six orders of magnitude, and a variable mass scaling is

defined. A minimum stable time increment target value of 0.002 s is iteratively identified. It is verified that these modelling settings do not introduce inertia effects, since the ratio of kinetic to internal energy is negligible.

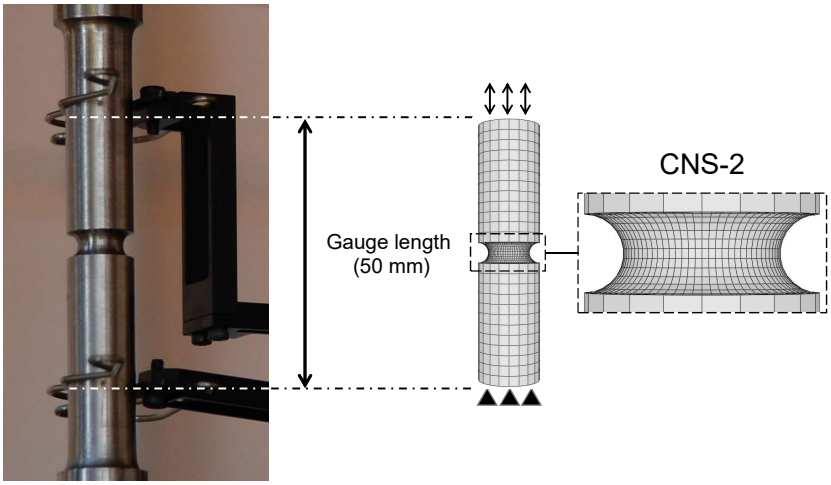

Figure 6.9. Three-dimensional FEM model reproducing the gauge length of CNS-2

To characterise the tensile response of the SSD material, an isotropic hardening constitutive model is defined using the true-stress/true-plastic-strain curve derived in Section 5.3.2. Figure 6.10 compares the numerical and experimental force-displacement curves of the monotonic tests. While a good agreement is achieved for CNS-2 and CNS-3, there is a noticeable difference between the numerical and experimental tensile responses of CNS-4.5. This scatter, which is not visible in the corresponding cyclic simulations (Figure 6.11), may be due to a small notch geometry inconsistency in the tested specimens.

To capture the hysteretic behaviour of the SSD material, an elastic plastic material model with combined isotropic and kinematic hardening is used. A detailed description of this constitutive model is provided in Section 4.2.1. Several simulations are iteratively conducted to identify the combined hardening parameters. Figure 6.11 shows the comparison between the experimental and numerical force-displacement curves of CNS-2, CNS-3 and CNS-4.5 under CA loading. A good correlation with the experimental force-displacement curves is achieved using the following values: σ^0 = 400 MPa, C_1 = 6,500 MPa, γ_1 = 30, C_2 = 100,000 MPa, γ_2 = 700, b = 5, and Q_∞ = 200 MPa.

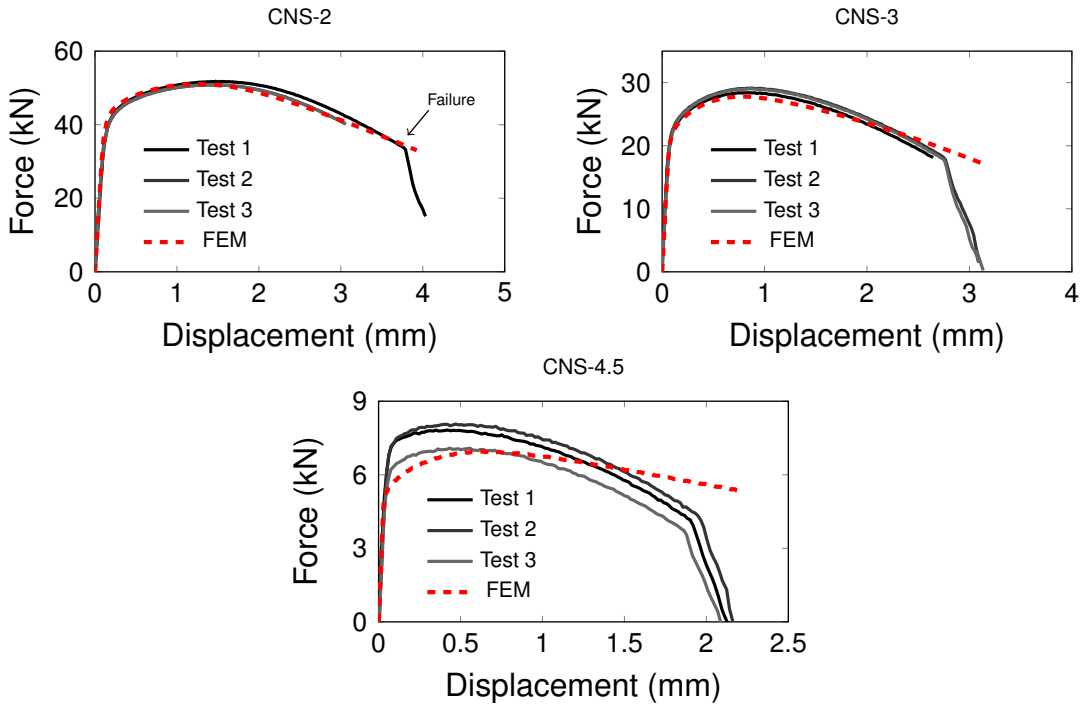

Figure 6.10. Tensile tests on CNSs: experimental-numerical comparison of force-displacement curves

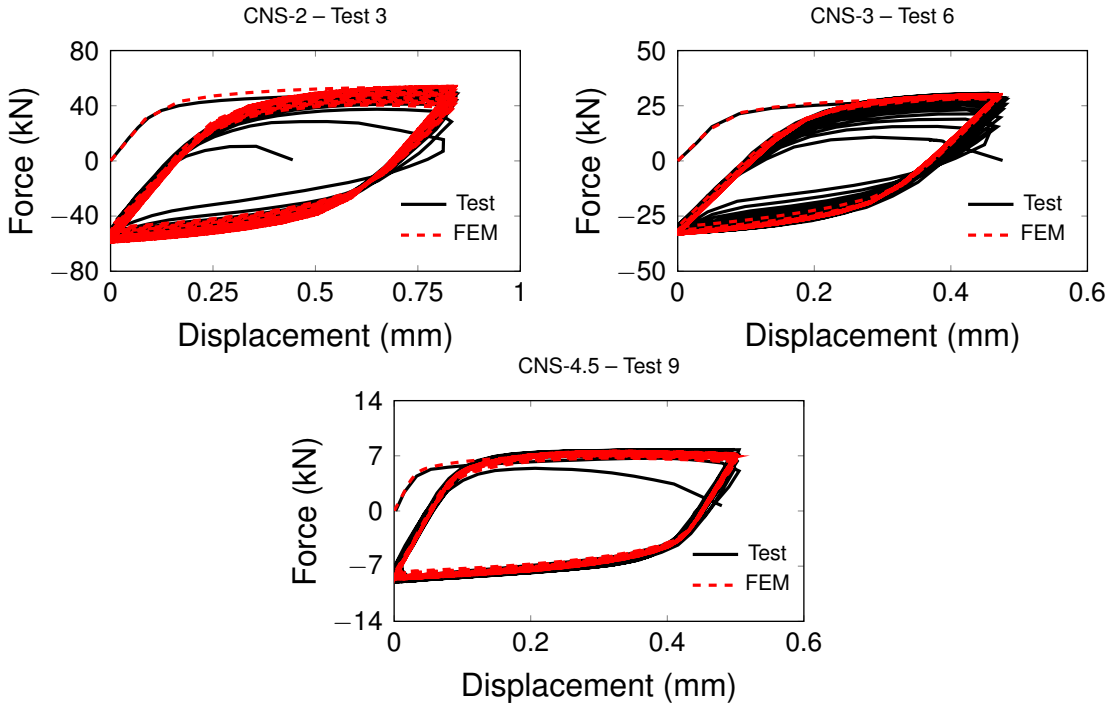

Figure 6.11. Experimental-numerical hysteresis of CNSs (without fracture simulation)

6.4.3 Calibration of CVGM

The parameters of the CVGM, i.e., VGI_D^{mono} and λ, are calibrated following the procedure described in Kanvinde & Deierlein (2007). The complementary FEM simulations of the monotonic CNS tests presented in the previous section are used to identify VGI_D^{mono}. Then, the cyclic damage parameter λ is estimated using the numerical analyses of the cyclic coupon tests.

The triaxiality T and plastic strain $\bar{\varepsilon}^{pl}$ histories are extracted at fracture location, typically at the centre of the notch. However, in CNS-2, these are taken at the free surface of the notch, where a concentration of plastic deformation is numerically observed (Figure 6.12). This is in line with observations of Jia & Kuwamura (2014) for specimens with a sharp notch, such as CNS-2.

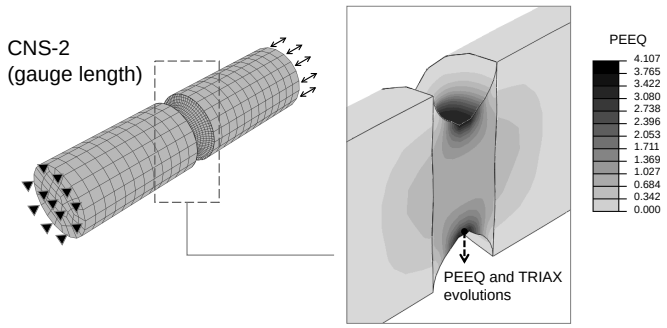

Figure 6.12. CNS-2: equivalent plastic strain contour in the notch

The extracted T and $\bar{\varepsilon}^{pl}$ evolutions are used to integrate Eq. (6.4) up to fracture initiation, which is assumed coincident with failure (Kanvinde & Deierlein 2007). As shown in Figure 6.10, failure under monotonic loading is associated with the sudden drop in the force-carrying capacity of the specimen. The obtained VGI_D^{mono} values for the three CNS geometries, summarised in Table 6.4, show a small standard deviation (in the region of 10%). The mean VGI_D^{mono} = 2.88 is in agreement with the results presented in Vasdravellis et al. (2014), where VGI_D^{mono} = 2.87 was found for the SSD material.

The coefficient λ represents the rate at which VGI_D^{mono} degrades under cyclic loading, as expressed in Eq. (6.12). The λ value is determined by deriving a relationship between the $VGI_D^{cyclic}/VGI_D^{mono}$ ratio and the associated $\bar{\varepsilon}^{pl}_{start}$ at fracture initiation (Kanvinde & Deierlein 2007). VGI_D^{cyclic} values are calculated by integrating Eq. (6.11) using T and $\bar{\varepsilon}^{pl}$ evolutions, up to the experimental fracture

Specimen		VGI_D^{mono}
CNS-2		2.66
CNS-3		3.21
CNS-4.5		2.77
	Mean	2.88
	Std dev	0.29

Table 6.4. Summary of VGI_D^{mono} values for the CNS tests

initiation cycle N_0 (see Table 6.3). By fitting an exponential function to the resulting $VGI_D^{cyclic}/VGI_D^{mono} - \bar{\varepsilon}^{pl}_{start}$ data, plotted in Figure 6.13, it is obtained that $\lambda = 0.12$. Since λ is in the range $0-1$ for structural steels, this small λ value reflects the slow cyclic deterioration process exhibited by the coupon specimens under ULCF.

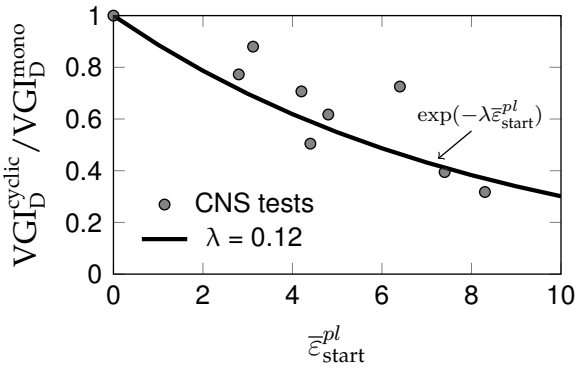

Figure 6.13. Calibration of λ based on $VGI_D^{cyclic}/VGI^{mono}$ ratios and associated $\bar{\varepsilon}^{pl}_{start}$ values from CNS tests

6.4.4 Calibration of Abaqus fracture initiation criterion

This section presents the calibration of the Abaqus fracture criterion for predicting fracture under ULCF. As discussed in Section 6.2.2, Jia & Kuwamura (2015) calibrated α_{cyclic} using monotonic tests on round specimens, to predict fracture under specific ULCF protocols characterised by few small cycles followed by a monotonic pull to fracture. However, the calibration of the CVGM has shown that ductile fracture of the CNSs under ULCF involves large cumulative plastic strains, indicating that α_{cyclic} has to be calibrated using the cyclic CNS tests rather than monotonic.

Therefore, the calibration of the fracture parameter α_{cyclic} is performed

against the cyclic CNS tests, using the same $\bar{\varepsilon}^{pl}$ and T histories extracted for the CVGM calibration. The fracture initiation index ω_D is determined by integrating Eq. (6.14). The α_{cyclic} value is iteratively determined imposing $\omega_D = 1$ at the start of N_0-th cycle.

Comparison of the experimental and numerical force histories of cyclic test no. 3 on CNS-2 is plotted in Figure 6.14a, with the indication of the N_0 cycle, i.e., fracture initiation (see Table 6.3). Figure 6.14b shows the corresponding ω_D history, where $\omega_D = 1$ at $N_0 = 18$ for $\alpha_{cyclic} = 10$. The fracture initiation index histories for the remaining cyclic tests are shown in Figure 6.15.

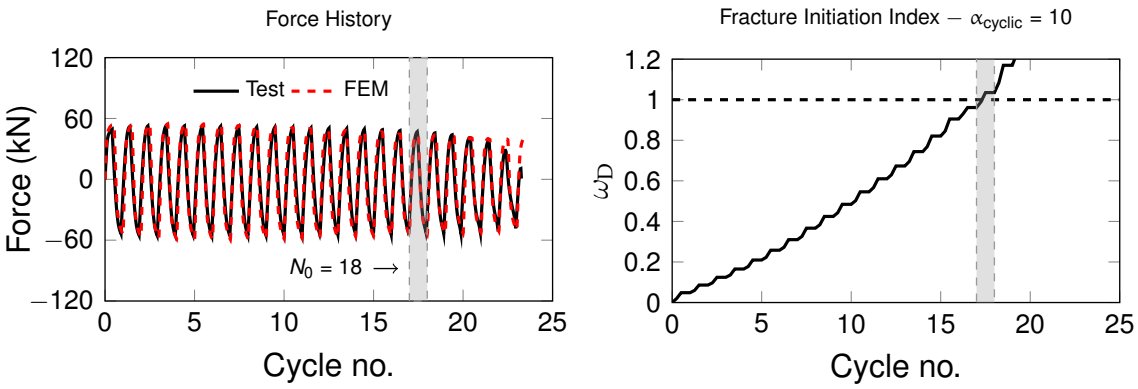

Figure 6.14. CNS-2 (test 3): (a) experimental-numerical force history; and (b) ω_D history

Specimen	Cyclic test	N_0	α_{cyclic}
CNS-2	1	p.t.f.	9.0
	2	16	5.5[a]
	3	18	10.0
CNS-3	4	16	11.2
	5	16	13.4
	6	32	9.9
CNS-4.5	7	p.t.f.	11.6
	8	18	9.5
	9	18	10.2
Mean			10.6
Std dev			1.4

[a] Value ignored as not representative.

Table 6.5. Summary of α_{cyclic} values for the CNS tests

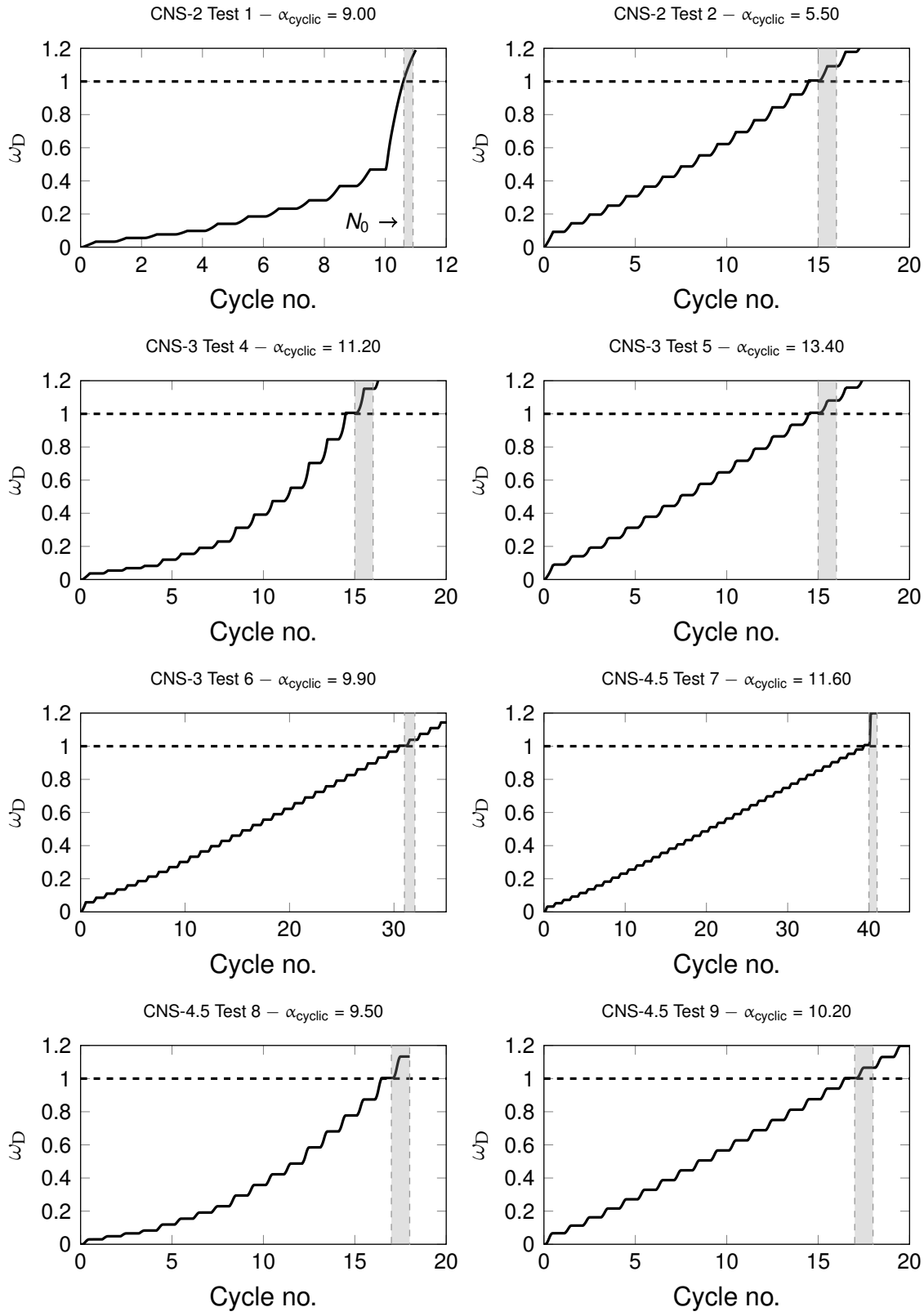

Figure 6.15. Calibration of Abaqus fracture initiation parameter α_{cyclic} for CNS tests

A summary of the α_{cyclic} values obtained for all tests is reported in Table 6.5. The excessively small α_{cyclic} for no. 2 test reflects the limited fracture capacity exhibited by the specimen, which sustained fewer cycles than in test 3, despite being subjected to a smaller amplitude. Therefore, α_{cyclic} = 5.5 is disregarded. The statistics show that the α_{cyclic} values have a relatively small dispersion, with a mean value of 10.6. For the simulation of the ductile fracture behaviour of SSPs under ULCF, α_{cyclic} = 10 can be conservatively used in Eq. (6.13) to define the $\overline{\varepsilon}^{pl}_{\text{D}}(T)$ function. Figure 6.16 illustrates the modified SMCS with α_{cyclic} = 10 and the cut-off at $T = -1/3$.

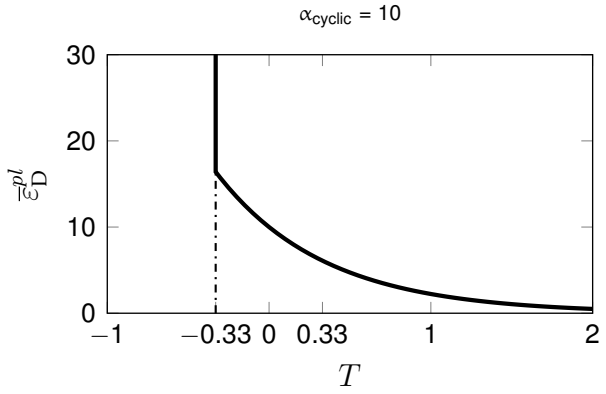

Figure 6.16. Abaqus fracture initiation model calibrated for ULCF

6.5 Calibration of Abaqus fracture evolution parameters

This section describes the calibration of the Abaqus fracture evolution parameters following the methodology developed by Pavlovic et al. (2013).

In the cyclic tests of SSPs, fracture initiation was characterised by small cracks, which gradually propagated up to the full-section failure of the specimen. To simulate the progressive degradation of the material following fracture initiation, Abaqus offers a damage evolution model based on the approach proposed by Hillerborg et al. (1976). The stress-strain definition can not accurately capture the degradation of the material, since strain localisation would introduce a strong mesh dependency. Abaqus overcomes this issue by introducing a damaged stress-displacement response (Dassault Systèmes 2014). The damage evolution variable, denoted as D_{evol}, is specified as a function of the equivalent plastic displacement $\overline{u}^{pl}$. The latter depends on the characteristic

length of a finite element L_{char}, as expressed in Eq. (6.18):

$$\dot{\overline{u}}^{pl} = L_{\text{char}} \, \dot{\overline{\varepsilon}}^{pl} \tag{6.18}$$

Before fracture initiation, $\dot{\overline{u}}^{pl} = 0$. Since L_{char} depends on the geometry and formulation of the finite element, the mesh dependency of the results is reduced (Dassault Systèmes 2014). In addition, the damage evolution capability offers the removal of the elements from the mesh when D_{evol} = 1.

Pavlovic et al. (2013) developed a practical procedure for the calibration of the Abaqus fracture evolution parameters based on tensile coupon tests on round bars. This study applies the methodology by Pavlovic et al. (2013), described below, to the results of the round bar tests presented in Section 5.3.2.

To account for strain localisation after necking, Pavlovic et al. (2013) introduced a variable gauge length l, as defined in Eq. (6.19):

$$l = L_0 + (L_{loc} - L_0)\left(\frac{L - L_{\text{n}}}{L_{\text{f}} - L_{\text{n}}}\right)^c \tag{6.19}$$

where L is the extensometer elongation, L_0 is the initial gauge length (i.e., 50 mm), L_{n} and L_{f} are the extensometer elongations at necking and fracture, L_{loc} identifies the necking zone, and c is the localisation rate factor ($c = 0.5$). All these parameters are known from the round bar tests conducted in this study, with the exception of L_{loc}, determined by Pavlovic et al. (2013) using digital image correlation measurements.

In absence of experimental data, L_{loc} is numerically identified by developing a FEM simulation of the round bar test. Figure 6.17a shows the three-dimensional model of the round bar. The same isotropic hardening material model defined for the simulation of the CNS monotonic tests is used. Figure 6.17b compares the experimental and numerical stress-strain curves, indicating that the FEM model is capable of tracing the monotonic response of the round bar. Figure 6.18a shows the distribution of true strains over the length of the specimen. By applying the principle of equal areas to the averaging areas of high and low strains, it is found that L_{loc} = 6.2 mm.

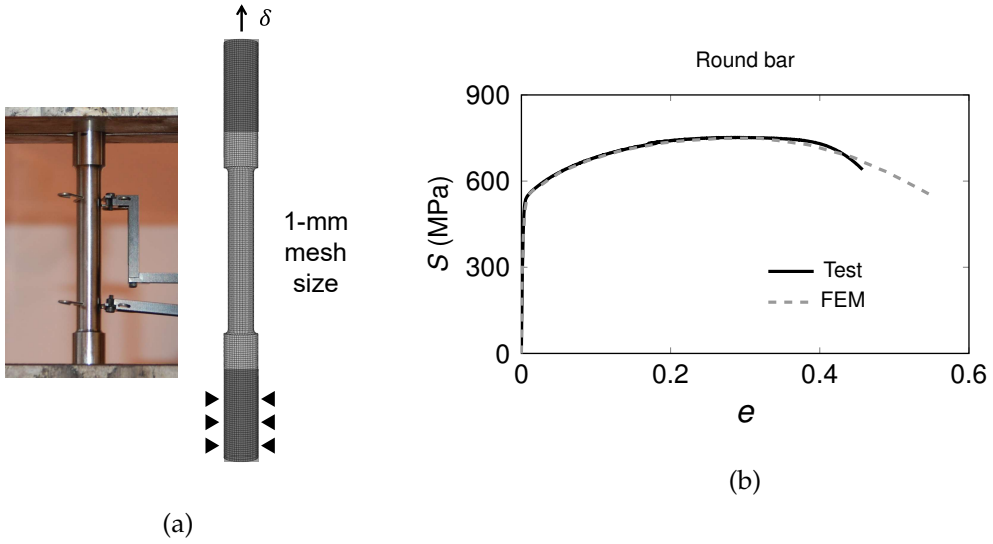

Figure 6.17. Round bar FEM model: (a) boundary conditions; and (b) experimental and numerical stress-strain curves

The damaged material engineering strain $e_{\text{i,dam}}$ at the i-th instant is computed using l, as expressed in Eq. (6.20):

$$e_{\text{i,dam}} = e_{i-1} + \frac{L_{\text{i}} - L_{\text{i-1}}}{l_{\text{i}}} \tag{6.20}$$

The damaged material true stress and true plastic strain are then calculated using Eqs. (6.21) and (6.22):

$$\varepsilon^{pl}_{\text{dam}} = \ln(1 + e_{\text{dam}}) - \varepsilon_{\text{y}} \tag{6.21}$$

$$\sigma_{\text{dam}} = S(e_{\text{dam}} + 1) \tag{6.22}$$

Figure 6.18b illustrates the obtained $\sigma_{\text{dam}} - \varepsilon^{pl}_{\text{dam}}$ curve of SSD undergoing damage. The undamaged material response (dashed) is given by the tangent to the true-stress/true-plastic-strain curve at the necking point.

The equivalent plastic displacement $\overline{u}^{pl}$ is calculated using Eq. (6.23):

$$\overline{u}^{pl} = \overline{u}^{pl}_{\text{f}} \cdot \frac{\varepsilon^{pl}_{\text{dam}} - \varepsilon^{pl}_{\text{dam,n}}}{\varepsilon^{pl}_{\text{dam,f}} - \varepsilon^{pl}_{\text{dam,n}}} \tag{6.23}$$

where $\varepsilon^{pl}_{\text{dam,n}}$ and $\varepsilon^{pl}_{\text{dam,f}}$ are the true damaged plastic strains at necking and fracture. The equivalent plastic displacement at fracture $\overline{u}^{pl}_{\text{f}}$ is given by Eq (6.24):

$$\overline{u}^{pl}_{\text{f}} = L_{\text{char}} \cdot (\varepsilon^{pl}_{\text{f,dam}} - \varepsilon^{pl}_{\text{n,dam}}) \tag{6.24}$$

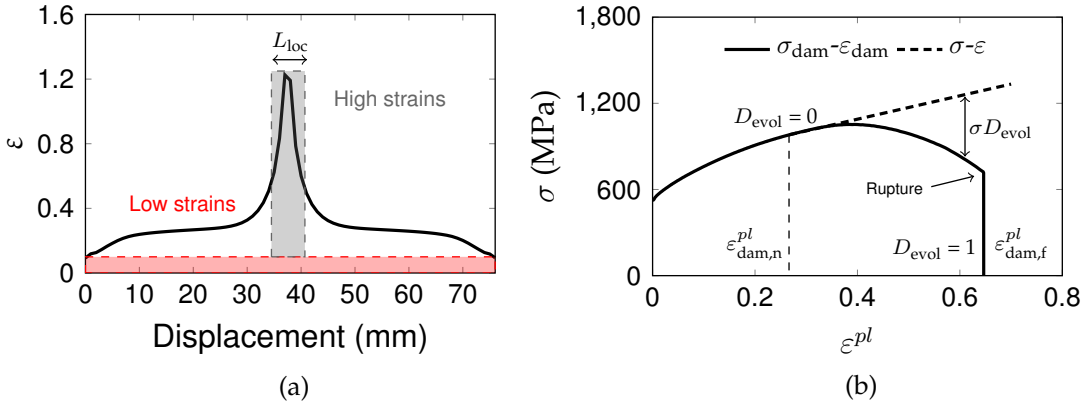

Figure 6.18. Calibration of fracture evolution model: (a) strain localisation effective length; and (b) damaged material stress/true-plastic strain response of SSD

where L_{char} is the characteristic length of a finite element, given by the product of the element size L_{E} and a factor λ_{E} accounting for the element type, e.g., $\lambda_{\text{E}} = 2.5 - 3.2$ for C3D8R elements (Pavlovic et al. 2013).

The evolution of the damage variable D_{evol} is specified as a tabular function of $\overline{u}^{pl}$. The element is eventually removed from the mesh when the condition in Eq. (6.25) is satisfied (Dassault Systèmes 2014):

$$D_{\text{evol}} = 1 - \frac{\sigma_{\text{dam}}}{\sigma} = 1 \tag{6.25}$$

To account for the effect of the typically non-uniform distribution of damage over the cross-section of a specimen, a factor $\alpha_{\text{D}} = 1.5$ should be applied to D_{evol}.

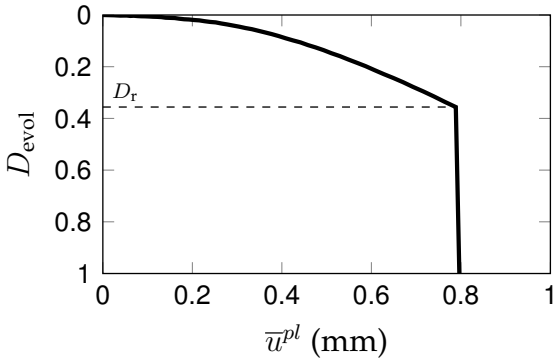

Figure 6.19. Fracture evolution model calibrated for the round bar FEM model

Figure 6.19 shows the calibrated damage evolution for the round bar. The specimen is discretised using C38DR elements and a mesh size of 1 mm, i.e., $\lambda_{\text{E}} = 3.1$ and $L_{\text{E}} = 1$ mm. The critical value $D_{\text{r}} = 0.35$ corresponds to the rupture point,

where a sudden loss in the force-carrying capacity occurs (see Figure 6.18b). The value of D_r is typically in the range of 0.2-0.65 for most steels subjected to tensile loading (Bonora et al. 2006, Lemaitre 1985).

6.6 Validation of Abaqus fracture parameters for coupon tests

This section presents the explicit fracture simulation of the coupon tests on round bars and CNSs, under both monotonic loading and ULCF. The Abaqus fracture initiation and evolution parameters are inputted in the FEM models of the round and notched specimens.

6.6.1 Fracture simulation of monotonic coupon tests

To simulate ductile fracture under monotonic loading, the calibrated evolution parameters are combined with a fracture initiation criterion defined as the SMCS model (Eq. 6.5). The fracture initiation parameter α_{mono} is calibrated against the monotonic CNS tests.

The calibration of the fracture evolution parameters proposed by Pavlovic et al. (2013), and adopted in this study, is based on the assumption that fracture initiates at necking. Therefore, the Abaqus fracture initiation parameter α_{mono} is calibrated by imposing that ω_D = 1 at necking.

The numerical force evolutions for the three monotonic tests on CNSs (Figure 6.20a) are used to identify the instant associated with fracture initiation. The triaxiality T and plastic strain $\overline{\varepsilon}^{pl}$ histories extracted at fracture location are used to integrate Eq. (6.5). The ω_D evolutions, shown in Figure 6.20b, are obtained using α_{mono} for which $\omega_D = 1$ at necking. As summarised in Table 6.6, the statistics of calibrated α_{mono} show a mean value of 0.86 and a small standard deviation. Therefore, α_{mono} = 0.8 is conservatively used for the explicit fracture simulations of the monotonic coupon tests.

The results of the explicit fracture simulations of the monotonic tests on round and notched specimens are presented below. Comparison of the experimental and numerical force-displacement curves of the round bar tests, plotted in Figure 6.21a, shows the ability of the FEM model to trace degradation and fracture of the material. Figure 6.21b illustrates the round bar in the final

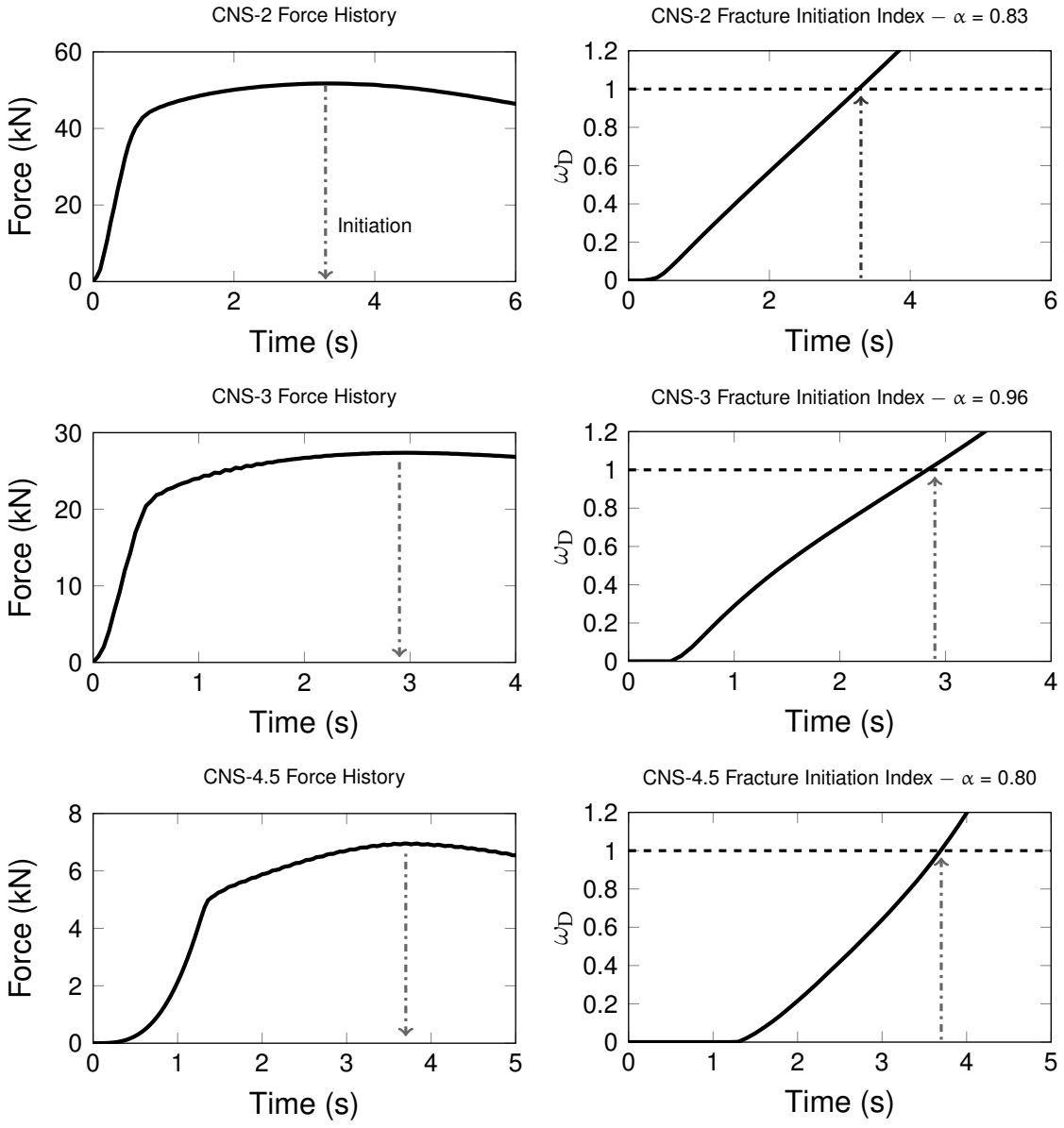

(a) (b)

Figure 6.20. Calibration of Abaqus fracture initiation parameter α_{mono} for monotonic tests of CNSs

Specimen		α_{mono}
CNS-2		0.83
CNS-3		0.96
CNS-4.5		0.80
	Mean	0.86
	Std dev	0.09

Table 6.6. Summary of α_{mono} values for the CNS tests

stages of the numerical simulation: ductile fracture initiates at the centre of the specimen following necking; then it evolves with the deletion of elements having reached $D_{\text{evol}} = 1$, up to the full section of the specimen.

The tensile tests of CNSs are simulated using a modified damage evolution model that accounts for the different mesh size L_{E} in the notch area (see Table 6.7). Figure 6.22 shows that a good correlation is achieved between the numerical and experimental force-displacement responses of the CNSs.

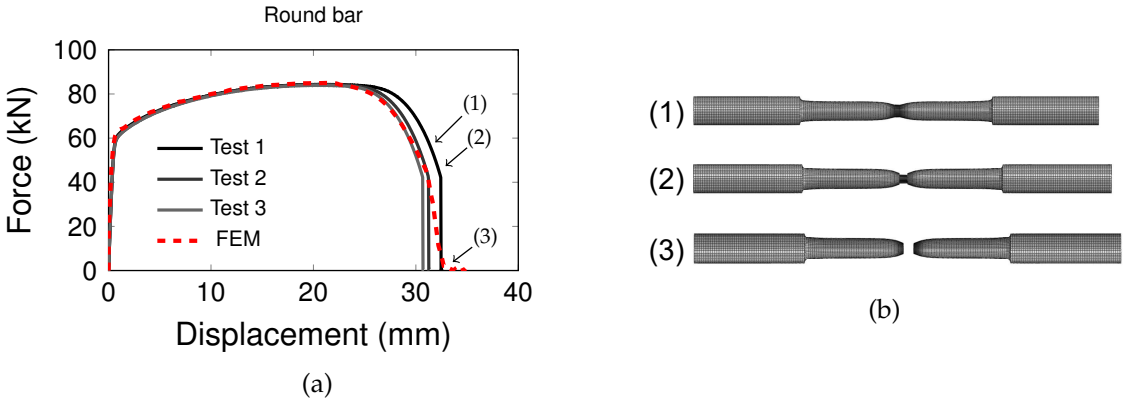

Figure 6.21. Round bar tests: (a) experimental and numerical force-displacement curves; and (b) FEM simulation of ductile failure

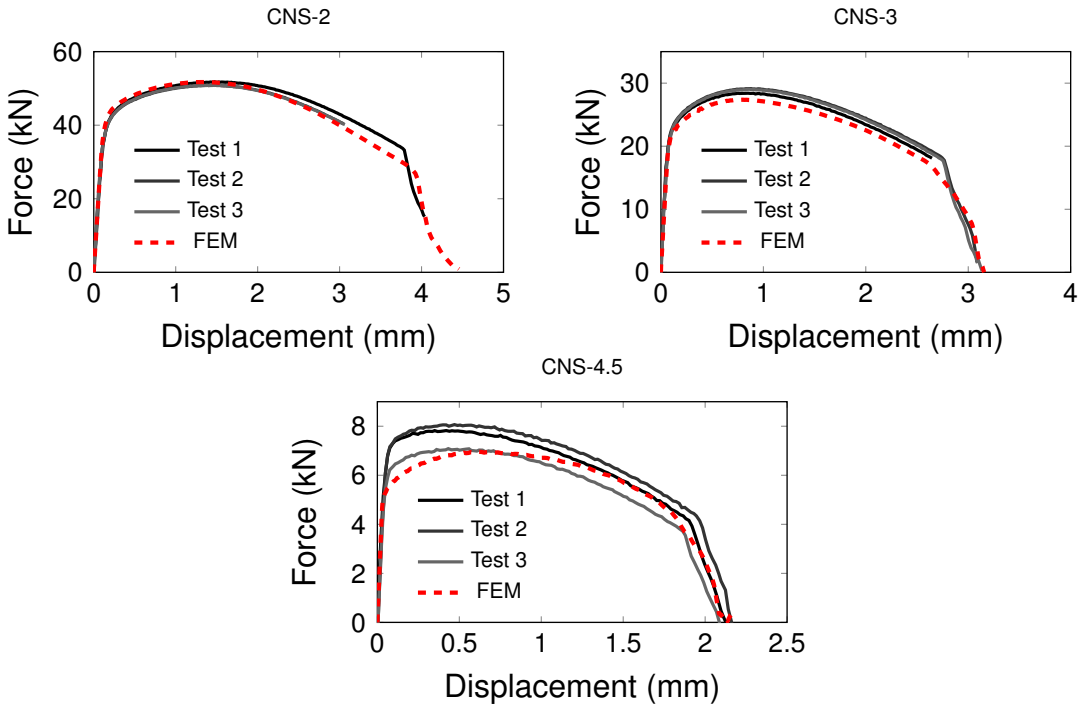

Figure 6.22. Tensile CNS tests: experimental-numerical force-displacement curves

Overall, the calibrated Abaqus fracture parameters for monotonic loading allow for an accurate simulation of ductile fracture initiation and evolution, both in round and notched specimens.

6.6.2 Fracture simulation of ULCF coupon tests

Fracture simulations of the CNS tests under ULCF are performed using the same fracture evolution parameters as in the monotonic analyses, and the calibrated α_{cyclic} = 10 for fracture initiation (see Section 6.4.4). One representative test is explicitly simulated for each notched geometry. The experimental and numerical hystereses and force evolutions of the cyclic tests are shown in Figure 6.23. It can be seen that the calibrated Abaqus fracture models are capable of tracing the ULCF fracture behaviour of the CNSs.

As expected, the simulation of ductile fracture initiation is consistent with the experimental fracture initiation cycle N_0, as shown in Table 6.7. Following fracture initiation, the FEM simulations are able to trace the degradation of the SSD material in the notch area up to the full-section failure of the specimen. The comparison between the number of cycles to failure sustained by each specimen and the corresponding numerical prediction (Table 6.7) shows that the fracture evolution parameters provide a good agreement with the experimental fracture behaviour.

Overall, the Abaqus fracture evolution model, combined with the initiation criterion, is found to accurately simulate the ductile fracture response of coupon specimens subjected to various ULCF protocols. This indicates that the calibrated Abaqus fracture parameters can be used for explicitly simulating the ductile fracture response of SSPs under ULCF.

Specimen	Test	Fracture initiation N_0			Failure			
		Test (cycle)	FEM (cycle)	FEM-test (cycle)	L_{E} (mm)	Test (cycle)	FEM (cycle)	FEM-test (cycle)
CNS-2	3	18	18	0	0.45	24	23	−1
CNS-3	6	32	32	0	0.33	39	39	0
CNS-4.5	9	18	17	−1	0.13	19	21	+2

Table 6.7. Abaqus predictions of fracture initiation and failure of CNS tests versus experimental results

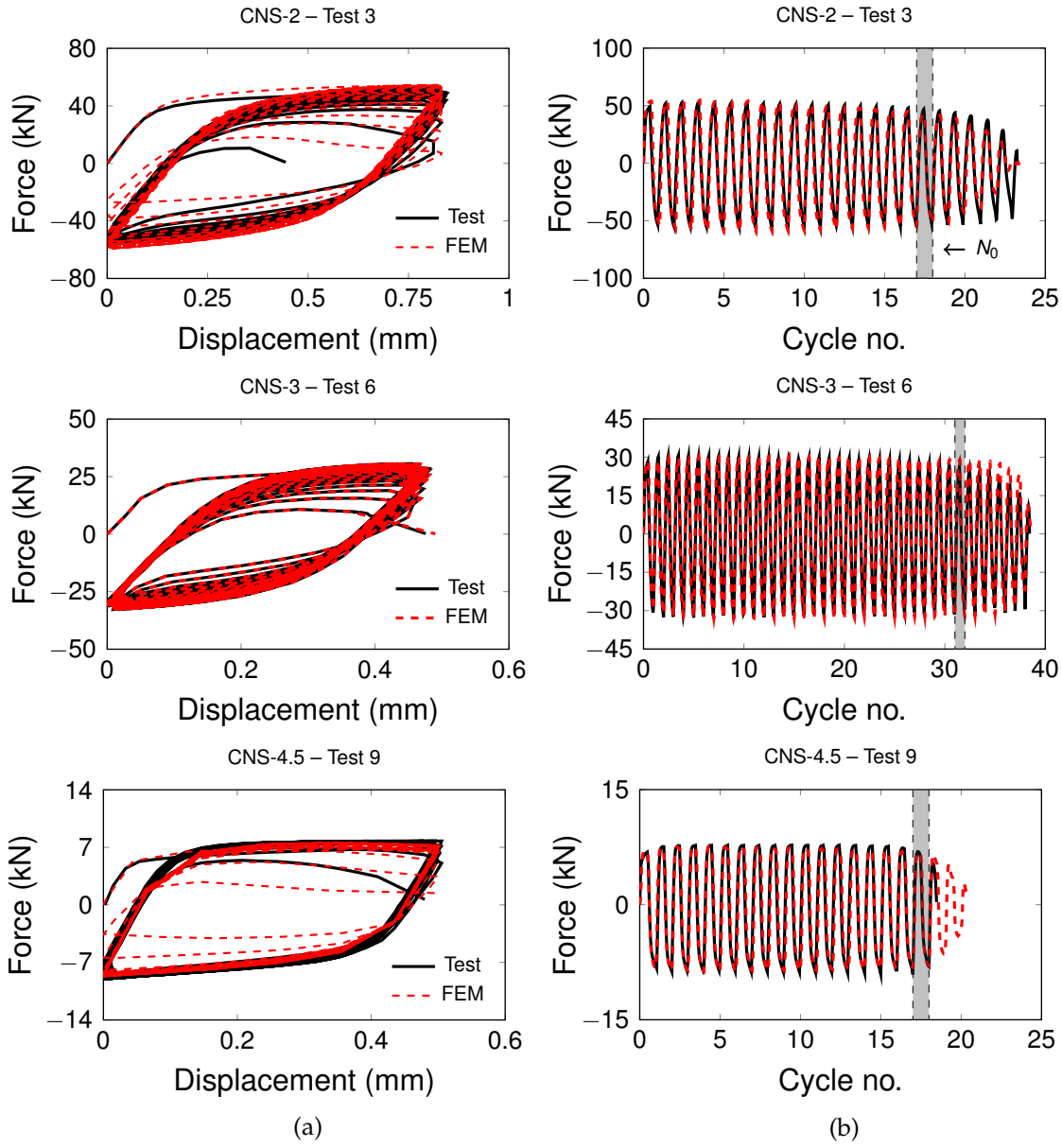

Figure 6.23. Fracture simulation of ULCF tests on CNSs versus experimental results: (a) force-displacement responses; and (b) force histories with indication of experimental ductile fracture initiation (cycle no.)

6.7 Explicit FEM simulations of SSP tests

For the simulation of fracture in the SSPs, three-dimensional FEM models are developed. This section presents the details of the FEM modelling and the validation of the hysteretic response of the SSPs against the experimental tests conducted in Chapter 5.

6.7.1 Three-dimensional FEM models of SSP tests

Three-dimensional FEM models of the full-scale tests on SSPs are developed in Abaqus. The detailed models of the two SSP geometries, tested in Chapter 5, are illustrated in Figure 6.24. Only half of the test setup is reproduced in full detail, due to its symmetric geometry. Of the upper supporting plate, only the lower 40-mm thick plate is modelled. The steel collar and the triangular stiffeners are included in the model, along with the steel plate that was welded to restore the boundary conditions in the SSP2 tests (see Figure 5.18a).

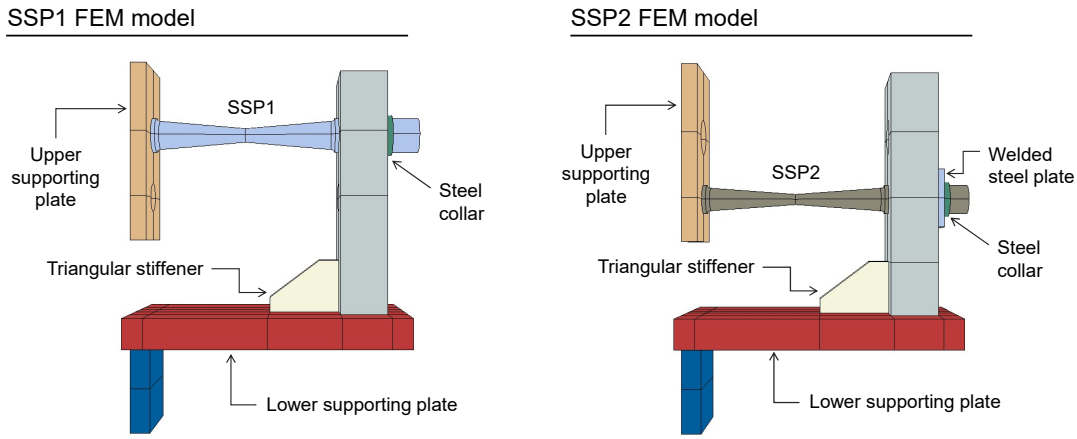

Figure 6.24. View of the three-dimensional FEM models of SSPs

Figure 6.25 illustrates the mesh discretisation applied to the FEM model of SSP1, along with the boundary conditions. A symmetry condition is defined for the surfaces on the symmetry plane. To simulate the grip of the testing machine jaw faces, the surface of the vertical plate welded to the bottom plate assembly is fully restrained. Displacement is applied to the upper supporting plate assembly. All the parts of the model are discretised using solid elements with reduced integration, denoted as C3D8R elements in Abaqus. A relatively coarse mesh is used for the steel plate assemblies, while a more refined mesh is applied to the SSPs, where inelastic deformations and fracture were experimentally observed. Given that the model is used to simulate relatively long cyclic loading protocols, a trade-off between computational time and the size of the mesh resulted in an average mesh size of 3 mm in the bending parts of the SSPs. Considering that, unlike fracture in existing crack tips or sudden geometric changes, the stress state in the SSPs is smooth, the mechanics-based fracture

models are less sensitive to the mesh size (Vasdravellis et al. 2014), and, therefore, the adopted mesh is considered acceptable.

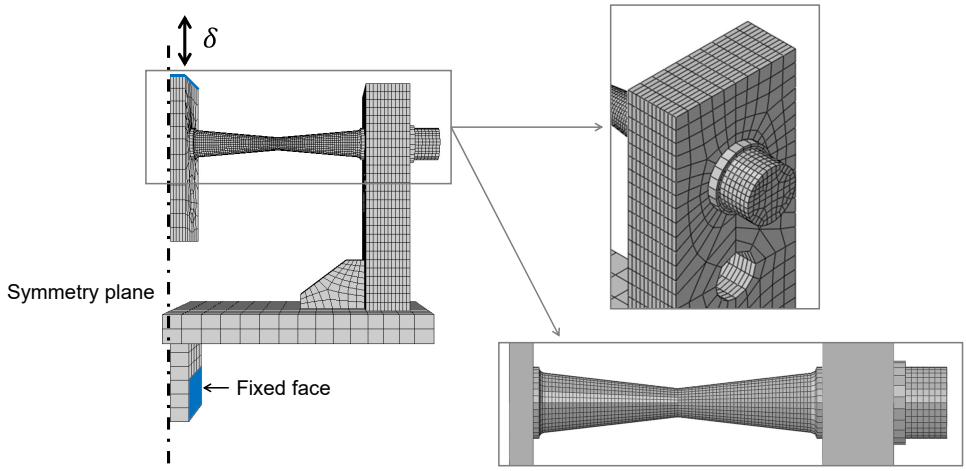

Figure 6.25. FEM model of SSP1: mesh discretisation and boundary conditions

Surface-based tie constraints, which impose equal displacements among the nodes of two surfaces, are used for modelling the welded joints in the two steel plate assemblies, i.e., between the lower and vertical plates, the triangular stiffeners at the base of the plates, and the steel washer welded onto the SSP. A general contact algorithm is defined to simulate the interaction between the specimen and the holes of the supporting plates. Based on experimental measurements, a clearance of 0.1 mm and 0.3 mm is used for the SSP1 and SSP2 models, respectively. A contact property with normal and tangential behaviour with a friction coefficient equal to 0.2 is defined.

The hysteretic behaviour of the SSD material is simulated by the elastic plastic material model with combined isotropic and kinematic hardening, previously calibrated in Section 6.4.2. An elastic plastic material with isotropic hardening behaviour is defined for the steel assemblies made of S355. The yield stress was conservatively reduced to 300 MPa to account for the large thickness of the steel plates (40−60 mm), since the yield stress reduces with increasing plate sections (EN 10025-2 2004).

The FEM model of SSP1 consists of 11,983 elements, 15,718 nodes, and 47,319 degrees of freedom, while a typical mesh for the FEM model of SSP2 is made of 13,023 elements, 16,469 nodes, and 49,972 degrees of freedom.

6.7.2 Explicit FEM simulations without fracture

The ability of the FEM models of tracing the hysteresis of SSPs is validated against the experimental results. For this purpose, the ULCF tests for each geometry are simulated without specifying any fracture criteria.

Displacement-controlled analyses are conducted in Abaqus Explicit under quasi-static loading conditions in the large displacement/strain nonlinear regime. The time step for one cycle is set equal to 60 s, so that the loading rate is relatively low and no dynamic effects influence the analysis. For instance, for an imposed amplitude of 49 mm, the load is applied at around 3 mm/s. To ensure a stable analysis, the density of the material is decreased by six orders of magnitude, and the displacement history is applied with a periodic amplitude. Based on the mesh size, a stable target time increment equal to 0.0001 s was iteratively identified.

The typical runtime for one imposed cycle is about 1h on a second-generation intel i7 CPU at 3.40 GHz and 16 GB of RAM running on a 64-bit Windows 7 platform. The total computational time of a cyclic analysis is in the range of 1-3 days, depending on the number of the cycles to failure.

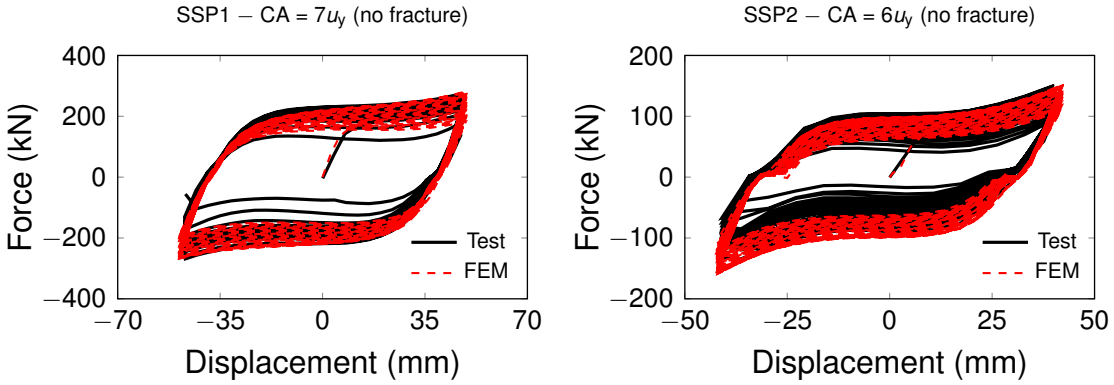

Figure 6.26. Experimental and numerical (without fracture criteria) hystereses: (a) SSP1 (CA = $7u_y$); and (b) SSP2 (CA = $6u_y$)

Figure 6.26a shows the comparison of the numerical and experimental hystereses of SSP1 under CA = $7u_y$ (no. 2 test). The results indicate that the FEM model is capable of tracing well the nonlinear behaviour of the specimen. A similar correlation is found for the simulation of SSP2 under CA = $6u_y$ (no. 12 test), as illustrated in Figure 6.26b. In this case, the FEM model slightly

overestimates the maximum forces in compression, where the reduced hardening behaviour experimentally exhibited by SSP2 is not captured (see Section 5.7.1). It can be observed that the FEM simulations capture the pinching effect at zero force, indicating that the clearance between the SSPs and the holes of the supporting plates is accurate.

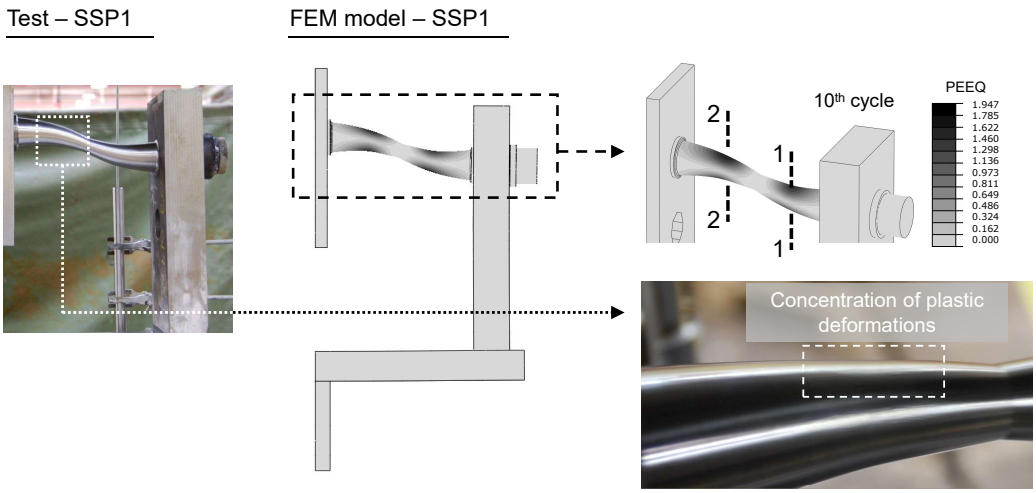

Figure 6.27. Comparison of experimental and numerical deformed shapes for SSP1 in test 2, with PEEQ contour plots at 10th cycle and experimental plastic deformations at the free surface in section 2

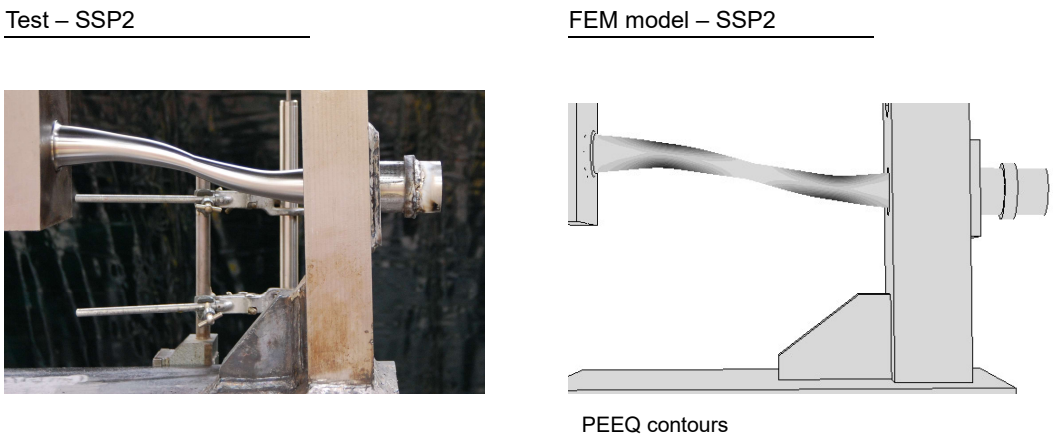

Figure 6.28. Experimental and numerical axial expansion of SSP2

Figure 6.27 illustrates the numerical and experimental deformed shapes of SSP1 at the 10th cycle of no. 2 test. The contours of the equivalent plastic strains (PEEQ) are plotted on the steel pin: the maximum $\bar{\varepsilon}^{pl}$ values are concentrated at the free surface at the middle of a half bending part in sections 1 and 2, in

agreement with the experimental evidence. In addition, the FEM model is also able to capture the axial elongation of the specimen, as shown in Figure 6.28 by the experimental-numerical comparison of the deformed shape for SSP2.

6.8 CVGM prediction of SSP fracture initiation under ULCF

The CVGM is applied to the ULCF tests of SSPs using the Abaqus explicit simulations described in the previous section. Stress and strain histories are extracted at the free surface in the area where plastic deformations are concentrated. As shown in Figure 6.27, the fracture location is at the centre of the half bending parts, in accordance with the experimental evidence.

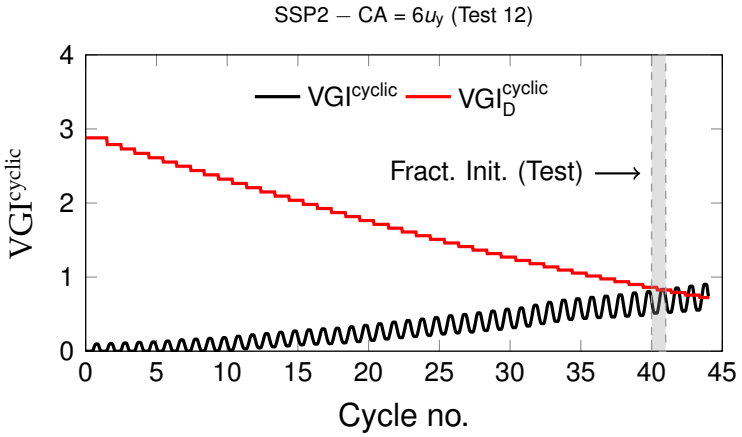

Figure 6.29. CVGM fracture prediction in SSP2 under CA = $6u_y$

The extracted T and $\bar{\varepsilon}^{pl}$ histories are used to integrate Eqs. (6.11) and (6.12). VGI_D^{mono} = 2.88 and λ = 0.12 calibrated in Section 6.4.3 are applied. Figure 6.29 shows the evolutions of VGI^{cyclic} and VGI_D^{cyclic} for the CA = $6u_y$ test of SSP2. While VGI^{cyclic} varies with the sign of T, VGI_D^{cyclic} is a stepwise function starting at VGI_D^{mono}, and decreasing at the start of each VGI^{cyclic} cycle according to the exponential decay function given by Eq. (6.12). The intersection of the VGI_D^{cyclic} and VGI^{cyclic} curves indicates fracture initiation. The CVGM prediction of fracture initiation is consistent with the N_0 cycle observed in the test. The application of the CVGM to other tests (Random, CA = $7u_y$ and $5u_y$) shown in Figure 6.30 reveals a good agreement with the corresponding experimental evidence.

The CVGM fracture initiation predictions are summarised in Table 6.8 for all the tests. The results indicate that the calibrated CVGM parameters predict with good accuracy fracture initiation, with a maximum error of 12%.

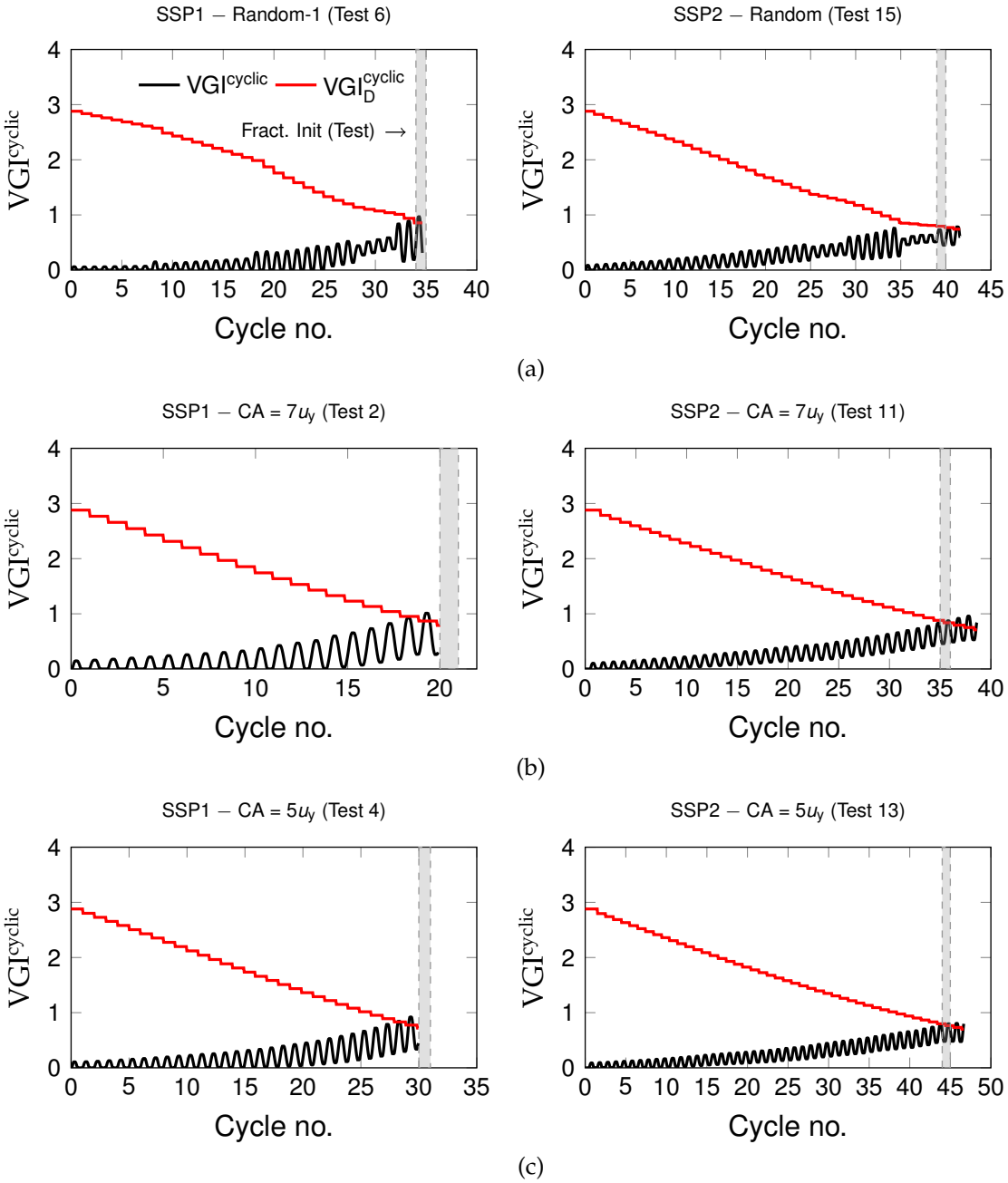

Figure 6.30. CVGM fracture prediction in SSPs: (a) random tests; (b) CA = $7u_y$ tests; and (c) CA = $5u_y$ tests

Specimen	Test	Protocol	Fracture initiation N_0			
			Test	CVGM	CVGM−test	
			(cycle no.)	(cycle no.)	(cycle)	(% error)
SSP1	2	CA = $7u_y$	21	19	−2	−10%
	3	CA = $6u_y$	25	28	+3	+12%
	4	CA = $5u_y$	31	29	−2	−6%
	5	CA = $4u_y$	43	42	−1	−2%
	6	Random-1	35	35	0	0%
	7	Random-2	25	28	+3	+12%
SSP2	10	CA = $8u_y$	30	33	+3	+10%
	11	CA = $7u_y$	36	36	0	0%
	12	CA = $6u_y$	41	41	0	0%
	13	CA = $5u_y$	45	45	0	0%
	14	CA = $4u_y$	54	48	−6	−11%
	15	Random	40	42	+2	+5%

Table 6.8. CVGM prediction of fracture initiation in SSPs versus experimental tests

6.9 Abaqus explicit simulation of SSP fracture under ULCF

Explicit fracture simulations of the SSPs are performed in Abaqus using the fracture initiation and evolution parameters calibrated in the previous sections. This section presents the results of the fracture simulation of ULCF tests. Additional simulations of the two monotonic tests on SSPs, presented in Appendix C, provide an estimation of the fracture capacity of SSPs under monotonic loading.

The Abaqus initiation criterion parameter for ULCF, i.e., $\alpha_{\text{cyclic}} = 10$, calibrated in Section 6.4.4, is used in combination with the fracture evolution parameters presented in Section 6.5. The latter are modified based on the mesh discretisation of the SSP bending parts.

The fracture initiation from the explicit simulations is compared with the experimental evidence in Figure 6.31, where the contours of the fracture initiation index, denoted as DUCTCRT in Abaqus, are plotted on the deformed SSPs. It can be seen that the numerical model simulates fracture initiation on the free surface at the centre of half bending parts, indicated as sections 1 and 2, in perfect agreement with the experimental tests.

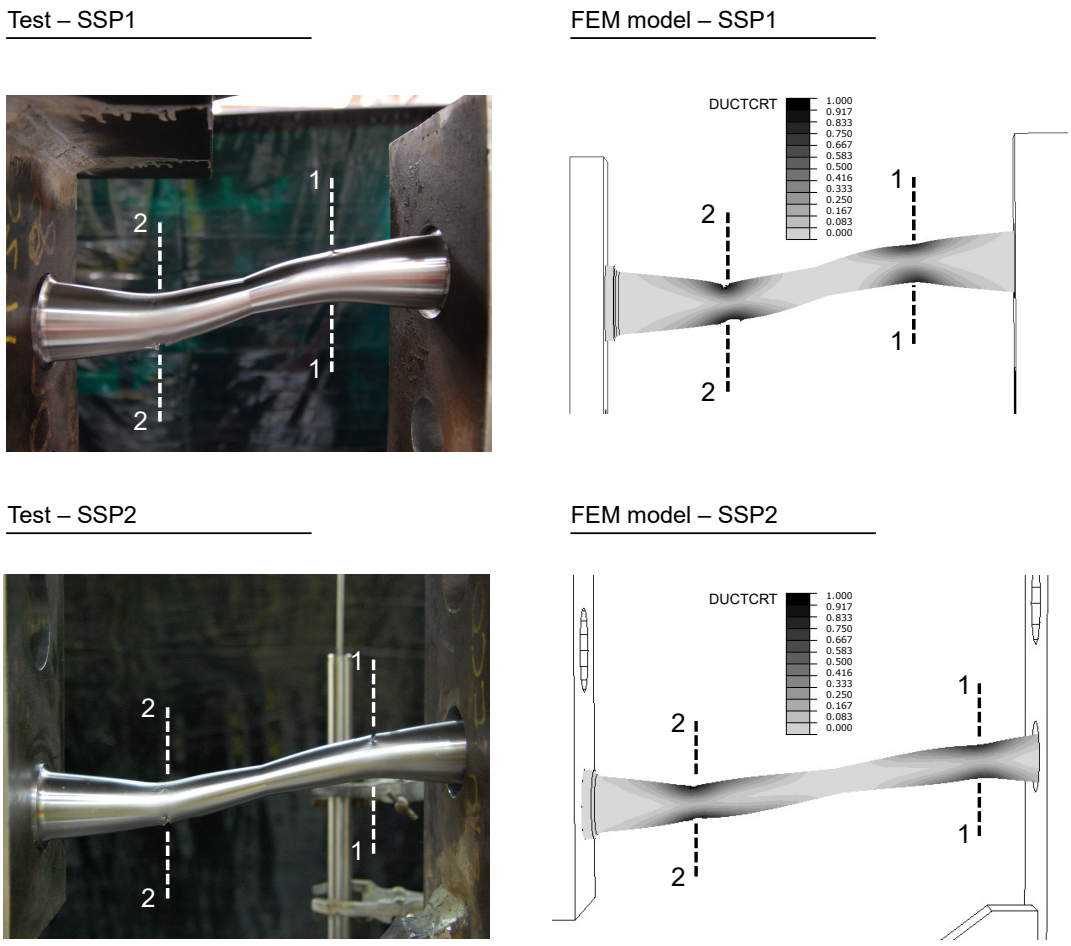

Figure 6.31. Experimental and numerical fracture sections of SSPs

The evolution of the variables governing ductile fracture, extracted from the simulation of SSP2 under the random protocol, are shown in Figure 6.32. The history of the fracture initiation index ω_{D} in Figure 6.32a shows that fracture initiation is predicted during the 41$^{\mathrm{st}}$ cycle (i.e., $\omega_{\mathrm{D}} = 1$); from that point, the finite element stiffness undergoes degradation, leading to its removal from the mesh in the next cycle when $D_{\mathrm{evol}} = 1$. The T history over three cycles of the simulation (Figure 6.32b), shows that triaxiality at the fracture section is characterised by alternating cycles of tension and compression, with maximum values in the range of 0.33-0.4. It can also be observed that, below the cut-off value of $T = -1/3$, no damage is accumulated, being ω_{D} constant. The histories of ω_{D} and $\overline{\varepsilon}^{pl}$ (Figure 6.32d) show that $\overline{\varepsilon}^{pl}$ monotonically increases both in tension and compression, while the fracture initiation index accounts for inhibition of fracture under compression. In addition, the stress state is characterised by axisymmetric condition, i.e., ξ = ±1, as shown in Figure 6.32c.

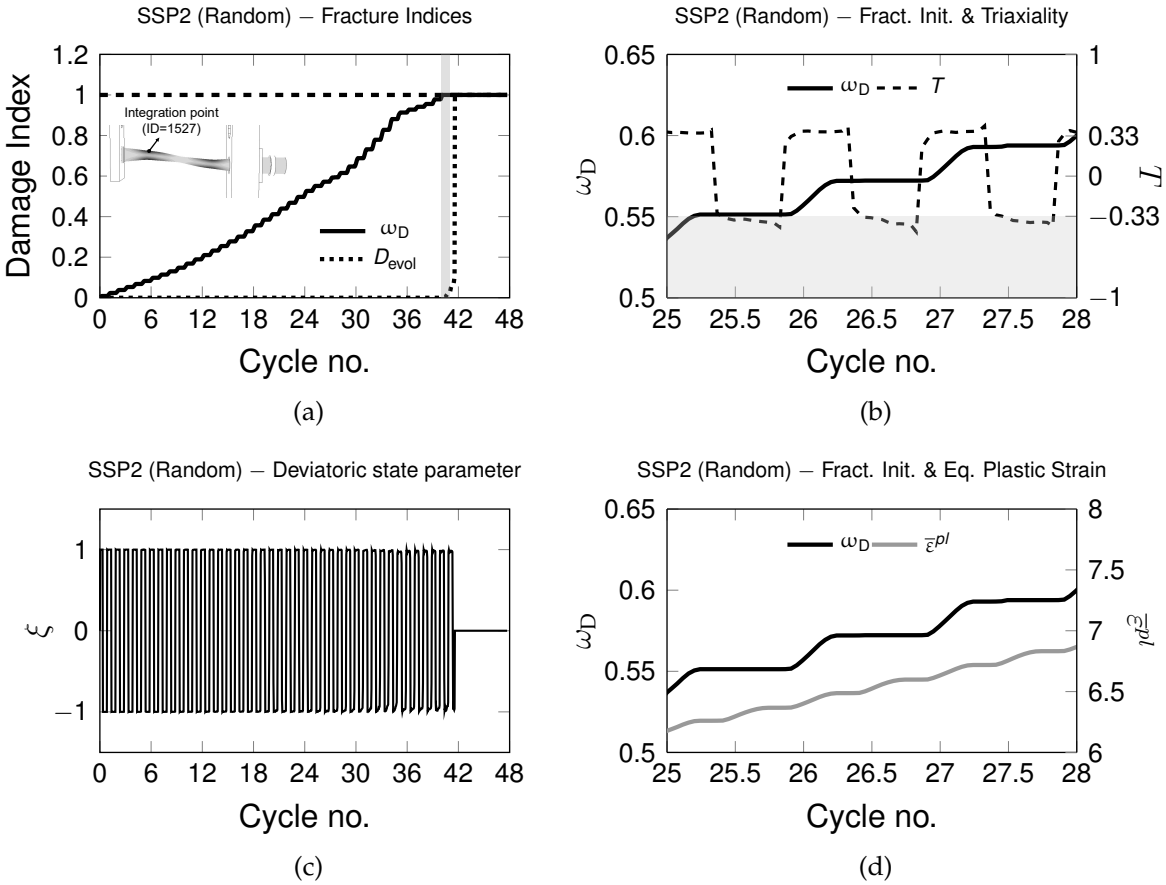

Figure 6.32. Evolution of stress, strain and fracture indices at the fracture section (SSP2 Random test): (a) ω_D and D_{evol}; (b) ω_D and T; (c) ξ; and (d) ω_D and $\bar{\varepsilon}^{pl}$

The results of fracture initiation predictions for all the ULCF test simulations are summarised in Table 6.9, where the cycle at which fracture initiates N_0 is compared with the experiments. Since the predictions are within ±10% error, it can be concluded that the calibrated Abaqus fracture initiation criterion is capable of providing an accurate prediction, even for the random tests. Comparison of these results with the CVGM predictions from Table 6.8 shows that the calibrated mechanics-based models applied to the ULCF tests of SSPs provide a similar prediction of fracture initiation.

Following fracture initiation, the numerical force-carrying capacity of the SSPs decreases as a result of the deletion of elements from the mesh according to the fracture evolution model. Figure 6.33 compares the simulated fracture evolution with the experimental photographic evidence of two representative cyclic tests (no. 2 and 12). The results show that the calibrated FEM model has the ability of accurately capturing the ULCF ductile fracture mechanism.

Specimen	Test	Protocol	Fracture initiation N_0			
			Test	Abaqus	Abaqus−test difference	
			(cycle no.)	(cycle no.)	(cycle)	(% error)
SSP1	2	CA = $7u_y$	21	21	0	0%
	3	CA = $6u_y$	25	26	+1	+4%
	4	CA = $5u_y$	31	29	−2	−6%
	5	CA = $4u_y$	43	40	−3	−7%
	6	Random-1	35	36	+1	+3%
	7	Random-2	25	26	+1	+4%
SSP2	10	CA = $8u_y$	30	32	+2	+7%
	11	CA = $7u_y$	36	37	+1	+3%
	12	CA = $6u_y$	41	42	+1	+2%
	13	CA = $5u_y$	45	45	0	0%
	14	CA = $4u_y$	54	49	−5	−9%
	15	Random	40	41	+1	+3%

Table 6.9. Prediction of fracture initiation in SSPs according to Abaqus fracture model versus experimental tests

However, comparison of the numerical and experimental force histories of the same tests in Figure 6.34 reveals that, once fracture initiates, the numerical force-carrying capacity decreases at a faster rate than in the experiments. A similar response can be seen in the numerical-experimental force evolutions of the remaining tests, illustrated in Figures 6.35, 6.36, and 6.37. This indicates that the FEM simulation tends to underestimate the numbers of cycles to failure. For instance, simulations of CA = $4u_y$ tests show a premature degradation of the force-carrying capacity of SSPs. Such discrepancy can be attributed to the relatively coarse mesh applied to the SSP bending parts. For an improved accuracy in simulating fracture evolution, a refined mesh should be ideally used at fracture locations; however, this would result in a significant increase in computational time.

Overall, the Abaqus fracture simulations provide an accurate prediction of fracture initiation of the SSPs under ULCF, but tend to overestimate the rate of the material degradation after initiation. This could be improved by either increasing the mesh size in the fracture locations or adopting a different evolution model.

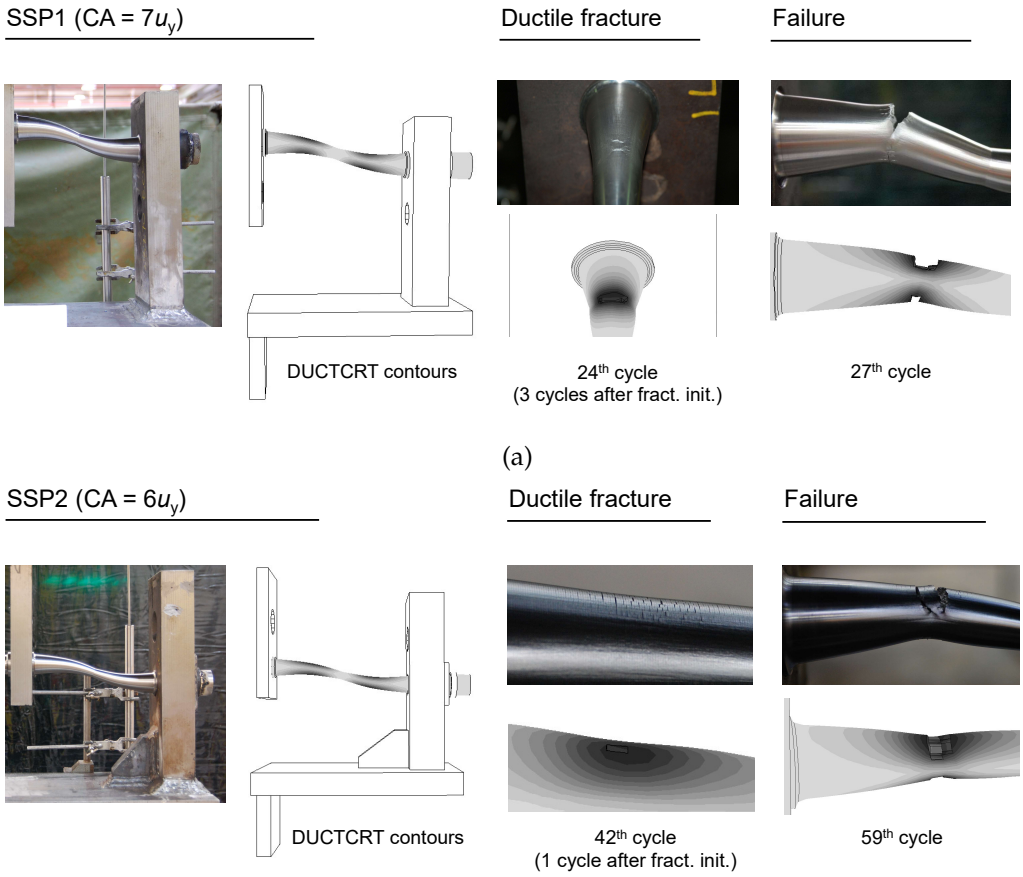

Figure 6.33. Comparison of experimental and numerical ductile fracture evolution in section 2 for: (a) SSP1; and (b) SSP2

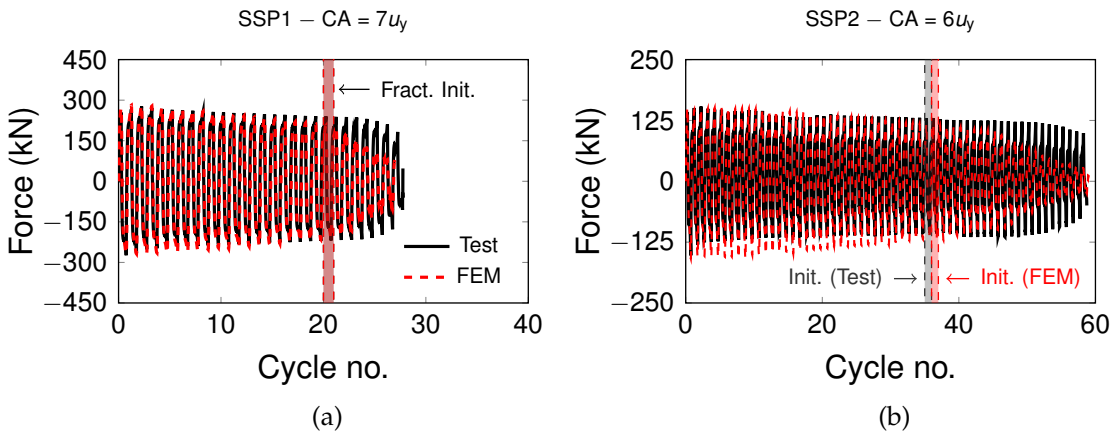

Figure 6.34. Experimental-numerical comparison of force histories of SSPs with indication of the fracture initiation cycle: (a) test 2; and (b) test 12

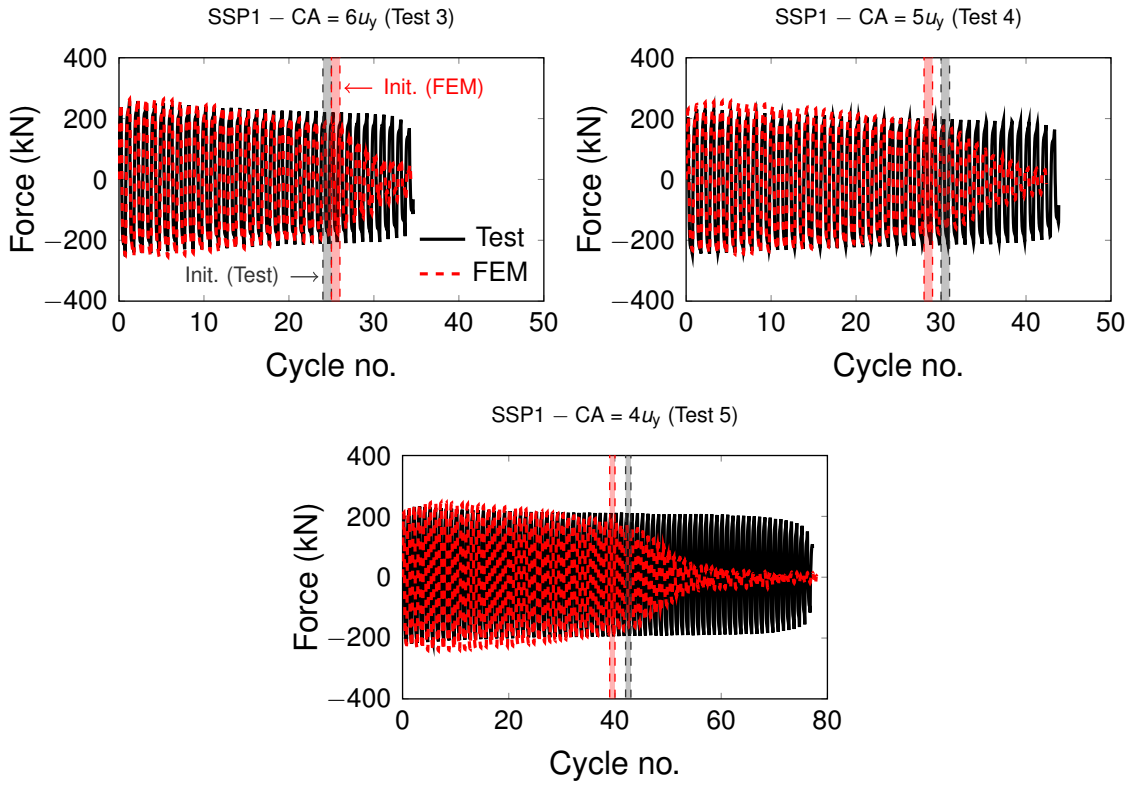

Figure 6.35. Experimental-numerical force histories of SSP1: CA tests

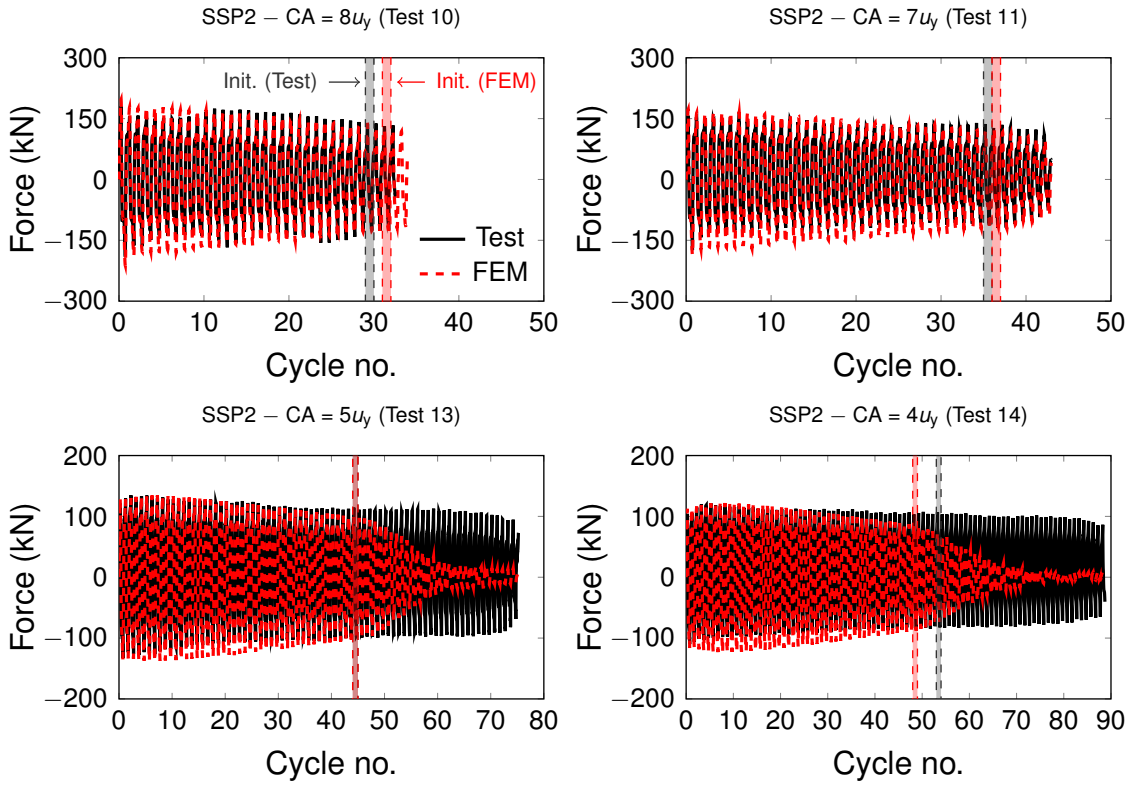

Figure 6.36. Experimental-numerical force histories of SSP2: CA tests

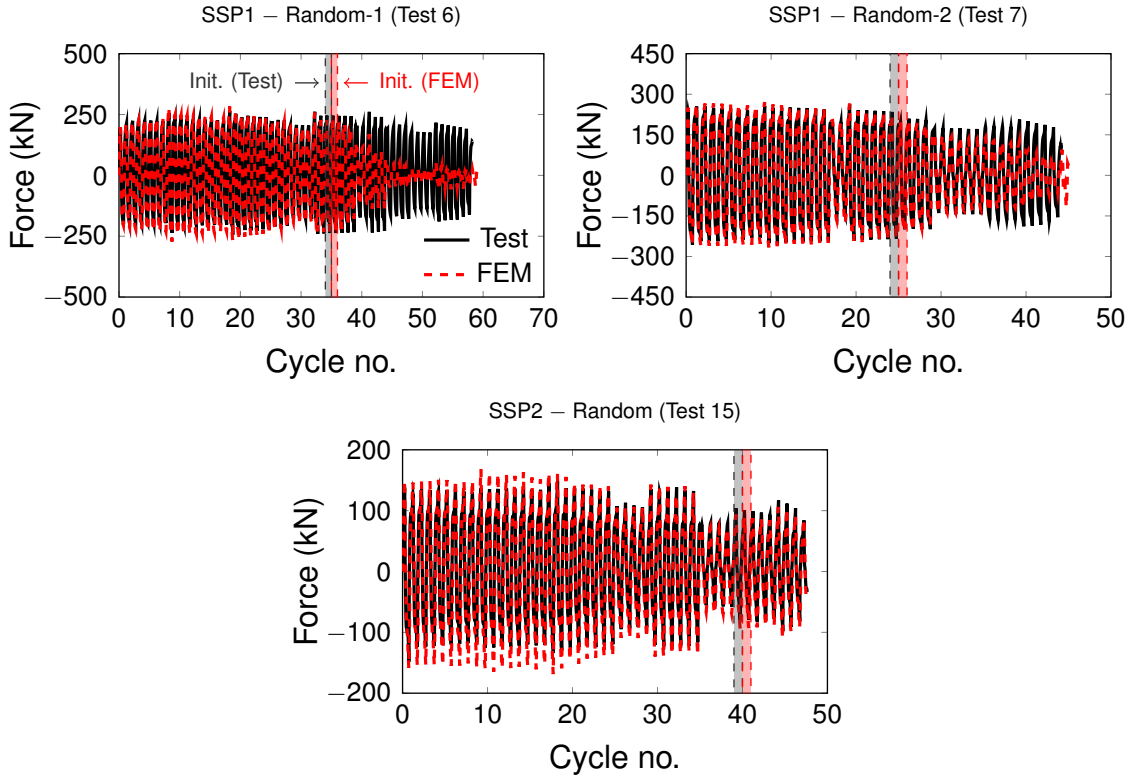

Figure 6.37. Experimental-numerical force histories of SSPs: random tests

6.10 Conclusions

This chapter investigated the ductile fracture of the SSPs employed in the dual CBF-MRF. To characterise the fracture capacity of SSPs under ULCF, a LCF model and two mechanics-based models, i.e., the CVGM and the Abaqus fracture criterion, were employed. While the LCF model, based on a Coffin-Manson-like relationship and Miner-Palmgren linear damage accumulation rule, predicts the fatigue life of the SSPs, i.e., full-section fracture, the mechanics-based criteria simulate ductile fracture initiation. The fracture initiation parameters of the CVGM and Abaqus criterion were calibrated against monotonic and ULCF tests on CNSs. In addition, the Abaqus initiation criterion was combined with a fracture evolution model, which allows to simulate the progressive damage following initiation. The fracture evolution parameters were calibrated against monotonic coupon tests following the method proposed by Pavlovic et al. (2013). The Abaqus fracture parameters for initiation and

evolution were validated against coupon tests. Three-dimensional FEM models of the SSPs were developed in Abaqus to simulate their hysteretic behaviour and fracture response. The CVGM was used to predict fracture initiation in the SSPs, while the Abaqus criteria were applied to explicitly simulate fracture initiation and evolution. Based on the results presented in this chapter, the following conclusions are drawn:

- The validation of the Miner-Palmgren rule against the random tests on SSPs indicates that the calibrated Coffin-Manson-like parameters can be used in a fatigue model to predict the SSP failure.
- The application of the CVGM and the Abaqus fracture criterion to the ULCF tests of SSPs provides an accurate prediction of their ductile fracture initiation, with an error in the region of 10% against experimental evidence.
- The simulation of fracture evolution under ULCF using the calibrated Abaqus parameters provides a good agreement for the coupon tests, while for the SSPs the explicit simulations generally underestimate the number of cycles to failure. This might be due to the larger mesh size employed for the SSPs.
- The CVGM and Abaqus fracture initiation parameters can potentially be used to predict the ULCF fracture capacity of SSPs having different geometries and boundary conditions, without the need for further experimental investigation. It is worth noting that the parameters of the Abaqus fracture initiation model are valid only under ULCF conditions, while the CVGM has the advantage of being suitable for predicting fracture under either monotonic or ULCF loading.

Chapter 7

Assessment of Seismic Collapse Potential of the Dual CBF-MRF

7.1 Introduction

When storey drifts are severe, a seismic-resistant frame may reach global collapse due to dynamic instability. $P-\Delta$ effects generate secondary actions that may not be resisted by the structure (Ibarra et al. 2005). This collapse mode, known as sidesway instability, can be substantially accelerated by the deterioration in stiffness and strength of structural components subjected to repeated plastic deformation (Karamanci & Lignos 2014). As cyclic degradation typically represents a primary contributor to collapse, modelling its effects is essential for predicting the collapse capacity of structural systems (Krawinkler & Zareian 2007).

Variability in ground motion characteristics and uncertainties in modelling and analysing structural systems contribute to the complexity of collapse prediction (Bruneau et al. 2011). To account for all these sources of uncertainty, probabilistic approaches have been recently proposed. The FEMA P695 (2008) document provides a methodology for quantifying the building collapse performance. Fragility curves are constructed using the results of incremental dynamic analysis (IDA) (Vamvatsikos & Cornell 2002), in which the structure is subjected to a set of ground motions progressively scaled up until collapse is reached. A low probability of collapse (i.e., $<$10%) is required for a well-designed structure under the MCE hazard level (FEMA P695 2008). As discussed in Chapter 2, seismic resilient structures should achieve even lower

collapse probabilities.

This chapter presents the collapse potential evaluation of the proposed dual CBF-MRF. The procedure adopted for the collapse assessment is shown in Figure 7.1. The 6-storey prototype frame designed in Chapter 3 is now revised based on the experimental results of the two SSPs geometries available from Chapter 5. The beam-solid FEM model of the dual frame employed in Chapter 4 is modified to explicitly account for ductile fracture in SSPs, modelled using connector elements. A plastic motion-based fracture macro-model capable of simulating ductile fracture under ULCF is validated against the experimental results presented in Chapter 5. IDA are conducted using the simplified model of the CBF-MRF under the same set of 22 far-field employed for the nonlinear time-history analyses in Chapter 4. The results of IDA are finally used to construct a fragility curve, providing a probabilistic evaluation of the collapse capacity of the dual frame. The influence of ground motion duration on the dynamic response of the proposed frame is also investigated.

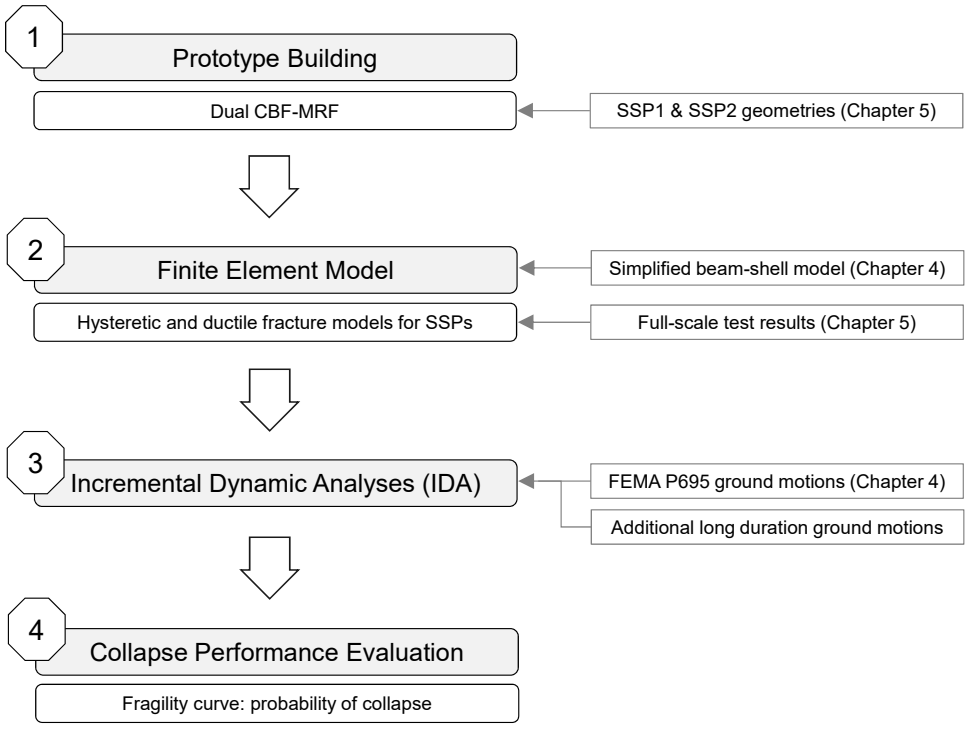

Figure 7.1. Procedure for seismic collapse evaluation of the dual CBF-MRF

7.2 Revised prototype building

The 6-storey prototype building described in Chapter 3 is used for the collapse potential assessment of the CBF-MRF. Since the original design of the dual frame had five different SSP geometries over the six storeys, a revised design is developed using only the two experimentally-tested SSP geometries. Following the design methodology adopted in Section 3.5, the energy dissipative braces are designed using either SSP1 or SSP2, while maintaining similar yield force $F_{y,tot}$ and global stiffness K_{tot} to the original CBF-MRF design. The SSP1 geometry is used for storeys 1 to 4, while SSP2 for the top storeys 5 and 6. The two design versions are compared in Table 7.1. The beam, column and brace sections are the same as in the original design. The fundamental period of vibration of the revised CBF-MRF is 0.78 s, comparable to that of the original frame (i.e., 0.75 s).

Design	Storey	Geometry	n_{SSP}	D_e (mm)	D_i (mm)	L_{SSP} (mm)	$F_{y,tot}$ (kN)	K_{tot} (N/mm)
Original	6	∼SSP2	4	36	18	210	240	42,000
(Chapter 3)	5	–	4	42	24	230	350	59,000
	4	∼SSP1	4	50	24	230	540	80,000
	3	SSP1	4	50	24	225	560	80,000
	2	–	6	46	22	215	650	108,000
	1	–	6	46	22	215	650	108,000
Revised	6	SSP2	4	40	18	225	300	44,000
(Chapter 7)	5	SSP2	5	40	18	225	375	55,000
	4	SSP1	4	50	24	225	600	80,000
	3	SSP1	4	50	24	225	600	80,000
	2	SSP1	5	50	24	225	750	100,000
	1	SSP1	5	50	24	225	750	100,000

Table 7.1. SSP design details for the original and revised dual CBF-MRF

7.3 Nonlinear FEM model of the dual CBF-MRF

The simplified FEM model of the dual CBF-MRF developed for the nonlinear time-history analyses (Section 4.5.1) is now used for the collapse assessment of the system. The beam-solid model, shown in Figure 7.2, is capable of simulating some of the mechanisms that can lead to collapse under extreme ground

motions, including the $P - \Delta$ effects from the gravity frame, and the deterioration of the beam fuses. However, the FEM model does not explicitly simulate ductile fracture of the SSPs, which is a critical failure mode for the dual frame. Therefore, to ensure a reliable collapse evaluation of the dual frame, a fracture criterion is introduced in the nonlinear connectors modelling the SSPs, as explained below.

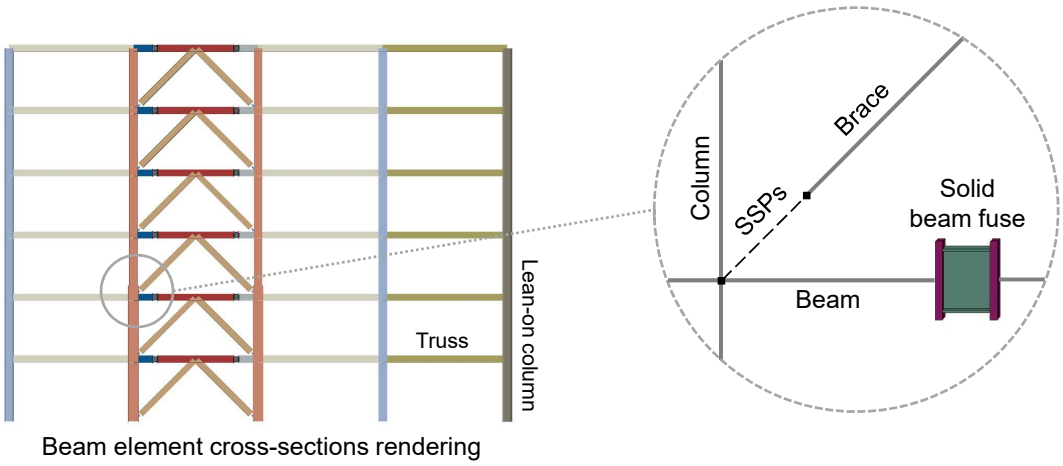

Figure 7.2. View of the simplified FEM model of the CBF-MRF using beam elements for the main structural members, solid elements for the beam fuse, and connector elements for the SSPs and friction pads

In the collapse assessment of the frame, it is assumed that the columns do not experience severe degradation due to local buckling under drifts smaller than 10%, since the HEB 500 sections are Class 1 (EC3 2003) and relatively stocky, i.e., $h/t_{\mathrm{w}} = 26.9$ and $b_{\mathrm{f}}/2t_{\mathrm{f}} = 5.4$. Experimental studies conducted on stocky wide-flange sections (i.e., $h/t_{\mathrm{w}} < 30$ and $b_{\mathrm{f}}/2t_{\mathrm{f}} < 8$) have shown that they can sustain storey drifts of 7-9% with minimal deterioration in flexural strength and stiffness (MacRae et al. 1990, Newell & Uang 2006). As discussed in Section 7.4.2, the global collapse is reached for inter-storey drifts of 10%, therefore it is assumed that the column deterioration would not significantly influence the results of IDA. However, a recent study by Elkady & Lignos (2015) has highlighted that deep stocky wide-flange sections (i.e., depth larger than 400 mm) may be susceptible to flange and web local buckling under cyclic loading, leading to a more rapid degradation of their flexural capacity. A numerical investigation should be carried out to verify that the HEB 500 sections of the CBF-MRF do not experience severe deterioration under drifts below 10%.

This section presents the calibration of the parameters defining the hysteresis and damage response of the connector elements based on the latest experimental results.

7.3.1 Calibration of hysteretic parameters for connectors

The hysteretic behaviour of the connectors modelling the SSP-brace connections is defined using an elastic-plastic force-displacement law. The inelastic response of a connector is given by the n_{SSP} SSPs working in parallel with each other, as shown in Table 7.1. The force-displacement curves of the full-scale tests are used to identify the half-cycle input data for a single SSP. A FEM model with a connector element is created using Abaqus. The half-cycle data input for each SSP geometry is obtained by a trial and error method using the CA loading protocols.

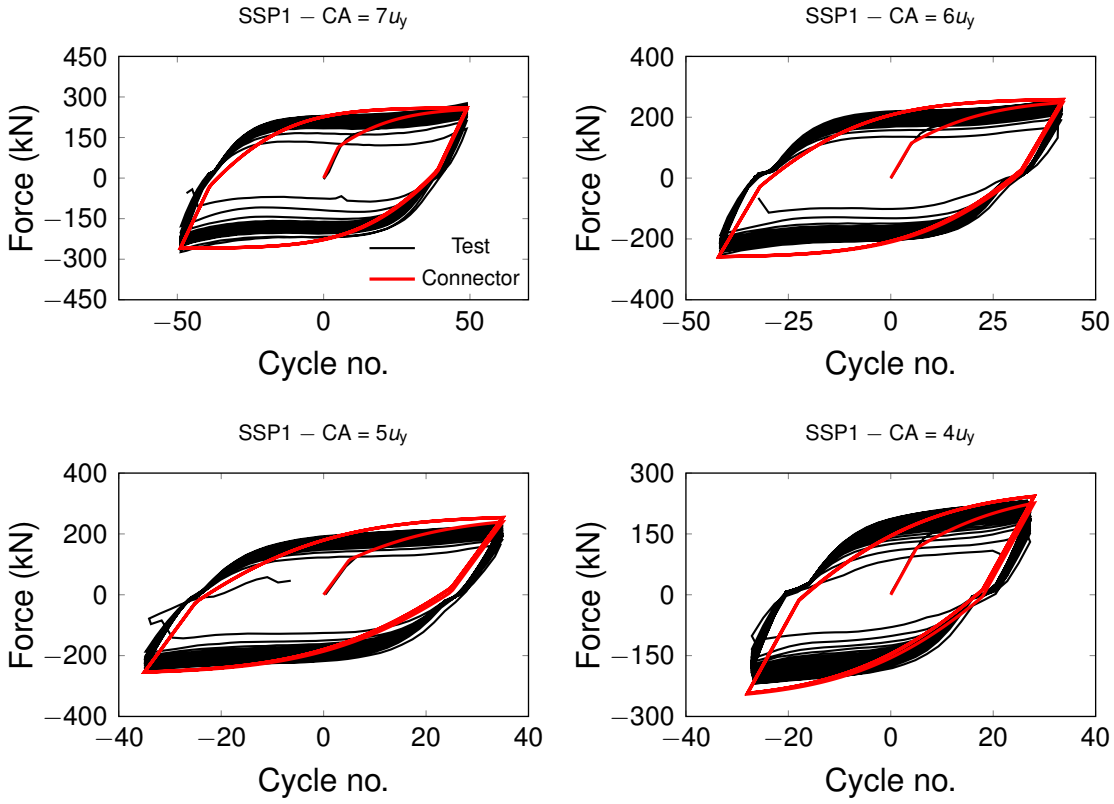

Figure 7.3. Experimental-connector comparison of the hysteresis of SSP1

Figures 7.3 and 7.4 show the comparison of the connector force-displacement responses with the experimental hystereses of SSP1 and SSP2, respectively. The results indicate that the selected cyclic hardening parameters provide a good

agreement with the experimental data. It should be noted that connector elements are not capable of capturing three-dimensional effects, such as the pinching effect at zero force and the reduced hardening that was experimentally observed in compression for SSP2.

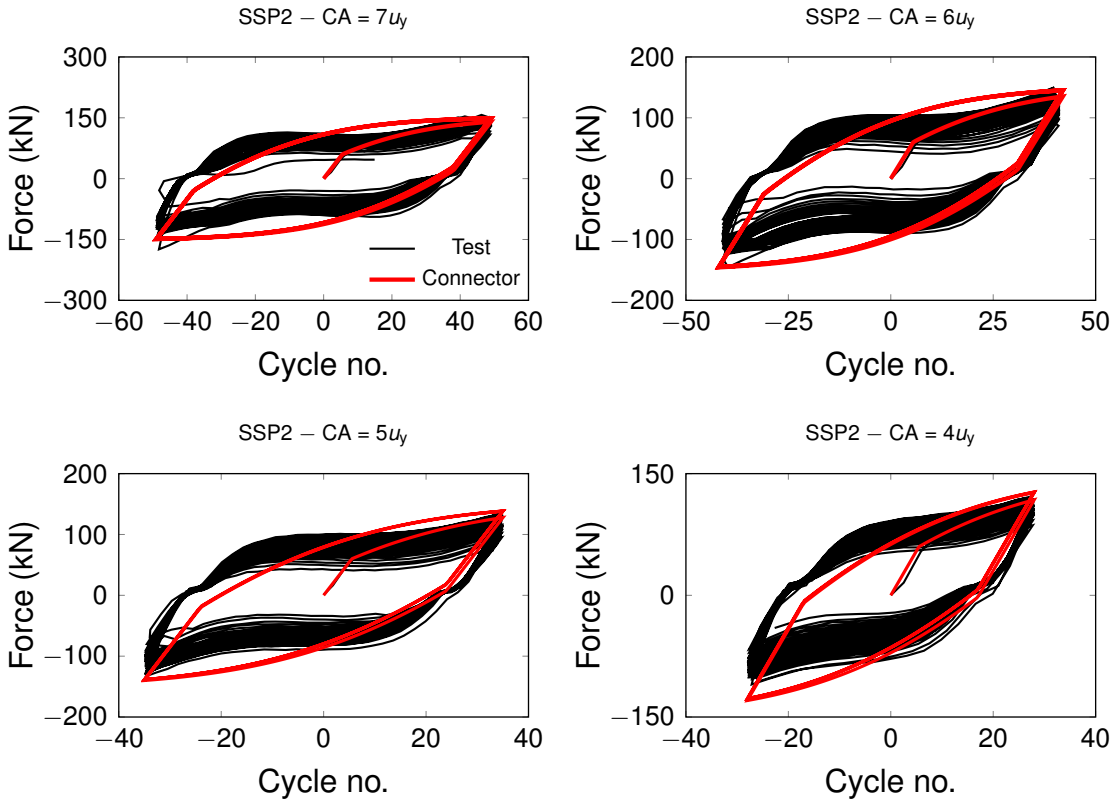

Figure 7.4. Experimental-connector comparison of the hysteresis of SSP2

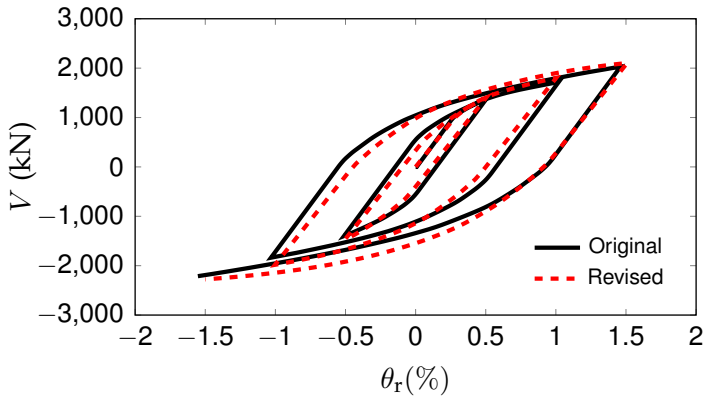

Figure 7.5. Nonlinear static push-pull response of the CBF-MRF using the revised and original connector parameters

A nonlinear cyclic (push-pull) static analysis is performed to compare the seismic performance of the revised CBF-MRF with that of the original design. Figure 7.5 plots the base shear (V) versus the roof drift (θ_r) responses of the revised and original frames subjected to three cycles up to the FOE, DBE, and MCE drift. It can be seen that the two design versions have comparable cyclic inelastic behaviour and energy dissipation.

7.3.2 Calibration of fracture parameters for connectors

To simulate ductile fracture of the SSPs subjected to ULCF, a damage criterion that degrades the elastic-plastic response in the connector elements is used. Abaqus offers a connector damage capability that employs a damage initiation criterion combined with an evolution law to degrade the force response. The damage model can use force-based, motion-based or plastic motion-based criteria (Dassault Systèmes 2014). When relative forces or motions in a connector satisfy certain criteria, damage initiates. Subsequently, the force response of the connector deteriorates in accordance with Eq. (7.1):

$$F = F_{\text{eff}} \cdot (1 - d_{\text{evol}}) \tag{7.1}$$

where F_{eff} is the response of the connector without degradation and d_{evol} is the connector damage evolution variable.

This study develops a plastic motion-based damage model. Ductile fracture initiation is tracked using the cumulative plastic displacement $\overline{u}^{pl}$, which is defined by the elastic-plastic connector behaviour. The numerical study presented in Chapter 6 has shown that fracture initiation is primarily controlled by the equivalent plastic strain $\overline{\varepsilon}^{pl}$. Other variables, such as the stress triaxiality and the deviatoric parameter, were found constant at the fracture locations. Similarly to $\overline{\varepsilon}^{pl}$, $\overline{u}^{pl}$ is a scalar accumulation variable that continuously increases under cyclic loading. It should be noted that a cumulative plasticity-based damage criterion is not appropriate at the continuum level, since it would not reflect that fracture is inhibited when the material is in compression. However, considering the global symmetric response of the SSPs (where fracture develops independently from the sign of the applied displacement), this plastic motion-based criterion can be suitably used in a connector element for tracking

the effects of ductile fracture under cyclic loading.

The connector fracture model assumes that fracture initiates in a SSP when the condition in Eq. (7.2) is satisfied:

$$D_0 = \frac{\overline{u}^{pl}}{\overline{u}_0^{pl}} = 1 \tag{7.2}$$

where D_0 is the connector fracture initiation index, and $\overline{u}_0^{pl}$ is the equivalent relative plastic motion at fracture initiation.

The experimental tests have shown that, after fracture initiation, the force-carrying capacity of the SSPs undergoes a slow degradation, with a significant drop in strength occurring only few cycles before complete failure. This highlights the need of using a damage evolution law in combination with

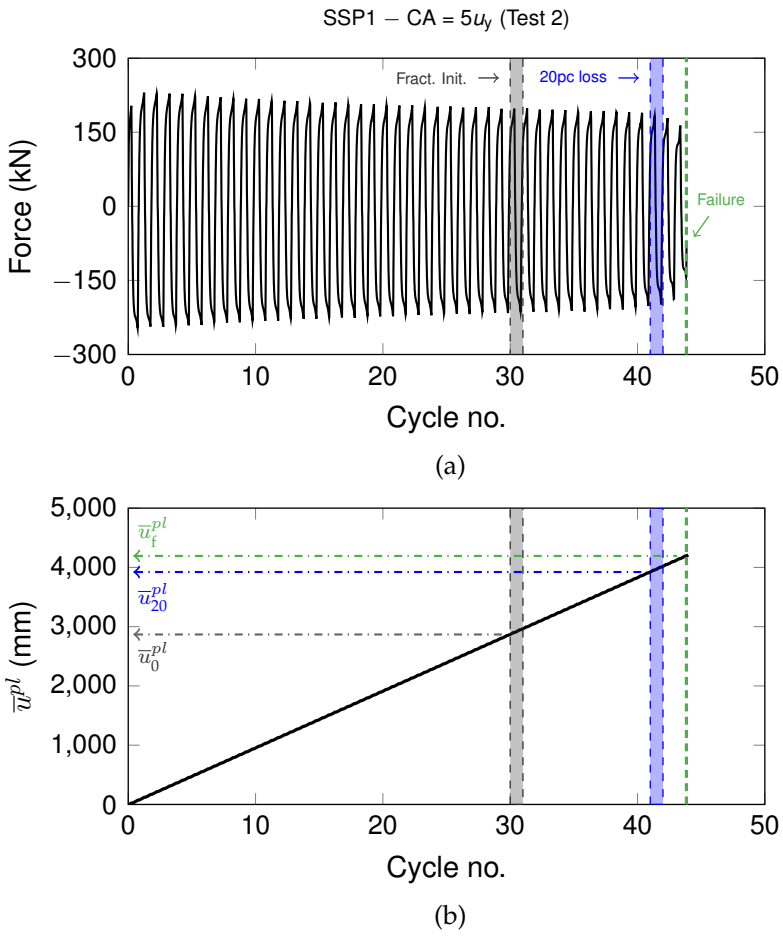

Figure 7.6. Connector damage calibration of SSP1 under CA = $5u_y$: (a) experimental force history; and (b) $\overline{u}^{pl}$ history extracted from connector analysis

Specimen	Test	Protocol		Fract. Init. ($d = 0$)		20pc strength loss ($d = 0.2$)		Failure ($d = 1$)	
				N_0 (no.)	$\overline{u}_0^{pl}$ (mm)	cycle (no.)	$\overline{u}_{20}^{pl}$ (mm)	cycle (no.)	$\overline{u}_{\mathrm{f}}^{pl}$ (mm)
SSP1	2	CA = $7u_{\mathrm{y}}$		21	3,006	27	3,911	28	4,180
	3	CA = $6u_{\mathrm{y}}$		25	2,945	34	4,053	35	4,256
	4	CA = $5u_{\mathrm{y}}$		31	2,868	42	3,922	44	4,194
	5	CA = $4u_{\mathrm{y}}$		43	2,924	73	5,016	78	5,381
	6	Random-1		35	2,800	58	4,907	59	5,030
	7	Random-2		25	3,106	44	4,357	45	4,480
			mean		2,942		4,340		4,587
			min		2,800		3,911		4,180
SSP2	10	CA = $8u_{\mathrm{y}}$		30	4,866	33	5,392	33	5,500
	11	CA = $7u_{\mathrm{y}}$		36	4,943	43	5,877	43	5,975
	12	CA = $6u_{\mathrm{y}}$		41	4,584	54	6,076	59	6,743
	13	CA = $5u_{\mathrm{y}}$		45	3,919	68	5,971	76	6,712
	14	CA = $4u_{\mathrm{y}}$		54	3,457	83	5,352	89	5,797
	15	Random		40	4,889	46	5,479	49	5,855
			mean		4,443		5,691		6,097
			min		3,457		5,352		5,500

Table 7.2. Summary of the connector fracture behaviour parameters for SSP1 and SSP2

the aforementioned initiation criterion. A plastic motion-based damage evolution criterion is defined as a tabular function of the difference between the equivalent plastic displacements at failure ($\overline{u}_{\mathrm{f}}^{pl}$) and fracture initiation ($\overline{u}_0^{pl}$). To accurately trace the degradation of the force response of the SSPs, the difference between $\overline{u}_{\mathrm{f}}^{pl}$ and the plastic displacement corresponding to a 20% loss in the force-carrying capacity, indicated as $\overline{u}_{20}^{pl}$, is also specified.

The connector damage behaviour is calibrated against the experimental data. The $\overline{u}^{pl}$ values at the considered three limit states are identified for each test by extracting the history of the corresponding output variable, denoted as CUPEQ in Abaqus, from the connector analyses performed in Section 7.3.1. The calibration of the damage parameters for SSP1 under CA = $5u_{\mathrm{y}}$ is shown in Figure 7.6, where Figure 7.6a illustrates the experimental force history, with indication of the three fracture stages, i.e., cycle no. 31, no. 42 and no. 44 for fracture initiation, 20 per cent strength loss, and failure, respectively. The $\overline{u}^{pl}$ history from the connector

analysis, shown in Figure 7.6b, provides the corresponding $\overline{u}^{pl}$ values at the three stages, i.e., $\overline{u}_0^{pl}$ = 2,868 mm, $\overline{u}_{20}^{pl}$ = 3,922 mm, and $\overline{u}_f^{pl}$ = 4,194 mm. The $\overline{u}^{pl}$ values for all the remaining cyclic tests, including the random tests, are summarised in Table 7.2. It can be observed that the SSP2 has greater mean $\overline{u}^{pl}$ values than the other geometry, as a result of its larger fracture capacity.

A comparison between the experimental and connector force histories for all the tests on the SSPs is made using the calibrated fracture parameters. Figures

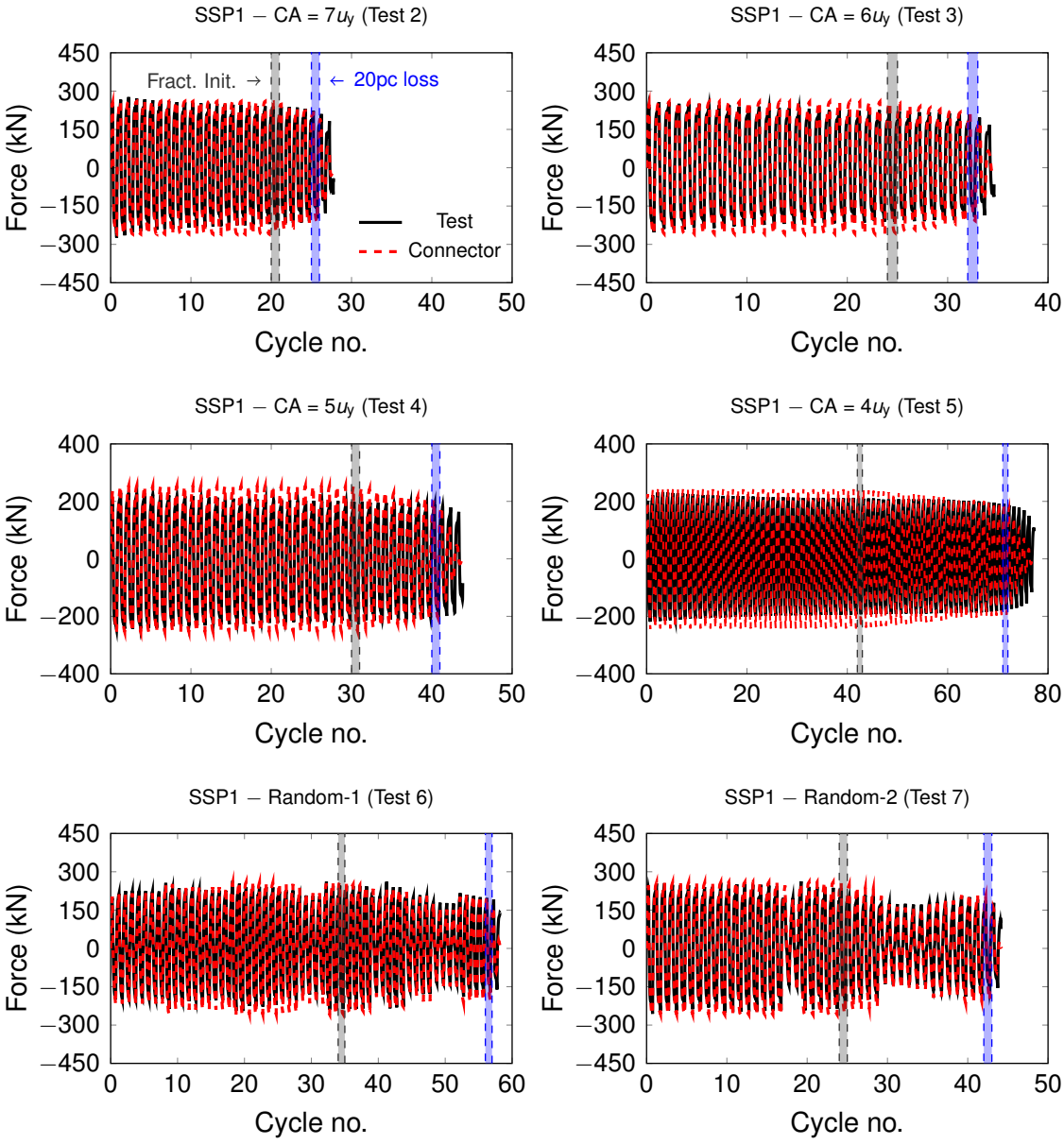

Figure 7.7. Experimental and connector model comparison of force responses of SSP1 tests

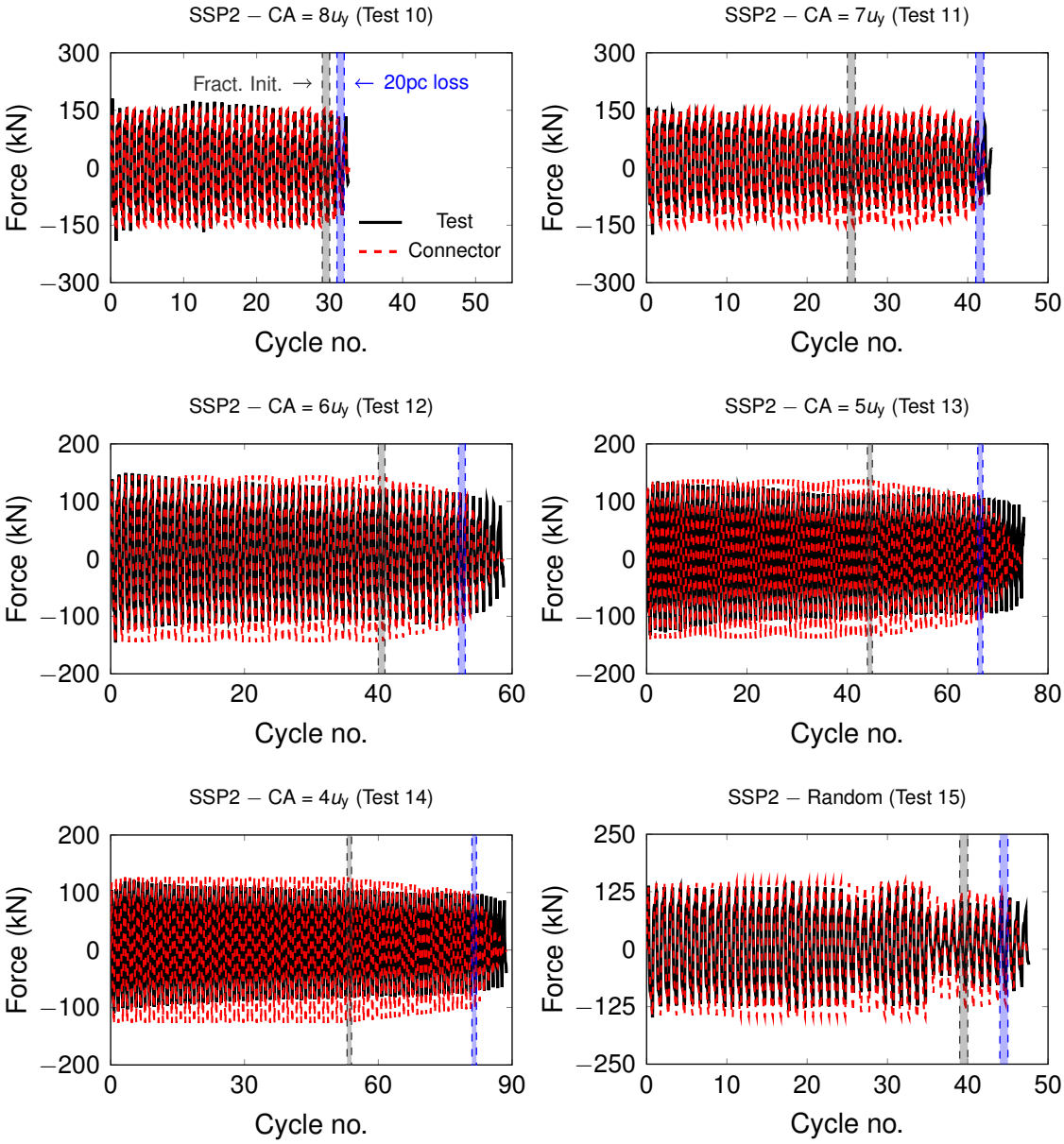

Figure 7.8. Experimental and connector model comparison of force responses of SSP2 tests

7.7 and 7.8 show the comparison between the experimental and numerical force histories for all the tests on SSP1 and SSP2, respectively, with indication of fracture initiation and 20% strength loss. The excellent agreement shows that the calibrated connector elements are capable of accurately tracing the degradation in the force response of SSPs due to ductile fracture.

Figure 7.9 plots the plastic motion laws for all the tests, where $d_{\text{evol}} = 0$ until fracture initiation, and $d_{\text{evol}} = 1$ at failure. The obtained $\overline{u}_0^{pl}$ values provide an indicative range for the fracture capacity of the SSPs under ULCF. It can be

noted that, while the $\overline{u}_0^{pl}$ values for SSP1 fall into a relatively small range, a larger deviation from the mean value is observed for the $\overline{u}_0^{pl}$ values of SSP2. A similar scatter is found for the $\overline{u}_{20}^{pl}$ and $\overline{u}_{\mathrm{f}}^{pl}$ values. Based on these results, the minimum $\overline{u}^{pl}$ values are conservatively used for the collapse assessment of the CBF-MRF.

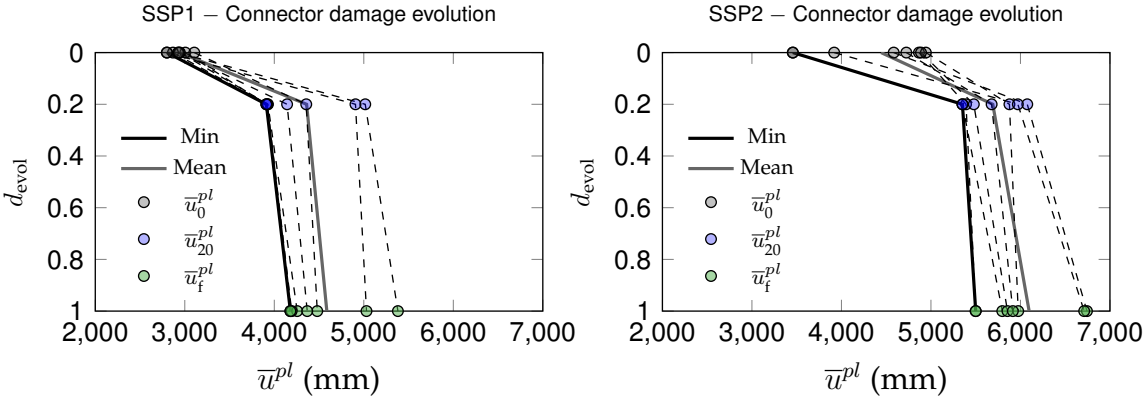

Figure 7.9. Calibrated fracture evolution laws for connectors

7.4 Incremental Dynamic Analysis (IDA)

In the last two decades, IDA has been widely used to quantify the seismic collapse potential of structures (Lin & Baker 2013). IDA is a parametric method involving nonlinear dynamic analyses of a structure under a suite of ground motion records, each scaled to increasing intensities until the occurence of global dynamic collapse (Vamvatsikos & Cornell 2002). IDA has been adopted in the U.S. FEMA 350 (2000) and FEMA P695 (2008) guidelines, which recommend to use the first-mode spectral acceleration $S_{\mathrm{a}}(T_1)$ as the seismic intensity measure (IM). In this work, the response of the structure is monitored by the maximum peak inter-storey drift $\theta_{\mathrm{s,max}}$, which is the engineering demand parameter (EDP).

IDA are performed using the revised simplified model described earlier in this chapter. The same modelling technique of the nonlinear dynamic analysis, presented in Section 4.5.1, is adopted.

7.4.1 Ground motions

IDA employs the set of 22 ground motion records from FEMA P695 (2008) previously used for the dynamic analyses in Chapter 4. Two additional records

are selected from Ruiz-Garcia (2010) to study the influence of ground motion duration on the dynamic response of the CBF-MRF, as discussed in Section 7.4.3. The 24 ground motions used for IDA are listed in Table 7.3.

To reduce the computational effort, $S_{\mathrm{a}}(T_1)$ is systematically scaled up in increments equal to $0.5S_{\mathrm{a,MCE}}(T_1)$, i.e., half the intensity at the MCE hazard level. For the dual CBF-MRF, $S_{\mathrm{a,MCE}}(T_1)$ = 1.04 g. To investigate the response near to collapse, smaller increments are applied.

Source	No.	Earthquake	Year	M	Recording Station	D_{5-95} (s)
FEMA P695 (2008)	1	Northridge, US	1994	6.7	Beverly Hills	9.2
	2	Northridge, US	1994	6.7	Canyon Country	6.2
	3	Duzce, Turkey	1999	7.1	Bolu	8.5
	4	Hector Mine, US	1999	7.1	Hector	11.6
	5	Imperial Valley, US	1979	6.5	Delta	51.7*
	6	Imperial Valley, US	1979	6.5	El Centro Array 11	7.8
	7	Kobe, Japan	1995	6.9	Nishi-Akashi	9.7
	8	Kobe, Japan	1995	6.9	Shin-Osaka	10.0
	9	Kocaeli, Turkey	1999	7.5	Duzce	11.7
	10	Kocaeli, Turkey	1999	7.5	Arcelik	11.0
	11	Landers, US	1992	7.3	Yermo Fire St.	17.5
	12	Landers, US	1992	7.3	Coolwater	17.2
	13	Loma Prieta, US	1989	6.9	Capitola	12.0
	14	Loma Prieta, US	1989	6.9	Gilroy Array 3	6.5
	15	Manjil, Iran	1990	7.4	Abbar	28.8*
	16	Superstition Hills, US	1987	6.5	El Centro Imp. Co.	15.0
	17	Superstition Hills, US	1987	6.5	Poe Road	13.8
	18	Cape Mendocino, US	1992	7.0	Rio Dell Overpass	15.3
	19	Chi-Chi, Taiwan	1999	7.6	CHY101	30.0*
	20	Chi-Chi, Taiwan	1999	7.6	TCU045	11.3
	21	San Fernando, US	1971	6.6	LA Hollywood Stor	10.7
	22	Friuli, Italy	1976	6.5	Tolmezzo	4.2
Ruiz-Garcia (2010)	23	Valparaiso, Chile	1985	8	El Amendral 50	48.5*
	24	Michoacan, Mexico	1976	8	La Villita 90	42*

* = long significant duration ground motion

Table 7.3. Ground motion records employed for IDA

7.4.2 IDA results

The collapse evaluation of the dual CBF-MRF subjected to 24 ground motions involved over 250 analyses. Detailed results of the response of the dual CBF-MRF at collapse for each ground motion are attached in Appendix D.

The IDA results for the 1979 Imperial Valley earthquake (no. 5 record) are presented below. Figure 7.10a shows the IDA curve for the considered ground motion, where each data point represents the $S_{\text{a}}(T_1)$ normalised to $S_{\text{a,MCE}}(T_1)$ and the recorded $\theta_{\text{s,max}}$. Straight lines are drawn between consecutive point data. The slope of the line between the origin and the first point defines the elastic stiffness of the IDA curve. Up to an intensity of $6S_{\text{a,MCE}}(T_1)$, the response of the CBF-MRF is elastic. Then, the curve rapidly flattens out and reaches a plateau at an intensity level of $6.5S_{\text{a,MCE}}(T_1)$, indicating dynamic instability of the structure. Figures 7.10b-d show θ_{s} time histories of the CBF-MRF under the same record scaled to 6, 6.5 and 7 times $S_{\text{a,MCE}}(T_1)$, respectively. The sequence of ductile fracture of the SSPs is illustrated in terms of fracture initiation and failure. It can be seen that ten out of twelve connectors reach fracture initiation, and this occurs more rapidly as the intensity increases. As a result, the number of connectors reaching failure increases from two at $6S_{\text{a,MCE}}(T_1)$ to eight at $7S_{\text{a,MCE}}(T_1)$. Under the highest intensity, the progressive failure of the SSPs accelerates the dynamic instability of the structure.

The occurrence of ductile fracture of the twelve connectors of the frame under $7S_{\text{a,MCE}}(T_1)$ intensity is shown in Figure 7.11a. The notation for each connector refers to the storey and bracing member where the SSPs are placed in the CBF-MRF (e.g., 3R is the right brace at the third storey). It can be observed that fracture initiation and failure occur first in the SSPs placed at the fourth and sixth storeys. The $\overline{u}^{pl}$ histories for all the connectors (Figure 7.11b) show that failure is reached in all the connectors at the top four storeys, while the SSPs at the bottom of the structure (at the first and second storeys) are less subject to ductile fracture. It can also be observed how connectors at the same storey reach failure at different stages. For instance, connector 4R fails much earlier than the left one (4L), which continues to withstand cycles until near collapse, as shown by the comparison of their hystereses in Figures 7.11c and d.

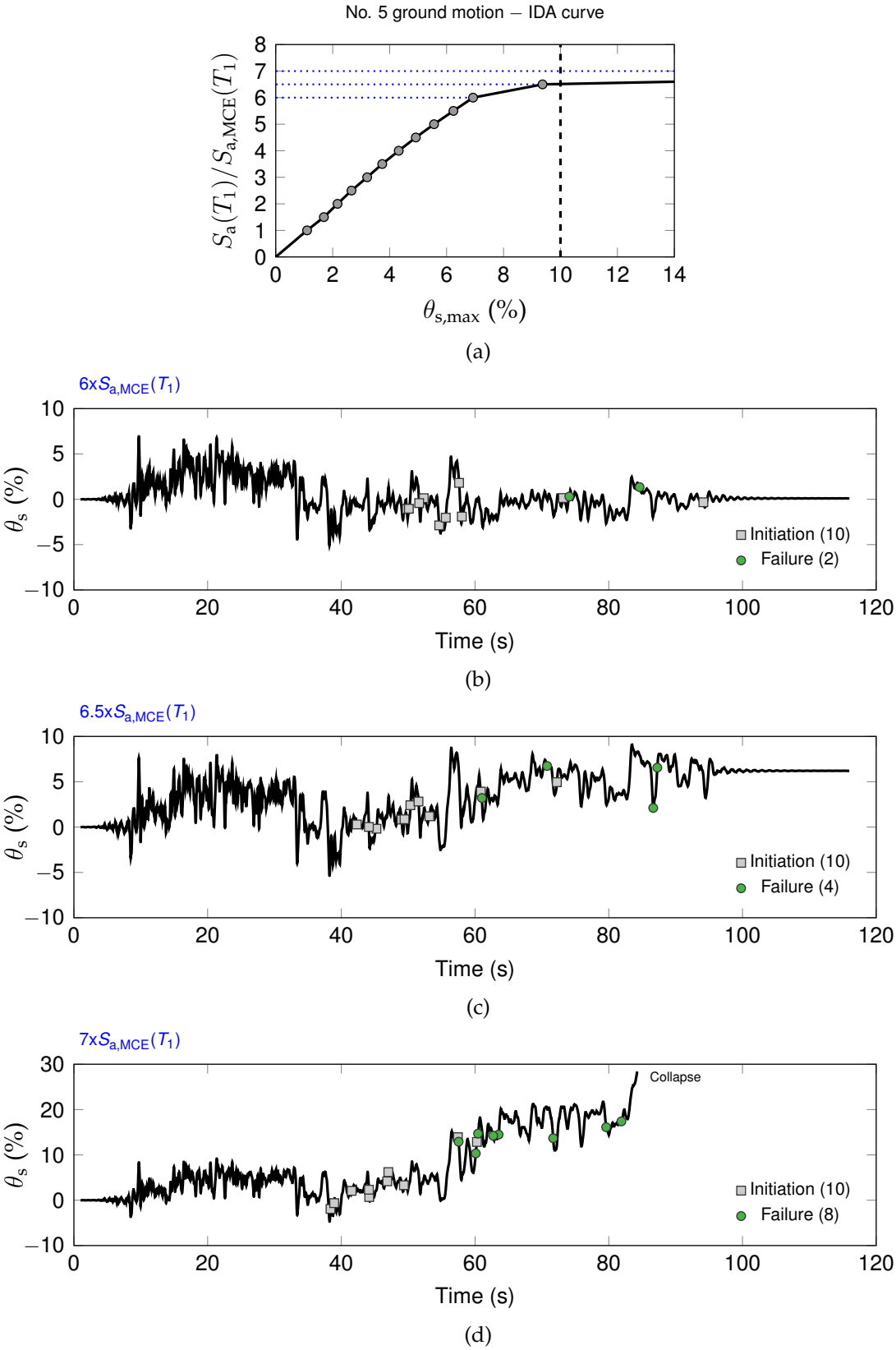

Figure 7.10. Ground motion no. 5: (a) IDA curve; (b-d) maximum peak inter-storey drift time histories at increasing intensities with occurrence of connector fracture

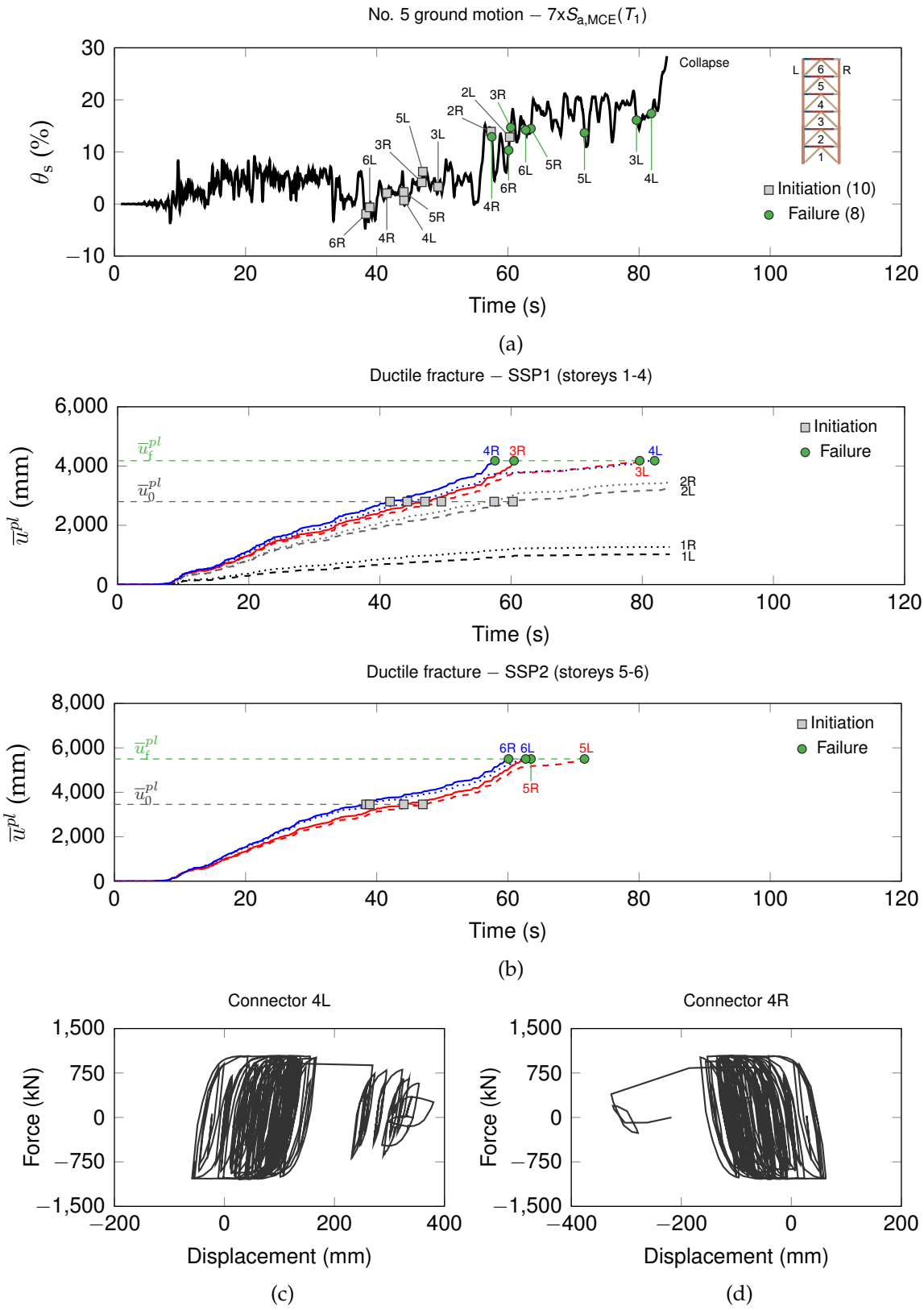

Figure 7.11. Ground motion no. 5 scaled to $7S_{a,MCE}(T_1)$: (a) fracture evolution in the connectors; (b) $\overline{u}^{pl}$ histories for the twelve connectors of the CBF-MRF; (c) and (d) hystereses of the left and right connectors at the fourth storey

To determine the collapse intensity $S_{a,col}(T_1)$ for each of the 24 ground motions, a combination of collapse capacity criteria is used. Generally, these criteria can be either IM- or EDP-based (Vamvatsikos & Cornell 2002). This study employs the following limit state rules that are also adopted in FEMA 350 (2000):

- The 20% tangent slope approach (IM-based rule): dynamic instability is incipient when the slope of the line between two consecutive $\theta_{s,max} - S_a(T_1)$ data points is less than 20% of the elastic stiffness. $S_{a,COL}(T_1)$ is identified with the lowest $S_a(T_1)$ point of this line.
- $\theta_{s,max} = 10\%$ (EDP-based rule): beyond this limit, it is assumed that any structural system would experience severe damage leading to global instability. This drift limit has been adopted also for BRBFs (Ariyaratana & Fahnestock 2011).

For instance, under no. 5 ground motion (Figure 7.10a), the lowest $S_{a,MCE}(T_1)$ at the plateau of the IDA curve is $6.5S_{a,MCE}(T_1)$. At this intensity, the associated $\theta_{s,max}$ is just below 10%, indicating that, between the two limit state rules, the IM-based criterion is met first, i.e., $S_{a,col}(T_1) = 6.5S_{a,MCE}(T_1)$.

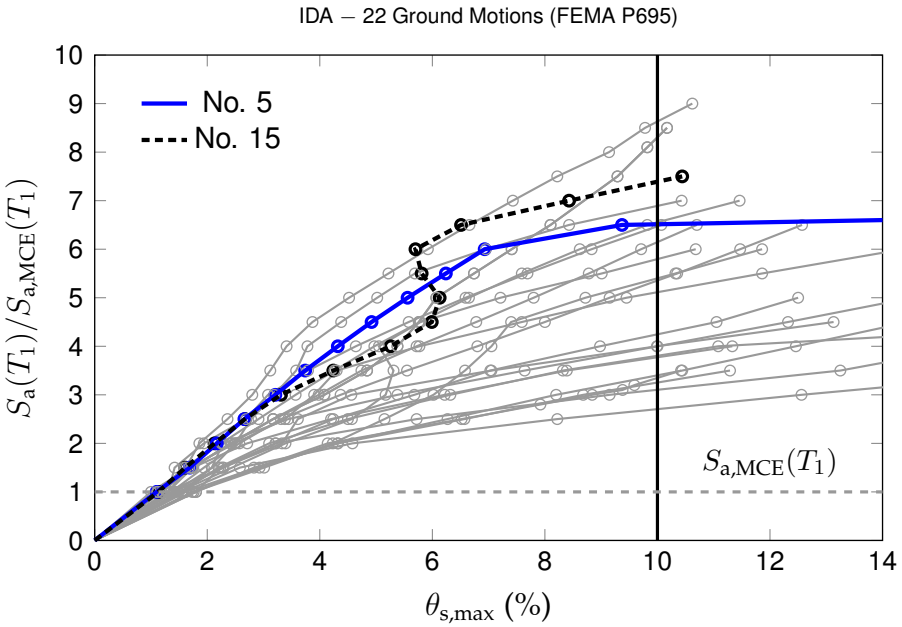

Figure 7.12. IDA curves of CBF-MRF for 22 FEMA ground motions

Source	No.	Earthquake	$S_{\text{a,col}}$		$D_{0,col}$
			(g)	($\times S_{\text{a,MCE}}$)	
FEMA P695 (2008)	1	Northridge, US	5.564	5.355	0.45
	2	Northridge, USA	3.535	3.402	0.20
	3	Duzce, Turkey	6.387	6.147	0.39
	4	Hector Mine, US	4.158	4.002	0.39
	5	Imperial Valley, US	6.750	6.500	1.00
	6	Imperial Valley, US	3.921	3.774	0.38
	7	Kobe, Japan	5.313	5.114	0.50
	8	Kobe, Japan	4.156	4.000	0.26
	9	Kocaeli, Turkey	3.230	3.104	0.22
	10	Kocaeli, Turkey	6.724	6.472	0.42
	11	Landers, US	2.810	2.705	0.30
	12	Landers, US	6.810	6.555	0.58
	13	Loma Prieta, US	8.630	8.306	0.60
	14	Loma Prieta, US	7.160	6.893	0.52
	15	Manjil, Iran	7.679	7.391	0.82
	16	Superstition Hills, US	6.026	5.800	0.33
	17	Superstition Hills, US	3.953	3.805	0.50
	18	Cape Mendocino, US	5.611	5.400	0.38
	19	Chi-Chi, Taiwan	4.410	4.247	0.64
	20	Chi-Chi, Taiwan	3.380	3.253	0.24
	21	San Fernando, US	3.480	3.349	0.35
	22	Friuli, Italy	8.632	8.970	0.40
Ruiz-Garcia (2010)	23	Valparaiso, Chile	5.710	5.500	1.00
	24	Michoacan, Mexico	2.670	2.572	0.60

Table 7.4. Summary of IDA results for the dual CBF-MRF

A summary of the CBF-MRF collapse performance is provided in Table 7.4 for the 24 ground motions. The IDA curves for the 22 ground motions from FEMA P695 (2008) are shown in Figure 7.12, where a large variability in the dynamic structural response can be observed. Under most of the ground motions, the IDA curve has an initial linear elastic region, followed by a softening up to the $\theta_{\text{s,max}} = 10\%$ limit. In many cases the IDA curve terminates once the collapse EDP-based capacity rule is reached.

The dashed curve in Figure 7.12, corresponding to ground motion no. 15, shows a typical twisting behaviour characterised by alternating hardening and softening regions, where the local stiffness of the curve increases or decreases

with higher intensities (Vamvatsikos & Cornell 2002). The θ_s time histories of the CBF-MRF under this specific ground motion (no. 15) scaled up to increasing intensities are shown in Figure 7.13. It can be seen that the collapse direction of the frame gradually moves from negative to positive θ_s values, resulting in the hardening of the IDA curve.

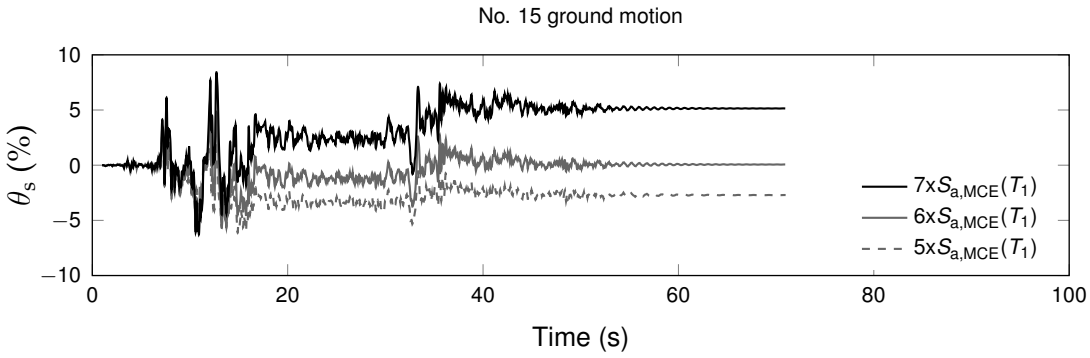

Figure 7.13. Storey drift time histories under no. 15 ground motion scaled to increasing intensities

The mechanism of the friction pad (FP) activation is shown in Figure 7.14 for no. 2 ground motion scaled to $3.5S_{a,MCE}(T_1)$. From t = 5 s, the frame is subjected to large drifts (Figure 7.14a), causing the FP to be activated multiple times. Figure 7.14b highlights the activation of the FPs in the left brace at the fourth floor (4L), showing the displacement histories of the individual SSPs and FP in separate graphs. The maximum FP elongation, denoted as $u_{FP,max}$, is about 125 mm. Details of the $u_{FP,max}$ values recorded at collapse for each ground motion can be found in Appendix D. Overall, $u_{FP,max}$ is found to be in the range of 150-200 mm. Figures 7.14c and d show the hystereses of the combined SSPs and FP, and of the individual SSPs. It can be observed that the FP prevents the SSPs from undergoing excessive displacements, indicating that the SSPs are subjected to cyclic loading conditions similar to those imposed in the experimental tests. This confirms that the cyclic tests on SSPs are appropriate for the calibration of the connector damage criterion for ULCF.

To characterise the scale of fracture reached in the SSPs under the earthquake records, a fracture initiation index at collapse $D_{0,col}$ is calculated, as the ratio between the $\overline{u}^{pl}$ recorded at collapse and the corresponding $\overline{u}_0^{pl}$. In Abaqus, the connector output corresponding to D_0 is denoted as CDIP. The results for the 24 ground motions are provided in Table 7.4. $D_{0,col}$ is below 1 for all the records,

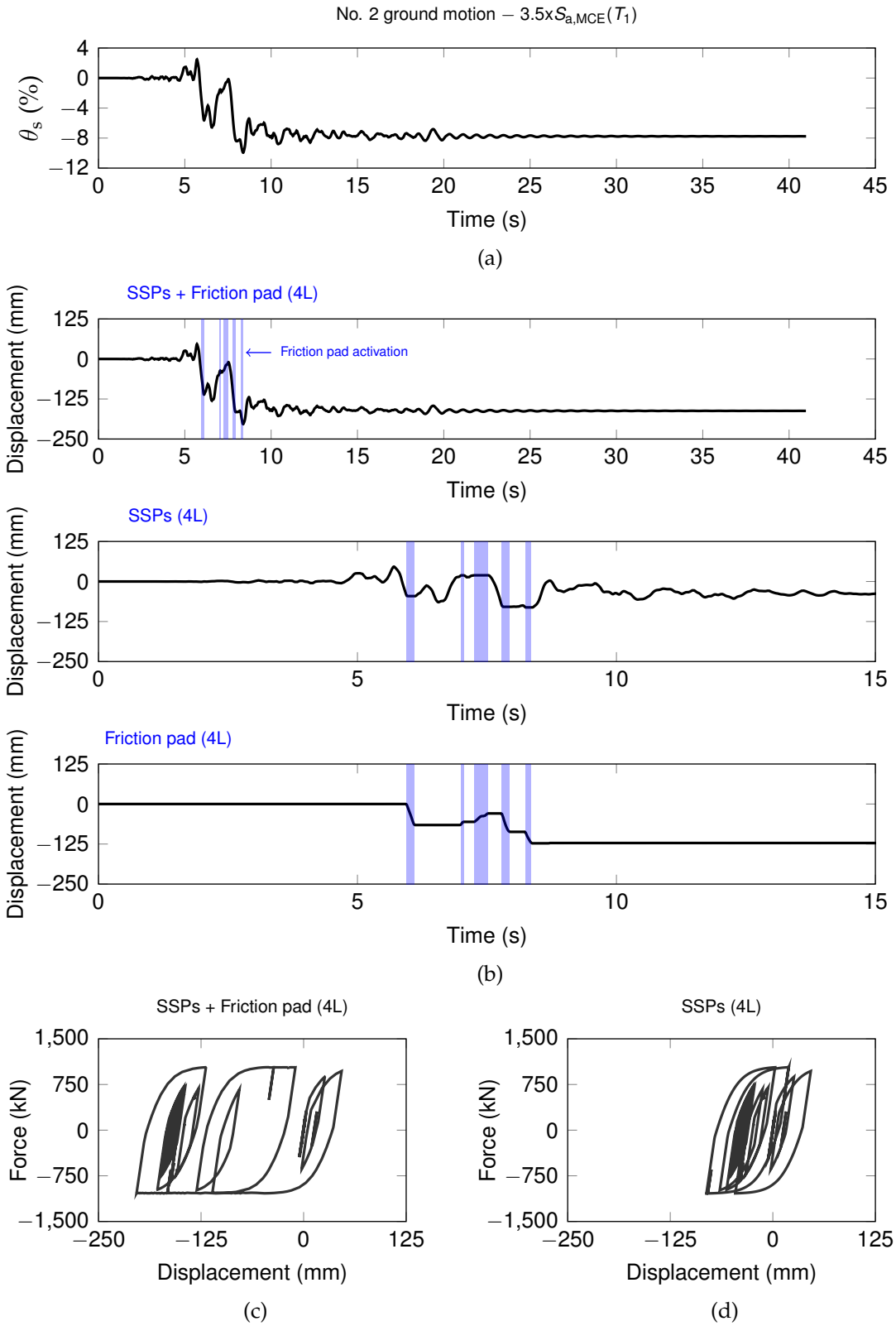

Figure 7.14. Ground motion no. 2: (a) maximum peak inter-storey drift time history; (b) axial displacement history of the left hand side brace at the fourth storey (4L), combining the SSPs and friction pad; (c) hysteresis of 4L; and (d) hysteresis of the SSPs

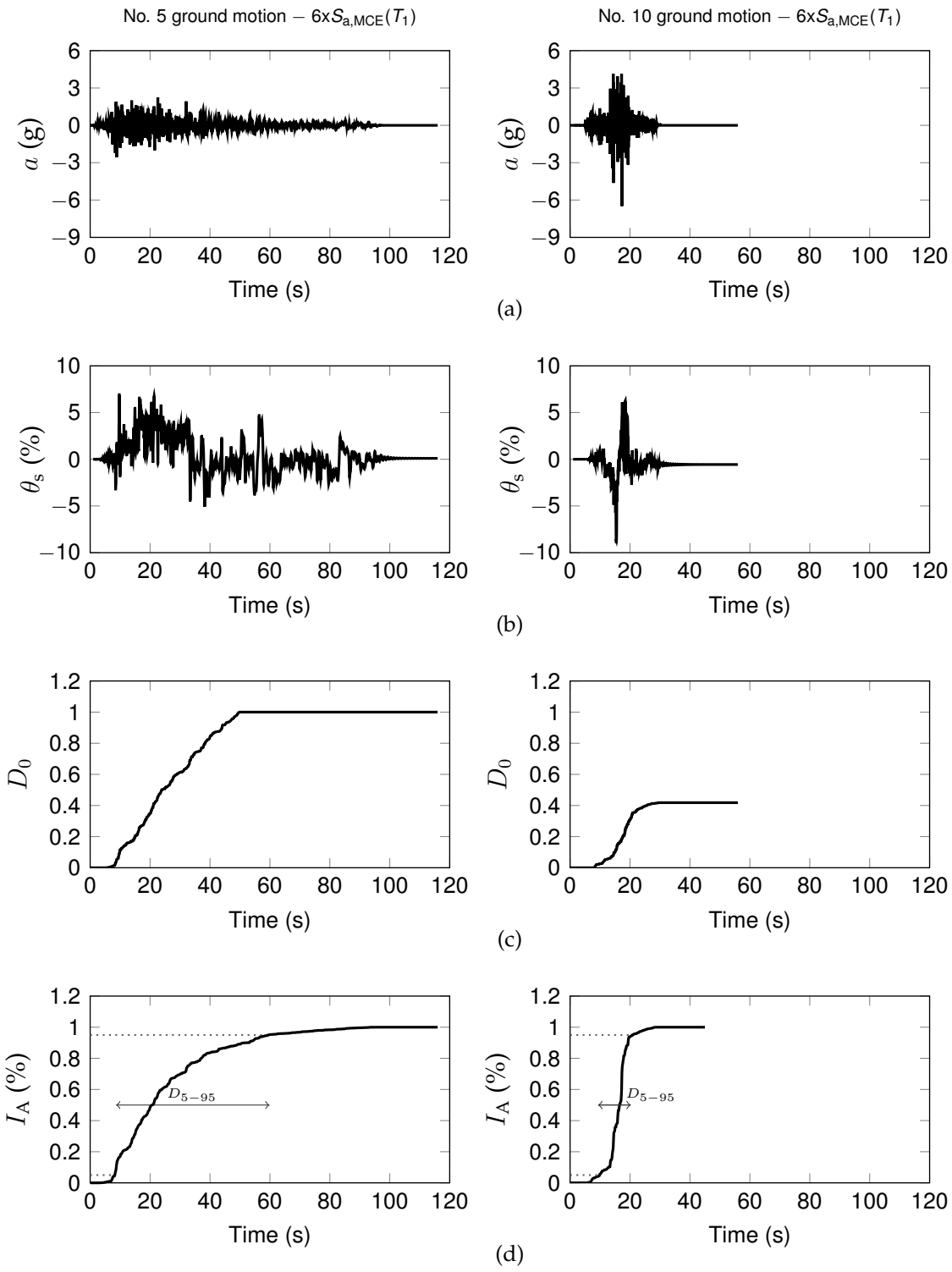

Figure 7.15. Comparison of no. 5 and 10 records scaled at $6S_{a,MCE}(T_1)$: (a) accelerograms ; (b) peak inter-storey drift time history; (c) damage initiation index time history; and (d) Arias intensity time history, with indication of significant motion duration parameter (D_{5-95})

with the exception of no. 5 ground motion from the FEMA database, and no. 23 ground motion from Ruiz-Garcia (2010). This indicates that fracture initiation, i.e., $D_{0,\text{col}} = 1$, occurs only under two out of the 24 ground motions.

It can also be observed that, under no. 5 and no. 10 records, the CBF-MRF shows a similar collapse capacity, but different safety margins against fracture, being $D_{0,\text{col}} = 1$ and 0.45, respectively. Figure 7.15a plots the record accelerograms scaled to $6S_{\text{a,MCE}}(T_1)$ and the corresponding θ_s and D_0 time histories are shown in Figures 7.15b and c. Although the peak drifts are greater under no. 10 ground motion, no. 5 record determines a larger cyclic energy dissipation, leading to fracture of the SSPs. For no. 10 record, the reduced D_0 value is due to the FP activation and shorter ground motion duration. This comparison shows how the ground motion duration can have an influence on the fracture of the SSPs. This correlation is further discussed in the section below.

7.4.3 Influence of significant ground motion duration

Recent studies have shown that the nonlinear response of structural systems subjected to cumulative damage is affected by ground motion duration-related parameters (Iervolino et al. 2006, Tsioulou & Galasso 2015). Different approaches can be used to evaluate duration. A widely-accepted parameter is the significant motion duration, proposed by Trifunac & Brady (1975), and defined as the time interval during which a certain amount of energy is dissipated (Kempton & Stewart 2006). Energy is measured using the Arias intensity I_A (Arias 1970), defined as:

$$I_\text{A} = \frac{\pi}{2g} \int_0^{t_\text{E}} a^2(t)\,\text{d}t \tag{7.3}$$

where $a(t)$ is the acceleration time history, and t_E is the total ground motion duration. A commonly-used significant motion duration parameter is D_{5-95}, which is defined as the time interval between the 5% and 95% of I_A.

The D_{5-95} figures obtained for all the 24 ground motions are listed in Table 7.3. Following the approach proposed by Ruiz-Garcia (2010), records are classified in short duration, i.e., D_{5-95} = 0−17.5 s, and long duration, i.e., D_{5-95} = 28.8−51.7 s. Out of the 22 records selected from FEMA P695 (2008), three are long duration motions and the remaining are short duration, while the two

additional records from Ruiz-Garcia (2010) are both long duration. The I_A time histories for no. 5 and no. 10 ground motions (i.e., long and short duration earthquakes, respectively) are shown in Figure 7.15d. Comparison of Figure 7.15c and d highlights the close correlation between the D_0 and I_A, demonstrating that both parameters are indicators of cyclic energy dissipation.

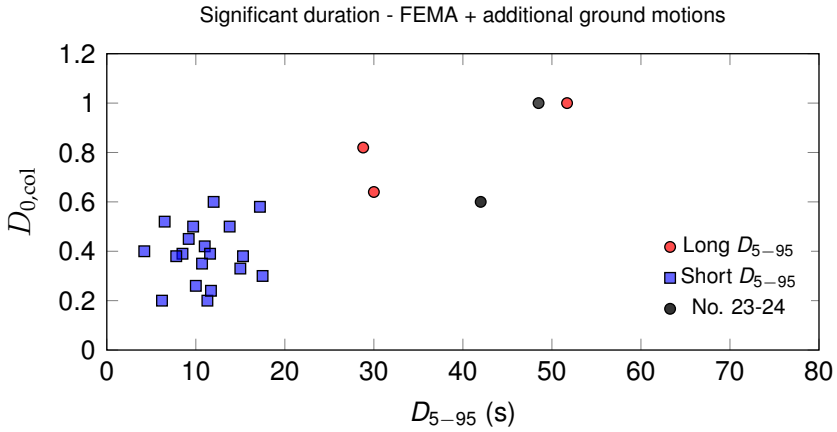

Figure 7.16. Significant motion duration vs. ductile fracture initiation index relationship for 22 FEMA ground motions and two additional records (no. 23 and 24) from Ruiz-Garcia (2010)

The distribution of the $D_{5-95} - D_{0,col}$ parameters, plotted in Figure 7.16, shows a large record-to-record variability. It can be observed that, while $D_{0,col}$ values for short records are in the range of $0.2-0.6$, long duration earthquakes determine a much smaller safety margin against fracture, where the corresponding $D_{0,col}$ is in the range $0.6-1$. This confirms that ductile fracture of SSPs is more likely to occur under earthquakes having long significant duration.

To further investigate the sensitivity of SSP fracture to significant motion duration, the CBF-MRF is subjected to the two additional long duration earthquakes, i.e, Valparaiso (no. 23) and Michoacan (no. 24). These records are among the longest ground motions used by Ruiz-Garcia (2010) in his study on the influence of significant duration on residual displacement demands. Figure 7.17a shows their accelerograms at collapse. From the corresponding I_A time histories, plotted in Figure 7.17b, it is found that D_{5-95} is equal to 48.5 s and 42 s for no. 23 and no. 24 records, respectively.

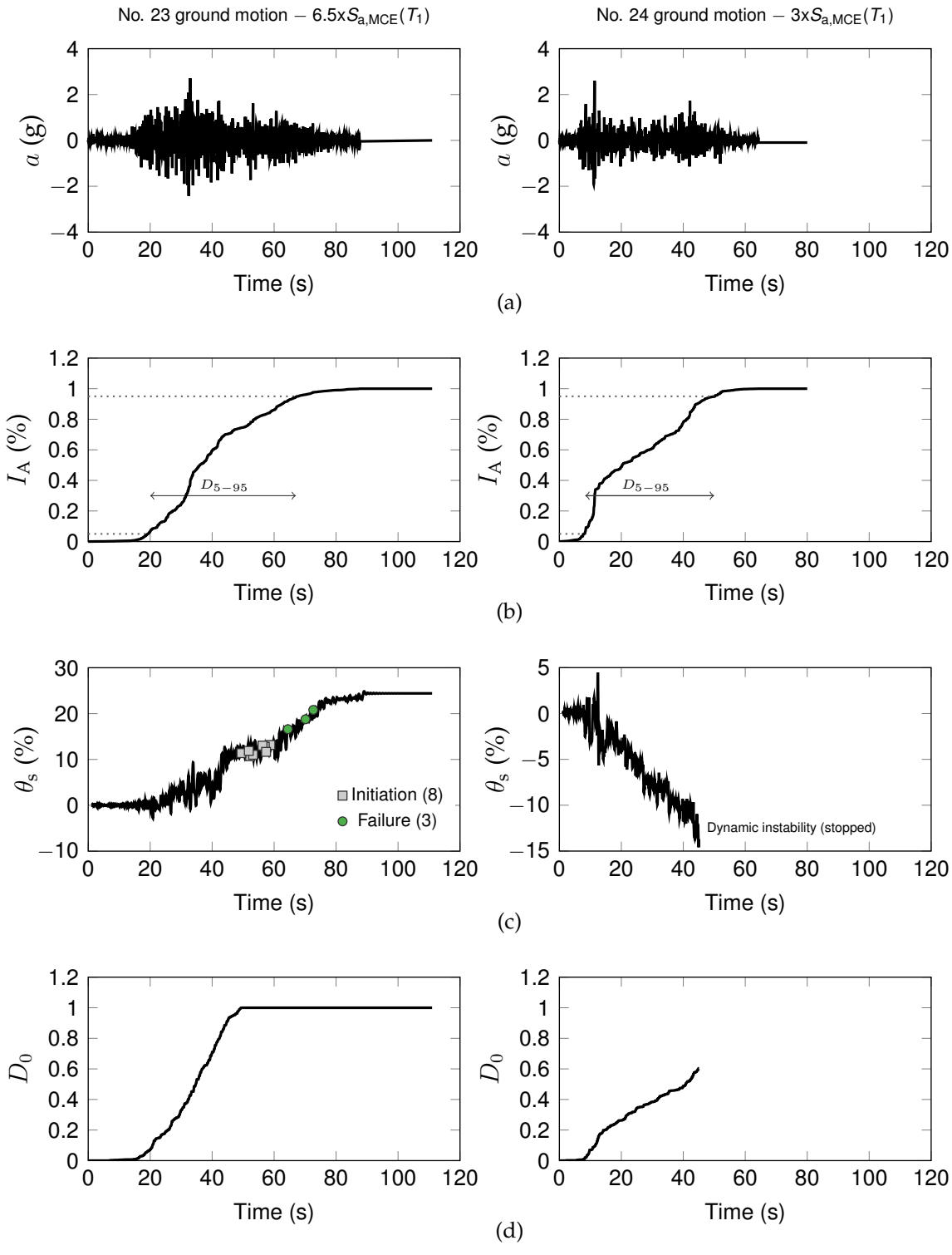

Figure 7.17. Comparison of no. 23 and no. 24 records at collapse: (a) accelerograms; (b) Arias intensity time history, with indication of significant motion duration parameter (D_{5-95}); (c) peak inter-storey drift time history; and (d) damage initiation index time history

A comparison between the IDA curves for these two long duration ground motions, and the 22 FEMA records is shown in Figure 7.18. The relative θ_s time histories of the CBF-MRF at collapse are illustrated in Figure 7.17c, and the evolution of D_0 for the connectors having the largest recorded $\overline{w}^{pl}$ value is shown in Figure 7.17d. The analysis of no. 24 record scaled to $3S_{a,MCE}(T_1)$ is prematurely terminated at large drifts due to the occurrence of numerical errors. It can be observed that the CBF-MRF undergoes collapse without fracture initiation in any connector. The associated $D_{0,col}$ value of 0.6 corresponds to the lower limit in the range identified for long duration earthquakes, as illustrated in Figure 7.16. Under the no. 23 ground motion, the IDA curve flattens at $5.5S_{a,MCE}(T_1)$, where the IM-based rule is met. The collapse mechanism shown at $6.5S_{a,MCE}(T_1)$ intensity (Figure 7.17c) involves the deterioration of eight connectors modelling the SSPs, three of which eventually fail.

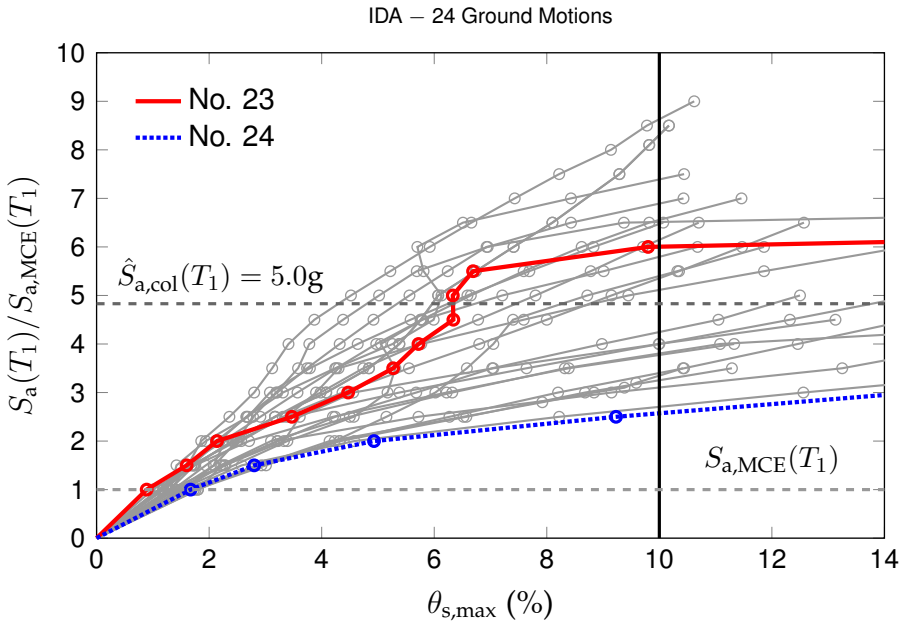

Figure 7.18. IDA curves of CBF-MRF for 24 ground motions, highlighting no. 23 and no. 24 records

7.4.4 Collapse fragility curve

The IDA results are used to produce a probabilistic evaluation of the collapse capacity of the CBF-MRF. The $S_{a,COL}(T_1)$ values (listed in Table 7.4) are ranked in ascending order, and are assigned the same chance of occurrence (Seo et al. 2014). The resulting probability of collapse versus ground motion intensity

$S_{\text{a}}(T_1)$ relationship for the 24 ground motions is plotted as point data in Figure 7.19. A collapse fragility curve is then constructed by fitting a lognormal distribution through the $S_{\text{a,COL}}(T_1)$ values (FEMA P695 2008). The median collapse intensity, denoted as $\hat{S}_{\text{a,col}}(T_1)$, which corresponds to a 50% collapse probability, is found equal to 5.0g. Therefore, the safety margin against collapse of the CBF-MRF, denoted as CMR and defined as the ratio of $\hat{S}_{\text{a,col}}(T_1)$ to $S_{\text{a,MCE}}(T_1)$, is equal to 4.81.

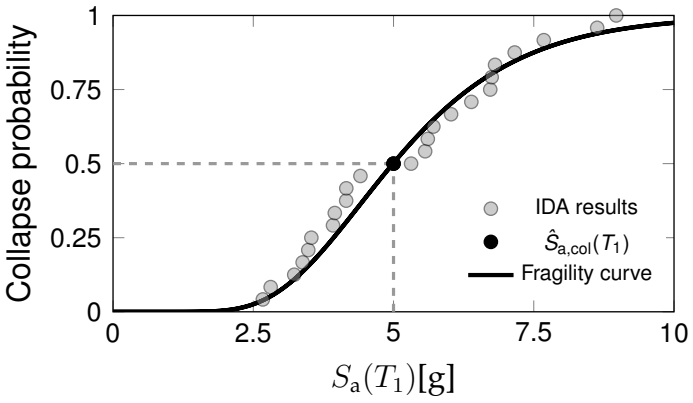

Figure 7.19. Collapse fragility curve of the CBF-MRF (fitted through IDA results)

The slope of the fragility curve is defined by the lognormal standard deviation β_{RTR}, which represents the record-to-record uncertainty. The fragility curve fitted through the IDA results has β_{RTR} = 0.35, which is in line with the range 0.2−0.4 indicated by FEMA P695 (2008). However, further sources of uncertainty should be accounted for. FEMA P695 (2008) defines different lognormal deviation parameters that account for the uncertainties related to the numerical modelling β_{MDL}, design requirements β_{DR}, and test data β_{TD}. By assuming that all these uncertainties are statistically independent, the total collapse uncertainty β_{tot} is given by Eq. (7.4):

$$\beta_{\text{tot}} = \sqrt{\beta_{\text{RTR}}^2 + \beta_{\text{MDL}}^2 + \beta_{\text{DR}}^2 + \beta_{\text{TD}}^2} \tag{7.4}$$

where the values of β_{MDL}, β_{DR}, and β_{TD} are conservatively assumed equal to 0.35, corresponding to a fair quality rating for numerical modelling, design requirements, and test data. As a result, β_{tot} = 0.7, which is consistent with the range identified by studies on modelling uncertainty (Tzimas et al. 2016, Liel et al. 2009). Figure 7.20 illustrates the collapse probability for $S_{\text{a,COL}}(T_1)$ values

normalised by $S_{a,MCE}(T_1)$, using β_{RTR} and β_{tot}. Based on the fragility curve with β_{tot}, the CBF-MRF has 1.2% collapse probability at the MCE level, which is largely below the 10% probability limit defined by FEMA P695 (2008). This indicates an excellent collapse performance of the proposed dual CBF-MRF, meeting the objective of seismic resilience.

The fragility curves in Figs. 7.19 and 7.20 do not account for the spectral shape of the ground motions, which has been shown to influence the collapse assessment (Baker & Cornell 2008). To investigate the impact of spectral shape characteristics on the collapse response of the dual CBF-MRF, the far-field ground motion set should be adjusted following the methodolgy recently proposed in Haselton et al. (2011).

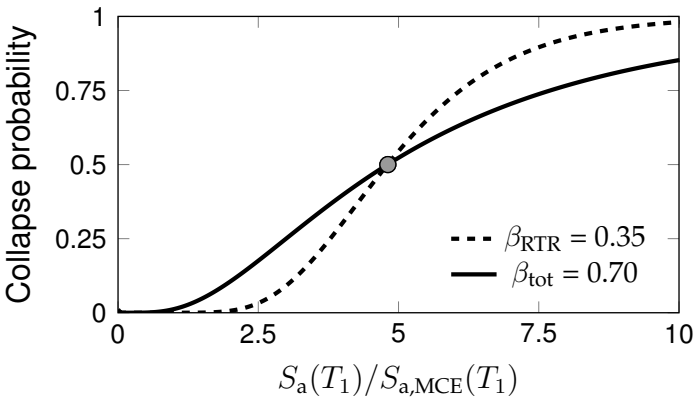

Figure 7.20. Collapse fragility curve of the CBF-MRF relative to record-to-record variability (β_{RTR}) and to total collapse uncertainty (β_{tot})

7.4.5 Connector fracture model versus OpenSees fatigue model

The accuracy of the connector fracture model employed for IDA is assessed against the fatigue material model available in OpenSees (Mazzoni et al. 2006). The fatigue material is a phenomenological model that simulates the effects of LCF. It was developed by Uriz (2005) to simulate damage in fiber elements modelling steel braces. In fact, it can also be used to trace damage in nonlinear spring elements that use a force-displacement hysteretic material, similarly to the connector models in Abaqus. This OpenSees fracture criterion uses the Palmgren-Miner linear damage accumulation rule, in combination with the Coffin-Manson relationship. A modified rainflow cycle counter developed by Uriz (2005) tracks the deformation history. Once the damage index D_f reaches 1

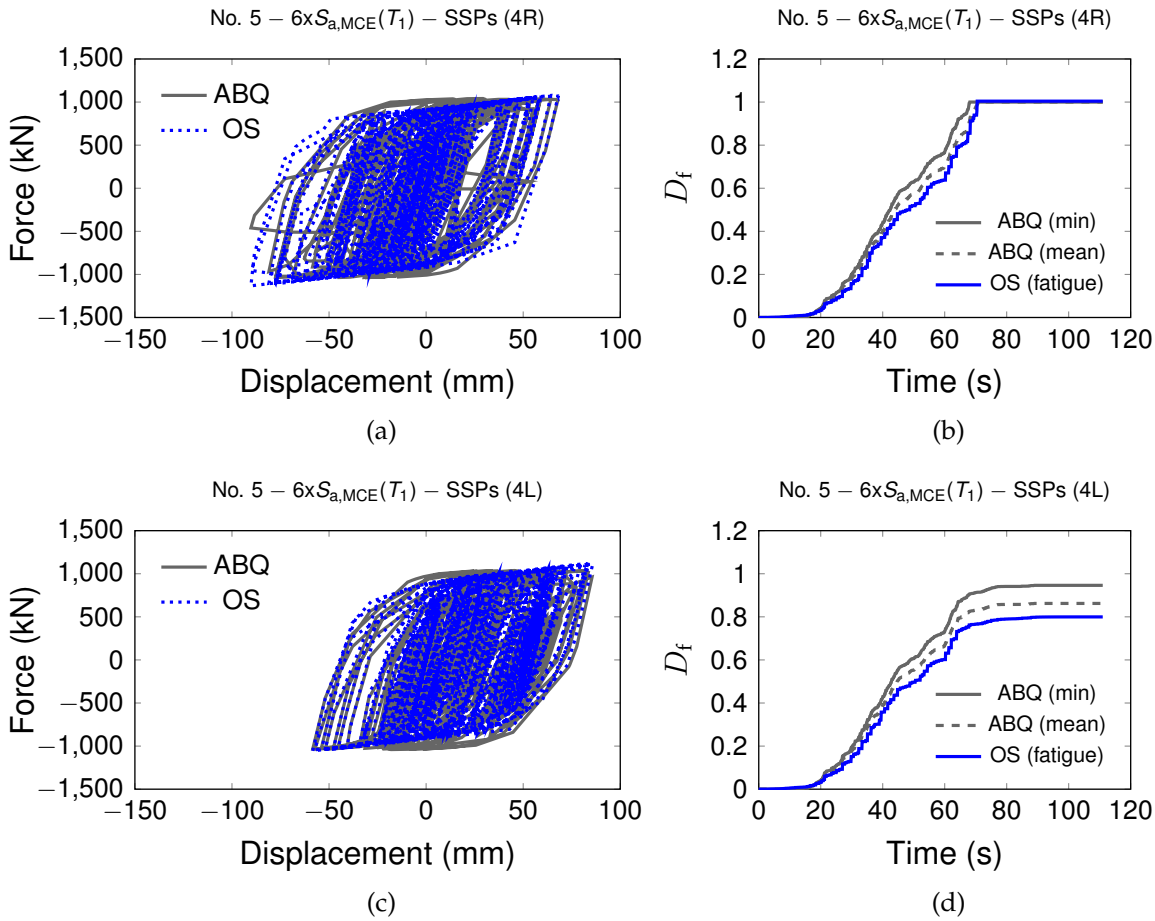

Figure 7.21. Comparison of Abaqus (ABQ) and OpenSees (OS) spring elements modelling SSPs at the fourth storey under no. 5 ground motion: (a and c) hystereses; (b and d) failure index

(i.e., failure), the force in the spring element becomes zero.

Similarly to Abaqus, a spring element is used to model the SSPs. Their hysteresis is simulated using the Menegotto-Pinto material model (Menegotto & Pinto 1973), denoted as Steel02 in OpenSees. The material parameters are calibrated against the experimental tests. The fatigue material model is calibrated using the Coffin-Manson relationship presented in Section 6.3.

The spring element is subjected to different displacement histories extracted from representative IDA analyses. Figure 7.21 compares the results of the OpenSees and Abaqus spring elements modelling SSPs in the braces of the fourth storey of the CBF-MRF, under no. 5 ground motion scaled to $6S_{a,MCE}(T_1)$. A good correlation is observed between the hystereses of the two elements, plotted in Figure 7.21a and c.

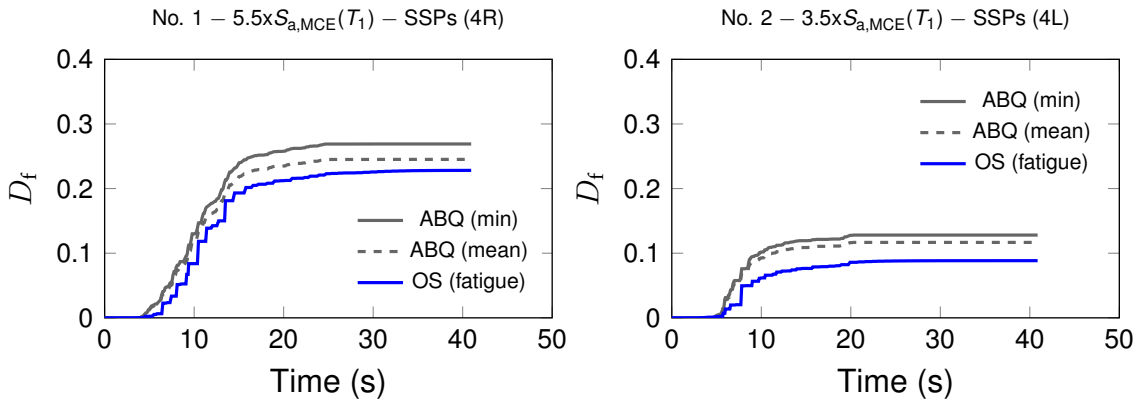

Figure 7.22. Comparison of Abaqus (ABQ) and OpenSees (OS) failure index of SSPs at the fourth storey under no. 1 and no. 2 ground motions

The damage level D_f recorded in the OpenSees spring element is compared with the corresponding Abaqus failure index, calculated as $\overline{u}^{pl}$ to $\overline{u}_f^{pl}$. The D_f time histories from the Abaqus and OpenSees analyses are shown in Figures 7.21b and d, where D_f from the Abaqus model is calculated using the mean and minimum $\overline{u}_f^{pl}$ (see Table 7.2). A fairly good correlation is observed between the two fracture models. The OpenSees fatigue model slightly overestimates the safety margin against collapse. A similar trend can be seen in Figure 7.22 for no. 1 and no. 2 ground motions. Overall, the Abaqus fracture criterion used for IDA appears capable of predicting the ductile fracture response of SSPs with a similar degree of accuracy to the widely-accepted fatigue material model available in OpenSees. In particular, the minimum $\overline{u}_f^{pl}$ values employed for the collapse assessment of the CBF-MRF provide more conservative predictions.

7.5 Conclusions

In this chapter, the earthquake-induced collapse potential of the dual CBF-MRF was numerically evaluated. The simplified Abaqus beam-solid model of the 6-storey prototype building developed in Chapter 4 was revised using the two SSP geometries tested in Chapter 5. The SSPs were modelled using connector elements with an experimentally-validated plastic motion-based criterion that simulates their ductile fracture behaviour. The calibrated fracture criterion for the connector elements enables to simulate both the initiation and degradation of the SSPs. Incremental dynamic analyses (IDA) were conducted using 24 ground motions selected from FEMA P695 (2008) and Ruiz-Garcia (2010).

Fragility curves were constructed based on the methodology proposed by FEMA P695 (2008) to assess the collapse probability of the dual CBF-MRF. Based on the results of the IDA, the following conclusions are drawn:

- The proposed dual CBF-MRF has an excellent seismic resistance against collapse, with a median collapse intensity 4.81 times the first-mode spectral acceleration. The collapse probability of the CBF-MRF at the MCE hazard level is 1.2%, largely below the required limit of 10%, indicating that the proposed system achieves the objective of increasing seismic resilience.
- As a result of the large fracture capacity of the SSPs, only two of the five long significant duration ground motions determined the failure of the SSPs. For the short significant duration records, the fracture initiation index was consistently below 0.6 at collapse. Therefore, the collapse performance of the CBF-MRF is marginally affected by the fracture of the SSPs.
- The plastic motion-based fracture criterion employed in the Abaqus connector elements was capable of predicting ductile fracture in the SSPs with similar accuracy to the widely-accepted fatigue material model available in OpenSees.

Chapter 8

Conclusions

This chapter presents a summary of the thesis and the main conclusions that are drawn from the preceding chapters. Recommendations for future work are then provided.

8.1 Summary

The aim of this thesis was to develop and validate an innovative dual concentrically-braced moment-resisting steel frame (CBF-MRF) for improved seismic resilience.

Chapter 2 presented a review of seismic-resistant steel frames, including conventional systems and the latest strategies in seismic resilience. It was highlighted that conventional steel frames can experience extensive structural damage and large residual drifts, leading to significant repair costs and socio-economic losses, or possibly to the building demolition. To address these limitations, researchers have developed new design approaches that can increase seismic resilience. Among these, increasing the post-yield stiffness of the structure and introducing structural fuses were identified as both effective and practical design strategies. While current guidelines do not provide specific criteria for damage and residual drift minimisation, this work adopts performance objectives based on the latest research on seismic resilience (McCormick et al. 2008, Tzimas et al. 2015). A resilient steel system should meet the following targets: (1) under the design-basis earthquake (DBE), residual drifts should be smaller than 0.5% to meet the immediate occupancy performance level; and (2) under the maximum-considered earthquake (MCE),

the probability of collapse should be well below the limit of 10% currently set for conventional structures by FEMA P695 (2008).

The design of the dual CBF-MRF was developed in Chapter 3. To reduce residual drifts and minimise damage in the main structural members, simple structural details were used: (a) braces equipped with energy-dissipating stainless steel pins (SSPs); and (b) structural fuses in the beams. The SSPs are made of duplex stainless steel (SSD) of high post-yield stiffness. The proposed CBF-MRF was designed to have stiffness and strength comparable to a conventional dual MRF with buckling restrained braces (BRBF-MRF). A 6-storey prototype building was designed as either the dual CBF-MRF or the BRBF-MRF, according to EC3 (2003) and EC8 (2004). A performance-based design procedure and appropriate capacity design rules were adopted in the design of the dual frames.

Chapter 4 was dedicated to the numerical evaluation of the seismic response of the proposed CBF-MRF, in comparison with the conventional BRBF-MRF. Nonlinear finite element models (FEM) of different complexity were developed using the Abaqus software. A detailed three-dimensional FEM model, based on the use of solid and shell elements, was constructed to study both the local and global behaviour of the dual CBF-MRF. All possible failure modes were identified through nonlinear monotonic and cyclic pushover analyses. To evaluate the global seismic response of the CBF-MRF, a simplified version of the detailed model was developed, using beam elements for the main structural members, nonlinear connector elements for the SSPs and solid elements for the beam fuses. Dynamic time-history analyses were performed using a set of 22 earthquake records scaled to three different seismic intensities (frequently-occurred earthquake FOE; DBE; and MCE). A comparative evaluation of the seismic behaviour of the CBF-MRF and BRBF-MRF was discussed in terms of overstrength, post-yield stiffness, peak and residual storey drifts, and structural damage.

Chapter 5 described the experimental programme conducted to assess the seismic response and the fracture behaviour of the SSPs, employed as energy-dissipation devices in the dual CBF-MRF. Two full-scale geometries were tested in a configuration reproducing the SSP-brace connection of the CBF-MRF. Coupon tests on round bars were performed to characterise the SSD material.

The seismic performance of sixteen specimens (eight for each geometry) was evaluated using various loading protocols: the AISC protocol recommended for the validation of buckling restrained braces; various constant amplitude (CA) and random protocols for replicating ultra-low cycle fatigue (ULCF) conditions; and monotonic loading. The hysteretic behaviour, energy-dissipation (ED) capacity, and ductile fracture were assessed for each geometry.

Chapter 6 was dedicated to the prediction and numerical simulation of ductile fracture in SSPs. From the review of existing models for predicting fracture in metals under ULCF, three approaches were considered: a low-cycle fatigue (LCF) model based on the Coffin-Manson relationship and the Palmgren-Miner damage accumulation rule; and two mechanics-based fracture models, i.e., the Cyclic Void Growth Model (CVGM) and the fracture initiation criterion available in Abaqus. The fracture parameters of the Coffin-Manson relationship were calibrated against the experimental tests of the SSPs and used for the OpenSees fatigue material model in Chapter 7. The two mechanics-based models were calibrated against ULCF tests on notched coupon specimens by means of complementary FEM simulations. Their ability of predicting fracture initiation was validated through three-dimensional explicit simulations of the ULCF tests on SSPs. In addition, the Abaqus fracture evolution model was calibrated and used in combination with the initiation criterion to explicitly simulate the fracture response of the SSPs.

Finally, the seismic collapse potential of the dual CBF-MRF was assessed in Chapter 7. Incremental dynamic analyses (IDA) were performed using a revised version of the simplified beam-solid model of the dual frame developed in Chapter 4. To simulate ductile fracture in the connector elements modelling the SSPs, a plastic motion-based fracture criterion was calibrated against the full-scale tests. The collapse capacity of the dual CBF-MRF was evaluated using a set of 24 earthquake records from FEMA P695 (2008) and Ruiz-Garcia (2010). The influence of the significant ground-motion duration on the dynamic response of the frame was discussed. Based on the IDA results, a fragility curve was constructed to probabilistically evaluate the collapse capacity of the dual CBF-MRF. In addition, the accuracy of the connector fracture model employed for IDA was assessed against an OpenSees fatigue model based on the calibrated Coffin-Manson parameters.

8.2 Main conclusions

Specific conclusions were drawn at the end of each chapter. The main conclusions of this work are summarised as follows:

- Nonlinear static analyses showed that the proposed design of the dual CBF-MRF guarantees that inelastic deformations are concentrated in the replaceable SSPs and beam fuses, while the main structural members are elastic even for drifts expected under the MCE.
- The proposed dual CBF-MRF exhibits a much higher post-yield stiffness than the conventional BRBF-MRF having similar stiffness and strength, owing to the high post-yield stiffness of the SSPs, as shown by the nonlinear static analyses on both frames.
- The results of nonlinear dynamic analyses demonstrated that residual drifts in the dual CBF-MRF are drastically minimised, as a result of the high post-yield stiffness of the SSPs and the elastic capacity of the MRF. The maximum residual drift is negligible under the FOE, while it has a mean value of 0.06% under the DBE and of 0.12% under the MCE. The residual drift under the DBE is largely below the reparability limit of 0.5%, demonstrating the potential for a return to service within an acceptable short time in the aftermath of a strong earthquake.
- The proposed CBF-MRF has a superior residual storey drift performance compared to the dual BRBF-MRF, while undergoing similar peak storey drifts. The maximum residual drift experienced by the BRBF-MRF is five times larger than in the CBF-MRF under the DBE, and nearly four times larger under the MCE. The residual drift response of the BRBF-MRF is in line with that observed in previous research studies on prototype BRBFs.
- The proposed SSPs are optimal energy-dissipating devices. Cyclic tests on the SSPs showed that they provide a stable and symmetric hysteresis under imposed displacements up to four and half times the demand under the DBE. This hysteretic behaviour is comparable to that offered by BRBs, meeting the requirements of the AISC protocol.

- The SSPs offer a large fracture capacity under cyclic loading. The ULCF tests demonstrated the ability of the SSPs of enduring several cycles under large imposed displacements before ductile fracture initiation. Ductile fracture was consistently found to initiate at the free surface, at a section half way between the maximum and minimum diameter. Following initiation, the SSPs were still able to provide a stable hysteresis, while cracks gradually propagated to reach full-section failure.

- The calibrated Abaqus fracture criterion and CVGM provided accurate predictions of ductile fracture initiation for the ULCF tests of SSPs. The margin of error of both fracture initiation models is considered satisfactory (within 12%). As such, the calibrated fracture parameters have the potential of being used to predict the ULCF fracture initiation of SSPs having different geometries and boundary conditions, without the need for further experimental tests.

- The Abaqus explicit fracture simulations of the SSP tests were capable of capturing well the hysteretic behaviour of the SSPs; however, the ability of tracing the degradation of the material following fracture initiation was less accurate due to the relatively coarse mesh applied to the bending parts of the SSP.

- The results of IDA showed that the dual CBF-MRF has a large seismic resistance against collapse, with a median collapse intensity 4.81 times the first-mode spectral acceleration under the MCE. By accounting for the record-to-record variability and modelling uncertainty, the dual CBF-MRF has a 1.2% collapse probability at the MCE level, which is largely below the permissible limit of 10% set in FEMA P695 (2008).

- The large collapse capacity of the dual CBF-MRF benefits from the excellent fracture capacity of the SSPs and the activation of friction pads for large drifts. Under most of the earthquake records used in IDA, the safety margin against fracture in the SSPs was considerable; failure occurred only for two ground motions having a long significant duration, i.e., severe energy dissipation demand.

8.3 Recommendations for future research

This work has shown that the proposed dual CBF-MRF provides enhanced seismic resilience, by reducing residual drifts and minimising damage in main structural members, and by ensuring a very low collapse probability under the MCE.

Further research work could be developed in these directions:

- For a more comprehensive assessment of the dual CBF-MRF seismic performance, more building typologies, other than the prototype building designed in this work, ought to be studied by varying, for instance, the structure height, the number of bays and the span length.
- A loss estimation study is recommended to quantify the economic losses associated with structural and non-structural damage, including the cost of replacing the structural fuses. Such estimation may be used in a cost-benefit analysis to assess the advantages of the dual CBF-MRF against conventional steel frames. This analysis should aim to compare the increased initial construction costs of the proposed system against the savings associated with the improved seismic resilience.
- Fracture investigation could be further developed by performing additional tests on SSPs of different geometry, and under new randomly-generated loading protocols. This would enable the validation of the calibrated fracture parameters for a larger experimental database. If additional tests will be conducted, it is recommended to design a test apparatus with the capability of accurately reproducing the constraint exerted by the brace section.
- The assessment of the dual CBF-MRF collapse potential would benefit from a numerical investigation on the column deterioration due to local buckling, since the IDA were developed based on the assumption that the stocky HEB 500 sections do not experience severe degradation under drifts of 10%.
- The influence of ground motion duration on the ductile fracture of the SSPs may be further investigated using an additional set of long significant duration records.

- To further validate the proposed system, full-scale tests may be conducted on a one-storey frame. This would allow to assess the feasibility of the erection of the CBF-MRF and the construction details required.

References

Accelor Mittal (2008), *Steel Buildings in Europe. Multi-Storey Steel Buildings. Part 3: Actions*, Accelor Mittal.

Anderson, T. L. (2005), *Fracture mechanics: Fundamentals and applications*, CRC, Boca Raton, FL.

ANSI/AISC 341/10 (2010), *Seismic provisions for structural steel buildings*, AISC, Chicago.

ANSI/AISC 358/10 (2010), *Prequalified connections for special and intermediate steel moment frames for seismic applications*, AISC, Chicago.

Arias, A. (1970), *A measure of earthquake intensity*, Seismic Design for Nuclear Power Plants, MIT Press, Cambridge, MA.

Ariyaratana, C. & Fahnestock, L. A. (2011), 'Evaluation of buckling-restrained braced frame seismic performance considering reserve strength', *Engineering Structures* **33**(1), 77–89.

Arup (2013), *REDi Rating System - Resilience-based Earthquake Design Initiative for the Next Generation of Buildings*, Arup.

ASCE/SEI 7-16 (2016), *Minimum design loads for buildings and other structures, ASCE/SEI 7-16*, American Society of Civil Engineers, Reston, VA.

ASM (2002), *Atlas of stress-strain curves*, ASM International.

Baiguera, M., Vasdravellis, G. & Karavasilis, T. L. (2016), 'Dual seismic-resistant steel frame with high post-yield stiffness energy-dissipative braces for residual drift reduction', *Journal of Constructional Steel Research* **122**, 198 – 212.

Baker, J. W. & Cornell, C. A. (2008), 'Vector-valued intensity measures incorporating spectral shape for prediction of structural response', *Journal of Earthquake Engineering* **12**(4), 534–554.

Balut, N. & Gioncu, V. (2003), Suggestion for an improved 'dog-bone' solution, *in* F. Mazzolani, ed., 'Proceedings of STESSA 2003: Behaviour of Steel Structures in Seismic Areas', Balkema, Lisse, Netherlands, pp. 129–134.

Bao, Y. & Wierzbicki, T. (2004), 'On fracture locus in the equivalent strain and stress triaxiality space', *International Journal of Mechanical Sciences* **46**(1), 81–98.

Black, C. J., Makris, N. & Aiken, I. D. (2004), 'Component testing, seismic evaluation and characterization of buckling-restrained braces', *Journal of Structural Engineering* **130**(6), 880–894.

Bleck, W., Dahl, W., Nonn, A., Amlung, L., Feldmann, M., Schäfer, D. & Eichler, B. (2009), 'Numerical and experimental analyses of damage behaviour of steel moment connection', *Engineering Fracture Mechanics* **76**, 1531–1547.

Bonora, N., Ruggiero, A., Esposito, L. & Gentile, D. (2006), 'CDM modeling of ductile failure in ferritic steels: Assessment of the geometry transferability of model parameters', *International Journal of Plasticity* **22**(11), 2015–2047.

Bridgman, P. (1964), *Studies in large plastic flow and fracture*, Harvard University Press, Cambridge, MA.

Bruneau, M., Uang, C.-M. & Sabelli, R. (2011), *Ductile design of steel structures*, McGraw-Hill.

Castiglioni, C. A., Kanyilmaz, A. & Calado, L. (2012), 'Experimental analysis of seismic resistant composite steel frames with dissipative devices', *Journal of Constructional Steel Research* **76**, 1–12.

Champion, C. & Liel, A. (2012), 'The effect of near-fault directivity on building seismic collapse risk', *Earthquake Engineering & Structural Dynamics* **41**(10), 1391–1409.

Chancellor, N. B., Eatherton, M. R., Roke, D. A. & Akbas, T. (2014), 'Self-centering seismic lateral force resisting systems: High performance structures for the city of tomorrow', *Buildings* **4**(3), 520–548.

Chen, S.-J., Yeh, C. H. & Chu, J. M. (1996), 'Ductile steel beam-to-column connections for seismic resistance', *Journal of Structural Engineering* **122**(11), 1292–1299.

Chou., C.-C., Chen, J.-H., Chen, Y.-C. & Tsai, K.-C. (2006), 'Evaluating performance of post-tensioned steel connections with strands and reduced flange plates', *Earthquake Engineering & Structural Dynamics* **35**, 1167–1185.

Chou, C.-C. & Chen, S.-Y. (2010), 'Subassemblage tests and finite element analyses of sandwiched buckling-restrained braces', *Engineering Structures* **32**(8), 2108–2121.

Christopoulos, C., Filiatrault, A., Uang, C.-M. & Folz, B. (2002), 'Post-tensioned energy dissipating connections for moment-resisting frames', *Journal of Structural Engineering* **128**(9), 1111–1120.

Christopoulos, C., Tremblay, R., Kim, H. & Lacerte, M. (2008), 'The self-centering energy dissipative (SCED) bracing system for the seismic resistance of structures', *Journal of Structural Engineering* **134**(1), 96–107.

Clifton, G. C., Bruneau, M., MacRae, G. A., Leon, R. & Fussell, A. (2011), 'Steel structures damage from the Christchurch earthquake series of 2010 and 2011', *Bulletin of the New Zealand Society of Earthquake Engineering* **44**(4), 297–318.

Clifton, G. C., Nashid, H., Ferguson, G., Hodgson, M., Seal, C., Bruneau, M., MacRae, G. A. & Gardiner, S. (2012), Performance of eccentrically braced framed buildings in the Christchurch earthquake series of 2010/2011, *in* 'Proceedings of the 15th World Conference on Earthquake Engineering (15 WCEE)', Lisbon, Portugal.

Coffin, L. F. (1954), 'A study of the effects of cyclic thermal stress on a ductile metal', *Transaction of the ASME* **76**, 931–950.

Computers and Structures Inc. (2005), *Static and Dynamic Finite Element Analysis of Structures*, Version 9.1.4. Computers and Structures Inc., Berkeley, CA.

D'Aniello, M., Della Corte, G. & Mazzolani, F. M. (2008), Full-scale tests of only-steel buckling-restrained braces for seismic retrofitting of reinforced concrete buildings, *in* R. Ofner, D. Beg, J. Fink, R. Greiner & H. Unterwegger,

eds, 'Proceedings of the 5th European Conference on Steel and Composite Structures (EUROSTEEL 2008)', Graz, Austria.

Dassault Systèmes (2014), *ABAQUS documentation*, 6.14 edn, Dassault Systèmes Simulia, Providence, RI.

EC1 (2004), *Eurocode 1: Actions on Structures, Part 1-4: General Actions - Wind Actions*, European Commitee for Standardization, CEN, Brussels.

EC3 (2003), *Eurocode 3: Design of steel structures, Part 1.1: General Rules and Rules for Building*, European Commitee for Standardization, CEN, Brussels.

EC8 (2004), *Eurocode 8: Design Provisions for Earthquake Resistance of Structures, Part 1: General Rules, Seismic Actions and Rules for Building*, European Commitee for Standardization, CEN, Brussels.

Elghazouli, A. Y. (2009), *Seismic design of Buildings to Eurocode 8*, Spon Press - Taylor & Francis, London and New York.

Elkady, A. & Lignos, D. G. (2015), 'Analytical investigation of the cyclic behavior and plastic hinge formation in deep wide-flange steel beam-columns', *Bulletin of Earthquake Engineering* **13**(4), 1097–1118.

EN 10002-1 (2001), *Metallic materials. Tensile testing. Part 1: Tests at ambient temperature*, European Commitee for Standardization, CEN, Brussels.

EN 10025-2 (2004), *Hot rolled products of structural steels. Part 2: Technical delivery conditions for non-alloy structural steels*, European Commitee for Standardization, CEN, Brussels.

Erochko, J., Christopoulos, C., Tremblay, R. & Choi, H. (2011), 'Residual drift response of SMRFs and BRB frames in steel buildings designed according to ASCE 7-05', *Journal of Structural Engineering* **137**(5), 589–599.

Erochko, J., Christopoulos, C., Tremblay, R. & Kim, H.-J. (2013), 'Shake table testing and numerical simulation of a self-centering energy dissipative braced frame', *Earthquake Engineering & Structural Dynamics* **42**(11), 1617–1635.

Fahnestock, L. A., Ricles, J. M. & Sause, R. (2007b), 'Experimental evaluation of a large-scale buckling-restrained braced frame', *Journal of Structural Engineering* **133**(9), 1205–1214.

Fahnestock, L. A., Sause, R. & Ricles, J. M. (2007a), 'Seismic response and performance of buckling-restrained braced frames', *Journal of Structural Engineering* **133**(9), 1195–1204.

FEMA 350 (2000), *Recommended seismic design criteria for new steel moment-frame buildings*, Federal Emergency Management Agency, CA.

FEMA 461 (2007), *Interim testing protocols for determining the seismic performance characteristics of structural and non-structural components*, Federal Emergency Management Agency, CA.

FEMA P695 (2008), *Quantification of building seismic performance factors*, Federal Emergency Management Agency, CA.

Garlock, M. M., Ricles, J. M. & Sause, R. (2005), 'Experimental studies of full-scale posttensioned steel connections', *Journal of Structural Engineering* **131**(3), 438–448.

Genna, F. & Gelfi, P. (2012), 'Analysis of the lateral thrust in bolted steel buckling-restrained braces. I: Experimental and numerical results.', *Journal of Structural Engineering* **138**(10), 1231–1243.

Gray, M. G., Christopoulos, C. & Packer, J. A. (2014), 'Cast steel yielding brace system for concentrically braced frames: Concept development and experimental validations', *Journal of Structural Engineering* **140**(4), 04013095.

Gray, M. G., Christopoulos, C. & Packer, J. A. (2017), 'Design and full-scale testing of a cast steel yielding brace system in a braced frame', *Journal of Structural Engineering* **143**(4), 04016210.

Haselton, C. B., Baker, J. W., Liel, A. B. & Deierlein, G. G. (2011), 'Accounting for ground motion spectral shape characteristics in structural collapse assessment through an adjustment for epsilon', *Journal of Structural Engineering* **137**(3), 332–344.

Hillerborg, A., Modeer, M. & Petersson, P. E. (1976), 'Analysis of crack formation and crack growth in concrete by means of fracture mechanics and finite elements', *Cement and Concrete Research* **6**, 773–782.

Ibarra, L. F., Medina, R. A. & Krawinkler, H. (2005), 'Hysteretic models that incorporate strength and stiffness deterioration', *Earthquake Engineering & Structural Dynamics* **34**(12), 1489–1511.

Iervolino, I., Manfredi, G. & Cosenza, E. (2006), 'Ground-motion duration effects on nonlinear seismic response', *Earthquake Engineering and Structural Dynamics* **35**(1), 21–38.

Iwata, Y., Sugimoto, H. & Kuguamura, H. (2006), Reparability limit of steel structural buildings based on the actual data of the Hyogoken-Nanbu earthquake, *in* 'Proceedings of the 38th Joint Panel on Wind and Seismic Effects', Vol. 1057, NIST Special Publication, pp. 23–32.

Jia, L. J. & Kuwamura, H. (2014), 'Ductile fracture simulation of structural steels under monotonic loading', *Journal of Structural Engineering* **140**(5), 04013115.

Jia, L. J. & Kuwamura, H. (2015), 'Ductile fracture model for structural steel under cyclic large strain loading', *Journal of Constructional Steel Research* **106**, 110–121.

Johnson, G. B. & Cook, W. H. (1985), 'Fracture characteristics of three metals subjected to various strains, strain rates, temperatures and pressures', *Engineering Fracture Mechanics* **21**(1), 31–48.

Kajima (1991), *Honeycomb Damper System*, Kajima Corporation, Japan.

Kanvinde, A. M. (2017), 'Predicting fracture in civil engineering steel structures: State of the art', *Journal of Structural Engineering* **143**(3), 03116001.

Kanvinde, A. M. & Deierlein, G. G. (2006), 'The void growth model and the stress modified critical strain model to predict ductile fracture in structural steels', *Journal of Structural Engineering* **132**(12), 1907–1918.

Kanvinde, A. M. & Deierlein, G. G. (2007), 'Cyclic void growth model to assess ductile fracture initiation in structural steels due to ultra low cycle fatigue', *Journal of Engineering Mechanics* **133**(6), 701–712.

Kanvinde, A. M., Marshall, K. S., Grilli, D. A. & Bomba, G. (2015), 'Forensic analysis of link fractures in eccentrically braced frames during the February 2011 Christchurch earthquake: Testing and simulation', *Journal of Structural Engineering* **141**(5), 04014146.

Karamanci, E. & Lignos, D. (2014), 'Computational approach for collapse assessment of concentrically braced frames in sesmic regions', *Journal of Structural Engineering* **140**(8), A4014019.

Kelly, J. M., Skinner, R. I. & Heine, A. J. (1972), 'Mechanisms of energy absorption in special devices for use in earthquake-resistant structures', *Bulletin of the New Zealand Society of Earthquake Engineering* **5**(3), 63–88.

Kempton, J. J. & Stewart, J. P. (2006), 'Prediction equations for significant duration of earthquake ground motions considering site and near-source effects', *Earthquake Spectra* **22**(4), 985–1013.

Kiggins, S. & Uang, C. M. (2006), 'Reducing residual drift of buckling-restrained braced frames as a dual system', *Engineering Structures* **28**, 1525–1532.

Kim, H. J. & Christopoulos, C. (2008), 'Friction damped posttensioned self-centering steel moment-resisting frames', *Journal of Structural Engineering* **134**(11), 1768–1779.

Krawinkler, H. & Zareian, F. (2007), 'Prediction of collapse - how realistic and practical is it, and what can we learn from it?', *The Structural Design of Tall and Special Buildings* **16**(5), 633–653.

Lemaitre, J. (1985), 'A continuous damage mechanics model for ductile fracture', *Journal of Engineering Materials and Technology* **107**(1), 83–90.

Liel, A., Haselton, C., Deierlein, G. & Baker, J. (2009), 'Incorporating modeling uncertainties in the assessment of seismic collapse risk of buildings', *Structural Safety* **31**(2), 197–211.

Lin, T. & Baker, J. W. (2013), Introducing adaptive incremental dynamic analysis: A new tool for linking ground motion selection and structural response assessment, *in* 'Proceedings of the 11th International Conference on Structural Safety & Reliability (ICOSSAR 2013)', Dept of Civil Engineering & Engineering Mechanics, Columbia University, The International Association for Structural Safety and Reliability, New York, US.

Mackenzie, A. C., Hancock, J. W. & Brown, D. K. (1977), 'On the influence of state of stress on ductile failure initiation in high strength steels', *Engineering Fracture Mechanics* **9**(1), 167–188.

MacRae, G. A., Carr, A. J. & Walpole, W. R. (1990), The seismic response of steel frames, Technical Report 90-6, Department of Civil Engineering, University of Canterbury, Christchurch.

MacRae, G. A. & Kawashima, K. (1997), 'Post-earthquake residual displacements of bilinear oscillators', *Earthquake Engineering & Structural Dynamics* **26**, 701–716.

Manson, S. S. (1953), Behavior of materials under conditions of thermal stress, *in* 'Heat Transfer Symposium', University of Michigan Engineering Research Institute.

Mansour, N., Christopoulos, C. & Tremblay, R. (2011), 'Experimental validation of replaceable shear links for eccentrically braced steel frames', *Journal of Structural Engineering* **137**(10), 1141–1152.

Mazzoni, S., McKenna, F., Scott, M. & Fenves, G. (2006), *Open System for Earthquake Engineering Simulation (OpenSees). User command language manual*, Pacific Earthquake Engineering Research Center, University of California, Berkley, CA.

McClintock, F. A. (1968), 'Criterion for ductile fracture by growth of holes', *Journal of Applied Mechanics* **35**(2), 363–371.

McCormick, J., Aburano, H., Ikenaga, M. & Nakashima, M. (2008), Permissible residual deformation levels for building structures considering both safety and human elements, *in* 'Proceedings of the 14th World Conference on Earthquake Engineering', number 05-06-0071, Beijing.

Menegotto, M. & Pinto, P. E. (1973), Method of analysis for cyclically loaded reinforced concrete plane frames including changes in geometry and non-elastic behavior of elements under combined normal force and bending, *in* 'IABSE Symposium on Resistance and Ultimate Deformability of Structures Acted on by Well Defined Repeated Loads', pp. 15–22.

Miner, M. (1945), 'Cumulative damage in fatigue', *Journal of Applied Mechanics, Transaction of ASME* **67**, A159.

Myers, A. T., Kanvinde, A. M. & Deierlein, G. G. (2010), 'Calibration of the SMCS criterion for ductile fracture in steels: Specimen size dependence and parameter assessment', *Journal of Structural Engineering* **136**(11), 1401–1410.

Newell, J. D. & Uang, C. M. (2006), Cyclic behavior of steel columns with combined high axial load and drift demand, Technical Report SSRP-06/22, Department of Structural Engineering, University of California, San Diego.

Okazaki, T., Arce, G., Ryu, H. C. & Engelhardt, M. D. (2005), 'Experimental study of local buckling, overstrength, and fracture of links in eccentrically braced frames', *Journal of Structural Engineering* **131**(10), 1526–1535.

Pampanin, S., Christopoulos, C. & Priestley, M. J. N. (2003), 'Performance-based seismic response of frame structures including residual deformations. Part II: Multiple-degree-of-freedom systems', *Journal of Earthquake Engineering* **7**(1), 119–147.

Panontin, T. L. & Sheppard, S. D. (1995), The relationship between constraint and ductile fracture initiation as defined by micromechanical analyses, *in* 'Fracture Mechanics Proceedings of the 26th National Symposium on Fracture Mechanics', ASTM International, Philadelphia, pp. 54 – 85.

Pavlovic, M., Markovic, Z., M., V. & Budevac, D. (2013), 'Bolted shear connectors vs. headed studs behaviour in push-out tests', *Journal of Constructional Steel Research* **88**, 134–149.

Pereira, J., de Jesus, A., Xavier, J. & Fernandes, A. (2014), 'Ultra low-cycle fatigue behaviour of a structural steel', *Engineering Structures* **60**, 214–222.

Pettinga, D., Christopoulos, C., Pampanin, S. & Priestley, M. J. N. (2008), 'Effectiveness of simple approaches in mitigating residual deformations in buildings', *Earthquake Engineering & Structural Dynamics* **36**(12), 1763–1783.

Popov, E. P. & Engelhardt, M. D. (1988), 'Seismic eccentrically braced frames', *Journal of Constructional Steel Research* **10**, 321–354.

Rice, J. R. & Tracey, D. M. (1969), 'On the ductile enlargement of voids in triaxial stress fields', *Journal of the Mechanics and Physics of Solids* **17**(3), 201–217.

Ricles, J. M., Sause, R., Garlock, M. & Zhao, C. (2001), 'Posttensioned seismic-resistant connections for steel frames', *Journal of Structural Engineering* **127**(2), 113–121.

Ricles, J. M., Sause, R., Peng, S. & Lu, L. (2002), 'Experimental evaluation of earthquake resistant posttensioned steel connections', *Journal of Structural Engineering* **128**(7), 850–859.

Rojas, P., Ricles, J. M. & Sause, R. (2005), 'Seismic performance of post-tensioned steel moment resisting frames with friction devices', *Journal of Structural Engineering* **131**(4), 529–540.

Roke, D., Sause, R., Ricles, J. M. & Gonner, N. (2009), Design concepts for damage-free seismic-resistant self-centering steel concentrically braced frames, *in* L. Griffis, T. Helwig, M. Waggoner & M. Hoit, eds, 'Structures 2009: Don't Mess with Structural Engineers: Expanding Our Role', ASCE, Austin, Texas, pp. 1421–1430.

Romero, P., D., R. L., Miller, P. J. & Okahashi, T. (2007), *Full Scale Testing of WC Series Buckling-Restrained Braces*, Department of Civil & Environmental Engineering, The University of Utah.

Ruiz-Garcia, J. (2010), 'On the influence of strong-ground motion duration on residual displacement demands', *Earthquakes and Structures* **1**(4), 327–344.

Ruiz-Garcia, J. & Miranda, E. . (2006*a*), 'Evaluation of residual drift demands in regular multi-story frame buildings for performance-based assessment', *Earthquake Engineering & Structural Dynamics* **35**(13), 1609–1629.

Ruiz-Garcia, J. & Miranda, E. . (2006*b*), 'Residual displacement ratios for assessment of existing structures', *Earthquake Engineering & Structural Dynamics* **35**(13), 315–336.

Sabelli, R., Mahin, S. & Chang, C. (2003), 'Seismic demands on steel braced frame buildings with buckling-restrained braces', *Engineering Structures* **25**, 655–666.

Sabelli, R., Roeder, C. & Hajjar, J. (2013), Seismic design of steel special concentrically braced frame systems, Seismic Design Technical Brief 8, NEHRP.

Sahoo, D. & Chao, S. (2015), 'Stiffness-based design for mitigation of residual displacements of buckling-restrained braced frames', *Journal of Structural Engineering* **141**(9), 04014229.

Sause, R., Ricles, J. M., Roke, D. A., Chancellor, N. B. & Gonner, N. P. (2010), Large-scale experimental studies of damage-free self-centering concentrically-braced frame under seismic loading, *in* S. Senapathi, K. Casey & M. Hoit, eds, '2010 Structures Congress', ASCE, Orlando, Florida, pp. 1498–1509.

Seo, C. Y., Karavasilis, T. L., Ricles, J. M. & Sause, R. (2014), 'Seismic performance and probabilistic collapse resistance assessment of steel moment resisting frames with fluid viscous dampers', *Earthquake Engineering & Structural Dynamics* **43**(14), 2135–2154.

Shen, Y., Christopoulos, C., Mansour, N. & Tremblay, R. (2011), 'Seismic design and performance of steel moment-resisting frames with nonlinear replaceable links', *Journal of Structural Engineering* **137**(10), 1107–1117.

Skinner, R. I., Kelly, J. M. & Heine, A. J. (1975), 'Hysteretic dampers for earthquake-resistant structures', *Earthquake Engineering & Structural Dynamics* **3**(3), 287–296.

Smith, C., Deierlein, G. & Kanvinde, A. (2014), A stress-weighted damage model for ductile fracture initiation in structural steel under cyclic loading and generalized stress states, Technical Report 187, The John A. Blume Earthquake Engineering Center, Stanford University, Stanford, CA.

Smith, C., Kanvinde, A. & Deierlein, G. (2017), 'A local criterion for ductile fracture under low-triaxiality axisymmetric stress states', *Engineering Fracture Mechanics* **169**, 321–335.

Thornton, W. A. (1984), 'Bracing connections for heavy construction', *AISC Engineering Journal* **21**(3), 139–148.

Tremblay, R., Lacerte, M. & Christopoulos, C. (2008), 'Seismic response of multi-storey buildings with self-centering energy dissipative steel braces', *Journal of Structural Engineering* **134**(1), 108–120.

Trifunac, M. & Brady, A. (1975), 'A study on the duration of strong earthquake ground motion', *Bulletin of the Seismological Society of America* **65**, 581–626.

Tsai, K.-C., Chou, C.-C., Lin, C. L., P. C. Chen, P. C. & Jhang, S. J. (2008), 'Seismic self-centering steel beam-to-column moment connections using bolted friction devices', *Earthquake Engineering & Structural Dynamics* **37**(4), 627–645.

Tsai, K.-C. & Li, J. W. (1994), Seismic analysis of passive energy dissipation subsystems by hybrid experiments, *in* 'Proceedings of the 12th International Modal Analysis Conference', Honolulu, Hawaii, pp. 1520–1526.

Tsioulou, A. & Galasso, C. (2015), Validation of ground motion simulations through spectral-shape and duration proxies for the nonlinear response of engineered systems, *in* 'Proceedings of SECED 2015 Conference: Earthquake Risk and Engineering towards a Resilient World', 9-10 July, Cambridge, UK.

Tzimas, A. S., Dimopoulos, A. I. & Karavasilis, T. L. (2015), 'EC8-based seismic design and assessment of self-centering post-tensioned steel frames with viscous dampers', *Journal of Constructional Steel Research* **105**, 60–73.

Tzimas, A. S., Kamaris, G. S., Karavasilis, T. L. & Galasso, C. (2016), 'Collapse risk and residual drift performance of steel buildings using post-tensioned MRFs and viscous dampers in near-fault regions', *Bulletin of Earthquake Engineering* **14**(6), 1643–1662.

Uriz, P. (2005), Towards Earthquake Resistant Design of Concentrically Braced Steel Structures, Doctoral dissertation, Department of Civil and Environmental Engineering, University of California, Berkeley.

Vamvatsikos, D. & Cornell, C. A. (2002), 'Incremental dynamic analysis', *Earthquake Engineering & Structural Dynamics* **31**(3), 491–514.

Vasdravellis, G., Karavasilis, T. L. & Uy, B. (2013), 'Large-scale experimental validation of steel post-tensioned connections with web hourglass pins', *Journal of Structural Engineering* **139**(6), 1033–1042.

Vasdravellis, G., Karavasilis, T. L. & Uy, B. (2014), 'Design rules, experimental evaluation, and fracture models for high-strength and stainless steel hourglass shape energy dissipation devices', *Journal of Structural Engineering* **140**(11), 04014087.

Vayas, I. & Thanopoulos, P. (2005), 'Innovative dissipative (INERD) pin connections for seismic resistant braced frames', *International Journal of Steel Structures* **5**(5), 453–464.

Watanabe, A., Hitomi, Y., Yeaki, E., Wada, A. & Fujimoto, M. (1988), Properties of brace encased in buckling-restraining concrete and steel tube, *in* 'Proceedings of the 9th World Conference on Earthquake Engineering', Vol. 5, Tokyo-Kyoto, pp. 719–724.

Whittaker, A. S., Bertero, V. V., Thompson, C. L. & Alonso, L. J. (1991), 'Seismic testing of steel plate energy dissipation devices', *Earthquake Spectra* **7**(4), 563–604.

Wierzbicki, T., Yingbin, B., Young-Woong, L. & Yuanli, B. (2005), 'Calibration and evaluation of seven fracture models', *International Journal of Mechanical Sciences* **47**(4-5), 719–743.

Wolski, M., Ricles, J. M. & Sause, R. (2009), 'Experimental study of a self-centering beam-column connection with bottom flange friction device', *Journal of Structural Engineering* **135**(5), 479–488.

Xia, C. & Hanson, R. D. (1992), 'Influence of ADAS element parameters on building seismic response', *Journal of Structural Engineering* **118**(7), 1903–1918.

Xie, Q. (2005), 'State of the art of buckling-restrained braces in Asia', *Journal of Constructional Steel Research* **61**, 727–748.

Zareian, F. & Medina, A. (2010), 'A practical method for proper modelling of structural damping in inelastic plane structural systems', *Computers & Structures* **88**(1), 45–53.

Appendices

Appendix A

Nonlinear Dynamic Analyses Results

This appendix provides a summary of the statistics of the results from the nonlinear dynamic analyses on the proposed CBF-MRF and the conventional BRBF-MRF, presented in Chapter 4.

Peak Storey Drifts - CBF-MRF

MCE

Storey	m (%)	σ (%)	$m+\sigma$ (%)	median (%)
6	1.06	0.28	1.34	0.98
5	1.15	0.30	1.46	1.15
4	1.25	0.34	1.58	1.27
3	1.27	0.35	1.62	1.19
2	1.10	0.35	1.45	0.97
1	0.62	0.23	0.85	0.54

DBE

Storey	m (%)	σ (%)	$m+\sigma$ (%)	median (%)
6	0.67	0.17	0.84	0.58
5	0.77	0.19	0.96	0.75
4	0.86	0.23	1.08	0.86
3	0.88	0.22	1.11	0.88
2	0.75	0.19	0.94	0.73
1	0.39	0.11	0.50	0.36

FOE

Storey	m (%)	σ (%)	$m+\sigma$ (%)	median (%)
6	0.37	0.08	0.45	0.35
5	0.43	0.08	0.51	0.41
4	0.46	0.09	0.55	0.46
3	0.48	0.09	0.56	0.49
2	0.40	0.06	0.47	0.41
1	0.21	0.03	0.24	0.21

Peak Storey Drifts - BRBF-MRF

MCE

Storey	m (%)	σ (%)	$m+\sigma$ (%)	median (%)
6	1.52	0.54	2.06	1.38
5	1.45	0.57	2.02	1.37
4	1.40	0.52	1.92	1.27
3	1.28	0.40	1.68	1.17
2	1.03	0.28	1.31	0.99
1	0.51	0.17	0.68	0.50

DBE

Storey	m (%)	σ (%)	$m+\sigma$ (%)	median (%)
6	1.02	0.35	1.38	0.96
5	1.01	0.36	1.37	0.95
4	0.99	0.33	1.32	0.97
3	0.91	0.28	1.19	0.87
2	0.75	0.18	0.93	0.73
1	0.36	0.09	0.45	0.36

Figure A.1. Statistics of peak storey drifts for CBF-MRF and BRBF-MRF

Residual Storey Drifts - CBF-MRF

MCE

Storey	m (%)	σ (%)	$m+\sigma$ (%)	median (%)
6	0.12	0.07	0.19	0.14
5	0.12	0.07	0.19	0.14
4	0.12	0.08	0.20	0.11
3	0.12	0.11	0.23	0.10
2	0.12	0.12	0.24	0.09
1	0.10	0.10	0.21	0.05

DBE

Storey	m (%)	σ (%)	$m+\sigma$ (%)	median (%)
6	0.06	0.05	0.11	0.06
5	0.06	0.04	0.10	0.06
4	0.06	0.04	0.10	0.06
3	0.06	0.04	0.10	0.05
2	0.06	0.05	0.11	0.05
1	0.05	0.04	0.09	0.04

FOE

Storey	m (%)	σ (%)	$m+\sigma$ (%)	median (%)
6	0.01	0.02	0.03	0.01
5	0.02	0.02	0.04	0.02
4	0.02	0.02	0.04	0.02
3	0.02	0.02	0.04	0.01
2	0.01	0.01	0.03	0.01
1	0.00	0.00	0.01	0.00

Residual Storey Drifts - BRBF-MRF

MCE

Storey	m (%)	σ (%)	$m+\sigma$ (%)	median (%)
6	0.44	0.36	0.80	0.37
5	0.42	0.35	0.76	0.35
4	0.37	0.32	0.69	0.30
3	0.31	0.28	0.59	0.22
2	0.23	0.22	0.45	0.19
1	0.13	0.14	0.26	0.09

DBE

Storey	m (%)	σ (%)	$m+\sigma$ (%)	median (%)
6	0.27	0.22	0.49	0.23
5	0.26	0.21	0.46	0.21
4	0.22	0.18	0.40	0.21
3	0.18	0.15	0.33	0.15
2	0.12	0.11	0.23	0.10
1	0.06	0.06	0.11	0.03

Figure A.2. Statistics of residual storey drifts for CBF-MRF and BRBF-MRF

SSP Maximum Demand - CBF-MRF

MCE

Storey	m (mm)	σ (mm)	$m+\sigma$ (mm)	median (mm)
6	18.85	5.43	24.28	17.07
5	20.61	5.56	26.17	20.29
4	22.38	6.22	28.60	23.14
3	23.49	6.55	30.04	21.77
2	20.17	6.62	26.80	18.20
1	11.45	4.39	15.84	9.77

DBE

Storey	m (mm)	σ (mm)	$m+\sigma$ (mm)	median (mm)
6	11.36	3.40	14.76	9.88
5	13.43	3.53	16.95	13.03
4	15.07	4.28	19.35	15.02
3	16.10	4.14	20.25	16.32
2	13.67	3.52	17.19	13.62
1	7.06	2.18	9.24	6.44

FOE

Storey	m (mm)	σ (mm)	$m+\sigma$ (mm)	median (mm)
6	5.66	1.67	7.33	5.17
5	6.88	1.55	8.43	6.29
4	7.57	1.59	9.16	7.44
3	8.40	1.57	9.96	8.70
2	7.11	1.21	8.32	7.18
1	3.59	0.55	4.14	3.63

Figure A.3. Statistics of maximum displacements of SSPs in CBF-MRF

Appendix B

Technical Drawings for the Experimental Programme

The technical drawings produced for the experimental tests on SSPs and coupon specimens are included in this appendix.

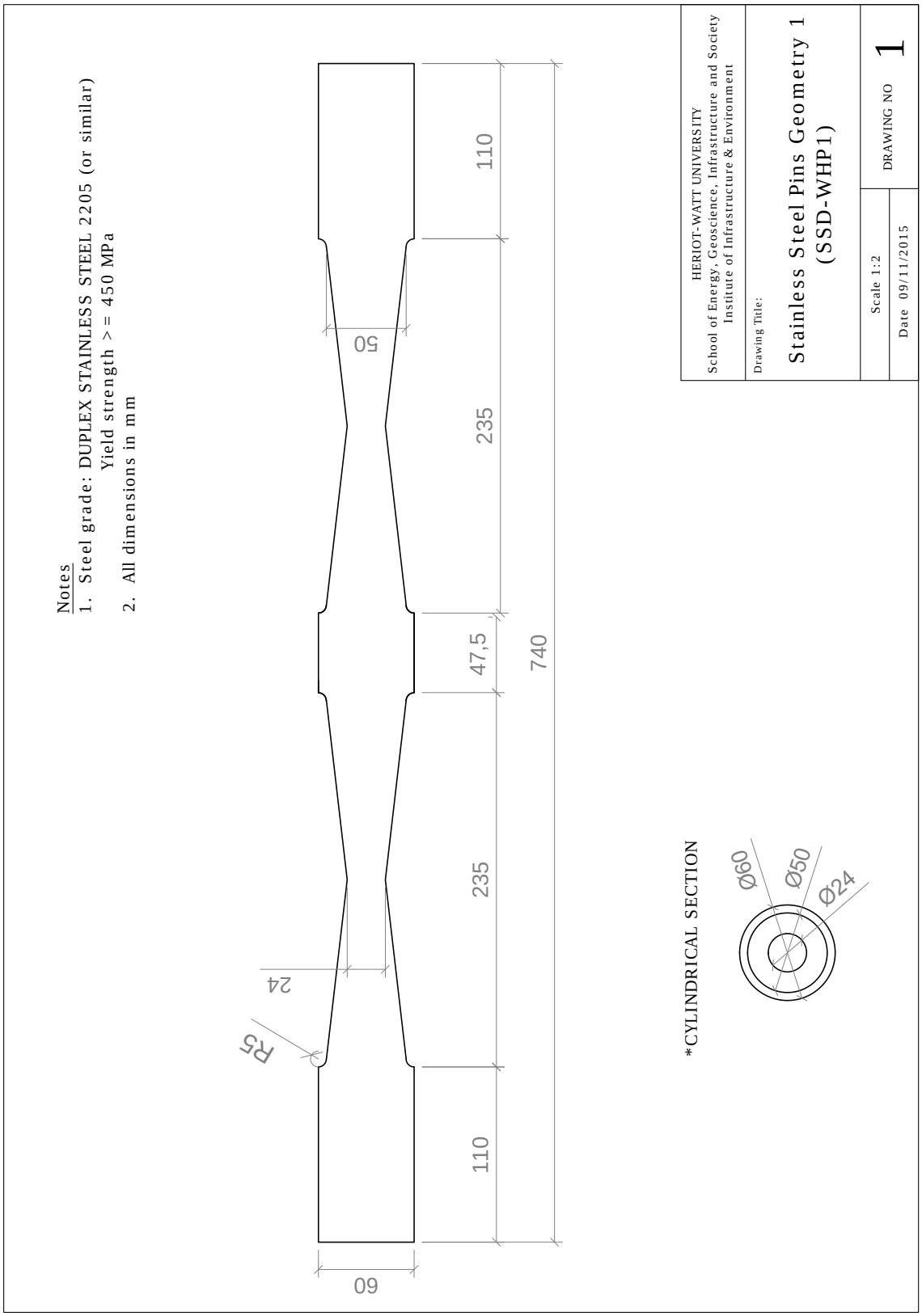

Figure B.1. Technical details of SSP1

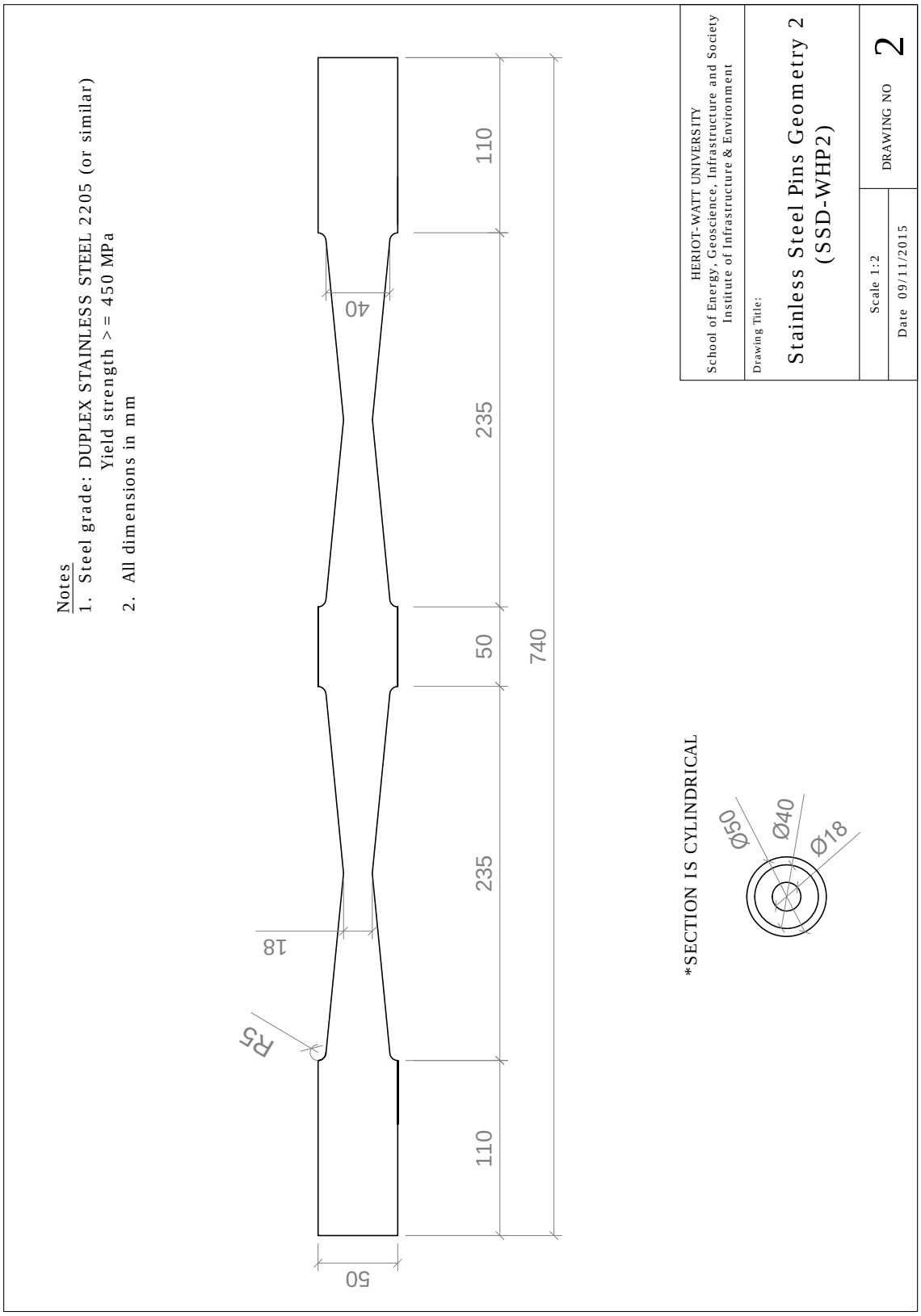

Figure B.2. Technical details of SSP2

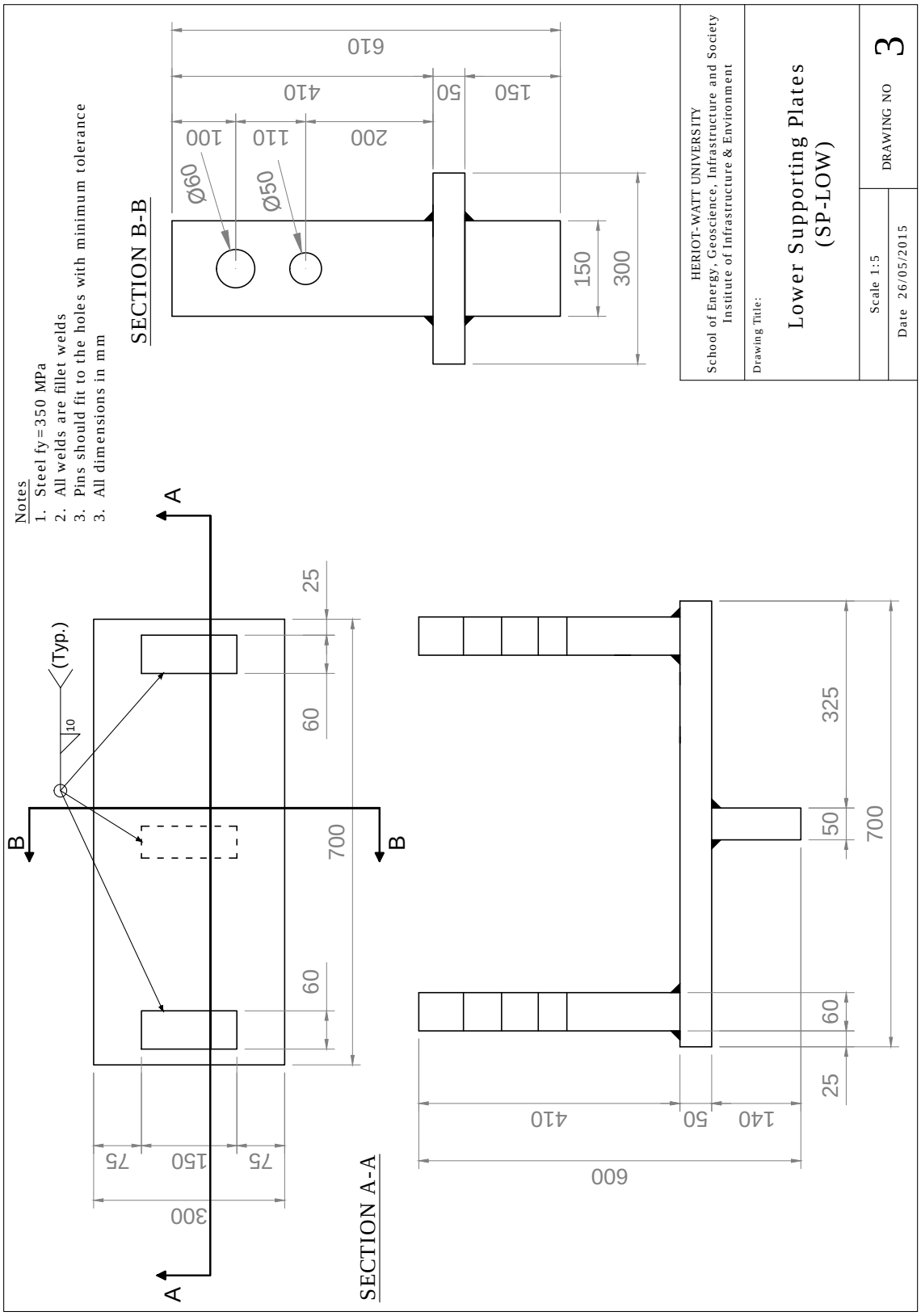

Figure B.3. Technical details of lower supporting plate

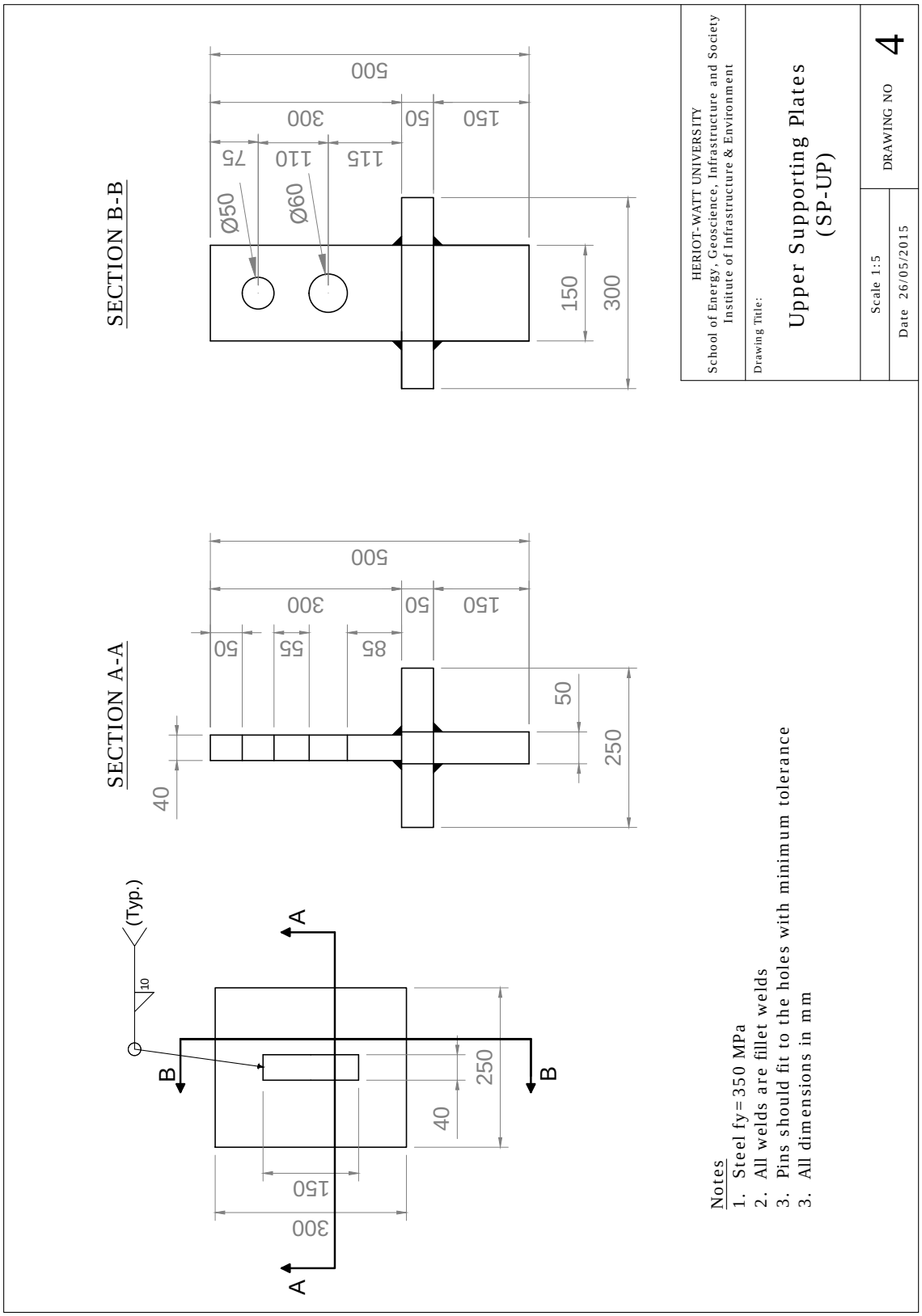

Figure B.4. Technical details of upper supporting plate

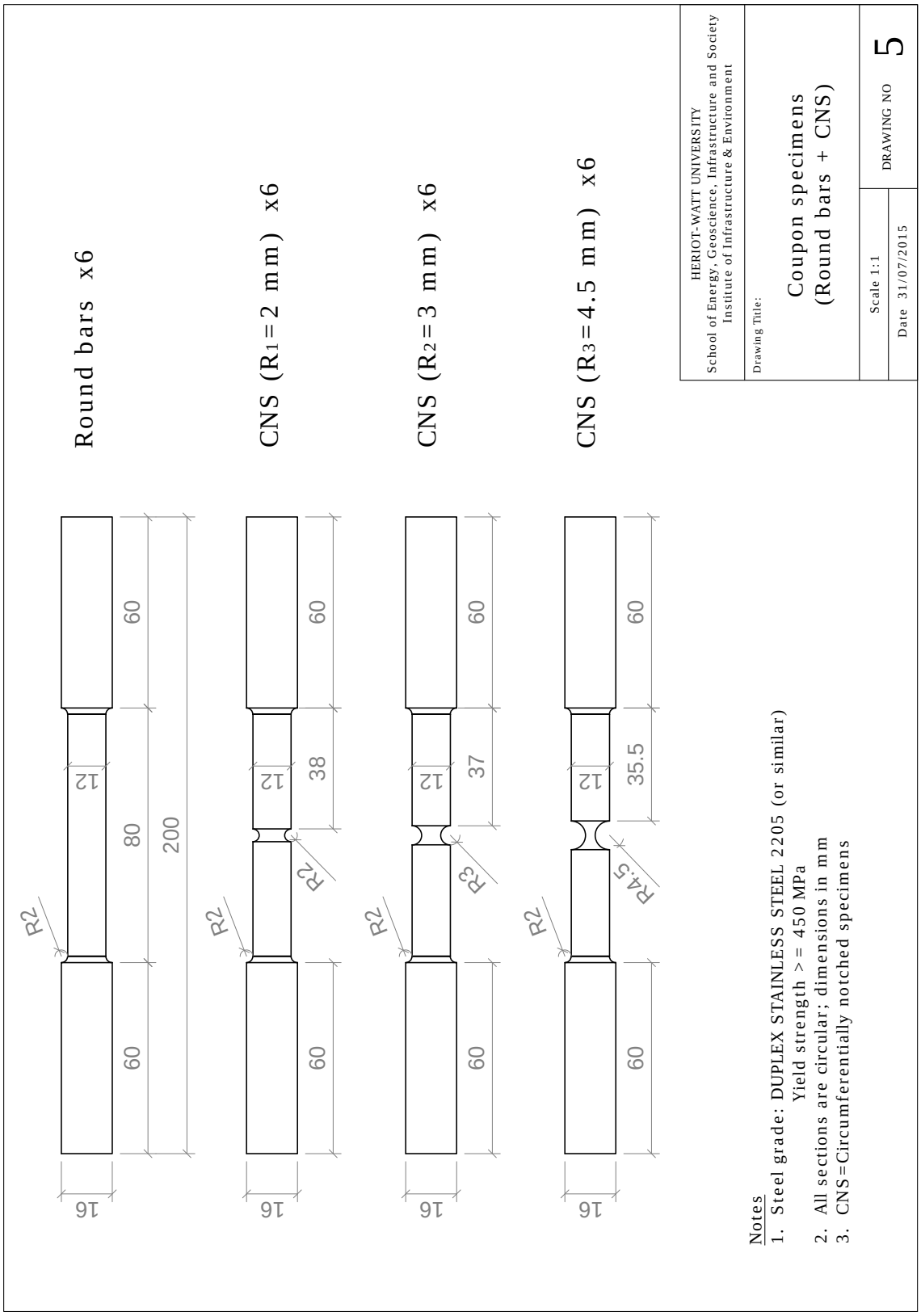

Figure B.5. Technical details of material coupon specimens

Appendix C

Abaqus Fracture Simulation of SSP under Monotonic Loading

Further to the simulation of SSP ductile fracture under ULCF presented in Chapter 6 (see Section 6.9), the fracture capacity of SSPs under monotonic loading is assessed. As described in Section 5.7.5, the monotonic tests on SSPs were terminated before reaching ductile fracture, to avoid excessive bending of the lower supporting plate. To provide an estimate of the SSP fracture capacity under monotonic loading, the monotonic tests of SSPs are numerically simulated.

To capture the pronounced bending of the lower supporting plate at large displacements, i.e., > 60 mm, the FEM models used for the cyclic tests of SSPs are modified. Instead of modelling the small steel plate welded to the U-shaped assembly, fully-fixed boundary conditions are defined directly on the horizontal steel plate. Such constraint is applied to a slightly larger area than the nominal footprint of the vertical plate to model the welded joints. In the experimental tests, the steel collars were welded onto the specimen at some distance from the plates to prevent excessive bending of the vertical plate in the test with SSPs. However, no contact was observed between the two during the tests, as the tight grip offered by the holes prevented the specimen from sliding. Therefore, the steel collar is not modelled.

The explicit analyses of the monotonic tests are performed imposing displacements up to the complete failure of the specimens. The Abaqus fracture initiation ($\alpha_{\text{mono}} = 0.8$) and evolution parameters calibrated for the monotonic coupon tests are used (see Section 6.6.1). Figure C.1a shows the numerical

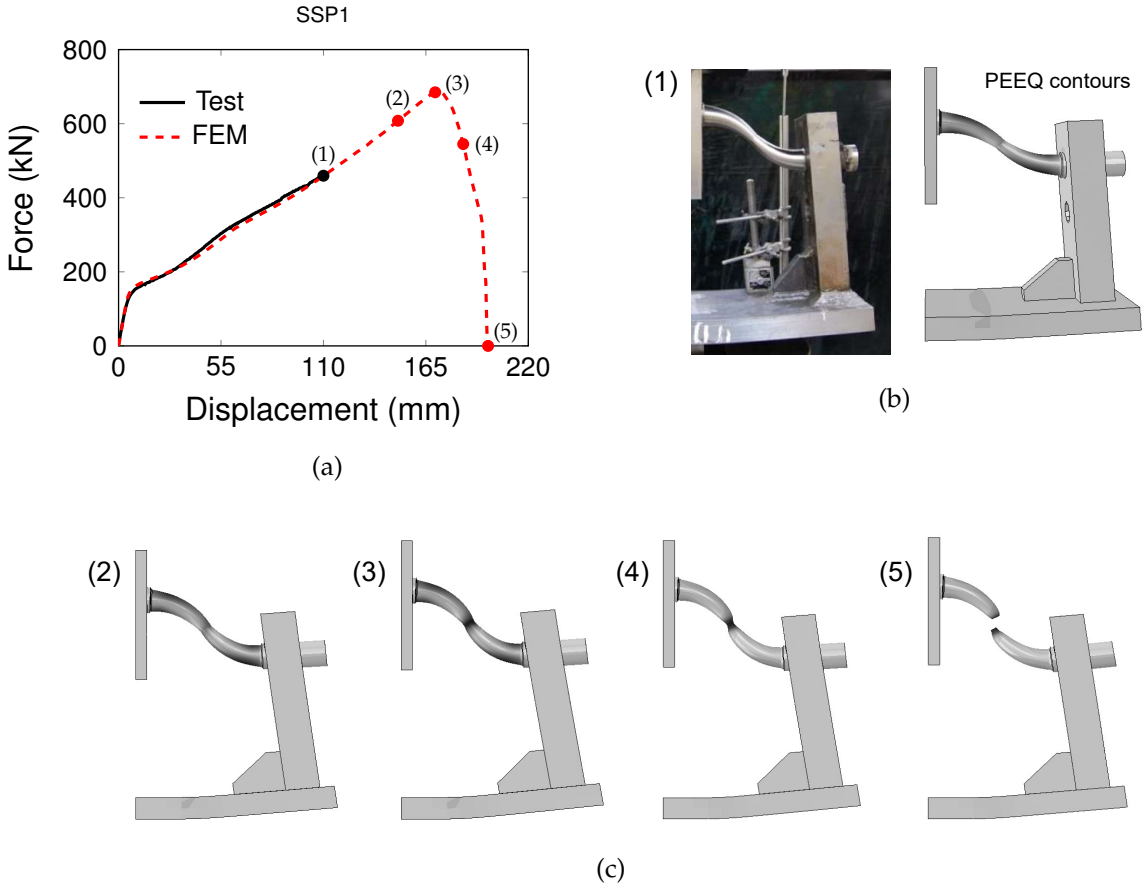

Figure C.1. Simulation of SSP1 monotonic test: (a) experimental-numerical force-displacement curves; (b) experimental-numerical deformed shapes at 110 mm displacement; and (c) numerical deformed shapes at successive stages up to failure

force-displacement response of SSP1: an excellent agreement is found with the experimental results up to the displacement at which the test was stopped (denoted as stage 1). The experimental and numerical deformed shapes of SSP1 at stage 1 are compared in Figure C.1b, showing that the FEM model is able to capture the significant bending of the lower supporting plate. Figure C.1c illustrates successive stages (2−5) of the numerical simulation, corresponding to the points indicated in the force-displacement curve in Figure C.1a. The numerical results show that the specimen exhibits high post-yield hardening up to stage 3, corresponding to an imposed displacement of 170 mm. At this stage, the PEEQ contours are characterised by a localised concentration of plastic deformations at the centre of the specimen, i.e., in the section having of minimum diameter D_i. As shown by the deformed shape in stage 4, such strain localisation results in a noticeable necking, leading eventually to the full-section fracture of the specimen at a displacement of 200 mm (stage 5), i.e., nearly

twelve times u_{DBE}. Such fracture mechanism reveals that the fracture capacity of SSPs under monotonic loading depends on the size of the internal diameter D_i.

The ductile fracture simulation of the SSP2 test is illustrated in Figure C.2: fracture initiates and develops at the centre of the specimen, similarly to SSP1. Full-section fracture is predicted to occur at an imposed displacement of 126 mm, i.e., nine times u_{DBE}. The reduced ductility of SSP2 is attributed to the smaller size of D_i. A comparison of the experimental and numerical force-displacement responses is shown in Figure C.2a, indicating a good correlation up to the displacement at which the test was terminated (stage 1). The FEM model is found to slightly underestimate the experimental hardening. This difference may be attributed to the clearance in the holes.

In the fracture sections of SSP1 and SSP2, the stress state is characterised by moderate triaxiality (T = 0.55) and axisymmetric stress state (ξ = 1). These stress conditions are similar to those produced in the CNSs tests, indicating the Abaqus

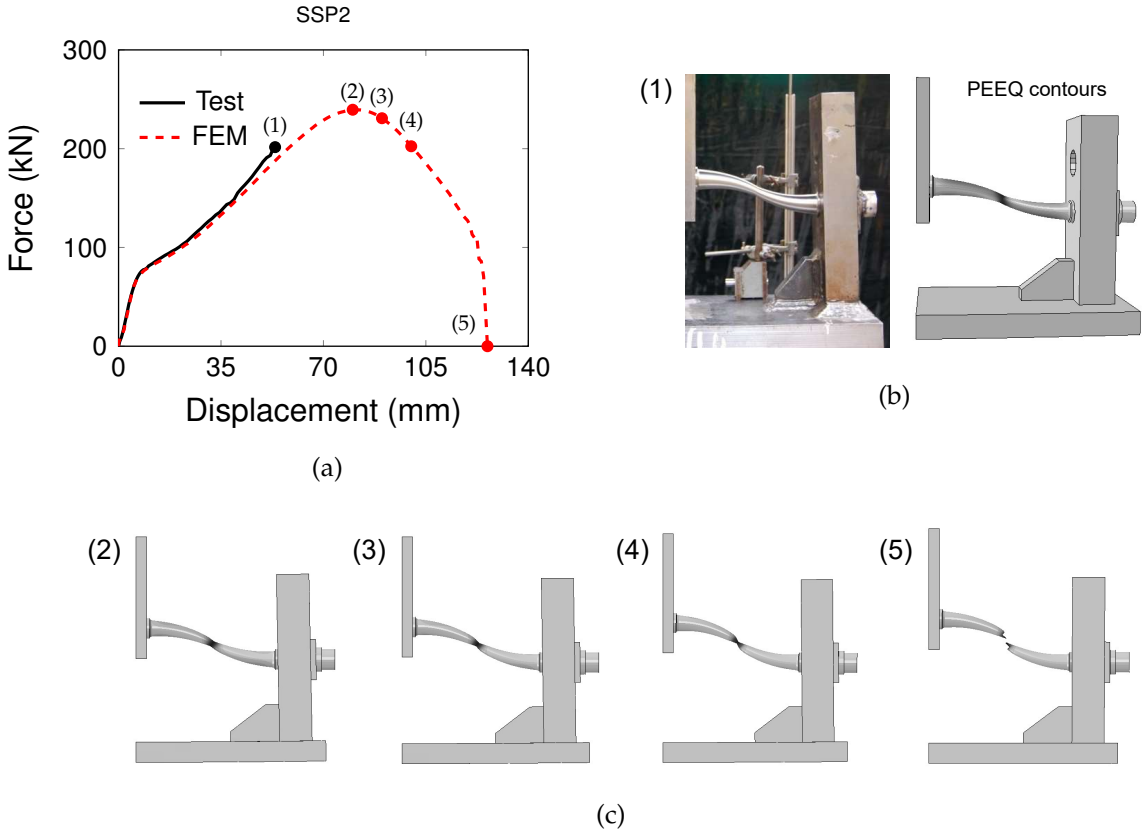

Figure C.2. Simulation of SSP2 monotonic test: (a) experimental-numerical force-displacement curves; (b) experimental-numerical deformed shapes at 55 mm displacement; and (c) numerical deformed shapes at successive stages up to failure

model calibrated using the monotonic CNS tests is suitable to predict fracture in SSPs under monotonic loading.

In conclusion, the experimentally-validated numerical simulations of the monotonic tests predict a large fracture capacity of SSPs under monotonic loading for the considered testing apparatus.

Appendix D

Incremental Dynamic Analyses (IDA) Results

This Appendix reports the detailed results of Incremental Dynamic Analyses (IDA) of the dual CBF-MRF under 24 ground motions (see Table 7.3), scaled to the collapse intensity.

Over 250 analyses were performed on a second-generation Intel i7 CPU at 3.40 GHz and 16 GB of RAM running on a 64-bit Windows 7 platform. The runtime for a single analysis varied depending on the duration, intensity and time step of the ground motion, ranging from 4 hours to a maximum of 20 hours.

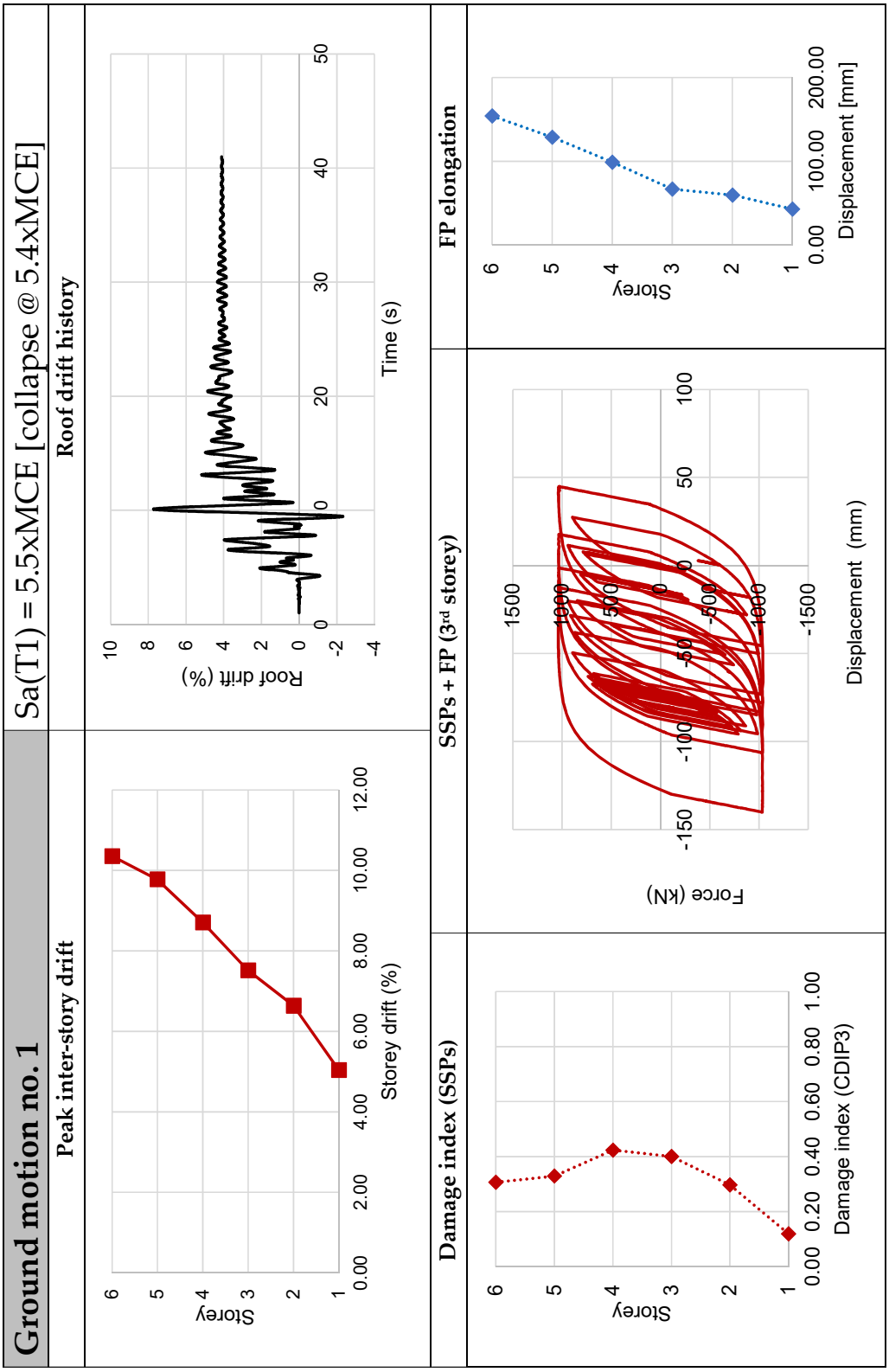

Figure D.1. IDA - Ground motion no. 1

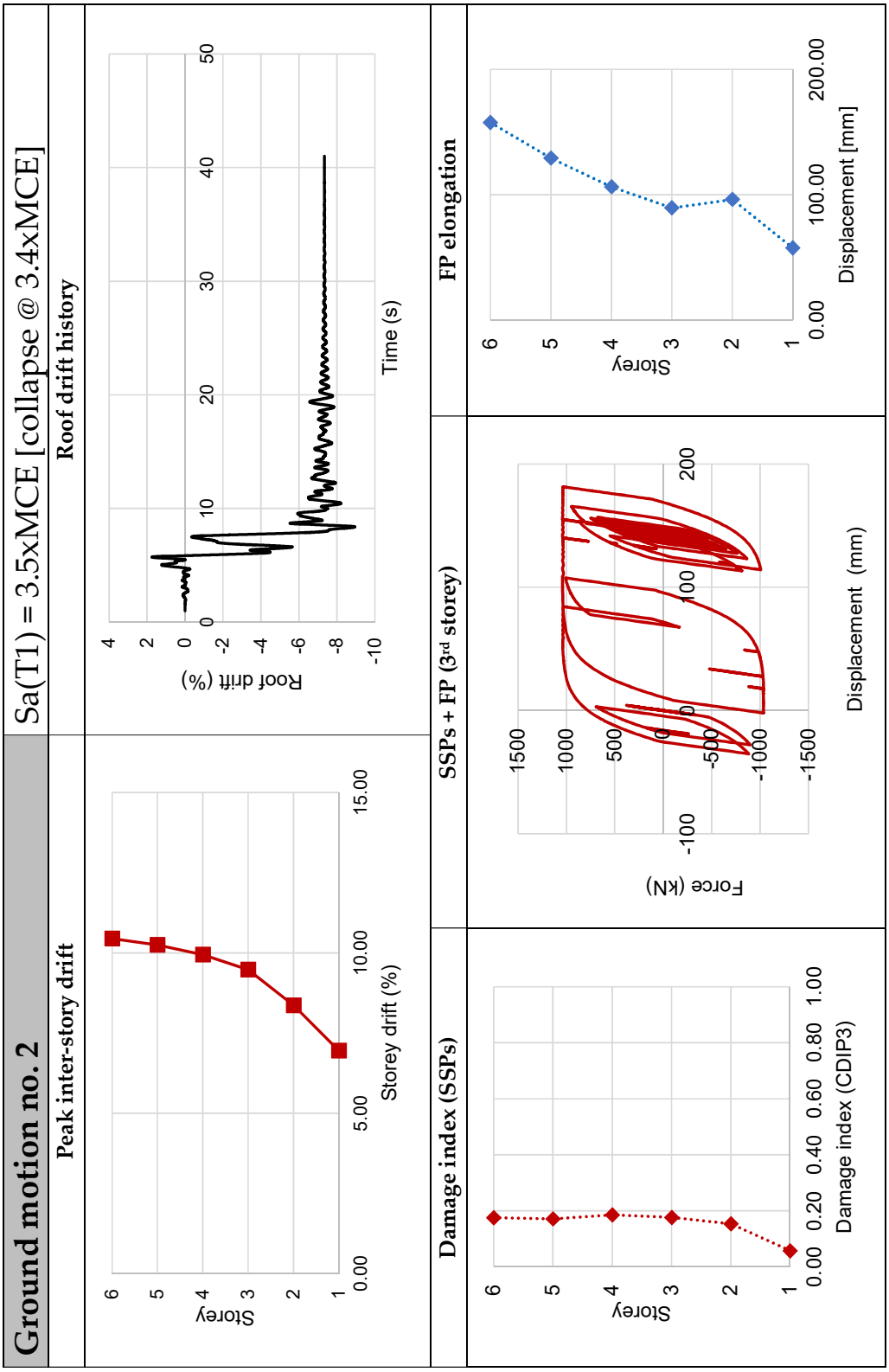

Figure D.2. IDA - Ground motion no. 2

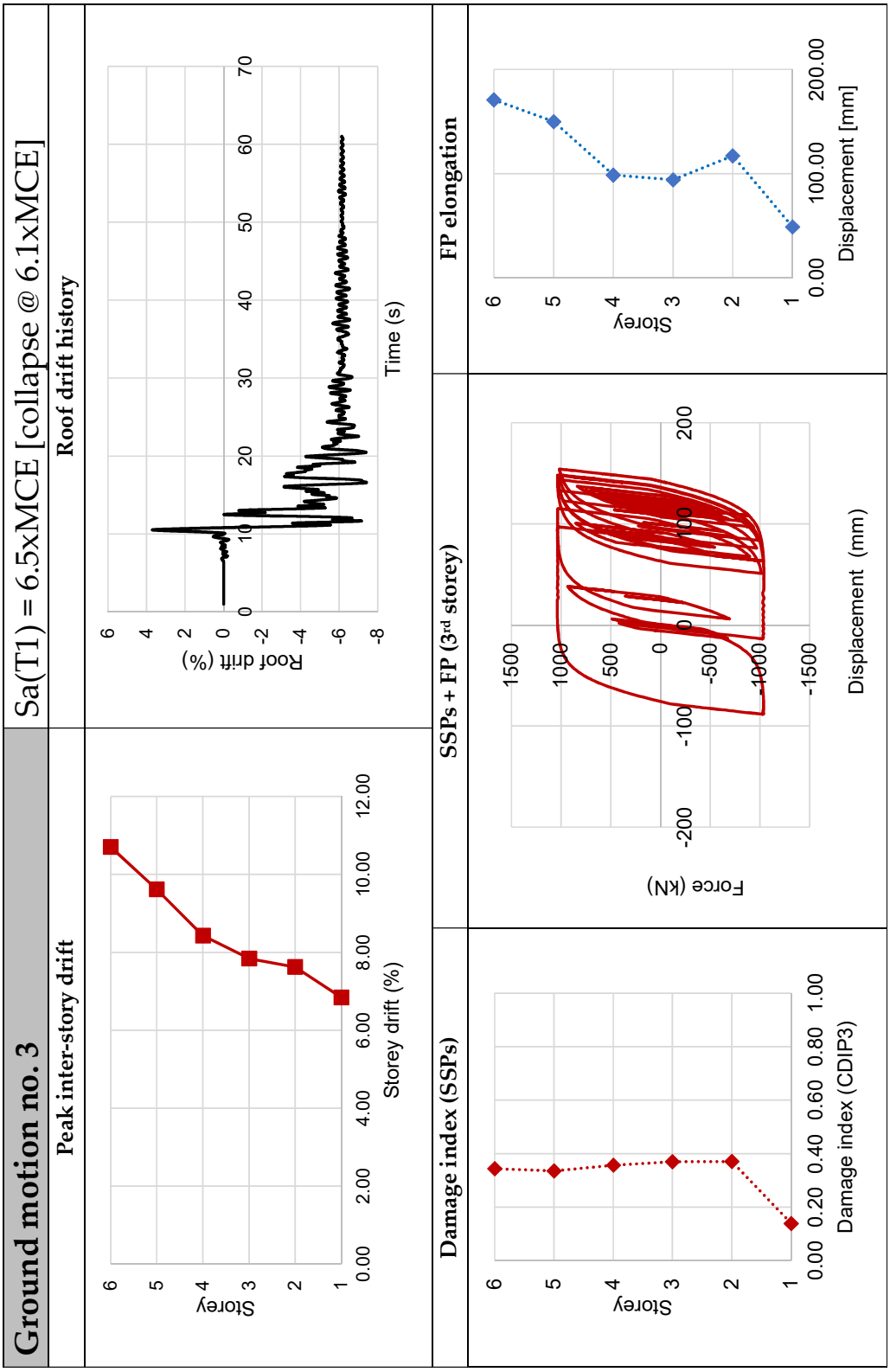

Figure D.3. IDA - Ground motion no. 3

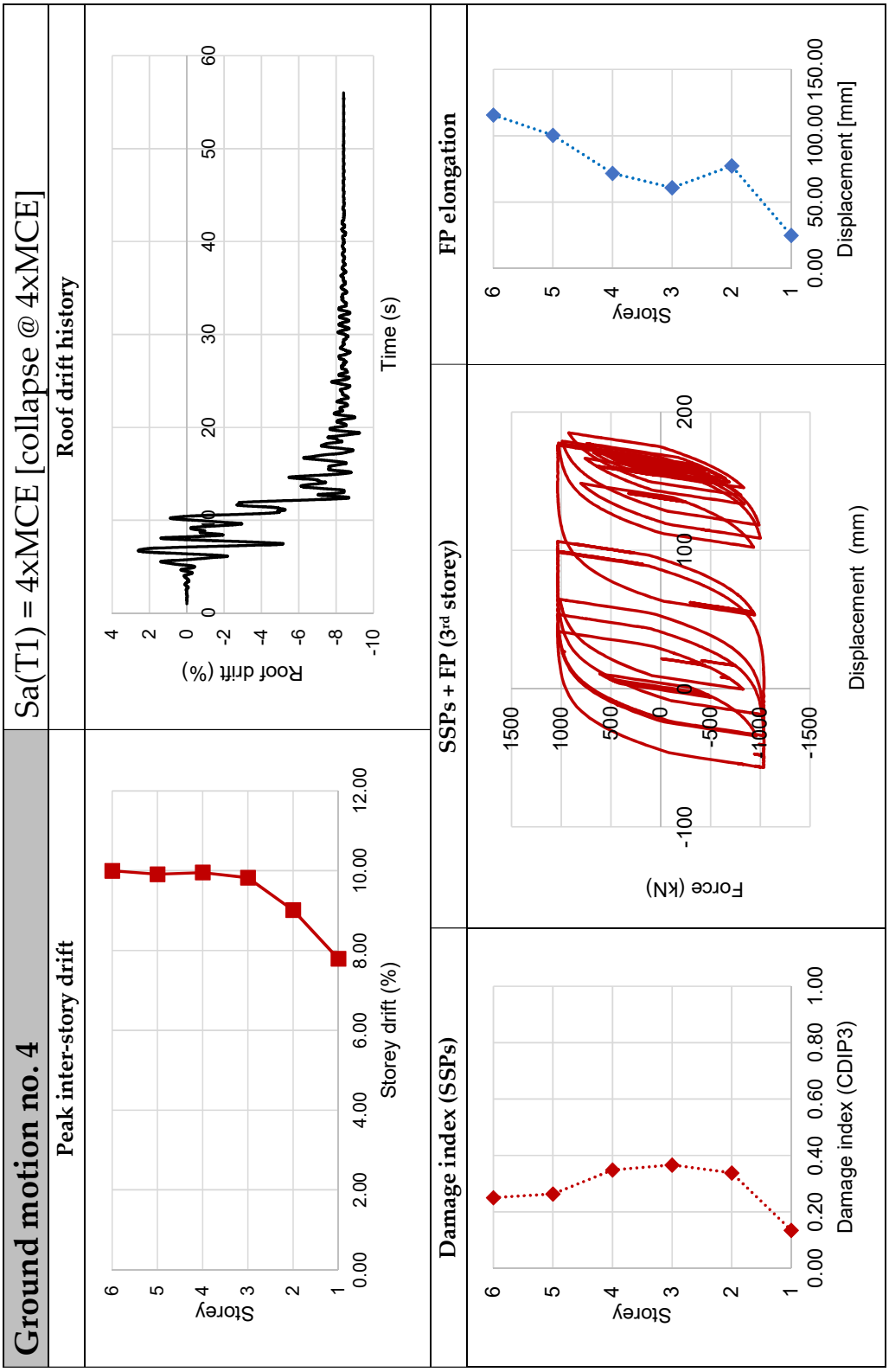

Figure D.4. IDA - Ground motion no. 4

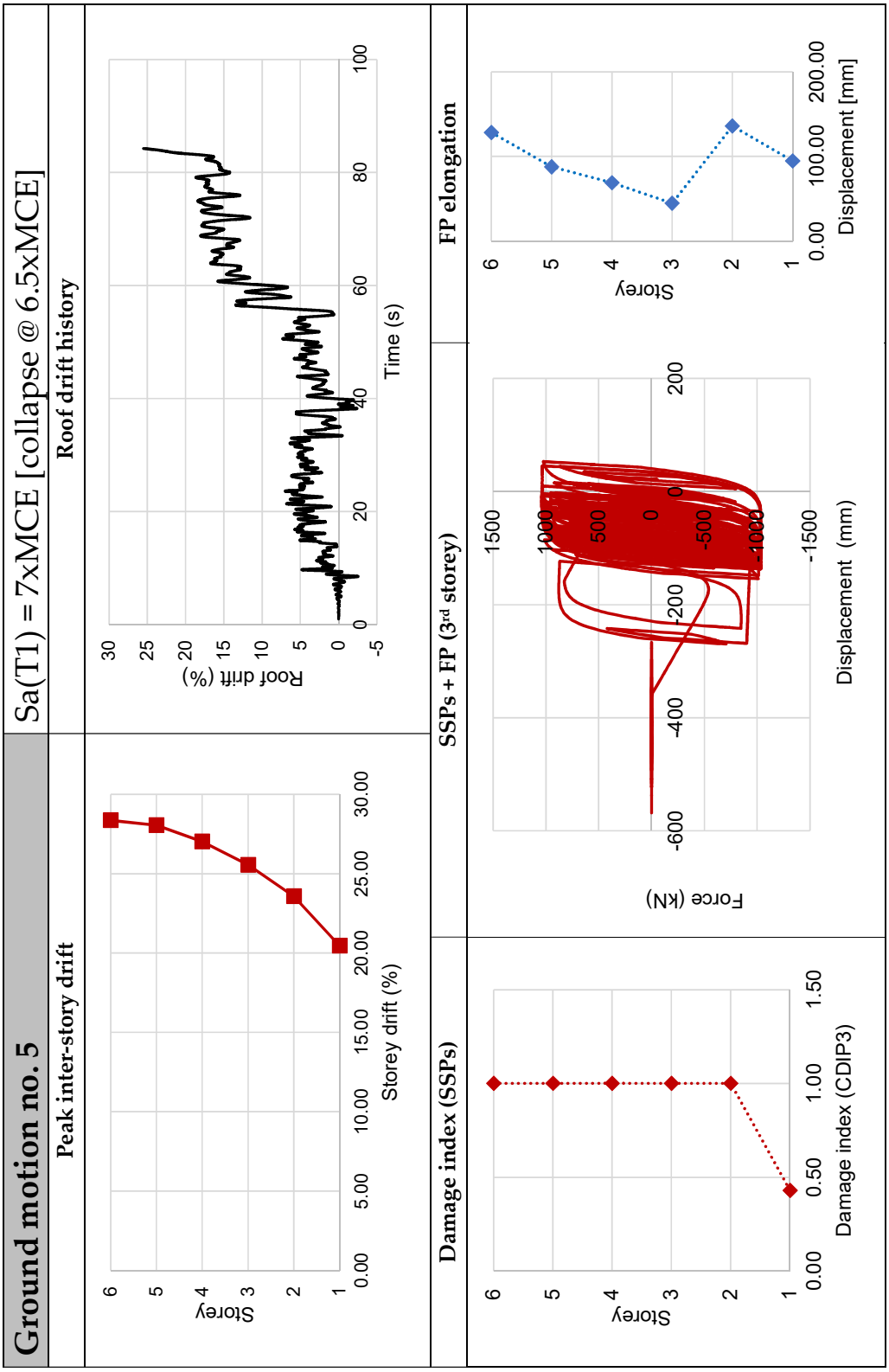

Figure D.5. IDA - Ground motion no. 5

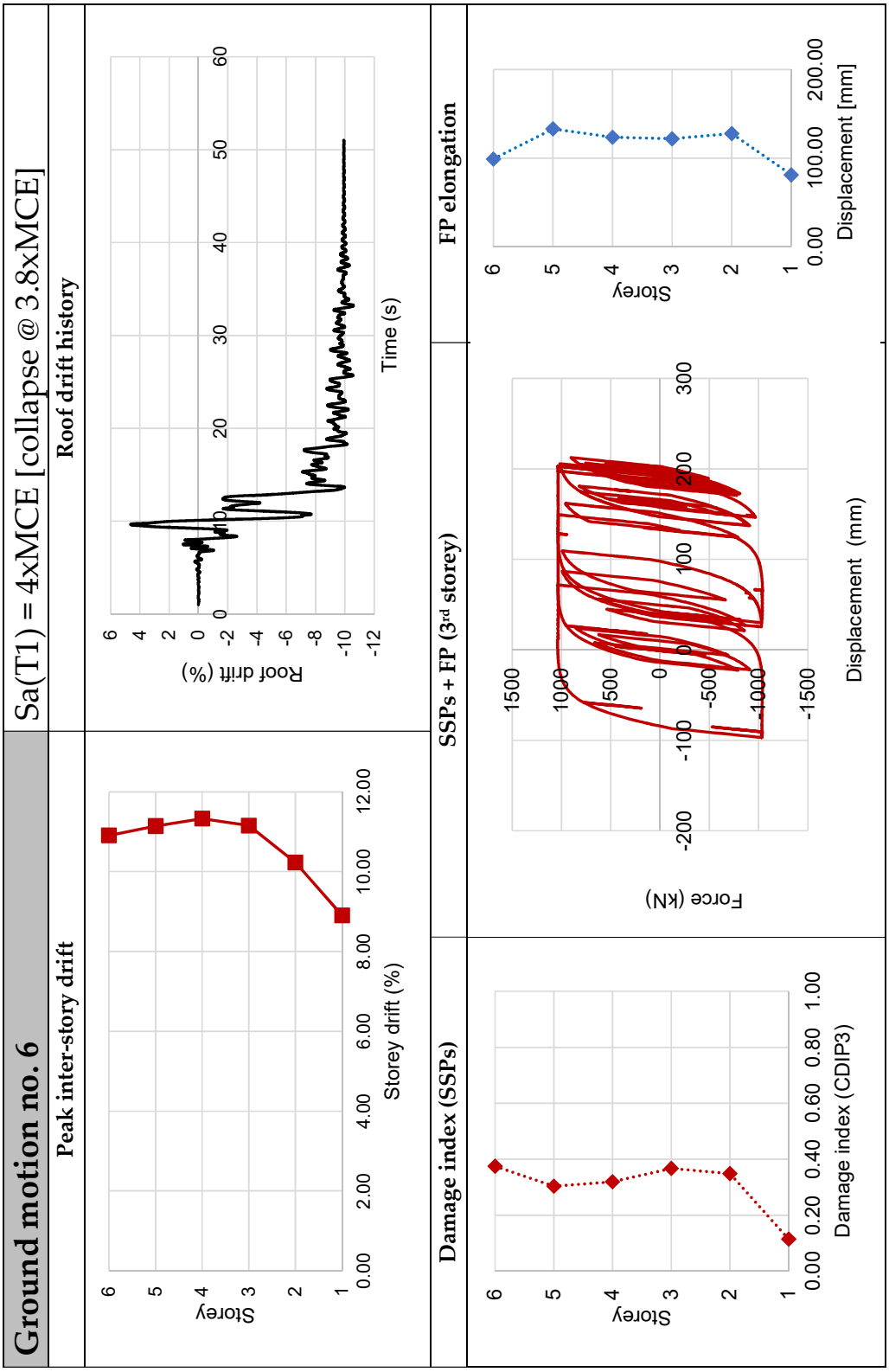

Figure D.6. IDA - Ground motion no. 6

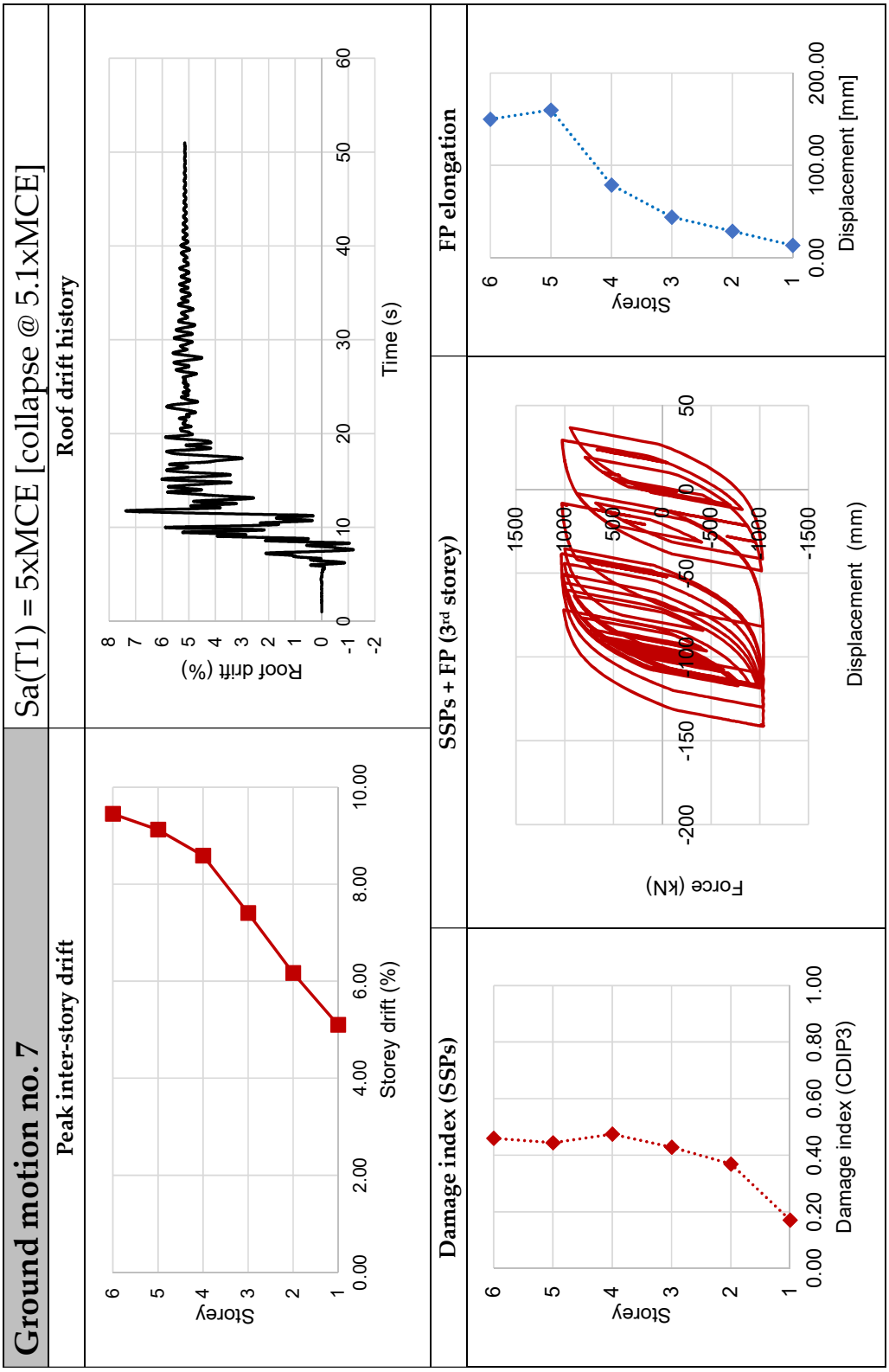

Figure D.7. IDA - Ground motion no. 7

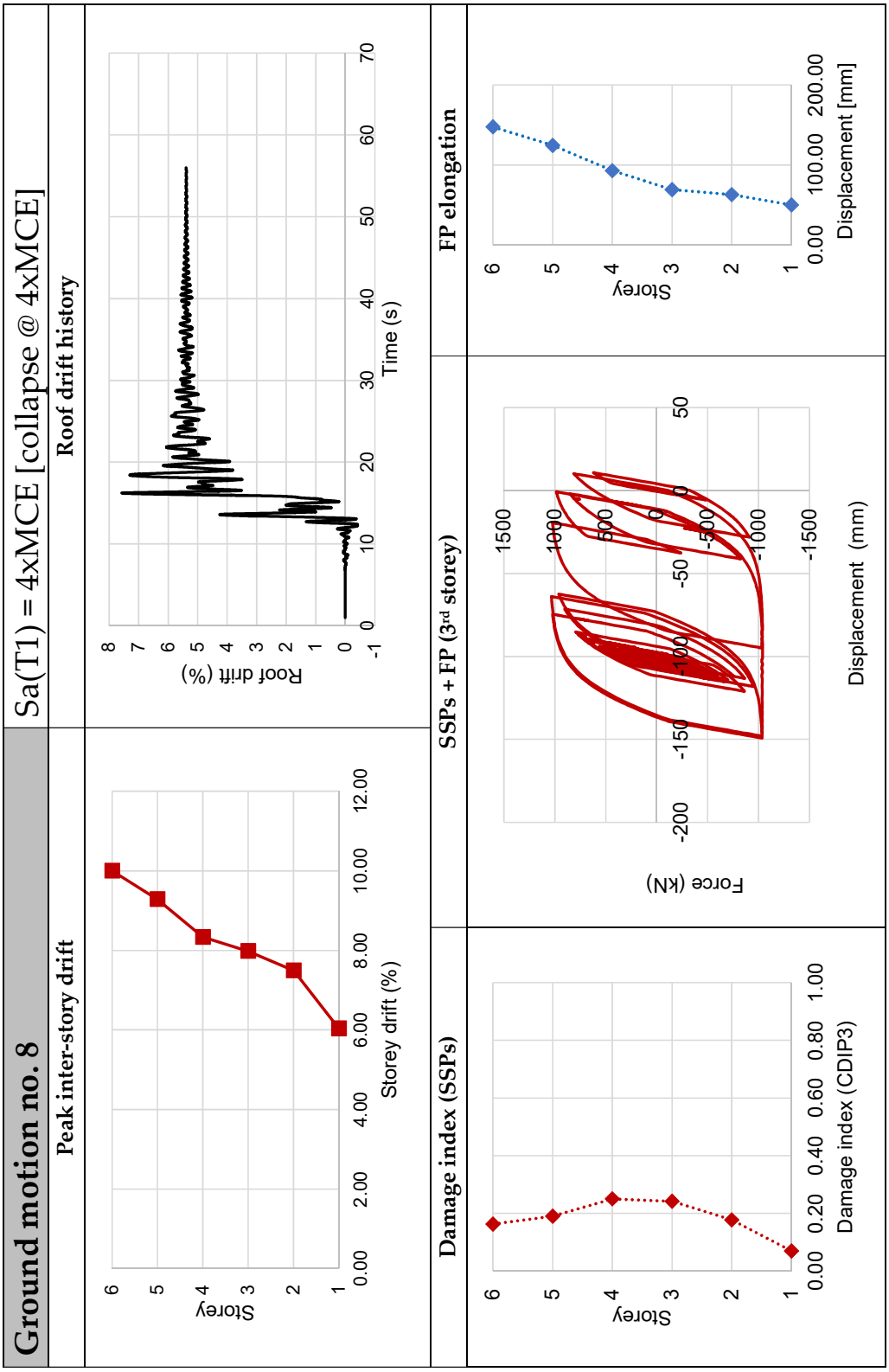

Figure D.8. IDA - Ground motion no. 8

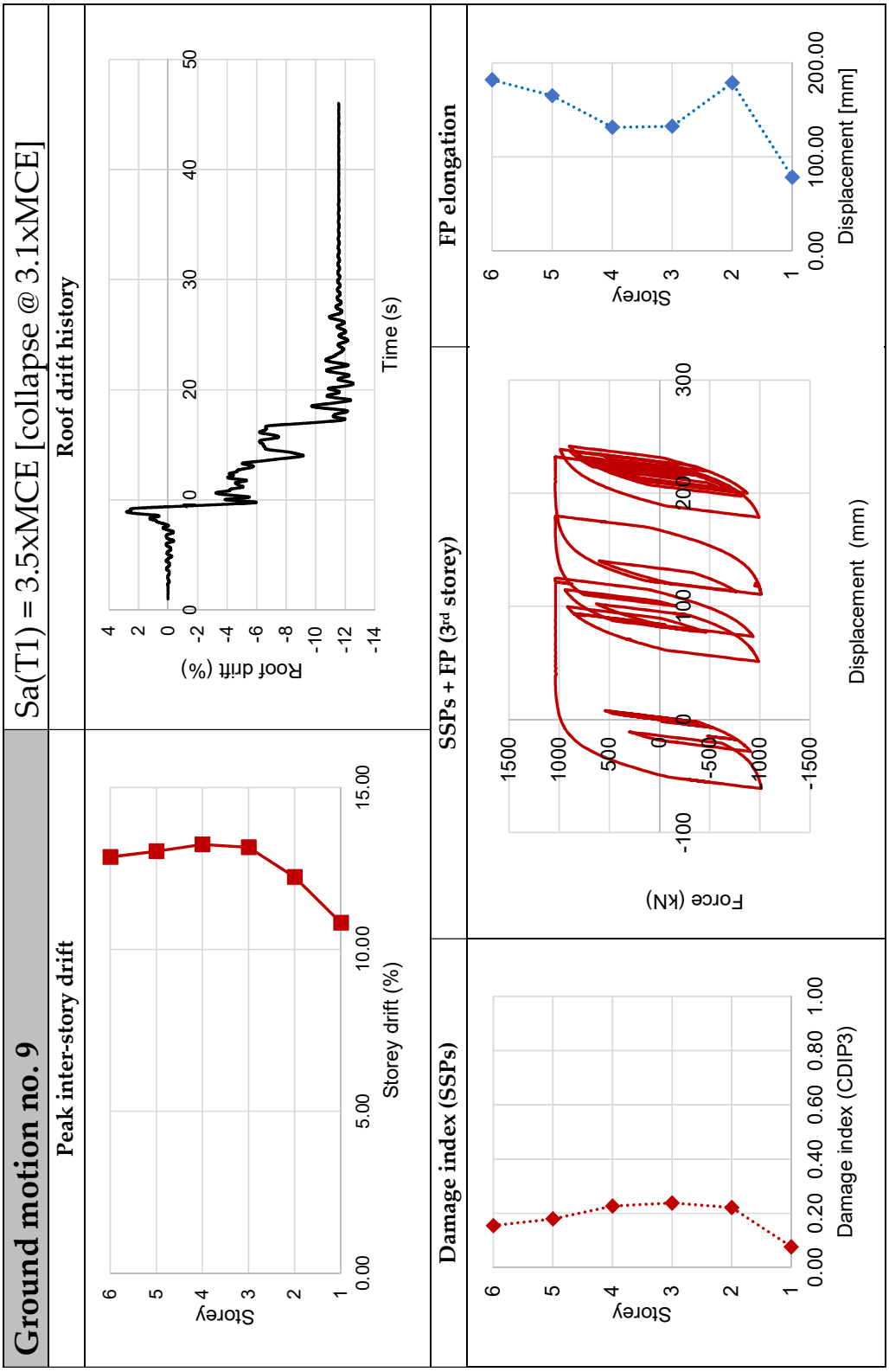

Figure D.9. IDA - Ground motion no. 9

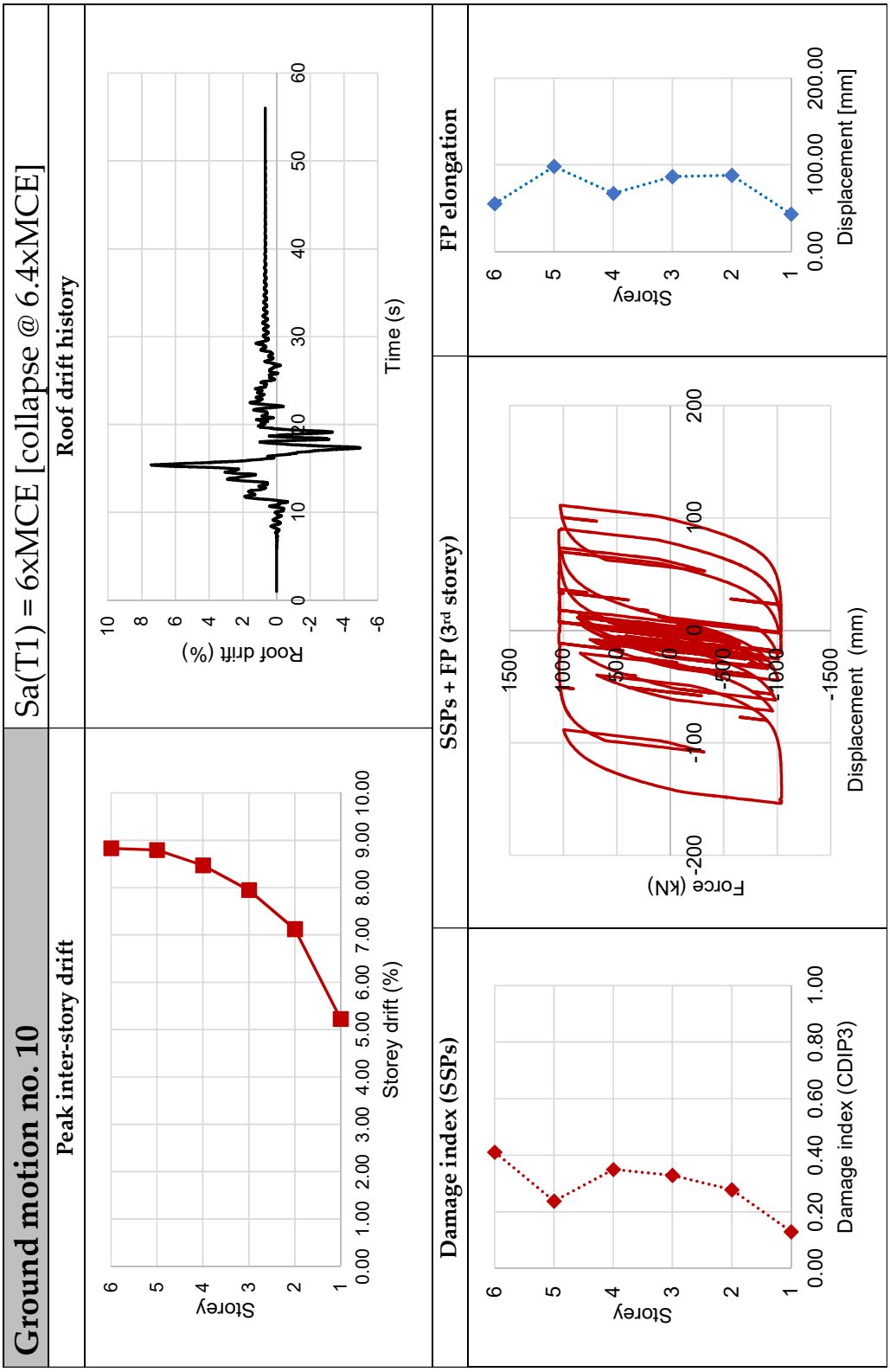

Figure D.10. IDA - Ground motion no. 10

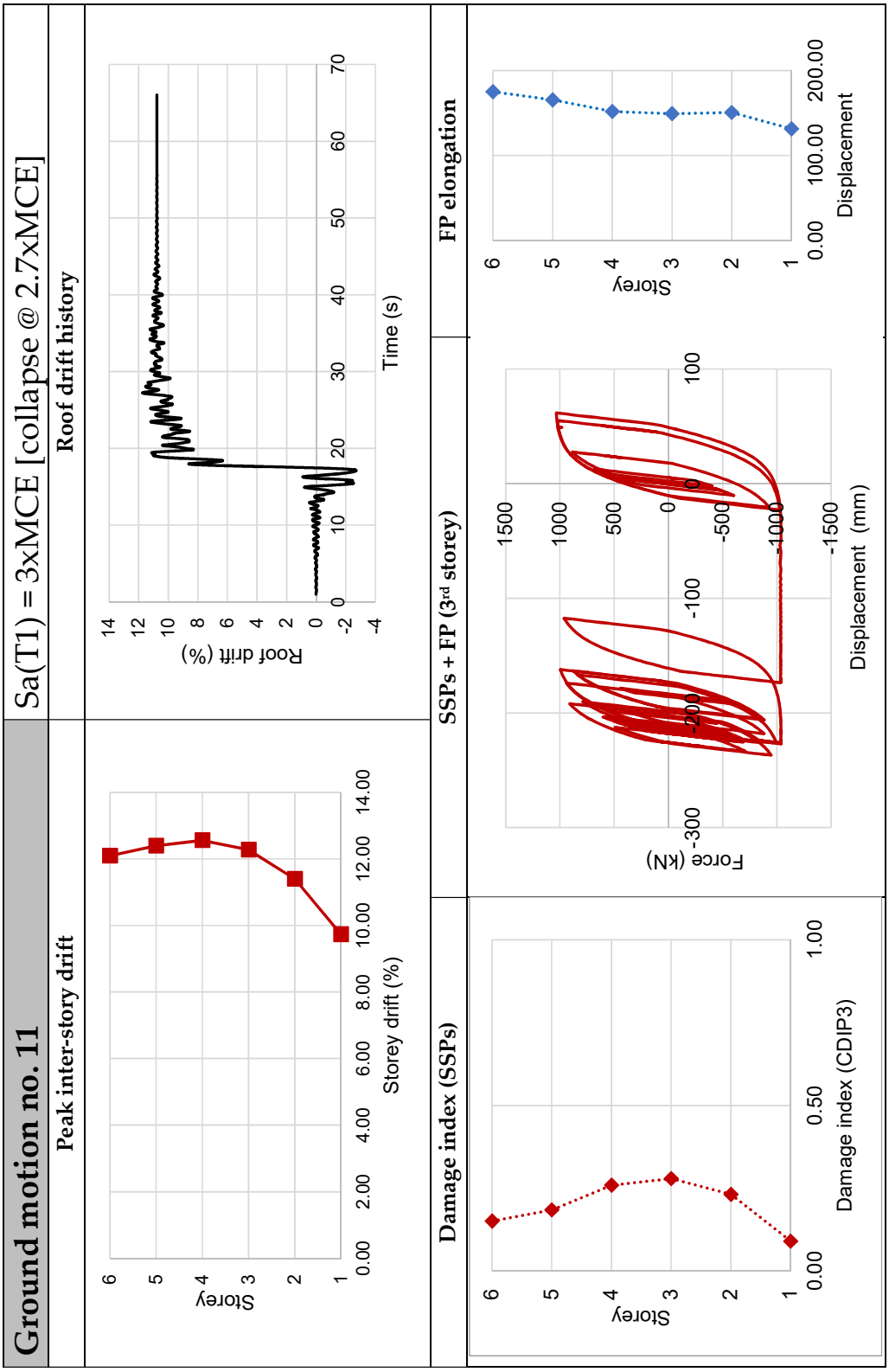

Figure D.11. IDA - Ground motion no. 11

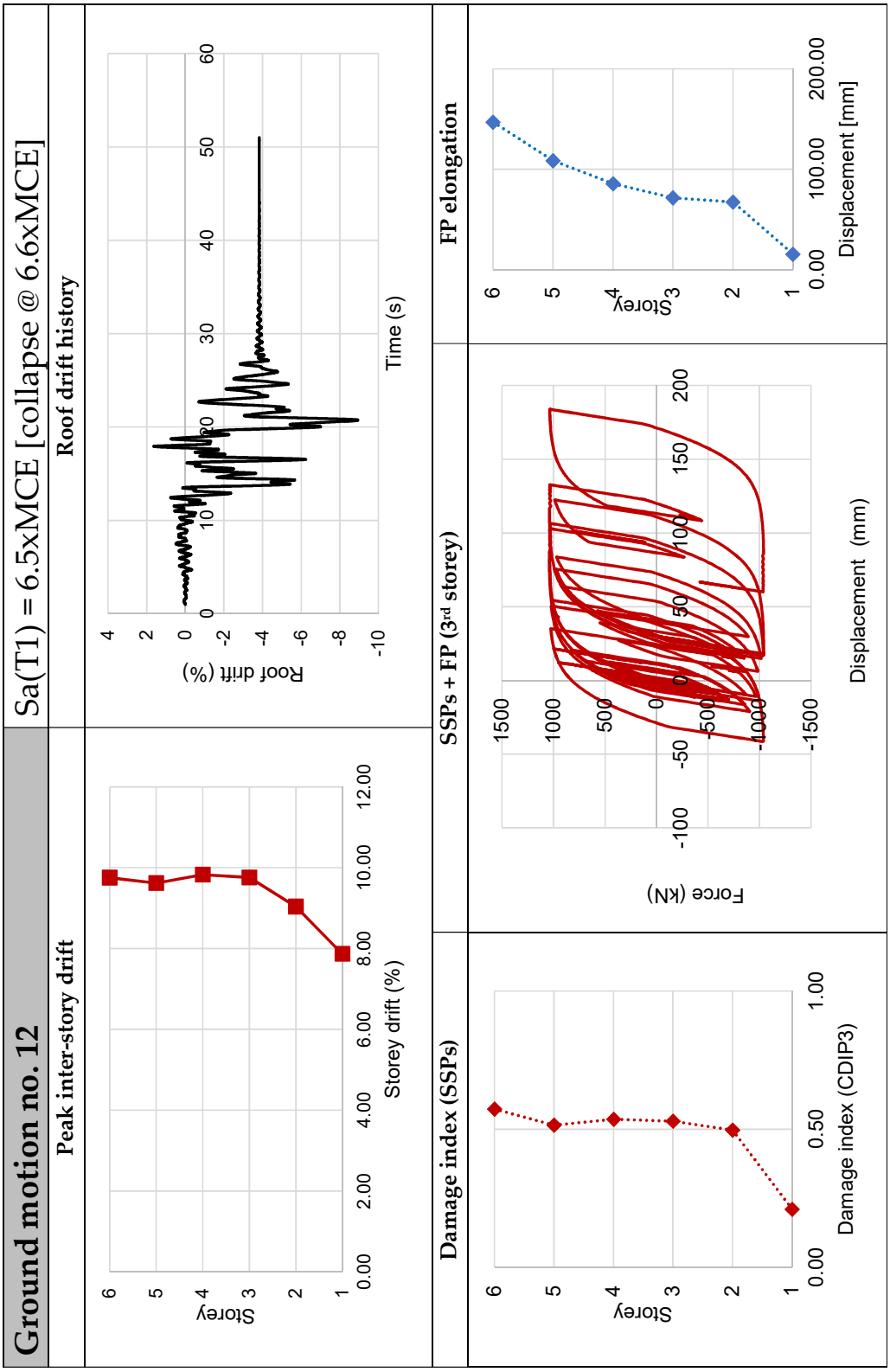

Figure D.12. IDA - Ground motion no. 12

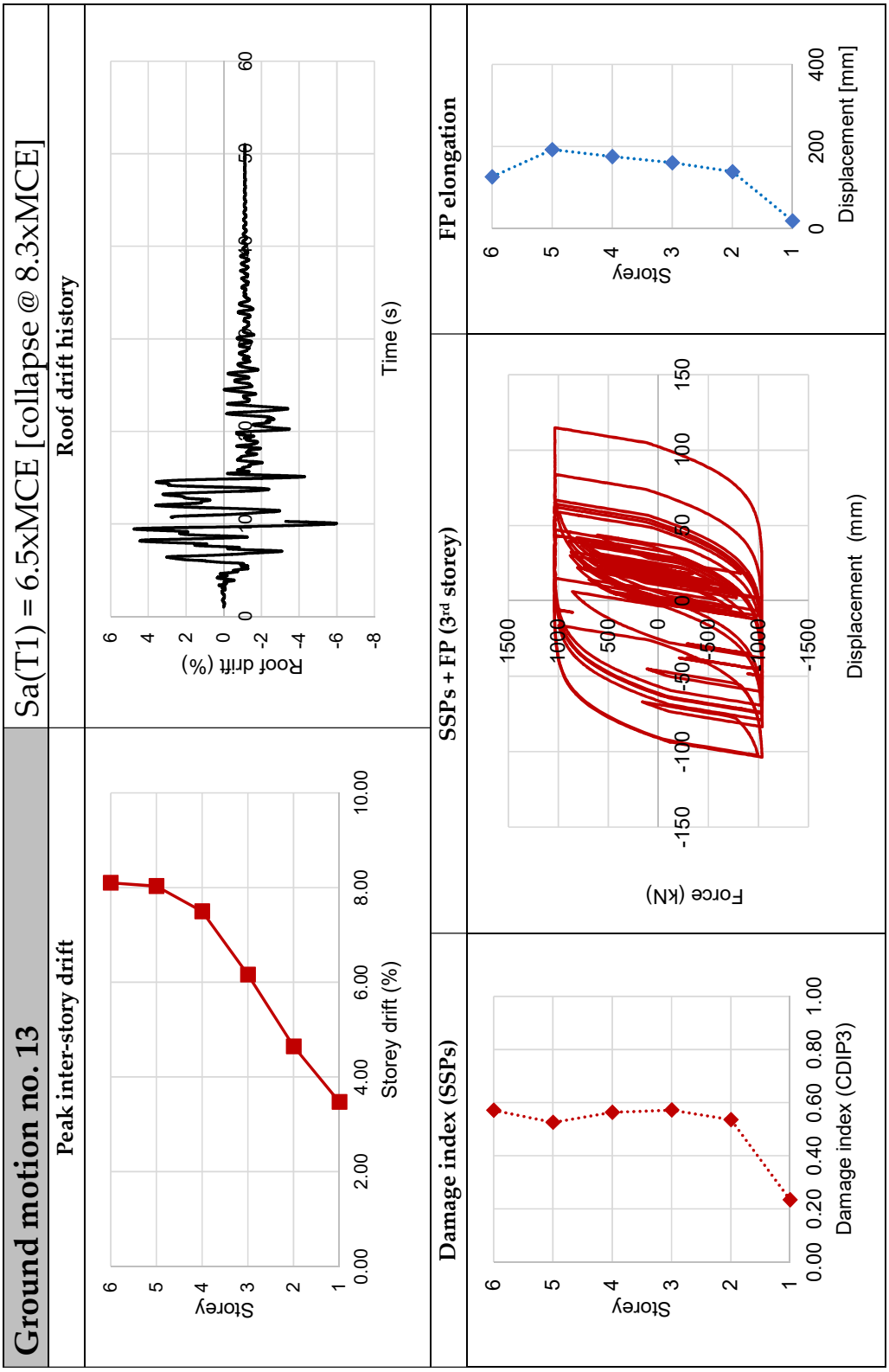

Figure D.13. IDA - Ground motion no. 13

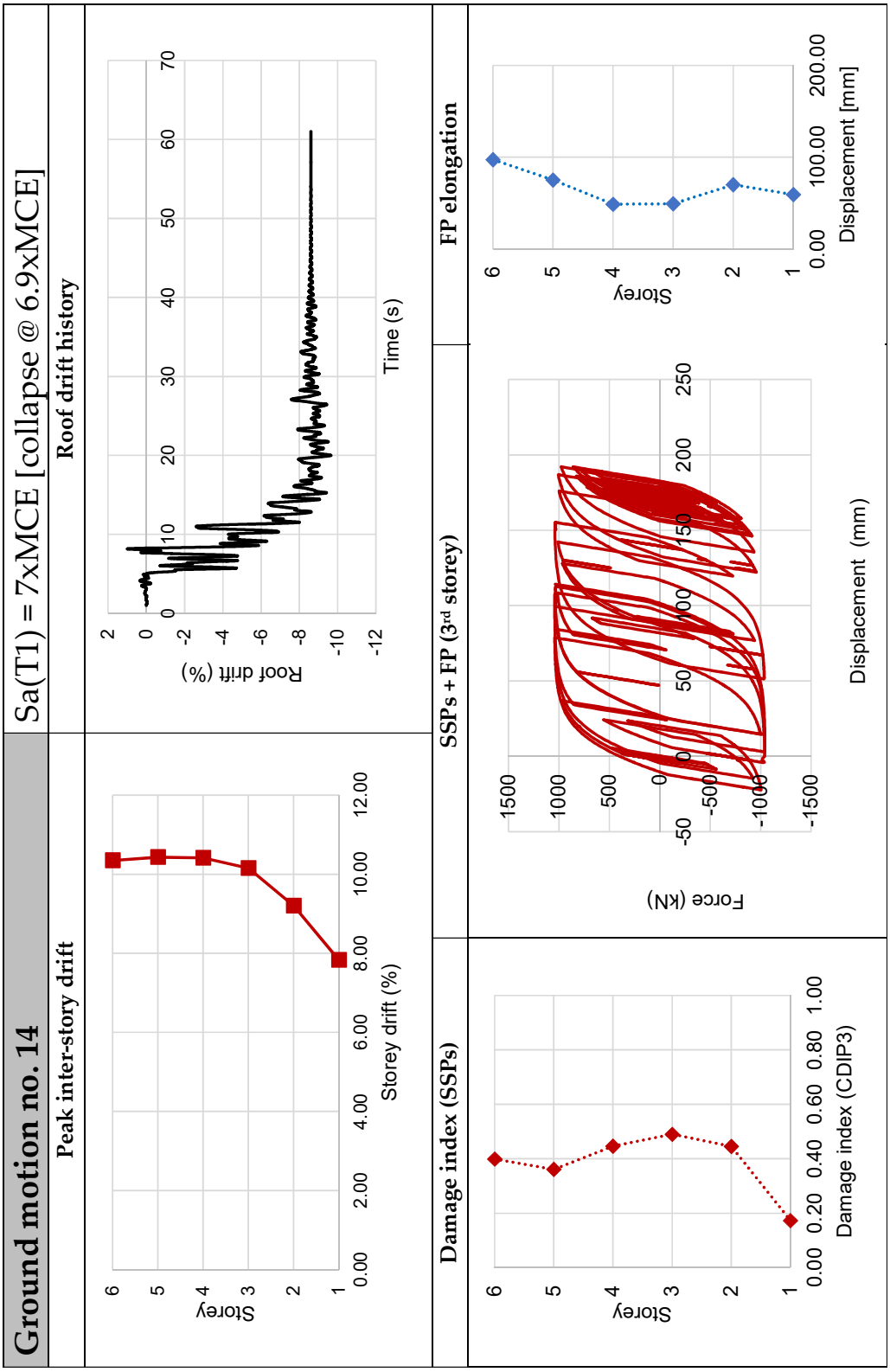

Figure D.14. IDA - Ground motion no. 14

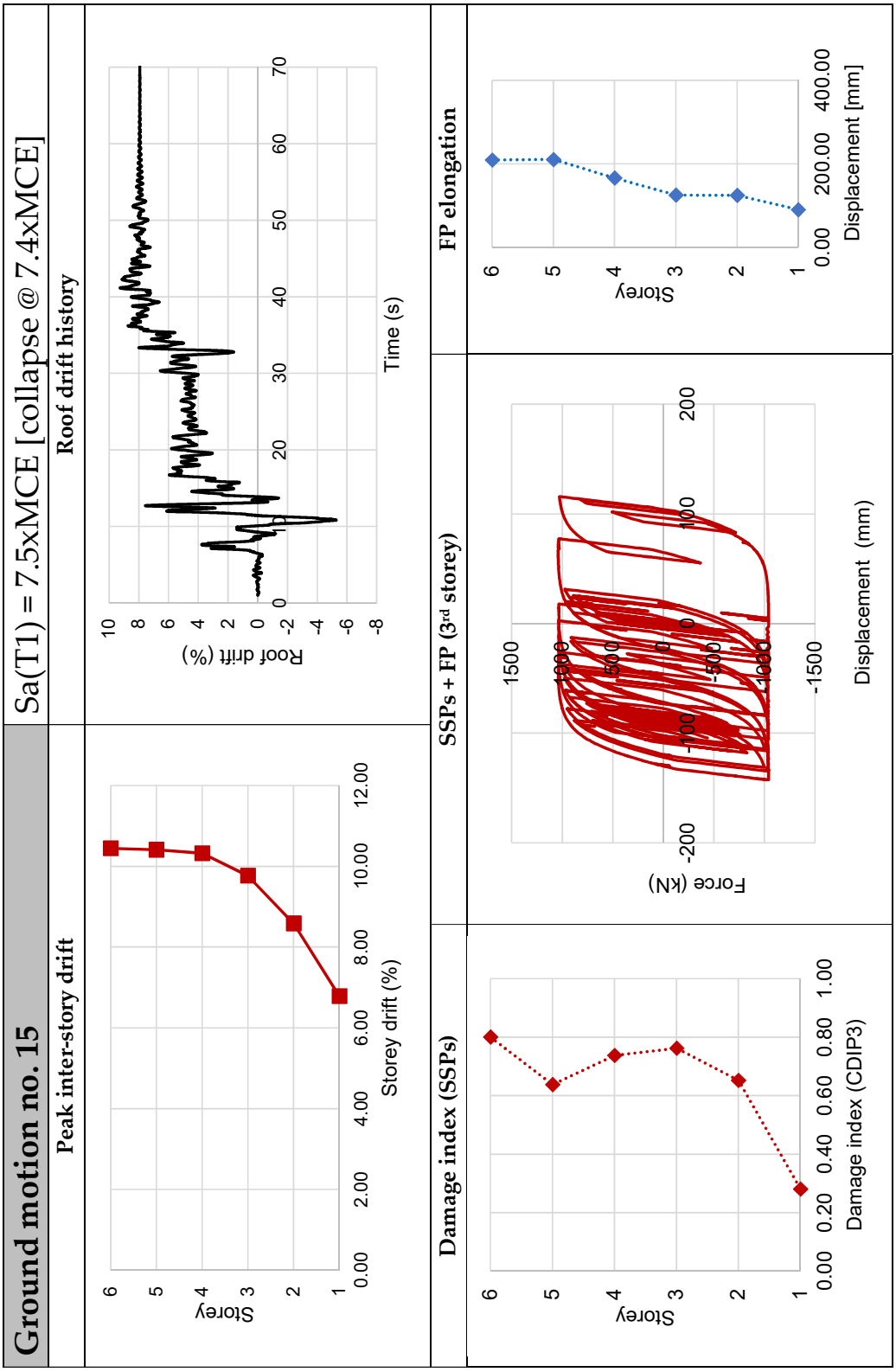

Figure D.15. IDA - Ground motion no. 15

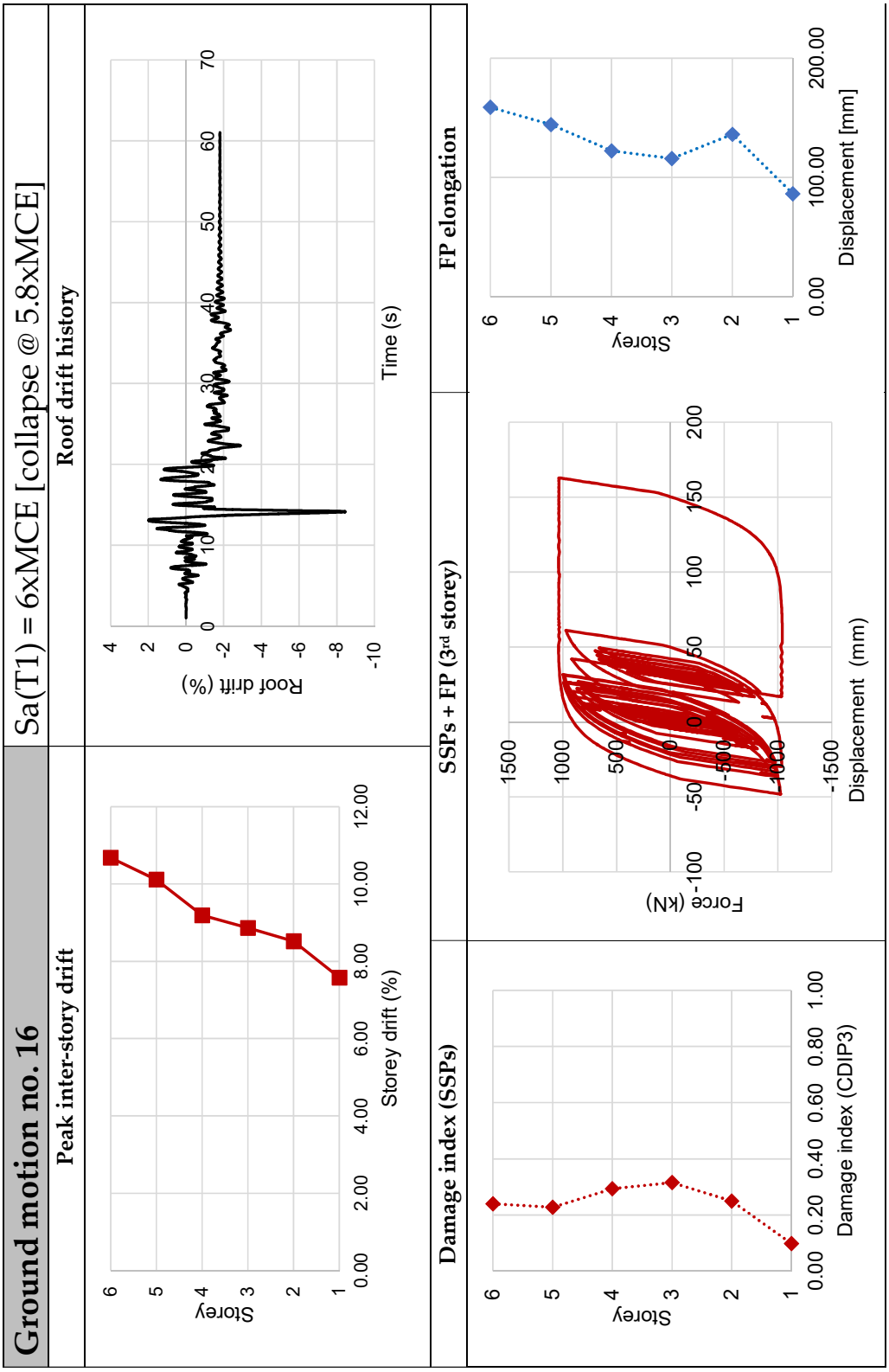

Figure D.16. IDA - Ground motion no. 16

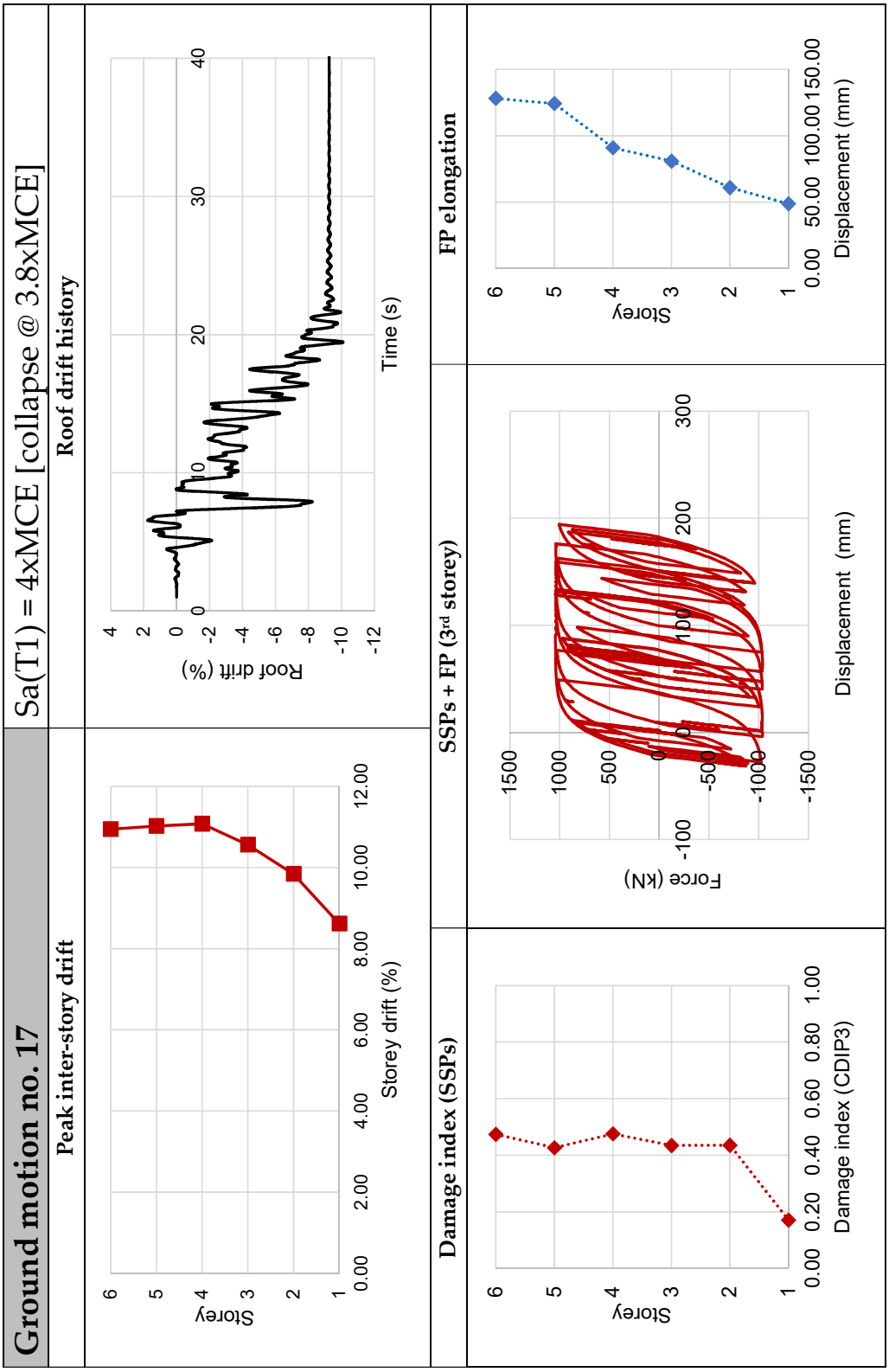

Figure D.17. IDA - Ground motion no. 17

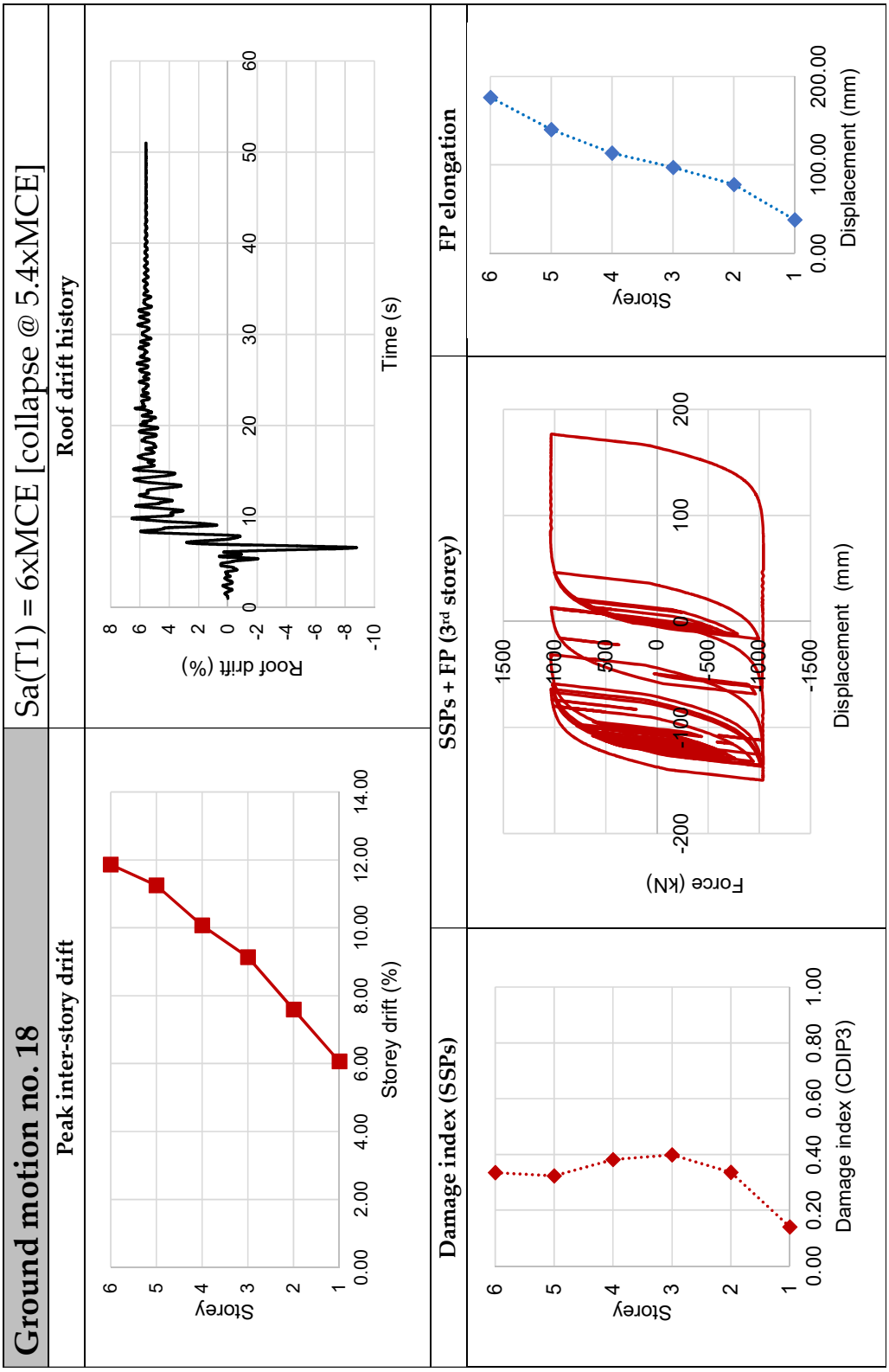

Figure D.18. IDA - Ground motion no. 18

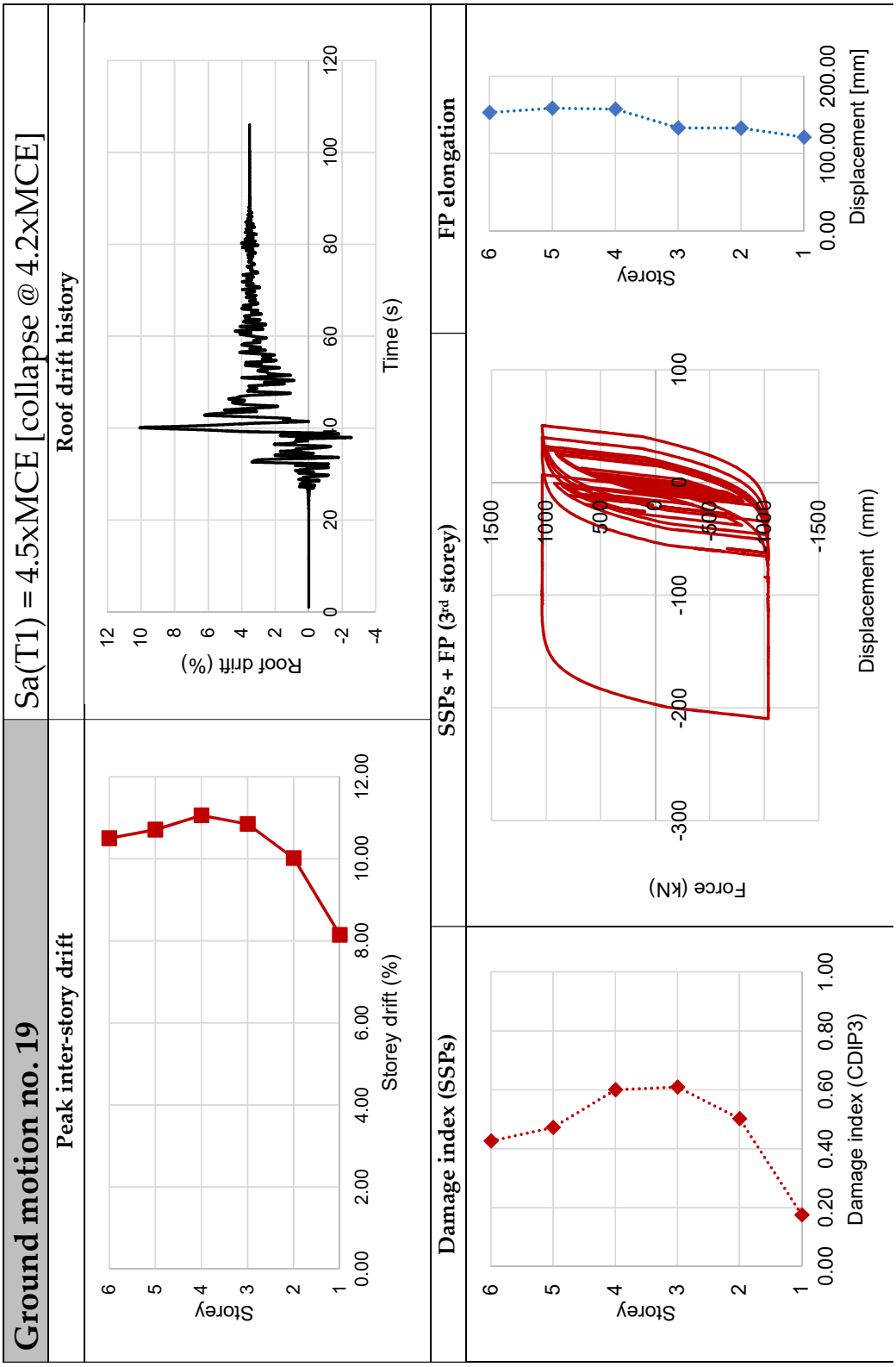

Figure D.19. IDA - Ground motion no. 19

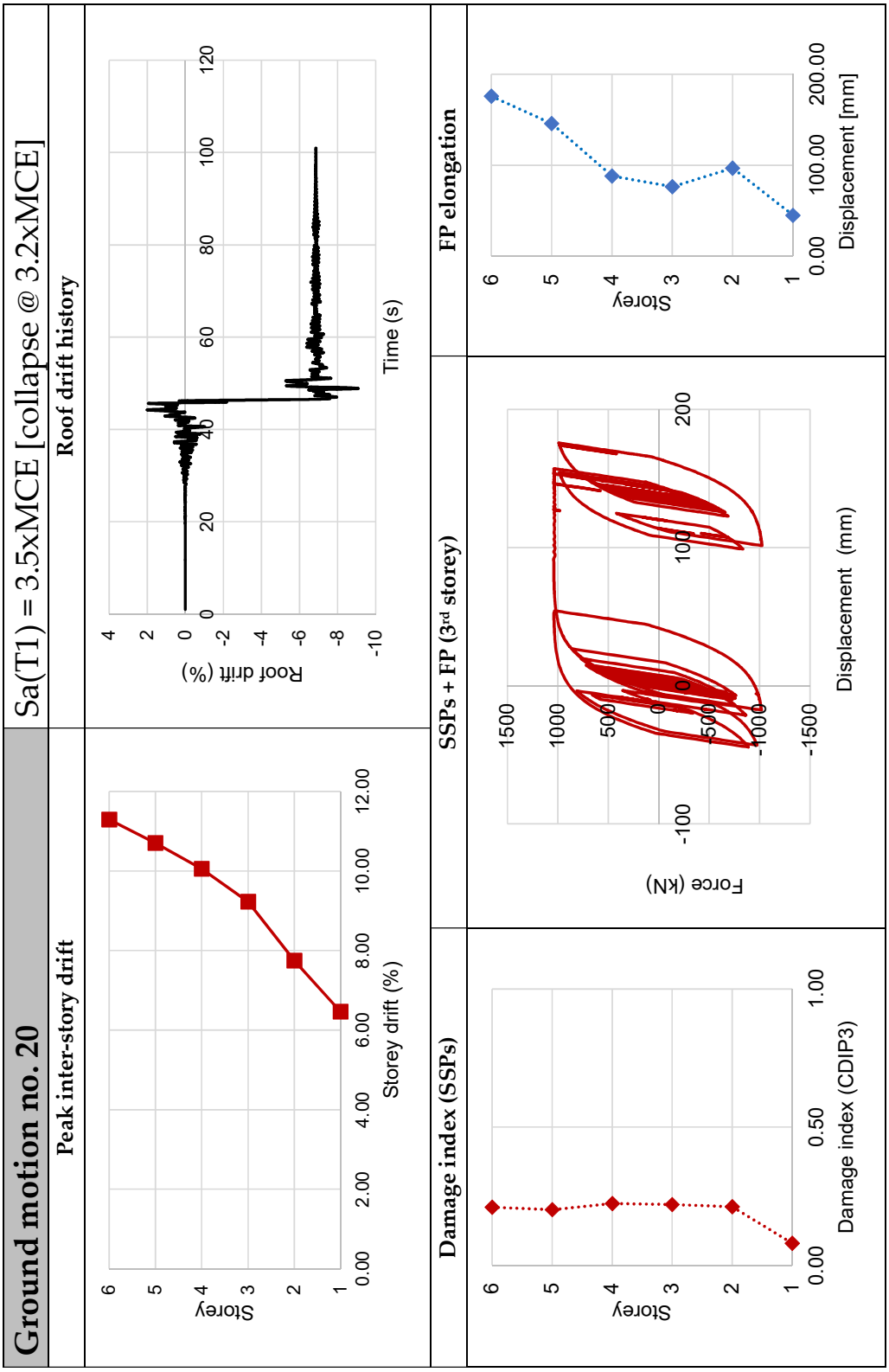

Figure D.20. IDA - Ground motion no. 20

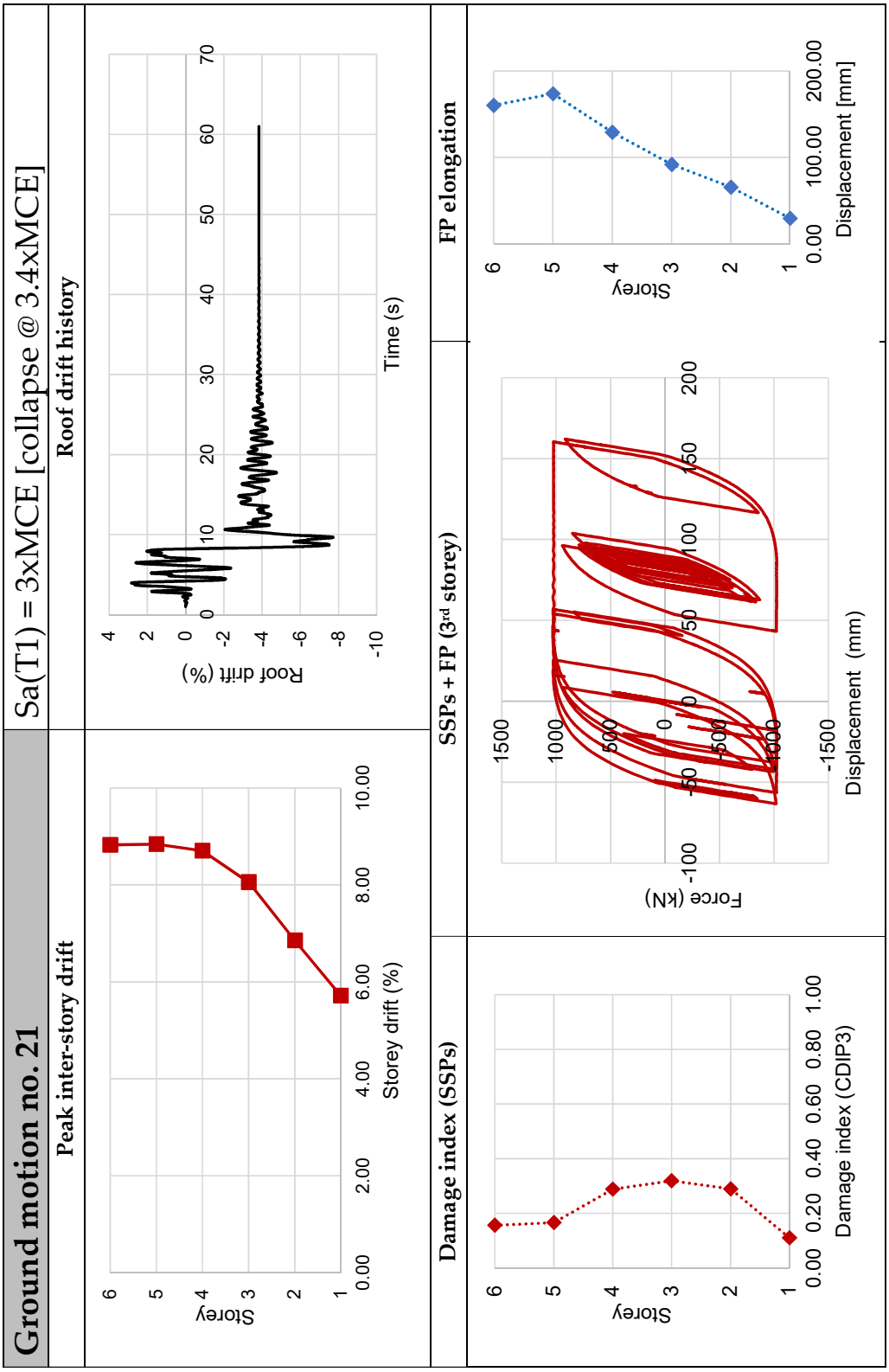

Figure D.21. IDA - Ground motion no. 21

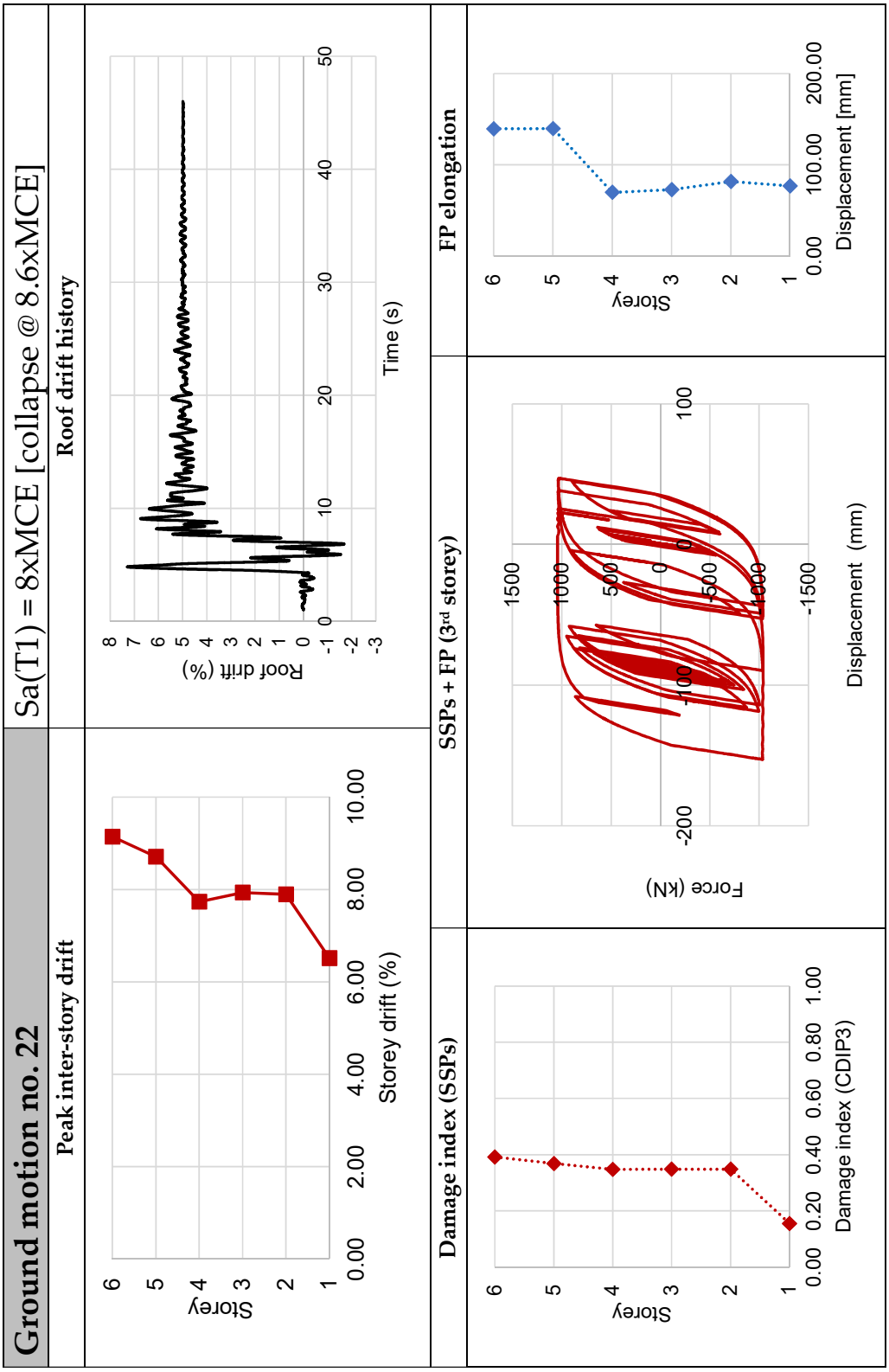

Figure D.22. IDA - Ground motion no. 22

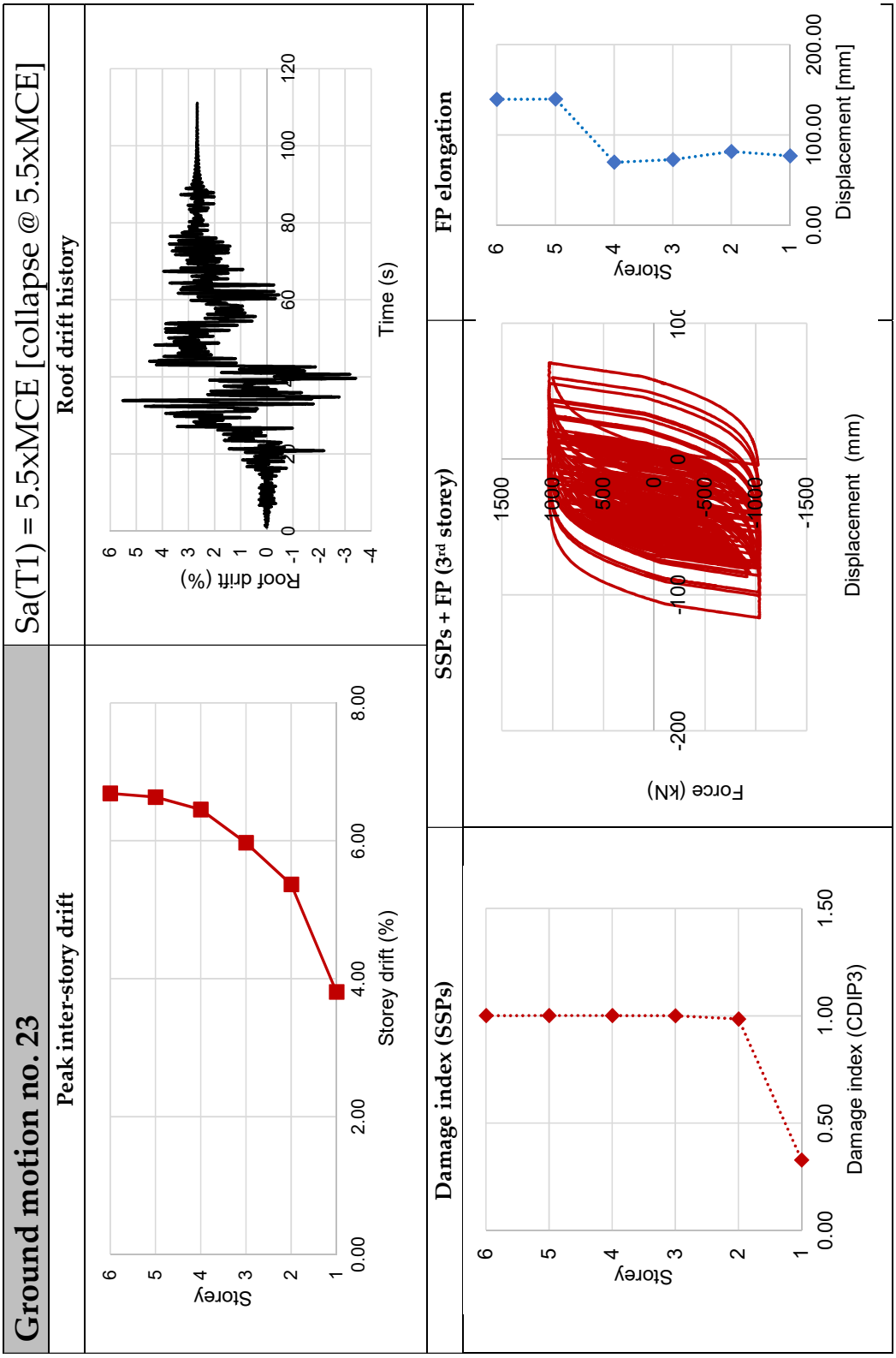

Figure D.23. IDA - Ground motion no. 23

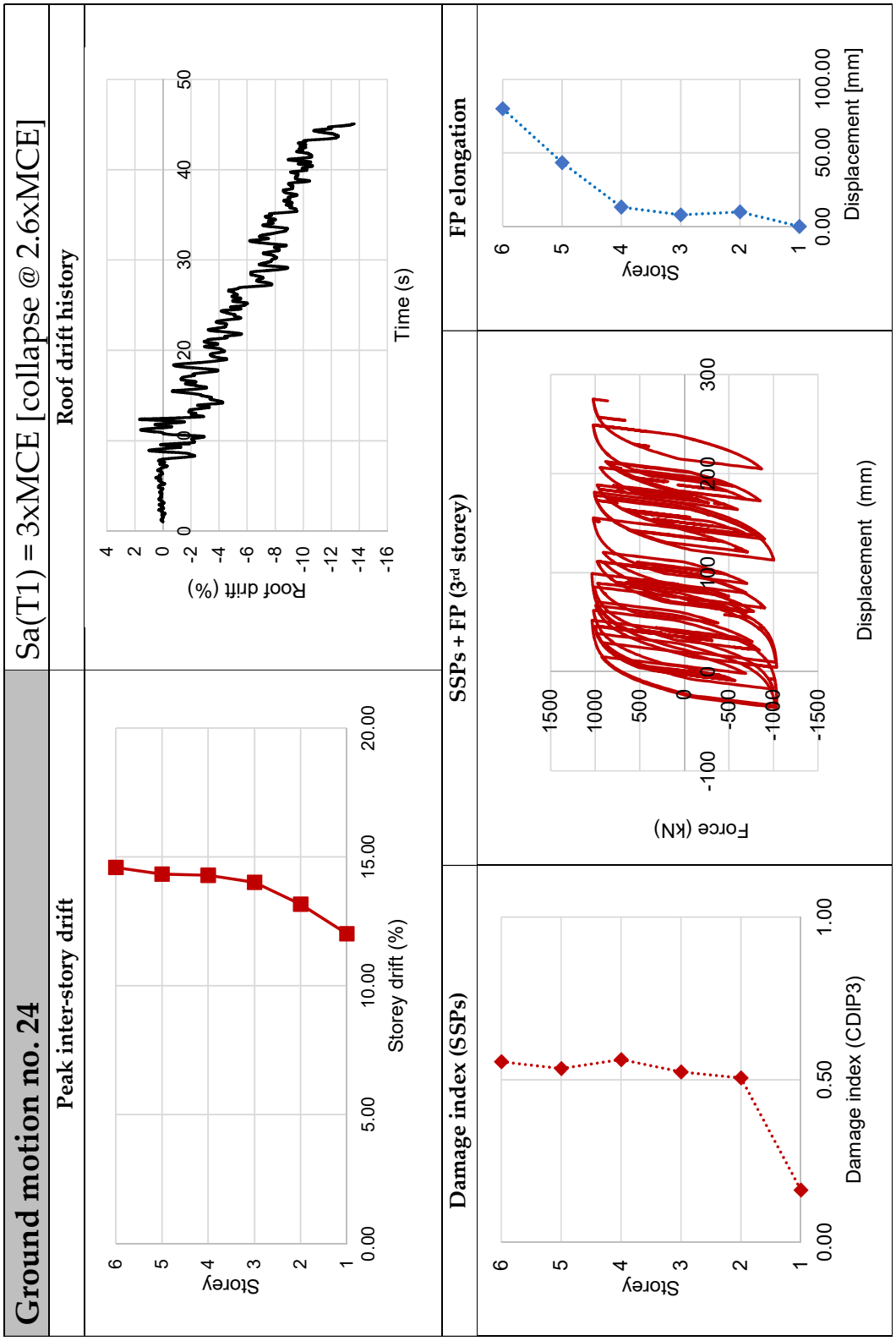

Figure D.24. IDA - Ground motion no. 24